GIMA

Geographical Information Management and Applications

Measuring the legacy of plants and plant traits using UAV-based optical sensors

Universiteit Utrecht

TU Delft

UNIVERSITY OF TWENTE.

WAGENINGEN UR

GIMA Master Thesis

Author: Bob van der Meij

Supervisor: dr. ir. Lammert Kooistra (WUR)

Professor: prof. dr. ir. Arnold Bregt (WUR)

February 2016

Colophon

February 2015
GIMA MSc Thesis

Contact information:
Bob van der Meij
Warande 144
3705 ZL Zeist
bobvandermeij@gmail.com

UU Student number: 3464091
ITC Student number: s6020518
WUR Student number: 910728-554-060

"Because the Earth is a dynamic system, sufficient understanding of the complex interactions among physical and ecological processes is needed (…). To achieve this goal, both long- and short-term observations are required to quantify, analyze, and subsequently understand the spatial and temporal variability, trend and magnitudes of changes in eco-systems dynamics"

(Qi et al, 2012, p79),

'(…) customer demand and general interest is present to the point that there are already some UAV geoinformation niche markets; in particular growing new market for small photogrammetric and remote sensing projects. The trend seems to be unstoppable.'

(Colomina & Molina, 2014, p93).

Summary

Although they have been effectively around for several decades, the societal interest for Unmanned Aerial Vehicles (UAVs) has recently taken off dramatically. The applicability of these remotely or automatically piloted aerial platforms is explored extensively in an endless array of different scientific fields, industries and professions. It is anticipated that (precision) agriculture (PA) in particular will represent the largest client of UAV technology in the coming decade. The ultimate objective of (PA) is to maximize productivity while minimizing economic costs and avoiding environmental harm. Consequently, practitioners of PA consider the presence of complex in field variability and require accurate and repeated information regarding crop statuses on a detailed small scale to adjust their intervening practices accordingly. Remote sensing has been extensively applied within agricultural sciences for this purpose in the past decades and proved capable of delivering intelligence on various biochemical and biophysical vegetation characteristics. Conventional sensing platforms and sensing systems, however, are generally unable to meet the combined spatial, temporal and, to a lesser degree, spectral resolutions required for establishing effective PA operations.

The advent of UAVs, however, is expected to invoke auxiliary possibilities within this industry due to unique enabling features provided by these platforms, particularly with respect to spatial and temporal resolutions. Additionally the relatively recent miniaturization of advanced hyperspectral sensor systems, delivering continuous spectral data in as many as hundreds of adjacent (narrow) bands, is increasingly considered for compatibility with precision agriculture agricultural applications. The resultant increase in spectral resolution has been demonstrated to grant access to analytic capabilities of a larger variety of vital agricultural parameters with enhanced precision and accuracy. Apart from the anticipated benefits, UAV based remote sensing and the resultant very high resolution data acquisition give rise to several potential drawbacks (i.e. space, payload and power (range) restrictions, in-flight susceptibility, processing power, large data volumes and data redundancy, visualization impracticalities, preservation of acceptable signal-to-noise and applicability of existing methodologies, among others), rendering the technology far from a self-fulfilling prophecy. In this study, the combined suitability of UAVs and hyperspectral cameras for small scale monitoring of crops is evaluated through utilization of a custom built UAV platform to which one of the latter sensing systems is mounted. At the Wageningen University & Research center a research is currently underway to investigate the assumed interrelationship between the legacies of plants present in soils and plant traits of current vegetation. It is this field experiment and the associated study area that provide the practical framework within which this research was shaped and subsequently conducted.

A UAV flight was conducted in the 2015 growing season over a field comprising of seventy separate plots cultivated with oats, each having received different treatments. Spectral data was acquired in the visible and near-infrared range (450-915nm) over 94 adjacent wavebands by a hyperspectral push broom scanner. Simultaneously, a RGB orthomosaic was acquired from which a Crop Surface Model (CSM) was eventually derived. Within the same time frame, in situ measurements of a variety of relevant agronomic crop parameters were retrieved from each plot (crop height, fresh biomass, nitrogen (N) content, carbon (C) content and leaf chlorophyll (Chl) content). Subsequently, the acquired hyperspectral data was related to distinct crop parameters in an independent calibration procedure through univariate regression analysis over individual wavebands, existing vegetation indices (VIs), new optimized indices and partial least squares (PLS) regression. For each trait, a selection of the best performing indices and models found during calibration was evaluated with respect to their precision and predictive accuracies on an independent validation set. Validation displayed considerably varied results, indicated by relatively high prediction capabilities for models estimating crop height (CVRMSE = 5.12%, R^2 = 0.79) followed by leaf chlorophyll content (CVRMSE = 14.5%. R^2 = 0.79). The best models related to prediction of N content (CVRMSE = 21.6%. R^2 = 0.68), fresh biomass

(CVRMSE = 20.8%. R^2 = 0.56) and C content (CVRMSE = 20.8%. R^2 = 0.52) exhibited larger prediction inaccuracies and lower precision. For all traits except height and leaf Chl content, derivation of new indices through an optimization algorithm considering all possible combinations of two narrow bands delivered enhanced performances. PLS regression only yielded higher prediction capabilities for fresh biomass, no improvements were observed for any of the remaining traits. Besides, the outcomes suggest that predictions through remotely sensed data for height, leaf Chl content, N content and, to a lesser degree, fresh biomass may be effectively further discriminated for different cultivars and their associated treatments

Next to quantitative results the research has illuminated a variety of additional points of interests that are to be considered in UAV based remote sensing (research). It is reasoned that the most considerable topic relates to demonstrated, and partially assumed, within plot heterogeneity on the one hand, and different densities at which field data was collect for distinct traits on the other. The latter resolves around the hypothesis of within plot homogeneity and the assumed representativeness of samples with respect to the remainder of distinct plots. Initially, however, it was observed that a selection of plots exhibited physical heterogeneity to various levels of severity. Furthermore, it has been reasoned that some of the inaccuracies observed in prediction of traits for separate plots may possibly be invoked by limited sampling procedures that inadequately reproduced (assumed) variability of the distribution of biophysical or biochemical crop attributes. Relatedly, the highest prediction accuracies were recorded for traits for which a comparatively higher sampling density was adhered to. Subsequently, it is believed that more intensive and homogenous sampling allows establishing of more robust relationships between spectral data and field data. It was also observed that the original data comprised of a heterogeneous image quality, indicated by various forms and degrees of radiometric flaws (i.e. illumination, striping and dead pixel issues) and geometric inconsistencies. The latter was accommodated for through the inclusion of a limited number of RTK-GPS measured ground control points and additional geometric processing of the data hereafter. Some of the radiometric errors were tackled through signal enhancement by vegetation indices although some (plausibly influential) errors have sustained. Alternative points of interest relate to the incorporation of two independent yet relatively small calibration and validation datasets, and the general applicability of the findings of this study. Regarding the former it has been observed that individual observations (plots) are allocated considerable leverage in regression analysis, hereby allowing potential errors originating from several stages of the (overarching) research to significantly influence the results. Relatedly, a considerable discrepancy was observed for fresh biomass and C content measurements in the calibration and validation set, which is argued to have affected the analysis at different stages to various degrees. At last, straightforward generalizing of the findings of this particular study to other studies and/or crops is considered questionable and should thus be treated with caution. Different plant species, their associated structure (e.g. planophile vs. erectophile), their developmental stage, among others, are known to (significantly) influence spectral signatures and, subsequently, the relationship(s) between spectral data (e.g. vegetation indices) and measured quantities of biophysical and biochemical properties. The latter variable relating to growth stage is argued to be particularly relevant in this instance. Spectral data on the oat plots was acquired when the crops had reached the maturation phase, only three weeks prior to harvesting. Various biochemical processes that are intensified throughout this phase have plausibly affected the spectra of crops, and the associated ability to discriminate in situ measurements. Calibration of relationships between both variables was found to be particularly complex in this final stage which, additionally, renders comparison of findings to previous studies focusing on a different developmental phase peculiarly problematic. Several suggestions believed to (partially) mitigate some of these concerns are presented throughout this report and the eventual discussion. Consequently, it is argued that the study of which the findings are presented in this document has yielded a variety of promising results from which auxiliary research in different directions may effectively depart.

Preface & Acknowledgements

Now that this document and the associated research have finally reached completion, a word of thanks is in place for those who have helped me along the way. In this regard I would like to specifically mention my thesis supervisor Dr. Lammert Kooistra. His support, continuous enthusiasm, benevolence and constructive feedback have greatly aided me in reaching this point. Subsequently, I would also like to thank Dr. Gerlinde de Deyn. Her involvement, assistance and sincere interest in all that has been going on in the past few months resulted in a very pleasant collaboration. At last I would like to thank Dr. Juha Suomalainen for his patience and willingness to improve the raw UAV data and enhancement of its quality and usability for this research.

I can still easily recall the first time I walked into Lammert's office at the end of August. Shortly after I was pinned down by a barrage of critical, yet highly legitimate, questions regarding my (lack of) prior knowledge and experience within the associated fields of research. Admitting the truth, I was initially overwhelmed by these deliberations and wondered whether my goals may have been too ambitious. Nonetheless, now that the process has been finished and the final document is in print, I am glad I took on the challenge after all. It has been a bumpy ride with various complications and hiccups along the way. More importantly, however, I have learnt significantly from the entire process, including those periods in which I was challenged excessively and progress seemed lacking. The individuals mentioned above continued to provide me with interesting and, above all, new insights into fields that I was relatively little familiar with and never refrained from motivating me to keep pushing ahead. Conversations and discussions were never tedious, to say the very least, but rather very informative and fascinating at times instead. I am looking forward to applying and further extending my gained knowledge, understanding of concepts and associated techniques in the years to come, during my internship and eventual professional career. Above all, however, I genuinely hope that this study adds to the existing body of knowledge and may possibly serve as a basis from which future research may depart.

All that remains for me now is to wish you all the best reading through the document in front of you. Please feel free to get in touch with me if questions or obscurities arise along the way, I will always be willing to provide you with additional information.

Table of Contents

Lists

Figures

Tables

Abbreviations

AVIRIS	Airborne Visible / Infrared Imaging Spectrometer
CASI	Compact Airborne Spectrographic Imager
C	Carbon
Chl	Chlorophyll
CSM	Crop Surface Model
DEM	Digital Elevation Model
DSM	Digital Surface Model
GIS	Geographic Information Systems
GPS-INS	Global Positioning System-Inertial Navigation System
Fa	Fallow (treatment)
FBM	Fresh Biomass
FDR	First Derivative Reflectance
HDC	Hyperspectral Data Cube
FV	Fitted Values
HS	Hyperspectral
HYMSY	Hyperspectral Mapping System
LAI	Leaf Area Index
Lp	*Lolium perenne* (treatment)
LiDAR	Light Detection And Ranging
N	Nitrogen
NDVI	Normalized Difference Vegetation Index
NIR	Near-Infrared (spectrum)
NLV	Number of Latent Variables
nm	Nanometer
MS	Multispectral
PA	Precision Agriculture
PLS(R)	Partial Least Square (Regression)
PRESS	Predicted Residual Error Sum of Squares
r	Correlation coefficient
R^2	Coefficient of determination
RGB	Red-Green-Blue (spectrum)
RSME(P)	Root Square Mean Error (of Prediction)
REP	Relative Error of Prediction
Rs	*Rapharus sativa* (treatment)
SAR	Synthetic Aperture Radar
SWIR	Short-wavelength Infrared (spectrum)
TI	Thermal Infrared (spectrum)
Tr	*Trifolium repens* (treatment)
UAV	Unmanned Aerial Vehicle
VIS	Visible (spectrum)
Vs	*Vicia sativa* (treatment)
WUR	Wageningen University & Research centre

Appendices

1. Introduction

1.1 Introduction

Ever since the first photograph of the Earth's surface was acquired from an aerial platform in the midst of the 19th century, the interest for the associated technology enabling human beings to collect remotely sensed imagery of our planet has developed at a formidable pace. Driven by an amalgam of sheer curiosity and conviction of its applicability within practically an endless number of fields, a wide array of different platforms and sensors have come into being over the course of the past decades for these means (Lillesand et al., 2014). Through the use of such sensors one may distil unique imagery of a specific study area from a distance in a non-destructive manner, sometimes including radiation oriented spectral information normally undetectable by the human eye, among others, such as thermal, atmospheric and three-dimensional intelligence (Campbell & Wynne, 2002).

For remote sensing purposes, sensors may be mounted on various platforms belonging to one of the following operational modes: ground-based, airborne or space borne (Ortenberg, 2012). Whereas space and airborne platforms are considered ultimately applicable for remote sensing on the regional and/or global scale, they subsequently fail to meet the conditions required for remote sensing purposes on (significantly) smaller scales (Bareth et al, 2014). Relatedly, though their potential was already considered three decades ago, Unmanned Aerial Vehicles (UAVs) have only recently received notable scientific and societal attention (Colomina & Molina, 2014). UAVs are capable of covering sizable areas in a relatively short period of time at equally short distances from the area and/or objects under study. These features allow imagery acquisition at uniquely high temporal and spatial resolutions (Eling et al., 2014). As a result, both commercial and scientific interest for UAV-based remote sensing and geo-information collection has expanded recently and is rapidly maturing (Bendig & Bareth, 2014). Relatedly, scholars worldwide are exploring its applicability within a wild array of interested fields, hereby further advancing the technology to allow tackling of the associated challenges and optimizing its pertinence (Colomina & Molina, 2014; Everaerts, 2009).

The potential of UAV-based imagery collection is now considered and explored within a diversified and continuously growing number of fields. The interest for agricultural vegetation monitoring using UAVs is increasing particularly substantial (Colomina & Molina, 2014). A related and relatively novice subfield within the agricultural industry to which UAV-based remote sensing technology is considered ultimately valuable is precision agriculture (PA) (Honkavaara et al., 2013; Zecha et al., 2013; Lelong, 2008). PA represents the ultimate example of agricultural practices becoming ever more efficient and profitable, through enhancing a more effective management of inputs (e.g. herbicides, seeds, fertilizers and soil content) zonally and adequately adjusting intervening practices (Huang et al., 2013). This notion suggests that farming methods should be executed with a fairly high level of precision, reaching plot or even plant level, to maximize yields and limit excessive use of potentially environmentally detrimental substances (Zhang & Kovacs, 2012). In precision farming, the challenge thus largely comprises tackling of issues related to scale and uncertainty, besides finding meaningful ways for delivering the information to practitioners (e.g. through prescription and/or variable rate application maps), preferably in near-real time (Dobermann et al., 2004; Lamb & Brown, 2001; Flemming et al., 2000). Resultantly, research incorporating miniaturized experimental agricultural plots to develop and evaluate innovative methods to optimize farming procedures is substantiating.

Distinct crop features such as structure, composition and quantitative characteristics interact spectrally different with incoming electromagnetic radiation (Homolová et al., 2013; Mulla, 2013). As a result, information derived from spectral remote sensors can aid in measuring and mapping of varying biophysical

and biochemical traits of crops, classification of different crops, crop growth, and soil mapping, among others (Zhang & Kovacs, 2012). Especially optical (narrow band) hyperspectral sensors have revolutionized the use of remote sensing for monitoring (agricultural) vegetation. It is generally accepted that, for these purposes, narrowband hyperspectral optical sensors are superior to broadband (e.g. multispectral) sensor systems (Ortenberg, 2012). This is due to their significantly enhanced ability to discriminate between unique vegetation properties of which anomalies in reflective behavior may only be discerned when their spectral signatures are measured at small continuous intervals (Mulla, 2013; Nguyen & Lee, 2006; Campbell & Wynne, 2002). Once collected and processed, the acquired data can be effectively utilized to support decision-making processes in crop management, yield forecasting and/or environmental protection (Thenkabail et al., 2012b; Haboudane et al., 2002). Zhang & Kovacs (2012), however, state that the application of remote sensing in small scale PA is still rather limited. Currently, PA oriented research is still mostly relying on time-consuming and labor intensive sampling methods. It is argued that this may be partially related to the notion that while conventional remote sensing platforms have proved a valuable means for agricultural purposes on the regional and larger scales, space and air borne remote sensing are either largely or completely unsuitable for application in PA solely by themselves (Nebiker et al., 2008). In this regard, issues resulting from frequent cloud cover, inadequate revisiting time, high operational costs, insufficient spectral and spectral resolution, among others, are frequently mentioned (Primicerio et al., 2012; Zhang & Kovacs, 2012; Mulder et al., 2011; Zhang et al., 2002).

Practitioners of PA are on a continuous quest to devise and implement new sustainable methods that preserve or improve the quality and reliability of information acquisition, besides meeting a variety of qualifications (Kooistra et al., 2014). In respect to considering remote sensing for application in PA, imagery ought to be affordable and provided at uniquely high spatial, spectral and temporal resolutions (Berni et al., 2009; Nebiker et al., 2008; Zarco-Tejada et al., 2008). Considering the inability of conventional ground, air and space based sensing systems to meet all of these requirements by themselves, UAVs offer unique and highly desired capabilities that may provide auxiliary intelligence for practitioners of PA, particularly when combined with alternative sources (i.e. ground/aerial/satellite platforms) of intelligence (Rango et al., 2009). More specifically, this relates to the combination of very high spatial (cm) and temporal (frequently and near real-time) resolution imagery, and an unprecedented operational resilience at limited costs and effort. Considering spectral capabilities, initial commercial UAV platforms were endowed with relatively simple (consumer) cameras operating in the VIS and/or NIR spectrum using broad bands (Konkavaara et al., 2013; Hunt et al., 2010). As technological capabilities advanced and sensor systems were increasingly miniaturized, the way for incorporating auxiliary and higher-order sensors on these platforms was successfully paved (Colomina & Molina, 2014). Principle examples include both multispectral (Retzlaff et al., 2014; Nebiker et al., 2008) and hyperspectral (Bareth et al., 2014; Calderón, 2014; Suomalainen et al., 2014) systems, when considering the purpose of mapping distinct plant traits in particular. Thanks to these enabling features, UAVs effectively bridge a gap that previously existed between other sensing systems (Xiang & Tian, 2010).

Finally, the number of hyperspectral systems on board UAV sensing platforms is still far outnumbered by its broadband multispectral counterparts (Suomalainen et al., 2014; Shippert, 2004). Likewise, hyperspectral remote sensing is still primarily utilized within the scientific community for experimental purposes, although commercial availability of hyperspectral sensors (e.g. CASI & Hymap) is gradually growing (Govender et al., 2007). These deliberations, however, may be partially ascribable to the notion that contemporary hyperspectral remote sensing suffers from several limitations, such as large data volumes and data redundancy, visualization impracticalities, preservation of acceptable signal-to-noise ratios, and the fact that some broadband oriented methodologies are unsuitable for processing of hyperspectral data, among others (Qi et al., 2012). Besides, hyperspectral sensors tend to be larger and

more expensive than their multispectral counterparts (Colomina & Molina, 2014; Huang et al., 2013). When hyperspectral sensors are utilized for agricultural purposes, they are therefore majorly space borne (e.g. Hyperion) or airborne (e.g. AVIRIS, CASI), and specifically applied for large scale agriculture (Mulla, 2013). Research in which hyperspectral spectroscopy from the sensor point of view, and UAVs regarding sensing platforms, are unified and applied for small scale agricultural applications is relatively scarce. It is argued here that evaluation of the application of high resolution hyperspectral imagery onboard UAV platforms is worth exploring considering the undeniable benefits both components are believed to offer to precision agriculture.

1.2 Background & practical relevance of research

At the Wageningen University & Research (WUR) center a field experiment is underway as of March 2014, investigating the legacies of various cover crops and combination of crop species. It is argued that the (un)successful growth of present vegetation is inherently determined by biological traces (i.e. phatogens, nematodes, phytotoxic substances) left by different types of preceding agricultural land use or cultivars, resulting in heterogeneous topsoil (Selige & Schmidhalter, 2006; López-Granados et al., 2005; Moran et al., 1997). Within the field experiment, an attempt is made to better understand the assumed interrelationship between dead plant material provided by preceding vegetation, the (resultant) biological composition and activity of soil, and various characteristics of current vegetation (e.g. productivity, composition and structure) respectively. Such legacies present in soil are one of the agronomical inputs practitioners of precision agriculture are increasingly trying to unveil in order to enhance management of crops and optimize yields more efficiently and effectively (McBratney et al., 2005; Whelan & McBratney, 2000).

Considering the labor-intensive and costly endeavors currently undertaken to perform manual analysis of traits of interest on relatively small spatial scales, as is currently done in this field experiment, the ability to execute such assessments differently in a fast, robust and cost-efficient manner is in high demand (Kuang & Mouazen, 2011; Nebiker et al., 2008). Given these deliberations, the applicability and usefulness of (advanced) optical sensors on board a UAV platform are currently being investigated at WUR, through integration of this analytical component into the overarching field experiment. The latter, focusing on the remote retrieval of crop attributes, is where this research comes into play.

1.3 Scientific & societal relevance

The following research is motivated from different directions, fueled by a combination of partially overlapping fields of interests in contemporary precision agriculture and remote sensing, and their anticipated future development. Conventional air and space borne remote sensing platforms are currently unable to meet the distinct needs of small scale precision agriculture, especially in regard to different dimensions of resolution, costs, flexibility, repeatability, and near real-time information provision (Mulla, 2013; Primicerio et al., 2012; Zhang & Kovacs, 2012; Mulder et al., 2011; Zhang et al., 2002). Therefore, precision agricultural experiments and practices are heavily relying on labor-intensive manual procedures, destructive sampling and spectral measurements of plants and soils on the ground, hereby challenging the associated goals of adequate, repeated and cost-effective farming (Nebiker et al, 2008). Resultantly, development and evaluation of new technologies for precise crop monitoring is considered one of the primary pillars in contemporary and future precision agriculture oriented research (Arnó et al., 2009; Dobermann et al., 2004). Mapping and quantification of in-field variation by UAV based remote sensing embodies one of these new technologies for which exploration in regard to its applicability to the industry is highly desired.

As far as remote sensing is concerned, the potential of UAVs for monitoring and mapping purposes was articulated on multiple occasions in the (recent) past. On these occasions, however, it was similarly stated that additional research into the performance of UAVs and their on board sensors for various applications is required continuously (Everaerts, 2008). This is especially relevant when one considers that some of the challenges UAVs potentially suffer from render their suitability and accuracy far from self-evident (Hardin & Jensen, 2015). Besides, in UAV based remote sensing research, hyperspectral systems are still clearly outnumbered by their multispectral counterparts (Suomalainen et al., 2014). Therefore, continued exploration of what UAVs are (not) capable of within different field of applications using different sensors, such as precision agriculture, is considered a valid topic in contemporary remote sensing research. More specifically, proper analysis methods and the associated (i.e. geometric and/or radiometric) accuracy of thereofs with respect to a distinct application, taking into account the resultantly increased resolution(s), require careful evaluation (Hardin & Jensen, 2015; Hruska et al., 2012; Lelong et al., 2008).

Regardless of the anticipated benefits for PA of both UAVs and hyperspectral spectroscopy, research which integrates all three components is still marginal. Agriculture oriented research incorporating hyperspectral remote sensing is still mostly geared towards large scale agriculture, relying on imagery acquired by airborne and/or space borne platforms (Zhang & Kovacs, 2012). Likewise, studies related to precision agriculture and the use of UAVs primarily cover sensors other than hyperspectral ones, such as multispectral optics. Therefore, research on the appropriate analysis methods for spectral decomposition should receive renewed attention, now that distinct hyperspectral spectroscopy and sensing platforms combined allow capturing of imagery at both spectral and spatial resolutions required for effective PA. In addition, it is considered ultimately vital to continuously investigate the possibility of generating new value adding and accurate spectral indices for measuring crop characteristics (Mulla, 2013).

1.4 Research Objectives

Given the deliberations presented in this introductory chapter thus far, the primordial objective of this explorative research is to evaluate how, and to which extent, UAV based optical sensors can assist agricultural practitioners in mapping and quantification of specific plant traits. Consequently, this study aims to demonstrate the potential of UAV based hyperspectral spectroscopy for precision agriculture, and to evaluate the suitability of the obtained mapping results regarding their possible integration into the associated practices. This includes evaluation and comparison of the performance of different data analysis approaches based on different (sensor) inputs. As was mentioned previously, UAVs and PA are relatively novice fields. Resultantly, the coverage of both elements, especially when hyperspectral spectroscopy is added to equation, is still limited. This thesis research therefore ultimately aims to add to the currently existing knowledgebase and potentially provide auxiliary directions for future research.

Although the research process flows through a substantial number of phases, three overarching stages can be identified. The first, exploration, comprises of an extensive literature review to acquire, expand and enhance the understanding of relevant theories, concepts, data processing techniques and jargon. This exploration is specifically geared towards UAVs, remote sensing and precision agriculture, as well as the associations between these themes. Preparation of both field and aerial UAV data embody the second stage. This relates to application of various corrections to the data, retrieval of trait metrics and generation of supportive datasets to aid in the analysis stage. In the third and final stage the data is subsequently processed, including spectral feature extraction analysis, calibration and validation of different models, and statistics, among others. Eventually, the results are evaluated, compared to the findings of the preceding literature stage and assessed in regard to accuracy and applicability for application in PA. In short, the final stage provides a synthesis of the preceding research and answers to the problem statement that is derived.

1.5 Research Problem Statement

In order to eventually reach the objectives of this research, the following problem statement has been formulated:

- *To what extent can optical sensors on board a UAV platform be used to identify, map and quantify biophysical and biochemical traits of crops?*

Here, the *identification* component relates to the ability to successfully discriminate between the different traits under study. The *mapping* aspect deals with the capacity to accurately locate the identified traits in space. Finally, *quantification* deals with the associated capability of distilling and predicting correct numerical values/quantities/proportions to the identified traits in respect to ground-truth measurements.

Subsequently, to further structure the research process, the following sub questions will be addressed:

- Which specific biophysical and biochemical crop traits are considered relevant for identification, mapping and quantification considering precision agricultural practices?
- Which remote sensing methods, requiring which data input, can be used to identify, map and quantify these traits?
- How do these different methodologies perform when applied to the selected traits, using UAV acquired imagery, in regard to precision and (prediction) accuracy?

1.6 Research scope

It is considered vital to adequately delineate the research, i.e. to define its scope. The problem statement and sub questions mentioned above relate especially to what *will* be covered by this study. The delineation is further clarified and completed by stating what the research objective is *not* about below:

- The research only covers the use of remote sensing of vegetation by means of optical sensor systems and reflected electromagnetic radiation in the visible and near-infrared spectral region Analysis of emitted radiation by means of thermal sensor systems and/or evaluation of data derived from Light Detection and Ranging (LiDAR) sensors are excluded. This is not to say they are irrelevant for vegetation monitoring (previous research has confirmed they are to various degrees), but rather the direct result of the notion that the UAV platform that will be used during this study does not carry any of such sensors.
- The research will not cover comparative analysis of agriculture oriented remote sensing by different platforms. UAVs are the primordial and only remote sensing platform considered here.
- The research will evaluate the use of optical sensors for crop phenology at a single moment in time. Dynamics and differences caused by crop growth/development through time are not included. This has been purposely decided for two specific reasons. The first is to limit the scope of the research and align its feasibility with the given time constraints. Secondly, the dataset's temporal resolution does not allow such analysis. The research deliverables, however, may provide auxiliary directions and input for future research that incorporates the temporal dimension.
- Overcoming contemporary relevant challenges currently facing the application of hyperspectral remote sensing (e.g. excessive data volumes, data redundancy, and visualization difficulties) may be partially or indirectly touched upon, but do not represent the focal point of this research by any means.

1.7 Conceptual model

Based on the initial exploration of the research, its objectives and the associated problem statement and sub questions provided in this introductory chapter, a conceptual model was established (figure 1.1). The model depicts the most fundamental concepts, themes and components related to this study, as well as their (assumed) interrelationship. It supposedly provides a simplified but comprehensive and directional visual representation of the research presented here. The left (green) and right (orange) side of the model depict the two major overarching fields of interest incorporated in this thesis, agriculture and remote sensing, respectively. Each is gradually broken down to more specific constructs, or variables, in boxes in the vertical direction. Connections depicted as one-way or two-headed arrows depict rather causal relationships between variables, indicating some sort of cause-effect or input-output dependency. Lines without arrows represent relationships that do not necessarily express causality. Textual additions to the relationships indicate how relationships are to be interpreted. At the very bottom, the linkage between distinct specifics of both fields of interest (crop monitoring for PA and UAV based optical remote sensing, respectively) put forward the eventual problem statement that will be covered in this thesis (in cyan).

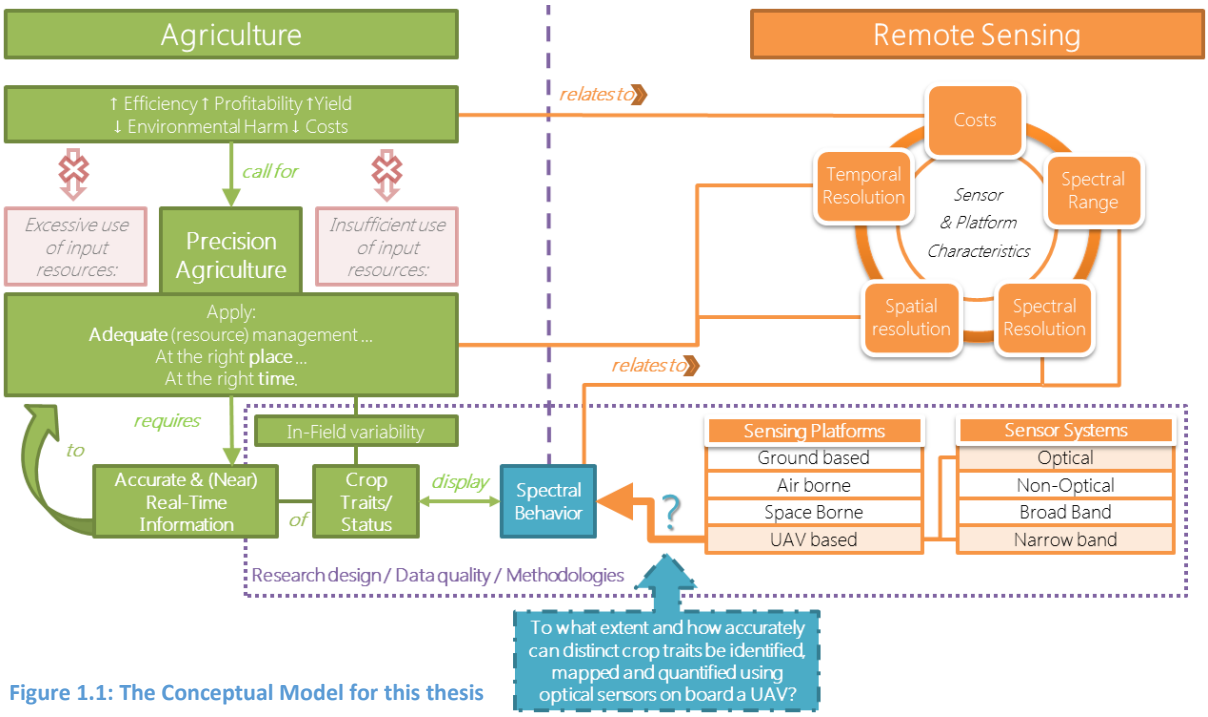

Figure 1.1: The Conceptual Model for this thesis

1.8 Thesis report structure

In order to enhance the readability of this extensive report a textual overview of the document's structure is provided here. The reader is strongly advised to take note of this supplement, to allow efficient locating of the components deemed relevant.

In the upcoming chapters, the relevant theoretical context of this research will be further and extensively elaborated on. The first theoretical chapter deals with remote sensing specifically, including a short history, its application, different platforms and (relevant) sensor systems, among other themes. Subsequently, the third chapter discusses the use of remote sensing in vegetation monitoring. Besides, the recent developments in the agricultural industry, particularly in regard to the advent of precision agriculture (PA), are discussed. Likewise, the requirements of PA in regard to application of remote sensing technology are mentioned. The fourth and final theoretical component is geared towards plant traits and their spectral behavior in the electromagnetic spectrum. More importantly, the chapter identifies the most vital agronomic traits of crops for PA practices and elaborates on their relevance. A tabular overview of existing indices used to map these traits in previous remote sensing studies is also provided, the textual elaboration on these matters is provided in appendix C. Next, chapter five elaborates on acquisition of the data included in this research. This section comprises of a description of the study area and the UAV platform used, and of how the data was collected in the field and from the air, respectively. Besides, various stages of pre-processing that were applied prior to this research are briefly discussed. In chapter six the methodological framework adhered to is presented, indicating the distinct phases within the overarching stages that characterize this study. This includes mentioning of different techniques to be used and justification of decisions that were made. A visual representation of the methodological framework, i.e. the operational design, is also given. From chapter seven onwards the actual analysis is commenced and its results presented. This includes an exploratory analysis of the data (chapter 7) and both calibration (chapter 8) and validation procedures (chapter 9), in addition to linking of the results to findings in existing research. These chapters are followed up by an extensive discussion in which relevant deliberations and possible limitations of this research are considered. Following from here, an array of directions for future research is presented. The study is brought to a conclusion in chapter eleven through some brief concluding remarks.

2. Theoretical context: Remote sensing & UAVs

2.1 Brief history of RS and its applications

Throughout its existence, various endeavors have been undertaken to concisely establish an all-encompassing definition that fits the field of remote sensing and the associated techniques and their applications. An overview of such definitions is presented by Campbell & Wynne (2002). Varied as they might be, each describes at least the importance of 1) acquiring information (passively or actively) of 2) objects or events from 3) a distance (Cracknell & Hayes, 2007; Elachi & Zyl, 2006). For acquired data to be considered as information, however, interpretation or processing is required. As a result, the relatively general yet broadly applicable definition adhered to here defines remote sensing as '*the collection and subsequent interpretation of information of an object, area or event that has been derived without contacting the target under study physically*'. Even though this theoretically implicates that conventional photography can too be considered a form of remote sensing, the latter is distinctly different due to the frequent use of different equipment and techniques to acquire alternative information, for example outside the visible wavelength range (Cracknell & Hayes, 2007). Nonetheless, initial progress in the field of remote sensing was, not surprisingly, a direct result of advancements in a related field of expertise, namely photography (Lillesand et al., 2014).

Remote sensing at its simplest comprises of several elements as visualized below in figure 2.1. The first embodies the energy source (e.g. the sun) that illuminates light or disseminates electromagnetic energy to one or multiple targets (1). Subsequently, as the energy passes to or from the target it interacts with the intermediate atmosphere (2). Eventually, the energy interacts with a target, although the distribution and level of energy over different wavelengths is particularly shaped by distinct properties of the target at the receiving end (3). Depending on how much energy is transmitted, absorbed, emitted and/or reflected, a (passive) sensor mounted on a platform at a distance may be used to measure the incoming remaining radiation (4). Finally, the received data requires transmission (5), processing, interpretation and analysis (6), to eventually arrive at one or multiple applications (7) (Sahu, 2008; Kumar, 2005).

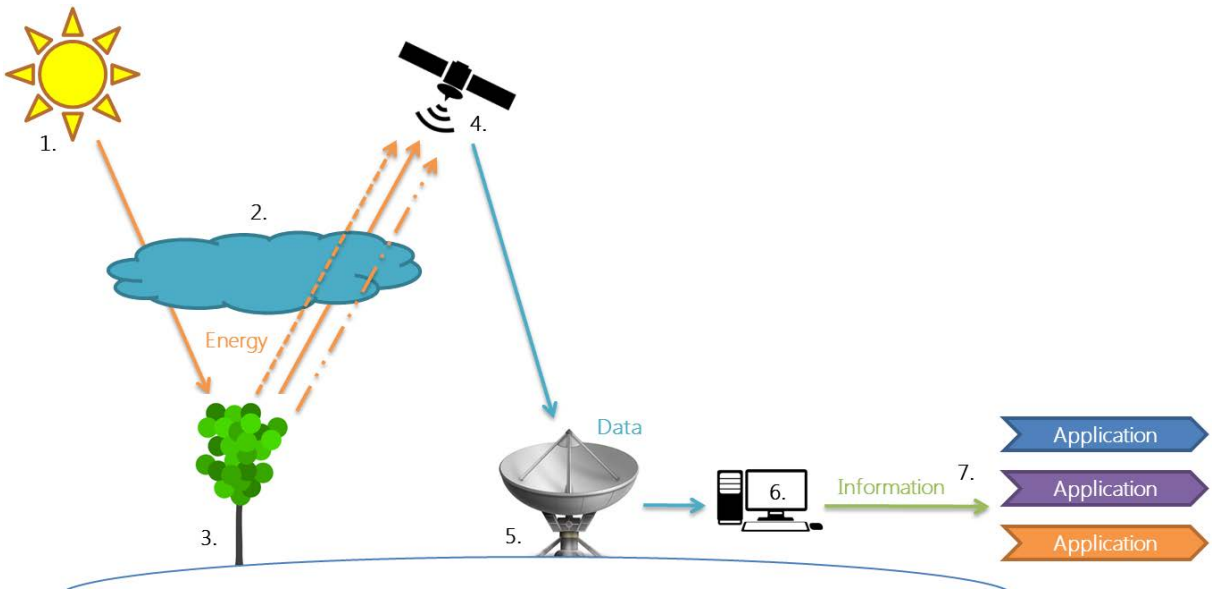

Figure 2.1: Simplified visual representation of the elements present in remote sensing. Please take note that here the sun is depicted as the energy source in case of passive RS (paragraph 2.3), although this could be replaced by an antenna in active RS. Likewise, targets other than vegetation may be incorporated. Similarly, the depicted satellite may be replaced by alternative operational modes.

The first known aerial photographs captured from a balloon in the midst of the 19th century, taken by Parisian photographer Gaspard-félix Tournachon, marked the initiation of remote sensing according to many sources (Lillesand et al., 2014). Subsequently, kites and pigeons were utilized to mount cameras on. In the early and late 20th century, development of remote sensing from aircraft and spacecraft was introduced, allowing image capturing under relatively controlled conditions. Concerning imagery, black and white photography was replaced by color photography in the 1930s, to be further extended into the near-infrared range soon after. Concurrently, active and passive microwave systems were also included from the early 20th century onwards, similar to radar systems. In the 1960s, multispectral sensors were developed and exploited from various platforms extensively (Elachi & Zyl, 2006). In approximately the same time frame laser instruments were developed. Narrow band hyperspectral imagery emerged more recently, in the 1980s (Qi et al., 2012).

Applications of remote sensing were initially geared towards topographic purposes, although remote sensing was increasingly used by the military for surveillance and reconnaissance, especially during WW II (Cracknell & Hayes, 2007; Elachi & Zyl, 2006). As of today, remote sensing is omnipresent in a highly varied array of industries and disciplines in which the associated techniques and output data are utilized for an equally substantial number of deviating purposes, such as land use mapping, geological and soil mapping, planning applications, forestry, (wildlife) ecology, geomorphology, archaeology, disaster management, climatology, agriculture, civil engineering, meteorology, pollution monitoring, among many more (Lillesand et al., 2014; Rees, 2013; Cracknell & Hayes, 2007).

2.2 RS Platforms

Platforms represent the vehicles or carriers for remote sensing equipment (Sahu, 2008, p 129). Sensors may be mounted on practically an endless variety of different platforms, ranging from simple ground equipment to advanced space complexes and everything in between, such as trucks, helicopters and zeppelins. Considering this diversity, an overarching classification comprising of ground, air and space based platforms is frequently adhered to for clarification. Due to the operating conditions that each environment invokes, each type of platform is familiar with a range of distinct advantages, challenges and limitations (Ortenberg, 2012). The eventual application of the remotely sensed imagery, however, ultimately determines what platform and its associated characteristics are more suitable than others.

2.2.1 Ground, air & space based systems

Ground based systems refer to those platforms physically handled on the ground by hand (e.g. spectroradiometers), from trucks, or in a laboratory environment (Qi et al., 2012). Due to the limited ground-sensor distance and the resultantly small Field-of-View (FOV), ground based systems are known to provide the highest spatial resolution, in the order of centimeters (Nebiker et al., 2008). Besides, ground based systems are relatively flexible and easily deployable, allowing analysis in (near) real-time (Ortenberg, 2012; Qi et al., 2012). Even though ground-based systems are, generally speaking, less costly to operate and maintain than air- and space borne systems, they provide a highly limited aerial extent rendering them less useful for covering larger areas repeatedly (Gopi et al., 2008). Ground based platforms are frequently utilized to calibrate sensor systems that are eventually exploited from either air- or space borne platforms (Ortenberg, 2012; Barrett & Curtis, 1999). Alternatively, measurements conducted by these ground based systems have been used to validate measurements from aerial or space borne platforms (Bareth et al., 2014).

Aerial platforms are majorly represented by conventional fixed-wing aircraft, although alternatively they may refer to other mobile vehicles such as balloons, helicopters and rockets, among others. In contrast to ground based platforms, aerial systems provide a substantially larger coverage and may be deployed practically anywhere (Gopi et al., 2008). In addition, airborne systems are generally more flexible than their space based counterparts in regard to flight scheduling and adjusting of sensing equipment/flying height to fit the required spectral and/or spatial resolutions, respectively (Qi et al., 2012). Depending on the aircraft's altitude and FOV of the camera, a sub meter ground resolution can be realized (Ortenberg, 2012; Nebiker et al., 2008). Due to the capturing of imagery based on the flight line direction and attitude of the aircraft, however, the data's geometrical quality is inherently influenced by environmental conditions such as wind, flight speed and alignment (Qi et al., 2012). Besides, especially in comparison to ground based platforms, aerial remote sensing suffers from significant operational costs (Primicerio et al., 2012). Likewise, compared to space borne equipment, airborne sensing is generally more expensive due to a smaller swath width and reduced speed of the platform (Qi et al., 2012).

The introduction of remote sensing into space provided a substantial boost to the development of the field and its applicability, due to opening up of an entirely new dimension allowing continuous observation of the Earth's surface on a global scale (Elachi & Zyl, 2006). As a result, global patterns (especially in climatology) have been illuminated and unraveled in the past that could not be accomplished using any of the other platforms (Gopi et al., 2008). Due to their high altitude, space borne systems are capable of covering large areas in relatively little time, producing cost-efficient imagery when considering costs per unit surface area (Qi et al., 2012). The costs associated with its development and maintenance of the required ground support facilities, however, render satellite remote sensing a far from inexpensive endeavor (Ortenberg, 2012). Besides, the large coverage equals a spatial resolution that may be considered too coarse for certain applications (Zhang & Kovacs, 2012). Compared to aerial platforms, space borne systems enjoy the benefit of being operable in all weather conditions, although cloud cover may effectively obstruct image acquisition (specifically in the VIS/NIR) at times (Mulla, 2013; Cracknell & Hayes, 2007). Besides, repetition and regular data acquisition deemed relevant for temporal studies may not be accommodated for by space borne sensing systems due to inadequate revisiting times (Zhang et al., 2002). Furthermore, as a result of the considerable ground-sensor distance, atmospheric distortions are likely to influence signals underway, requiring adequate radiometric correction prior to analysis (Cracknell & Hayes, 2007).

2.2.2 Unmanned Aerial Vehicles (UAVs)

Even though the fields of photogrammetry and remote sensing identified the potential held by Unmanned Aerial Vehicles (UAVs) several decades ago already, recent advancements in robotics, geomatic engineering and computer vision have recently taken the promises of Unmanned Aerial Vehicles to a whole new level (Colomina & Molina, 2014). During the 2008 ISPRS congress in Istanbul it was articulated that UAVs are ingenious sensing platforms, believed to be capable of introducing auxiliary directions for remote sensing to a larger group of (new) users (Everaerts, 2008). In fact, UAV represents a rather generic term that refers to a substantial number of different platforms that vary with respect to their physical shape (e.g. fixed-wing, glider, or rotor shaped), degree of (auto) piloting, size (nano, micro, mini) (payload) weight, range (close, short, medium), flying altitude, and nature of application (Colomina & Molina, 2014). Regardless of the vast diversity of differences between unique UAVs, however, all essentially comprise of an aircraft (platform) component, a sensing payload and a ground control unit (Watts et al., 2012).

UAVs are believed to offer (partially) unique advantages for distinct purposes compared to more conventional platforms, such as repeated deployment at relative ease, less expensive (and arguably safer)

than piloted aircraft, reduced operational complexity, flexibility with regard to altitude adjustments and provision of access to high resolution imagery in the order of centimeters (Carrivick et al., 2013; Everaerts, 2009; Rango et al., 2009). In accordance with more generic remote sensing jargon, benefits of UAVs are frequently described along the lines of an enhanced spatial and temporal resolution at affordable costs, alternatively complemented by a high spectral resolution, depending on the sensor system(s) (Kooistra et al., 2014; Zhang & Koavacs, 2012; Berni et al., 2009). Nebiker et al. (2008) summarize the benefits presumably offered by UAVs as being able to effectively fill the (resolution) gaps between air- and space borne remote sensing on one side and ground based sensing on the other. It is worth mentioning, however, that the extent to which these advantages may be realizable, if at all, is further influenced by the purpose of use and local regulations and legislations, respectively.

Besides, one should note that UAVs face several challenges in contemporary remote sensing practices as well, especially regarding space, payload and electrical power (range) restrictions (Caris & Stanko, 2014). Besides, the relatively low weight of the platform renders it susceptible to in-flight distortions, such as wind buffeting, which potentially affects adequate capturing of images under stable camera, tilting and illumination conditions (Hardin & Jensen, 2015; Lelong et al., 2008). In addition, considering typical payload limitations of approximately 20-30% of the UAVs bare weight, imaging system's weight may only be in the order of few ounces or kilo's when considering most micro or mini UAVs (Nebiker et al., 2008). The advent of different sensing payloads in UAV based remote sensing is therefore inherently depended on the progress in miniaturization of such sensors (Colomina & Molinda, 2014). In this regard, (commercial) RGB cameras have dominated the UAV sensor market since its initiation (Konkavaara et al., 2013; Hunt et al., 2010). In contrast, miniaturization of multi- and especially hyperspectral optical cameras is relatively challenging (Nebiker et al., 2008). The latter in particular are more expensive and larger in size, and therefore heavier, challenging overall financial feasibility and UAV payload restrictions, respectively (Colomina & Molina, 2014; Huang et al., 2013). As a result, only few hyperspectral cameras suitable for mounting on a UAV platform have been developed thus far. The same notion applies for laser scanners and SAR equipment, as well as thermal optics to a lesser degree (Colomina & Molina, 2014), although examples of thermal optics for water-stress mapping (Bellvert et al., 2014) and laser scanning aperture for 3D scenic reconstruction (Wallace et al., 2012) on board UAV platforms are existent. For a full overview of sensing payloads available to UAV systems recently, the reader is directed to Blyenburgh (2013).

Given these deliberations, the potential of UAV-based imagery collection is considered valuable to a large number of fields, such as for studying geophysical dynamics (Niethammer et al, 2012), infrastructure inspection (Metni & Hamel, 2007), military purposes (Bento, 2008), (real-time or post) disaster management (Stuart & Friedland, 2011) and meteorological studies (Martin et al., 2011). Nonetheless, the relative importance of these fields is dwarfed by the advent of UAV based remote sensing in the increasingly information driven and smaller scale agricultural industry (paragraph 3.3). Subsequently, it is believed that (precision) agriculture oriented applications will account for more than 80 percent of the anticipated growth of the commercial UAV market in the coming decade (Stehr, 2015; Odido & Madara, 2013).

2.3 Optical Sensor Systems

A substantial number of different sensors are existent, all of which were designed to accommodate a distinct purpose. Each opens up possibilities within different overarching types of remote sensing, the latter which can be classified along the lines of adherence to different energy sources and spectral coverage accommodated by sensors. Classification along these paths results in the distinction of passive and active remote sensing on the one hand, and of reflective visible/infrared, emitted thermal infrared and microwave remote sensing on the other (Gopi et al., 2008; Schowengerdt, 2006; Campbell & Wynne, 2002) (figure 2.2).

Even though the variety of different sensor systems and their suitability to equally varying applications is significant, this theoretical elaboration is solely geared towards passive optical remote sensing in the reflective visible and (near-)infrared, to enhance overall readability. This focus is in accordance with the different sensor systems that are present on the HYMSY UAV platform used for this research, as mentioned in paragraph 5.3. The readers interested in alternative forms of remote sensing and the associated types of sensors are advised to further explore Lillesand et al. (2014), Warner et al. (2009), Gopi et al. (2008) and Campbell & Wynne (2002).

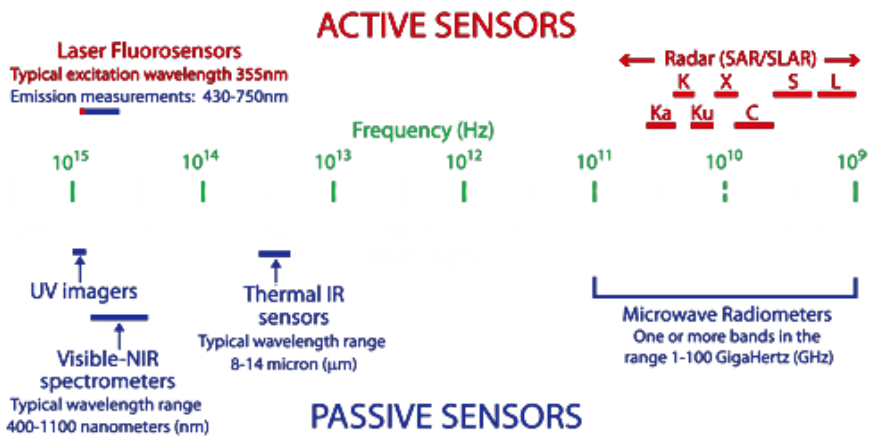

Figure 2.2: Different types of remote sensing and sensors, categorized along the lines of active and passive sensors and different coverages of the electromagnetic spectrum. (Source: SEOS, 2015)

Optical remote sensing represents one of the most frequently utilized types of RS for a diversity of applications, particularly in vegetation monitoring endeavors (Homolová et al., 2013). Electronic optical sensors measure incoming radiation as reflected by one or multiple targets in the visible (VIS, 0.4-0.7µm), near infrared (NIR, 0.7-1.1µm), short wave infrared (SWIR, 1.1-2.5µm), mid wave infrared (MWIR, 2.5µm-7.5µm) and long wave infrared (LWIR, 7.5µm-15um) range (Warner et al., 2009). From the VIS through the SWIR region the sun acts as the primary source of energy. The radiation as perceived by optical sensors in this region represents solar energy that is partially reflected by the earth's surface or objects thereon, or which was scattered by particles in the atmosphere alternatively (Schowengerdt, 2006). Beyond approximately 3.0um, materials constituting objects on the Earth's surface initiate to actively emit (thermal) radiation by themselves, allowing sensors in this region to measure emitted rather than reflected energy (Gopi et al, 2008). This notion effectively marks the dividing line between the classifications of reflective visible/infrared and emitted thermal infrared remote sensing mentioned earlier. Considering the extent and diversity of the entire optical range, sensors are often developed to cover only one or two of the sub regions mentioned here (Warner et al., 2009). Not surprisingly then, especially considering payload limitations for UAV sensing platforms, the HYMSY platform's sensors only cover the visible and near infrared region, or more specifically the spectral range from 0.45µm to 0.915µm.

Apart from the spectral coverage of optical sensors, the manner in which spectral features are selected or collected, or more specifically the sensor's spectral resolution (paragraph 2.5), represents an additional vital variable of such optics. In essence, the associated spectral resolution can fall in either of two categories, being multispectral or hyperspectral. The former refers to sensors incorporating few and often discrete spectral bands, each covering a relatively broad spectral range (Govender et al., 2007). The simplest example of such a system is a conventional digital consumer camera, capturing reflectance in red, green and blue spectral bands to produce traditional color composites (Kerekes & Schott, 2007). Multispectral sensors on the other hand, in general, accommodate up to approximately ten relatively broad bands, which are not necessarily adjacent to one another in the electromagnetic spectrum (Navulur, 2007). In contrast,

hyperspectral imagers comprise of significantly more (up to hundreds) contiguous narrow bands (Warner et al., 2009). The latter notion with respect to contiguity is considered more important for classification of a sensor as hyperspectral than is the number of bands alone (Qi et al., 2012; Shippert, 2004). Besides, according to Ortenberg (2012) and Thenkabail et al. (2012a), the width of individual hyperspectral bands should ideally not exceed 10_{nm} (Ortenberg, 2012; Thenkabail et al., 2012a). Too narrow bands, however, are likely to induce noise and adherence the $5\text{-}10_{nm}$ range is therefore recommended (Thenkabail et al., 2012b). The majority of hyperspectral optics measure reflected solar radiation in the 0.4-2.5um (VNIR/SWIR) range, although sensors frequently cover either the VNIR (> ±1000nm) or SWIR (± 1000nm <> 2500nm) (Qi et al., 2012; Shaw & Burke, 2003). In the resultant imagery, each pixel is considered a vector containing reflectance values for each narrow band at that specific location in space. Consequently, the entirety of the image is considered a three dimensional cube or hyperspectral data cube (Yao et al., 2012) (figure 2.3).

Particularly for remote sensing of vegetation it has been demonstrated by previous research that an increased spectral resolution, as is provided by hyperspectral imaging systems, enables mapping distinct characteristics of vegetation more accurately (Kooistra et al., 2014). The use of these systems on conventional platforms has yielded promising results in the field of phenotyping, i.e. the methodologies and protocols for measuring plant growth, architecture, and composition (Fiorani & Schurr, 2013). Due to the ability to extract highly detailed and contiguous spectral data, hyperspectral imagers are better capable of discerning subtle variations in reflectance behavior resulting from, for example, differences in the chemical or physical structure, composition or other characteristics of objects such as plants (Mulla, 2013; Nguyen & Lee, 2006; Campbell & Wynne, 2002). In contrast, broadband (multispectral) imagery is generally only suitable for rough discriminatory analysis of vegetation due to its reduced sensitivity to relatively small but vital differences in spectral reflectance at distinct wavelengths. Likewise, the latter may only be considered suitable for discriminating between different types of vegetation, whereas hyperspectral optics enable a more in-depth analysis of the constituents of vegetation (Govender et al., 2007) Besides, radiation measurements in multispectral imagery tend to saturate as biomass and leaf area index of the vegetation increases, hereby further limiting retrieval of accurate estimates of particular features of interest (Thenkabail et al, 2012). Due to the permissive features of hyperspectral remote sensing, spectroscopy is expected to enable significant cost savings for the development of vegetation monitoring systems in comparison to more traditional alternative practices (Ortenberg, 2012).

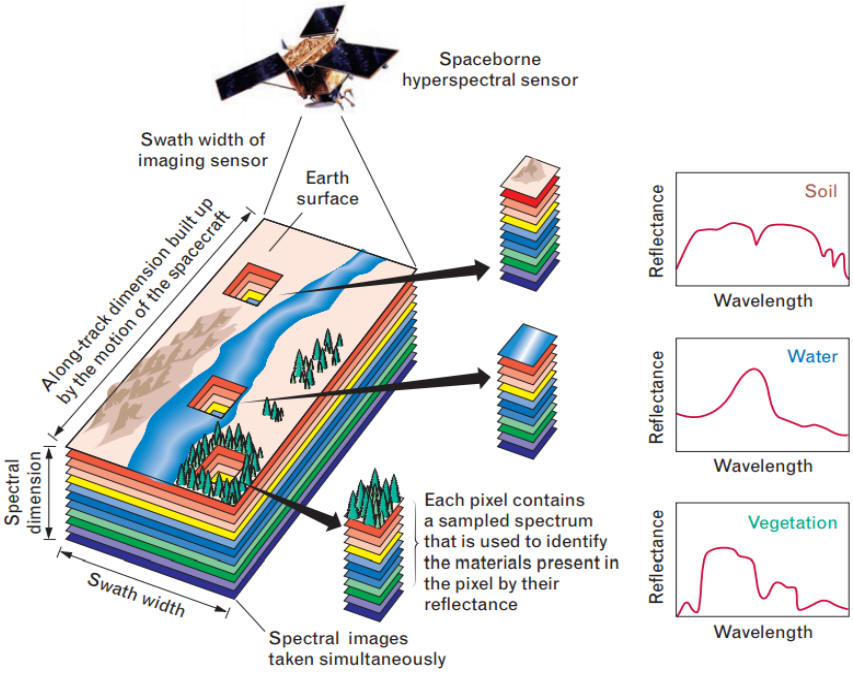

Figure 2.3: Visual representation of a Hyperspectral Data Cube (HDC). The three-dimensional (comprising of two spatial dimensions in the x-y direction and one spectral dimension) cube stores reflectance values for each individual pixel as is measured on that specific location in each hyperspectral band (nm). The contiguous narrow band measurements enable generation of distinct and highly detailed spectral signatures, as shown to the right. Please note that the satellite platform can be replaced by any other platform carrying the appropriate sensor (Source Shaw & Burke, 2003).

2.4 Geometric errors in RS

In remote sensing, geometric distortions in the raw output imagery are pertaining issues that have existed as long as the field itself. The type and severity of distortions are inherently determined by multiple factors and differ notably between different sensing systems, acquisition campaigns and/or locations (Toutin, 2004). Causes are, for example, related to factors such as lens distortions, misalignment, inconsistent sampling rates, variability of the platforms altitude and attitude, the curvature and rotation of the Earth, different viewing angles, and topographic relief, among others (Xiang & Tian, 2011). Concerning sensor systems, for example, traditional photographic frame cameras represent vastly advanced and highly calibrated instruments, providing instant exposure over relatively larger areas and therefore allowing adequate tackling of geometric errors (Congalton et al., 1991). In contrast, point (whiskbroom) and line array (pushbroom) scanners are more prone to geometric distortions given a certain spatial coverage as a result of the platforms continuous movement during the process of image building (Schowengerdt,, 2012; Bajwa et al., 2004). UAV based remote sensing is unique in this respect due to the notion that image acquisition is frequently conducted in a haphazard manner (variable overlap and cross-over patterns), relatively large perspective deviations due to the small sensor-ground distance and highly variable illumination and resolutions. Likewise, the weight of UAV is generally low which renders the platform relatively susceptible to in-flight distortions as a result of environmental factors (Hardin & Jensen, 2015). Besides, exterior parameters are often either unknown or inaccurate, due to the reliance on relatively low cost GPS and IMU devices (Eling et al., 2014; Turner et al., 2012). Consequently, more advanced processing (software) is often required to deal with the limitations invoked by this specific platform (Colomina & Molina, 2014). Regardless of the geometric error's source(s), such distortions are to be removed or minimized prior to utilization of the data in a GIS, particularly to allow for correct overlays with other data and/or multi-temporal studies (Pudelko et al., 2012; Rocchini & Rita, 2005; Hirano et al., 2003). This condition may be particularly valid if the data is to be incorporated into precision agricultural practices, as geometrically deformed data disallows accurate retrieval of surface area metrics of different types of vegetation, its condition and the associated resource requirements (Xiang & Tian, 2011).

2.5 Resolutions

Up until now, the concept of resolutions has been coined numerous times. Resolution is a vital component within all sorts of remote sensing and comes in a variety of different shapes. In essence, resolution is inherently related to the properties offered by distinct platforms and their on board sensors.

Spatial resolution relates to the amount of detail discernible in an image, or at its simplest to ability to separate two closely spaced objects in image space (Sahu, 2008). For example, an image's resolution of 5 meters indicates that individual objects equaling or exceeding that size are identifiable, whereas those that are smaller are likely not (Quattrochi & Goodchild, 1997). The spatial resolution is ultimately determined by the combination of a sensor's opening angle and the associated image forming pixel capabilities, and its distance to the studied object (Liang et al., 2012; Maas, 2008; Hall et al., 2002). Related to spatial resolution is the concept of Ground Sample Distance (GSD), described as the ground area that is represented by an individual pixel in the acquired imagery. GSD can theoretically equal the spatial resolution of a sensor, although it is equally likely that the two deviate as a result of image manipulation, conversion procedures and resampling (Lillesand et al., 2014). Spatial resolution is further influenced by the additional factors, such as recorded contrast, aspect ratio of features, number of objects in the scene, flight speed and associated blurring, extent and the uniformity of background. As a result, objects that are smaller than the spatial

resolution may in fact still be discernible, or vice versa. (Suomalainen et al., 2014; Campbell & Wynne, 2002). Equally important is the interplay between the image's spatial resolution and structure of the ground area an image depicts. The coarser the spatial resolution, the more likely it is that the pixel represents mixed pixels, i.e. the pixel combines radiance values from different objects present within the pixel. As a result it is generally applicable that as the resolution becomes coarser, the ability to discern and retrieve details from an image is decreased (Lillesandet al., 2014).

Spectral resolution refers to a combination of factors, being the number of spectral bands, location of these bands in the electromagnetic spectrum and the width of individual spectral bands in which a distinct sensor acquires data (Govender et al., 2009; Verbyla. 1995). In short, it relates to what segment of the electromagnetic spectrum is covered by a sensor, and how. Generally speaking, it suffices to state that the narrower the width of individual bands, the more accurate distinct objects can be identified and distinguished, and the more bands are required to cover a certain spectral range (Kooistra et al., 2014; Sahu, 2008). As was mentioned previously, sensors come in a substantial variety of configurations and may, for example, cover a single broadband (panchromatic), multiple broad bands (multispectral) or a large number of narrow bands (hyperspectral) (Lillesand et al., 2014).

Temporal resolution is specifically applicable to data time series and the associated temporal density, or the interval between acquisition dates of subsequent data sets (Verbyla, 1995). More specifically, it relates to how frequently measurements were conducted, and the resultant ability to identify changes in the object or area studied over a given period of time (Lillesand et al., 2014). When an application is geared towards studying dynamics in a relatively dynamic environment, temporal resolution may be valued highly, whereas this is less so in static environments and/or for applications not aimed at change detection (Campbell & Wynne, 2002).

Radiometric resolution at last is determined by a sensors ability to detect and record relatively subtle differences in brightness of a scene (Verbyla, 1995). More technically speaking, it is determined by how many different gray levels divide the darkest from the brightest pixels and the sensor's associated sensitivity to different levels of incoming electromagnetic energy The larger the number of gray levels, the finer the radiometric resolution and the larger the interpretability of an image (Lillesand et al., 2014; Campbell & Wynne, 2002).

It is worth mentioning that trade-offs between different types of resolutions are apparent and it is ultimately important to consider the distinct application in order to evaluate the relative importance of each (Campbell & Wynne, 2002). For example, in order to establish a relatively high spatial resolution, a small IFOV, or a sensor's ground foot-print, is preferred (Sahu, 2008). As the ground area covered is minimized, however, so is the amount of energy that can be extracted by a sensor, hereby invoking a decrease in radiometric resolution. The only way of circumventing the latter without giving up on spatial resolution is by increasing the widths of individual spectral bands, which implicates a lower spectral resolution (NRCan, 2013; Campbell & Wynne, 2002).

3. Theoretical context: The use of RS Spectral Analysis in Vegetation Monitoring & Agriculture

3.1 RS for Vegetation Monitoring

Remote sensing is considered ultimately suitable for monitoring vegetation for a diverse range of purposes due to the inherent relationship between plant constituents and their interaction with radiation at different wavelengths (Pinter et al., 2003). Consequently, both remote sensing experts and vegetation physiologists have incorporated radiation based analysis in a diversity of studies related to investigations of plant canopies (Jones & Vaughan, 2010). In essence, this interaction can be ascribed to three distinct and related physical mechanisms, namely absorption, reflection and transmission of electromagnetic energy in vegetation (Homolová et al., 2013). Pigments, such as chlorophylls, for example, absorb light particularly in the blue ($\pm 430_{nm}$) and red ($\pm 660_{nm}$) regions of the electromagnetic spectrum to fuel photosynthesis (NASA, 2015; Mulla, 2013). The incident radiation at green wavelengths ($\pm 550_{nm}$) is absorbed less intensively thereby enhancing minor reflectance, hence the green appearance of healthy and photo synthetically active vegetation. In contrast, absorption significantly decreases in the near-infrared ($700\text{-}1300_{nm}$) region due to transparent cell walls, pigments and scattering by mesophyll cell walls, resulting in increased reflectance and transmittance (Guyot, 2013; Mulla, 2013; Nguyen & Lee, 2006; Pinter et al., 2003; Thorp & Tian, 2004) (figure 3.1).

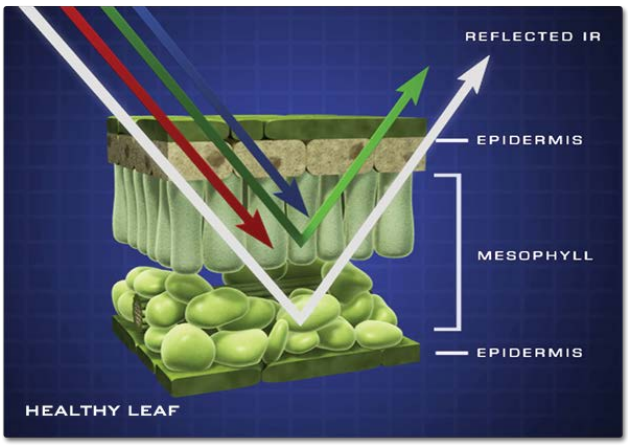

Figure 3.1: Visual representation of the different interactions of vegetation with radiation over different wavelengths (Source: NASA, 2015)

As these properties present in plants, in addition to other frequently studied variables such as Leaf Area Index (LAI), biomass, plant structure, moisture content, and nitrogen content, are varied and interrelated, the spectral properties of vegetation is similarly altered in various directions at different wavelengths (Thenkabail et al., 2012a). As a result of this heterogeneity in spectral behavior, remote sensing theoretically enables isolating, discriminating and subsequently identifying between different types of vegetation cover (Franklin, 2013). Additionally, by performing spectral measurements, using distinct remote sensing instruments, particular quantifiable vegetation properties can be estimated (Mulla, 2013; Qi et al., 2012). Alternatively, the temporal dynamics inherent to vegetation may be assessed on different scales when remotely sensed imagery is acquired successively through time (Zhang et al., 2003).

Even though a diverse array of methodologies for studying vegetation has been developed, the advent of vegetation indices (VIs) have proven to be most decisive in the advancement of remote sensing for application in vegetation monitoring (Jones & Vaughan, 2010). Such indices can be derived in multiple different ways through mathematical manipulation of raw spectra from two or more wavelengths (Goswami et al., 2015; Thorp & Tian, 2004). The primary motivation underlying the use of these indices relates to the notion that they are assumed to be stronger related to distinct plant traits than raw spectra of individual wavelengths thanks to isolation and enhancement of the spectral signal (Chuvieco, 2011; Delécolle et al., 1992). Due to the potential influence of background soil and atmospheric effects on spectral responses of vegetation, various (hybrid) indices were developed to minimize distortions originating from these sources (Thenkabail et al., 2012a; Pinter et al., 2003). Consequently, vegetation indices enable both qualitative and

quantitative analysis of vegetation and its properties (Teillet et al., 1997) through, for example, establishing statistical correlation models between VI data and vegetation characteristics (Liang et al., 2012). Regardless of the ever continuing development of techniques for measuring distinct vegetation characteristics by means of indices, for example, canopy structure remains a complicating factor that affects their interpretation and negatively impacts the retrieval of accurate quantitative measurements (Homolová et al., 2013). Due to variations in leaf area, illumination angle, shadowing effects, background surfaces, multiple layers of stacked leafs and orientation of leafs, among others, the reflective behavior of individual leafs deviates from the spectral signature of entire vegetation canopies (Thorp & Tian, 2004).

3.2 Traditional large scale agriculture and remote sensing

The introduction of remote sensing in the field of agriculture commenced approximately in the 1930s, when aerial photography was utilized for soil and crop mapping (Allan, 2013; Nellis et al., 2009; Thorp & Tian, 2004). This advent was largely fueled by the notion that conventional field sampling is both time-consuming and costly, particularly considering the sizable spatial regions over which traditional agriculture is practiced (Chen et al., 2008). As was mentioned in paragraph 2.3 and 3.1, different parameters of vegetation (e.g. their structure, composition, and/or status) provoke different spectral behavior at different wavelengths. This renders remote sensing useful in agricultural practices, as it allows detection and characterization of many agricultural phenomena by utilizing different segments of the electromagnetic spectrum (Thenkabail et al., 2012; NRC, 1970). Relatedly, accurate, objective, reliable, systematic and timely monitoring of agricultural land and the associates practices is vital for the management of agricultural markets and the formulation of relevant policies at various scales (Wu & Meng, 2013). In the past decades, research relating agronomic properties of plants to spectral reflectance behavior derived by remote sensing has substantiated vastly (Nebiker et al., 2008). Subsequently, once such monitoring data has been collected and interpreted accordingly, it may serve as an aid for agricultural practitioners during their decision-making processes (Thenkabail et al., 2012a; Haboudane et al., 2002).

Until present day, remote sensing in agriculture has been primarily dominated by conventional airborne, space borne and, to a lesser extent, ground-based platforms (Colomina & Molina, 2014; Zhang & Kovacs, 2012). Using these operational modes, various global but especially regional agricultural campaigns have been accomplished. These are mainly geared towards applications such as crop identification and cropland mapping, monitoring of crop growth, prediction of crop yield, and retrieval of biophysical and biochemical properties of crops (Chen et al., 2008). Even though passive broad band optical systems represent the ones most frequently applied in traditional agriculture in the past and present (Homolová et al., 2013), microwave, thermal and laser scanning instruments have also been exploited for application in agriculture more recently (Mulla, 2013; Liang, 2008). Likewise, the relatively recent development of narrow band hyperspectral spectroscopy is believed to further revolutionize the use of remote sensing in agriculture thanks to its deliverance of auxiliary opportunities with increased precision (Yao & Huang, 2013). According to Seelan et al. (2003), however, the adoption of remote sensing by individual farmers remains relatively limited, regardless of the theoretical potential that it offers.

3.3 The advent of small scale precision agriculture

3.3.1 Precision agriculture

Considering the current and anticipated growth of the world's population at a formidable pace and the increasingly limited arable land resources, the pressure on efficiently and effectively exploiting existing productive land is larger than ever before (Seelan et al., 2003). Besides, agricultural practitioners in recent

times ought to consider to which extent striving for expanded yields outweigh the (environmental) costs associated with a more resource intensive management of agricultural land (Zhang & Kovacs, 2012; Rascher et al., 2011). The culmination of these developments and the growing societal awareness of their importance have led to a novel direction in agriculture practices from the mid-1980s onwards, denoted as precision agriculture, precision farming or precision crop management (Mulla, 2013). In order to enhance readability, however, the naming convention of precision agriculture (PA) will be adhered to throughout this report.

Similar to remote sensing, various endeavors to define PA have been undertaken. Although the resultant definitions are vastly diverse, the most essential point of interest resolves around the assumption that substantial variations exist within the spatial-temporal layout of agriculturally productive lands. In PA, these variations (e.g. crop status, presence of important nutrients, soil conditions) ought to be identified and managed accordingly by considering local field needs (Prasad et al., 2007). Realization of this ambition was further fueled by enabling features provided by the advancement of GPS, GIS, electronics and remote sensing (Huang et al., 2013). Through timely collection of data on field variability at the appropriate scales, the increasingly information-driven (precision) agricultural practices are expected to further enhance efficiency, reduce loss of productivity and minimize environmental harm (Zhang & Kovacs, 2012; Herwitz et al., 2004; Moran et al., 1997). Such site-specific management of crops and resource inputs in an attempt to better accommodate in-field variability, is identified as the most important development in agricultural practices in the past decade (Pinter et al., 2003). As a result, the introduction of PA gave rise to a new concept that came to be known as the *management zone*. In PA, management zones represent a sub sections within a larger agricultural field in which the supposed variation is minimal and distinct properties are relatively homogeneous (Yao & Huang, 2013). In recent years, PA gradually transformed from a field of expertise that was majorly practiced under experimental conditions to a fully operational endeavor in contemporary agriculture industries (Foody et al., 2009). Though vastly diverse and situation dependent, PA can be broken down in four subsequent steps according to Zhang & Kovacs (2012) (figure 3.2).

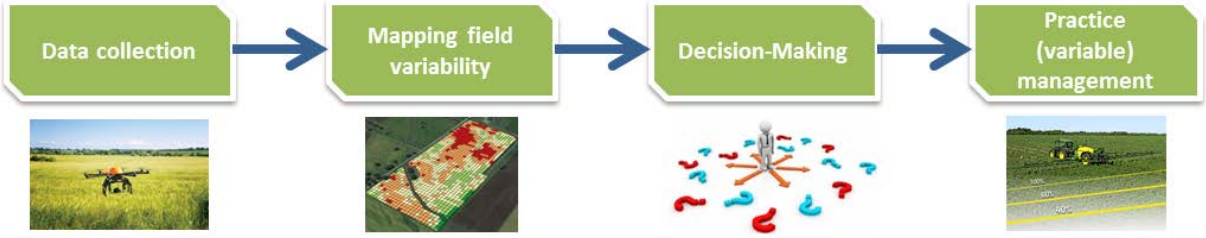

Figure 3.2: Visual representation of the four stages in precision agriculture according to Zhang & Kovacs (2012)

3.3.2 The case for UAV RS in PA

The extent to which remote sensing undertakings in regard to monitoring traits in agricultural land may be considered successful is ultimately determined by the spatial, spectral and temporal resolution provided by platform and sensor systems on the one hand, and their (mis)alignment with the resolutions required for a distinct application on the other (Wulder et al., 2009). In respect to such desired resolutions, PA is distinctly different from traditional agriculture due to its profound focus on using the *'right management practice at the right place and the right time'* (Mulla, 2013, p. 358). More specifically, effective practicing of PA requires frequent and near real-time revisiting times, to constantly fuel information on the status of the aerial land throughout the growing season(s) of crops (Berni et al., 2009; Nebiker et al., 2008; Seelan et al., 2003), in a cost-efficient manner (Zhang et al., 2002). In addition to the temporal component, the requirements of very high spatial (sub meter) resolution imagery, access to VIS/NIR (and potentially TIR) spectral bands, and a high spectral resolution with narrow bandwidths to allow appraisal of pivotal biophysical and biochemical crop parameters, should be mentioned (Zarco-Tejada et al., 2008). As will be

subsequently explained below, conventional sensing platforms are generally unable to adequately meet these requirements. Hence, contemporary PA is frequently undertaken in a time-consuming and therefore costly, destructive and selective manner, demanding weekly visual and metric probing in order to map and quantify relevant plant and/or trait parameters on the ground (Nebiker et al, 2008). The desire to advance from such randomly selected samples to high density and accurate maps embodies the primary fuel for the advent of remote sensing in precision agriculture (Alchanatis & Cohen, 2012).

Satellites have been utilized for applications in agricultural management ever since the 1970s and even though their spatial resolution has notably increased ever since it is still in the order of meters (Mulla, 2013; Wu et al., 2005). Their spatial resolution is generally too coarse to allow for retrieval of information on plant characteristics on a plot by plot basis (Zhang & Kovacs, 2012; Mulder et al., 2011) Besides, the revisiting times of these platforms in the order of multiple days is frequently considered inadequate for application in PA (Seelan et al., 2003). This notion, relating to the temporal resolution provided by platforms, may be circumvented by mounting sensors on flexibly deployable ground based systems, although this significantly lowers the spatial coverage and associated feasibility (Homolová et al., 2013). Ground based sensing systems also face limited issues regarding portability and accessibility in the case of tall crops and dense canopy structures (Sugiura et al., 2005). Besides, Colomina & Molina (2014) and Zhang et al. (2002) mention the substantial cost associated with high resolution space based remote sensing as a supplementary barrier. This is an especially valid argument, because it is still unsure whether a sufficiently large commercial demand exists among PA practitioners to minimize data procurement costs satisfactorily (Lamb & Brown, 2001). In addition, cloud cover effectively obstructs repeated retrieval of remotely sensed imagery in the visible and near-infrared from satellite platforms, and aerial platforms to a lesser degree (Mulla, 2013). Even though aerial remote sensing may theoretically circumvent some of the pertaining challenges mentioned here, image acquisition by air borne platforms suffers from high operational costs (rendering it economically feasible only for large scale campaigns) and potential inflexibility due to complex flight scheduling (Primicerio et al., 2012).

The deliberations briefly listed here lie at the foundation of the growing scientific and societal demand for exploring the potential of (hyperspectral) UAV based remote sensing techniques for application in precision agriculture (Honkavaara et al., 2013). Particular relevant in this respect are those platforms sufficiently large to carry the desired instrument, but small enough to operate outside official airport control (Suomalainen et al., 2014). As formulated by Colomina & Molina (2014, p. 91), '*UAVs have successfully introduced the smaller, cheaper-to-operate platform paradigm among the (vegetation) remote sensing community*'. Their anticipated potential is primarily motivated by their assumed ability to provide imagery at considerably high and flexible spatial and temporal resolutions, enabled by their limited altitude and slow cruising speed (Zhang & Kovacs, 2012; Herwitz et al., 2004) (figure 3.3). In regard to operational complexity Nebiker et al. (2008) mentions the integration of flight control systems in the majority of modern UAV system, enabling autonomous stabilization of the platform and automated piloting based on predefined way points in some cases. Particularly in comparison to manned aerial remote sensing assets, the fabrication and operation costs of UAVs may be low(er) or competitive at least (Colomina & Molina, 2014; Berni et al., 2009; Herwitz et al.,

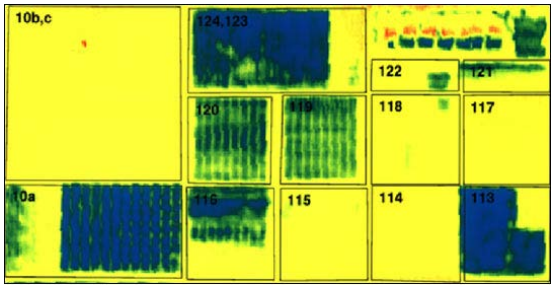

Figure 3.3: Vegetation density derived from a multispectral optical sensor on board a UAV sensing system. Dark blues and greens indicate lush vegetation while reds indicate areas of bare soil. The resultant high spatial resolution is demonstrated by the easily discernible individual rows of crops and/or individual plants below the plot level. (Source: Urbahs & Jonaite, 2013)

2004). The estimation of per-hour pricing for different platforms and the overall validity of the cost argument, however, is complicated and ultimately influenced by the scale of operation, desired resolution, frequency of use and sensor requirements, among other variables (Watts et al., 2012; Zhang & Kovacs, 2012). Relatedly, depending on the type of frame and the sensors it incorporates procurement of such systems can still be a rather costly undertaking. The spectral resolution provided by UAV based remote sensing is, obviously, depended on the type of sensor system(s) mounted to their frames. Due to payload restrictions the availability of sensors is still rather limited compared to those available to platforms able to carry more weight, although miniaturization of sensors is advancing at a formidable pace (Colomina & Molina, 2014; Berni et al., 2009; Everaerts, 2008). Regardless of these benefits supposedly enabled by UAV platforms, their applicability in various disciplines should not be taken for granted due to different unresolved challenges as mentioned in paragraph 2.2.2.

3.3.3 Existing research on the use of UAVs in precision agriculture

Not surprisingly, given the continuous technological advancement within the field and growing societal and scientific demand, research on the implementation of (optical) UAV based remote sensing into agricultural practices has recently intensified (Huang et al., 2013; Berni et al., 2009). In accordance to previous statements, however, it should be exemplified at this point that the inclusion of hyperspectral optics on these platforms is still rather limited (Suomalainen et al., 2014; Shippert, 2004). The Workshop on UAV-based vegetation monitoring, held in Cologne in 2013, is indicative of this, given the relative abundant coverage on multispectral sensors compared to hyperspectral ones (Bendig & Bareth, 2014). A brief review of a selection of related studies is provided below.

In 2009 and 2010, Calderón et al. (2014) performed a study on the early detection of Verticillium wilt using multispectral, hyperspectral and thermal camera sensors on board a UAV platform at different altitudes. In following years, Retzlaff et al. (2014) evaluated the ability to assess leaf canopy and vigor properties (e.g. chlorophyll) using vegetation indices derived from a six band VIS/NIR multispectral sensor on board a similar platform. Besides, the influence of different camera viewing angles on data throughput was assessed. Relatedly, Rasmussen et al. (2013) explored the applicability of a conventional RGB camera on board a UAV for assessing distinct crop resistance parameters and mapping leaf cover, in addition to evaluating the influence of different flying heights on the output. Tattaris et al. (2014) investigated how NDVI values computed from multispectral UAV data compared to NDVI measurements on the ground, and how these correlated with agronomic traits such as biomass and yield (g/m^2). Using a broad band camera covering the Blue-Green-NIR range mounted on a fixed-wing UAV, Hunt et al. (2010) generated Green NDVI values over an experimental field and found strong linear relations with LAI for plots with limited canopy density. Drauschke et al. (2014) performed two different experiments to demonstrate the ability to construct 3D scenic models utilizing RGB images collected by a UAV, and to classify different trees on-demand using multispectral imagery and a powerful classifier algorithm, respectively. In addition, Zarco-Tejada et al. (2012) employed a narrow band hyperspectral camera and a thermal camera to assess their capability of detecting various water stress indicators in citrus trees when mounted on a UAV, by means of correlating various indices derived from the aerial data with in-situ measurements on the ground.

More technically oriented but related studies, such as those of Eling et al. (2014), Xiang & Tian (2011) and Neeland & Kraft (2014), are primarily aimed at further engineering UAV platform components to increase their suitability for vegetation monitoring purposes, through developing direct on board georeferencing technology, navigation systematics, and enhancing on board processing speed of data, respectively.

4. Theoretical context: Plant traits & Spectral behavior

At the core of this research lies the analysis of distinct plant traits or attributes by remote sensing techniques. From an agronomical perspective, as described in chapter 3, adequate spatial quantification of such traits, whether they be biochemical or biophysical of nature, enables farmers to evaluate essential factors and adjust their practices (e.g. nutrient supply, irrigation, etc.) accordingly (Alchanatis & Cohen, 2012; Thenkabail et al., 2012a; Zhang & Kovacs, 2012). As a result, enhancing of plant phenotyping capabilities has recently intensified, in order to assess plant performance through unraveling relevant agronomic traits (Rascher et al., 2011).

Spectral data derived from a study area may be ascribed to global or regional zones, fields, plots or even individual plants and subsequently related to distinct vegetation traits, depending on the sensing system, the associated resolutions and the application (Ustin & Gamon, 2010). In this chapter, the most meaningful traits and their agronomic relevance will be elaborated on. Subsequently, a tabular overview of existing vegetation indices (VIs) that were employed in a variety of previous studies to remotely map these traits is provided (table 4.1 & 4.2). A textual commentary on how and why these specific indices and associated wavelengths were derived is presented as a supplement in appendix C. Both overviews are purposely and solely geared towards indices, related wavelengths or other indirect inputs that are accommodated for by the UAV platform incorporated into this research, being (hyperspectral narrow bands in) the 450-915$_{nm}$ range and plant height, respectively (paragraph 7.3). Different approaches relying on different equipment and/or divergent segments of the electromagnetic spectrum, however, are existent.

Hundreds of different VIs have been developed ever since the advent of remote sensing in vegetation monitoring applications, resulting from the influence of different factors (e.g. RS platforms and vegetation types) on the performance of distinct models. Some these will be evaluated in this research, hereby serving as a benchmark. Including all of these in the subsequent analysis provided in this report is an impossible endeavor and therefore discarded. Instead, a selection of indices was excerpted from existing studies, based on their demonstrated success for correlating well with one or more of the traits included in this research. In order to narrow down the selection and provide a logical and representative distinction, the literature review on the use of these indices majorly focused on research on remote sensing of crops relatively similar to the oat crops studied here. More specifically, the exploration was geared towards studies incorporating other cereal crops, such as maize/corn, rice, wheat, barley, among others. It is believed that this collection is satisfactory to assess the suitability of the HYMSY platform and the associated sensor system(s) to estimate distinct traits.

4.1 Biophysical plant traits

4.1.1. Biomass

In-season signaling of crop production and yield prior to harvesting relates to one of the imperative fundamentals of precision farming practices (Alchanatis & Cohen, 2012). In this respect, adequate estimates of biomass are considered highly desirable, as it is suggested to provide valuable information of vegetation productivity (Gnyp et al., 2014; Cho et al., 2007). In agronomy, different methodologies exist to relate crop biomass to eventual yield through harvest indexing (Rascher et al., 2011). Consequently, within-season biomass estimation model outputs are regularly incorporated into crop development simulations as a means to predict crop yield (Pinter et al., 2003). Accurately tracking of green biomass in both remote sensing and agronomical studies, however, has remained a complicated and ultimately challenging endeavor (Alchanatis & Cohen, 2012).

4.1.2 Plant height

Even though plant height as a trait has been less frequently covered in previous studies, it serves as an input parameter for a wide variety of indicators, such as capabilities of individual plants to compete with others and indirectly for LAI (Homolová et al., 2013). In addition, Cornelissen et al. (2003) associate the trait with parameters such as plant fertility, health, growth rate and tolerance/avoidance of distinct (climatic/nutrient) stress factors, as well as with other traits such as biomass, rooting depth, lateral spread and leaf size. Freeman et al. (2007), for example correlated ground measurements of corn plant height with biomass, yield and nitrogen uptake. Significant correlations were found for all possible combinations, although the strength differed for distinct growth stages. Consequently, measured plant height may aid in quantification of variable rate application of distinct fertilizers or pesticides (Ehlert et al., 2008). According to Thenkabail et al. (2000), plant height is the third most important estimator for crop yield prognosis, after FBM and LAI, respectively.

4.2 Biochemical plant traits

4.2.1 Chlorophyll (Chl)

Concerning optical remote sensing for mapping plant trait purposes, plant pigments are most frequently studied. In this regard, especially chlorophylls have received notable attention, whereas other pigments such as carotenoids and anthocyanin's are less frequently elaborated upon (Homolová et al., 2013). Chlorophyll represents the most vital pigment in green plants regarding photosynthesis. In healthy green vegetation, chlorophyll absorbs significantly in the blue and red region of the visible (VIS) spectrum and slightly less in the green, hence their green appearance. Leaf's strong reflectance in the NIR region, however, is mostly the result of very limited absorption of chlorophylls, in addition to internal leaf scattering (Knipling, 1970). Diseased plants facing various forms of stress (e.g. shortage of nitrogen (N)), hindering effective production of chlorophyll, absorb less in the blue and red region as a result (Alchanatis & Cohen, 2012). Gitselson (2012) provides a comprehensive visual and textual elaboration on how leaf reflectance behavior changes considerably in the visible range as a result of different chlorophyll levels in healthy and diseased plants, respectively. Non-optimimal photosynthesis resulting from decreasing chlorophyll levels may be highly undesirable for agricultural practices, due to potentially sincere implications in regard to reduced crop growth, yield and carbon fixation (Clevers & Kooistra, 2012). Therefore, discrimination of chlorophyll content by spectral remote sensing can provide an excellent and necessary means for assessing the condition of vegetation, such as nutrient status, primary production capacity, developmental stage and plant stress (Alchanatis & Cohen, 2012; Gitelson, 2012; Gitelson et al., 2005). As a result, provision of estimates regarding chlorophyll content is considered ultimately important for practices in precision agriculture (Wu et al., 2008).

Estimating of chlorophyll statuses of vegetation, however, may be complicated due to a spatially and temporally variable distribution of chlorophylls throughout different plant components (i.e. petioles, leaf blades, stem, grains, etc.), and due to the influence of plant height thereon. It was found for dill plants, for example, that as they increased in height the proportional differences of chlorophylls in the upper parts of plants changed, increasing for the stem in particular (Lisiewska et al., 2006). This is argued to be a relevant deliberation considering the relative (in)visibility of individual plant components in (optical) remote sensing and due to, for example, the viewing geometry used herein. Consequently, it has been demonstrated by Yoder & Pettigrew-Crosby (1995) that spectral proxys for chlorophylls at the leaf level do not straightforwardly propogate to the canopy level, or vice versa. Relatedly, considering the influence of additional plant structure relates variables (e.g. LAI, canopy architecture, cover, illumination, etc.), plausibly

irregularly concealing lower parts of plants, quantities of chlorophylls in these upper canopy components show stronger relationship with VIs than (lower) leaves do (Blackburn, 1998; Broge & Leblanc, 2000). Similarly, correlations with canopy measured chlorophyll content were also found to be stronger for top to middle positioned leafs than for those located at lower positions on maize crops by Ciganda et al. (2009). Adequate estimation of chlorophyll content in leafs through VIs remains specifically problematic in instances of relatively variable canopy structures (Sims & Gamon, 2002), and may be more effectively executed through physically based models that consider the interchange of radiation throughout canopies (Houborg et al, 2009).

4.2.2 Nitrogen (N)

As has been mentioned previously, chlorophyll and nitrogen content in vegetation are related, i.e. the majority of leaf N is contained in chlorophyll molecules (Netto et al., 2005, p. 200). Likewise, there exists a strong linear relationship between the amount of nitrogen present in vegetation and its respective capacity to photosynthesize (Sellers et al., 1992). Deficiencies of N in plants invoke a lowering of chlorophyll concentration, causing reduced photosynthesis capacities, decreasing plant growth, minimization of carbon fixation and reduction of overall yield formation and vegetation quality (Zhao et al., 2014; Homolová et al., 2013; Clevers & Kooistra, 2012; Smith et al., 2002). Nitrogen and chlorophyll content in plants are thus biochemically and functionally linked closely (Weiss et al., 2001). In contrast, excess of nitrogen poses an environmental risk when it is transported into soil or aquatic systems when vegetation no longer absorbs the substance (Chen et al., 2010; Pinter et al., 2003; Haboudane et al., 2002). Either way application of N is considered highly decisive for optimizing both yields and economic returns to agricultural practitioners (Khosla et la., 2002). Due to the relevance of N for crop growth, estimation of N status to detect potential nitrogen stress and subsequent generation of prescription maps to aid in nutrient management are vital to precision agricultural management (Yao et al., 2012; Hansen & Schjoerring, 2003). According to Haboudane et al. (2002), of all common fertilizer compounds, nitrogen is the most vital yet potentially limiting factor for agricultural productivity of crops.

4.2.3 Carbon (C)

In general, individual fresh plants comprise mostly of water, ranging from 50 percent to as much as 95 percent, most of the remainder material is represented by dry matter (biomass). The latter composition is primarily shaped by carbon (C), and to a lesser extent Oxygen (O). According to Magnussen and Reed (2004), the carbon content across highly varied types of vegetation approximately amounts to between 45 and 50% of (oven dry) biomass. Using different complex processes, plants act as individual units within the biosphere that produce dry (organic) matter by condensing CO_2 from their environment into biomass, known as carbon fixation (Lieth, 1963). Carbon has been at the epicenter of multiple remote sensing based environmental studies, primarily motivated by enhancing the understanding of the (changing) Earth systems with respect to complex exchange of carbon in ecosystems and the associated carbon cycle (Gitelson et al., 2006; Veroustraete et al., 1996; Schimel, 1995; Sellers et al., 1992). Agricultural crops in particular are stated to represent one of the most influential biomes regarding the exchange of carbon and related policy making due to their pervasive and extensive presence worldwide (Peng et al., 2011 Lobell et al., 2003). From an agricultural perspective carbon is considered a relevant parameter due to its ability to act as an indicator for crop growth and subsequently crop yield, as the productivity of a plant is inherently connected to the rate at which it is able to assimilate carbon by means of photosynthesis (Barber & Baker, 1985). Relatedly, it was demonstrated by Cure & Acock (1986) that when crops are exposed to higher levels of CO_2 concentration in their environments, photosynthesis and carbon biomass accumulation are accelerated, eventually resulting in expanded yields.

Table 4.1: Tabular overview of all the existing indices that were used in this study during calibration and validation, including there (reference) name, formulation and plant traits to which they were related in previous studied. The table depicts the original formulation of indices. As will be mentioned in 6.4.2.2, in order to allow their utilization, the original bandwidths were replaced by the closest wavelength accommodated for by the HYMSY's HDC.

Index name	Formulation	Trait				
Simple Ratios		FBM	H	CHL	N	C
SR_a	$\frac{R734}{R629}$			X		
SR_b	$\frac{R780}{R710}$-1			X	X	X
SR_c	$\frac{R780}{R550}$-1			X	X	X
SR_d	$\frac{R760}{R550}$				X	
SR_e	$\frac{R706}{R755}$	X				
MSR	$\frac{(R750/R705)-1}{\sqrt{(R750/R705)+1}}$			X		
NDVIs						
NDVI_a	$\frac{R689-R521}{R689+R521}$	X				
NDVI_b	$\frac{R584-R471}{R584+R471}$			X		
NDVI_c	$\frac{R732-R717}{R732+R717}$			X		
NDVI_d	$\frac{R750-R734}{R750+R734}$				X	
NDVI_e	$\frac{R770-R717}{R770+R717}$				X	
NDVI _f	$\frac{R820-R720}{R820+R720}$	X				
NDVI_g	$\frac{R750-R705}{R750+R705}$			X		
NDVI_h	$\frac{R740-R667}{R740+R667}$			X		
NDVI_i (NDRE)	$\frac{R780-R710}{R780+R710}$			X		
NDVI_j	$\frac{R760-R550}{R760+R550}$				X	
NDVI_k	$\frac{R750-R710}{R750+R710}$				X	X
NDVI	$\frac{\lambda 2-\lambda 1}{\lambda 2+\lambda 1}$		X			

Other Indices						
REP_a	$700 + 45 * \frac{Rre - R700}{R740 - R700} \qquad Rre = \frac{R670 + R780}{2}$	X		X	X	
MCARI_a	$[(R750 - R705) - 0.2(R750 - R550)](\frac{R750}{R705})$			X		
MCARI_b	$[(R750 - R710) - 0.2(R750 - R550)](\frac{R750}{R710})$					X
TCARI/OSAVI	$\frac{3[(R750 - R705) - 0.2(R750 - R550)(R750/R705)]}{(1 + 0.16)(R750 - R705)/(R750 + R705 + 0.16)}$			X	X	X
MCARI/OSAVI	$\frac{[(R750 - R705) - 0.2(R750 - R550)](R750/R705)}{(1 + 0.16)(R750 - 705)/(R750 + R705 + 0.16)}$			X	X	
MTCI	$\frac{R754 - R709}{R709 - R681}$			X	X	X
TGI	$-0.5[190(R670 - R550) - 120(R670 - R480)]$			X		
MCARI/MTVI2	$\frac{(R700 - R670 - 0.2(R700 - R550)) * (R700/R670)}{1.5(1.2(R800 - R550) - 2.5(R670 - R550))/\sqrt{((2R800 + 1)^2} - (6 * R - 5 * \sqrt{(R670)}) - 0.5}$				X	

Table 4.2: The references from which the indices were originally retrieved and/or their inventor.

Index name	Source(s)
Simple Ratios	
SR_a	*Yu et al. (2012)*
SR_b	*Kooistra et al. (2014); Clevers & Kooistra (2012); Gitelson (2012), Peng et al. (2011), Wu et al. (2009), Gitselson (2003a), Gitelson (2003b)*
SR_c	*Kooistra et al. (2014); Clevers & Kooistra (2012); Gitelson (2012), Peng et al. (2011), Gitelson (2003a), Gitelson (2003b)*
SR_d	*Zhao et al. (2014)*
SR_e	*Mutanga & Skidmore (2004)*
MSR	*Wu et al. (2008)*
NDVIs	
NDVI_a/b/c/d/e	*Hansen & Schjoerring (2003)*
NDVI _f	*Thenkabail et al. (2000)*
NDVI_g	*Wu et al. (2008)*
NDVI_h	*Yu et al. (2012)*
NDVI_i (NDRE)	*Kooistra et al. (2014), Hunt et al. (2013), Barnes et al. (2000)*
NDVI_j	*Zhao et al. (2014)*
NDVI_k	*Wu et al. (2009)*
Other Indices	
REP	*Cho et al. (2007), Clevers & Kooistra (2012)*
MCARI_a	*Wu et al. (2008)*
MCARI_b	*Wu et al. (2009)*
TCARI/OSAVI	*Kooistra et al. (2014), Clevers & Kooistra (2012), Tian et al. (2011), Chen et al. (2010), Wu et al. (2008)*
MCARI/OSAVI	*Clevers & Kooistra (2012), Wu et al. (2008)*
MTCI	*Clevers & Kooistra (2012), Tian et al. (2011), Wu et al. (2009), Zhang et al. (2008)*
TGI	*Hunt Jr. et al. (2013)*
MCARI/MTVI2	*Tian et al. (2011), Chen et al. (2010)*

5. Data acquisition in the study area

5.1 Study area

The study area for this research is located at the agricultural grounds surrounding the facilities of Wageningen UR and corresponds to the study area of the overarching field experiment mentioned in paragraph 1.2 (figure 5.1). The area comprises of 120 squared (3x3 meter) agricultural plots, positioned in a gridded format. Spacing between the plots is 1.5 meter in the NE-SW direction and 2 meter in the SE-NW direction. During the 2014 growing season (March-August) half of the plots were cultivated with oats, the remainder with endive. Both cultivars were purposely decided on due to the presence of various related species in Dutch grasslands on which parallel experiments are carried out in a greenhouse environment. Once each crop type was harvested, groups of twenty plots (10/10 for oats/endive) received seven different treatments between autumn and spring. In this period, plots were vegetated with either one of four different cover crops (*Lolium perenne (Lp), Vicia sativa (Vs), Rapharus sativa (Rs) and Trifolium repens (Tr)*), a combination of Lp + Tr in one subplot and Rs + Vs in the other, or left fallowed (Fa). *Lolium perenne* and oats belong to the same plant family whereas such overlap between cultivars and intermediate treatment is not existent for endive, hereby allowing assessment of whether such biological (dis)similarities exert influence on growth patterns of crops. From here onwards, the smaller subplots having received combined treatment of cover crops are treated as individual plots, resulting in a total of 140 plots (i.e. experimental units) within the study area. During the subsequent growing season (2015), cultivation was again equally divided for oats and endive species. Half of the plots were cultivated with the same crop as was the case in the previous growing season; the other half was swapped with the alternative vegetation. Only the plots cultivated with oats (n = 70) will be studied in this research. Samples for a wide variety of plant specific traits were taken from oat crops, whereas the samples acquired from endive crops cover only few plant characteristics. The more extensive sampling of oat crops therefore allows for incorporation and analysis of a larger number of traits.

Figure 5.1: Zooming in onto the study area from the Netherlands (A), the grounds north of the WUR (B) and the gridded pattern of the field experiment (C)

5.2 Field data collection

Plant samples were acquired during the second growing season to allow quantification of several biophysical and biochemical parameters from within each plot, including fresh biomass (FBM) nitrogen content (N), carbon content (C), leaf chlorophyll content (Chl), and plant height. The monoculture plots (i.e. plots cultivated with a single cover crop only) were divided into a left subplot (a) and a right subplot (b), similar to split plots accommodating different polycultures cultivation in each subplot. For the latter plot type biomass samples were acquired from both subplots for each polyculture, whereas for monoculture plots either of two sides (left or right) was randomly selected and subsequently used for the retrieval of samples, other than height and SPAD readings. For biomass sampling (02-07-2015), a selection of plants in the northern segment of each (both or randomly selected) subplot was clipped using a 25x25 centimeter quadrant frame and weighted afterwards to retrieve fresh biomass (g m^{-2}). It was then dried at 70°C for 48 hours and weighted immediately afterwards to record dry biomass (g m^{-2}). Dry samples were then weighted in tin cups and grounded to pass through a screen, after which N concentration and C concentration (% g^{-1} dry weight) were read out after combustion and thermal conductivity processing in an automated NA1500 CN elemental analyzer (Carlo Erba – Thermo Fisher Scientific). Aerial metrics of N and C content (mg m^{-2}) were subsequently calculated based on the measured concentration of each and dry biomass (g m^{-2}), respectively. One day prior to the UAV campaign (30-06-2015), plant height was measured in centimeters by means of a ruler on four locations (a-North, a-South, b-North, b-South) in monoculture plots, or two locations in polyculture subplots (a/b-North, a/b-South). At each location a single plant of representative height, considering its surroundings, was selected and measured. The SPAD readings were collected on the same day as the UAV campaign (01-07-2015) using a SPAD-50 meter. Measurements were taken from the top three leaves of one individual plant in each quadrant for monoculture plots, or two plants in each half of the polyculture subplots. The readings are converted to leaf chlorophyll concentration (mg per g leaf fresh weight) and content (g m^{-2} projected leaf area) using the regression functions derived by Uddling et al. (2007) for wheat crops. A visual overview of the field data collection of specific plant traits is presented in figure 5.2. Given the relatively small size of individual plots it is assumed that both the treatment and traits are homogenous herein, and the samples are thus considered representative for the entire plot.

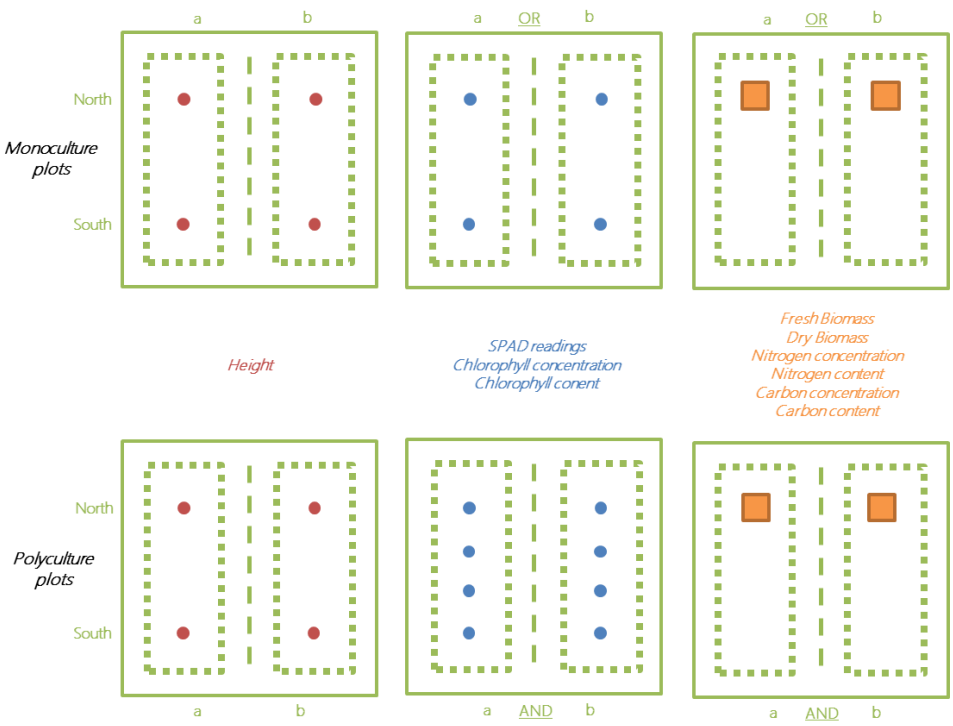

Figure 5.2: Visual representation of individual plots and the approximated location at which samples for distinct traits were acquired. The exact location in reality might differ from this approximation. The stripped line in the middle of each plot indicates the dividing line between subplots a (left) and b (right). The dotted lines represent the 30cm margins from either the middle of the plot or the plot's edges adhered to during the field experiment.

5.3 The HYMSY platform

Aerial images were acquired by means of an octocopter UAV carrying the Hyperspectral Mapping System (HYMSY), the latter which was developed by Wageningen UR itself. The frame comprises of mostly off the shelf parts. Once the HYMSY sensor is mounted onto the frame, the total weight of the platform in ready-to-fly configuration amounts to approximately 2.0kg. The HYMSY mapping system itself comprises of a custom push broom spectrometer (450-915$_{nm}$ range, 9$_{nm}$ spectral resolution, ~20 lines/s, 328 pixels/line), a 16MPix RGB consumer camera, a GPS-INS and several components dedicated to synchronization and data storage (figure 5.3a). The slowest possible smooth flight of the platform is in the range of 2 m/s, allowing capturing of imagery at a higher resolution than fixed wing UAVs with similar fps (frames-per-second) sensor specifications (Rasmussen et al., 2013). A unique post-flight processing chain was developed to radio metrically and geometrically process the data captured in flight (paragraph 5.4.2). In a significant number of test flights over varied terrain in the past, the HYMSY platform demonstrated to be capable of generating RGB orthomosaics at 1-5cm resolution, DSMs at 5-10cm resolution and HDCs with a resolution in the range of 10-50cm. (Suomalainen et al., 2014, p 11026).

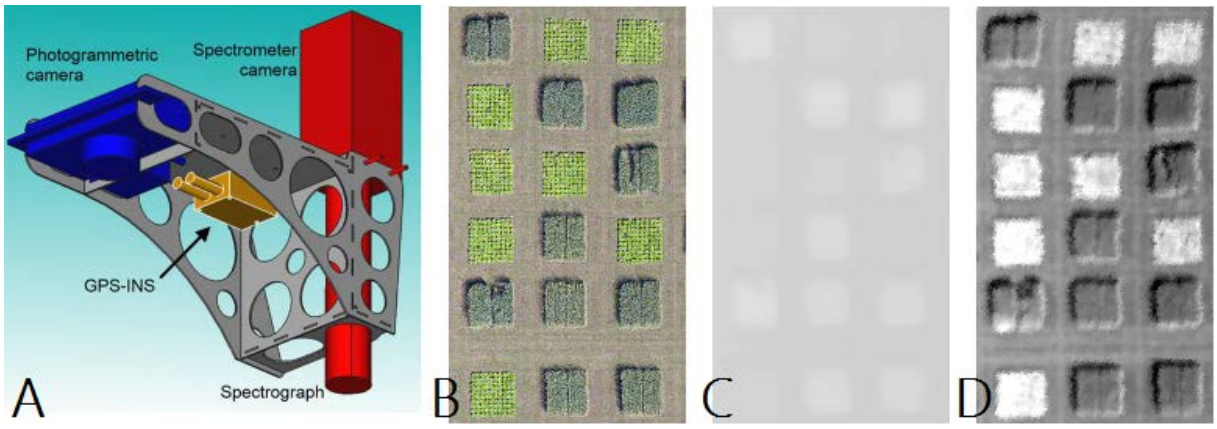

Figure 5.3: a) Schematic figure of the HYMSY frame and its main components b) RGB orthomosaic of part of the study area at 29mm spatial resolution c) the DSM at 29mm resolution, and d) the hyperspectral dataset at 13,4cm spatial resolution, visualized at 750 nm.

5.4 UAV data collection

5.4.1 UAV Data Collection

A UAV campaign was conducted during the 2015 growing season on the 1st of July, shortly prior to harvesting to harvesting of the crops and only a few days apart from when the field measurements were taken. Shortly prior to take-off and directly after landing, the sensors were field calibrated for incident irradiance by means of a 25% Spectralon reference panel. Through processing of the imagery acquired during paralleled flight lines with ~80% overlap, the data as depicted in table 5.1 (and figure 5.3b/c/d and appendix A) was generated. Even though the initial spectral resolution of the hyperspectral camera (9$_{nm}$) fits the recommendation to adhere to a bandwidth between 5-10$_{nm}$ (Thenkabail et al., 2012b), significant noise remained observable in the raw data. Consequently, it was decided to utilize a secondary level data product instead, being a hyperspectral data cube with a 30nm FWHM. The DSM was generated using photogrammetric algorithms during the post-flight processing chain, as will be discussed in more detail in the upcoming paragraph. For the full specifications and technical workings of the HYMSY platform, the reader is directed to (Suomalainen et al., 2014).

Table 5.1: Data produced of the study area by means of the HYMSY UAV-platform, including the data's associated specifications

Sensor	Data output	Spatial Resolution	Spectral Range	Spectral resolution
16MPix consumer camera	RGB Orthomosaic	1.5cm – 30cm	450 – 690_{nm}	B/G/R
	Digital Surface Model	2.9cm – 30cm	n.a.	n.a.
Hyperspectral camera	Hyperspectral Data Cube	13.4cm – 30cm	450 – 915_{nm}	$>9_{nm}$

5.4.2. The HYMSY's post-flight processing chain

As has been mentioned, a dedicated post-flight processing chain was specifically developed for the HYMSY platform and its associated data throughput, comprising of a radiometric and geometric components, respectively. A detailed elaboration of the chain can be found in Suomalainen et al. (2014), a brief overview is provided below.

5.4.2.1 Radiometric calibration

The primary step comprised of transforming the 'true' upwelling spectral radiance as observed by the hyperspectral sensor in digital numbers (DN) to units of radiance (L), which is executed on a pixel by pixel basis using dark current and flat field calibrations. Subsequently, the wavelengths were standardized through resampling to enable observing of (dis)similarities in spectral data derived from different locations in the study area. A resampling interval of 5_{nm} was chosen and processed using the accordant Gaussian filter on each linear column captured by the pushbroom scanner, resulting in columns of 328 pixels in length and 111 wide. At last, the radiance units (L) were translated into reflectance factors (R) through a conversion function that is calculated based on the measured radiance of the reference panel at each wavelength during flight, the average of pre- and post-flight measured radiance of the reference panel, and exposure times of the sensor (Suomalainen et al., 2014). The radiometric processing of the HDC is completed prior to geometric calibration of the data, as only the radiometrically correct hyperspectral data will serve as input for the succeeding process.

5.4.2.2 Geometric calibration

It has been stated previously in paragraph 2.4 that remote sensing imagery is prone to a variety of different errors or distortions with respect to geometry. This notion is equally, if not specifically, valid for imagery acquired by UAVs (Hardin & Jensen, 2015; Turner et al., 2012). The geometric component of the processing chain aims to deal with these errors accordingly, in addition to producing an auxiliary data product, namely the DSM.

During geometric processing, first positional and attitudinal metrics for each image were calculated based on the GPS-INS data, timestamps of image acquisitions, and boresight calibration parameters of the platform, respectively. Subsequently, a photogrammetric Structure-from-Motion (SFM) algorithm was applied to locate tie points between individual images (using *PhotoScan Pro, v1.0.0, Agisoft*). The latter are then fed into a block bundle algorithm together with the image orientations to produce a RGB orthomosaic, comprising of a three dimensional DSM overlaid with a mosaic of all aerial images, and optimized camera orientations (Suomalainen et al., 2014). In contrast to conventional photogrammetry, SFM is able to work with unstructured images, deviating resolutions and/or platform positions, in an image- rather than pixel-based manner, and therefore more suitable for UAV based imagery acquisition (Carrivick et al., 2013; Colomina & Molina, 2014). In the final step the adjusted camera orientations are carried through to the orientations of the hyperspectral sensor using the known boresight calibration specifications which are

hereafter utilized to georectify the hyperspectral data and project the HDC over the DSM (using *PARGE, 3.2beta, ReSe*) (Suomalainen et al., 2014).

Regardless of the various calibration steps within the overarching processing chain, the initial output still exhibited notable geometric distortions in different directions to different degrees as is visualized in figure 5.4 for the RGB mosaic. These distortions are inherently related to the notion that the orientation data relied on a relatively low-cost and inaccurate single band GPS-INS instrument and the fact that Ground Control Points (GCPs) were not included in the photogrammetric process. Therefore, the four corners of the study area and their coordinates (measured in RTK-GPS) were incorporated as Ground Control Points (GCPs) during a repetition of the processing chain. The improvements, due to enhancement of the camera orientations' precision and the data's global accuracy, are also visualized in figure 5.4.

Figure 5.4: Segment of the study area as captured by the HYMSY's 16MPix consumer camera after geometric processing without (left) and including GCPs (right)

The reprocessing of the data significantly enhanced its geometry, particularly with respect to the RGB orthomosaic from which the DSM was then derived. The improvements were less notable in the outputted HDC. This, however, was to be expected considering the challenges associated with pushbroom line array scanners, especially when mounted onto a platform that is situated close to the ground and relatively susceptible to in-flight attitude deviations due to environmental conditions. Inclusion of a larger number of GCPs covering multiple columns captured by the scanner would likely enhance the HDC's geometry, but considering the absence of such GCPs the current output represents the best result currently achievable by the processing chain. A final georectification procedure was therefore applied to the hyperspectral output in an attempt to further enhance its geometric correctness; this will be discussed in paragraph 6.2.1.

6. Methodological framework

It was mentioned in the introductory chapter that the research passes through three general overarching stages, namely a theory oriented exploration stage, data preprocessing, and data analysis followed by assessment of the results. Each of these stages, however, comprises of multiple smaller or larger consecutive phases. Distinct phases are directly or indirectly aimed at finding answers to the research objectives. In the following paragraphs, the framework of different stages and phases is presented in detail. The important dependencies between phases, i.e. how one relates to another, are also mentioned. Besides, the principles and techniques adhered to are presented. At various moments vital decisions had to be made, these are elaborated on and justified thereafter. This chapter illuminates the research strategy that outlines how intermediate data products were derived and how the research was undertaken. The workflow depicted in figure 6.1 represents this research' analysis design; a simplified and summarized visual representation of the methodological framework and the associated stages adhered to in this study. It should be mentioned that the scheme suggests a very linear and straight forward process, but iterations and feedback loops are inherently present.

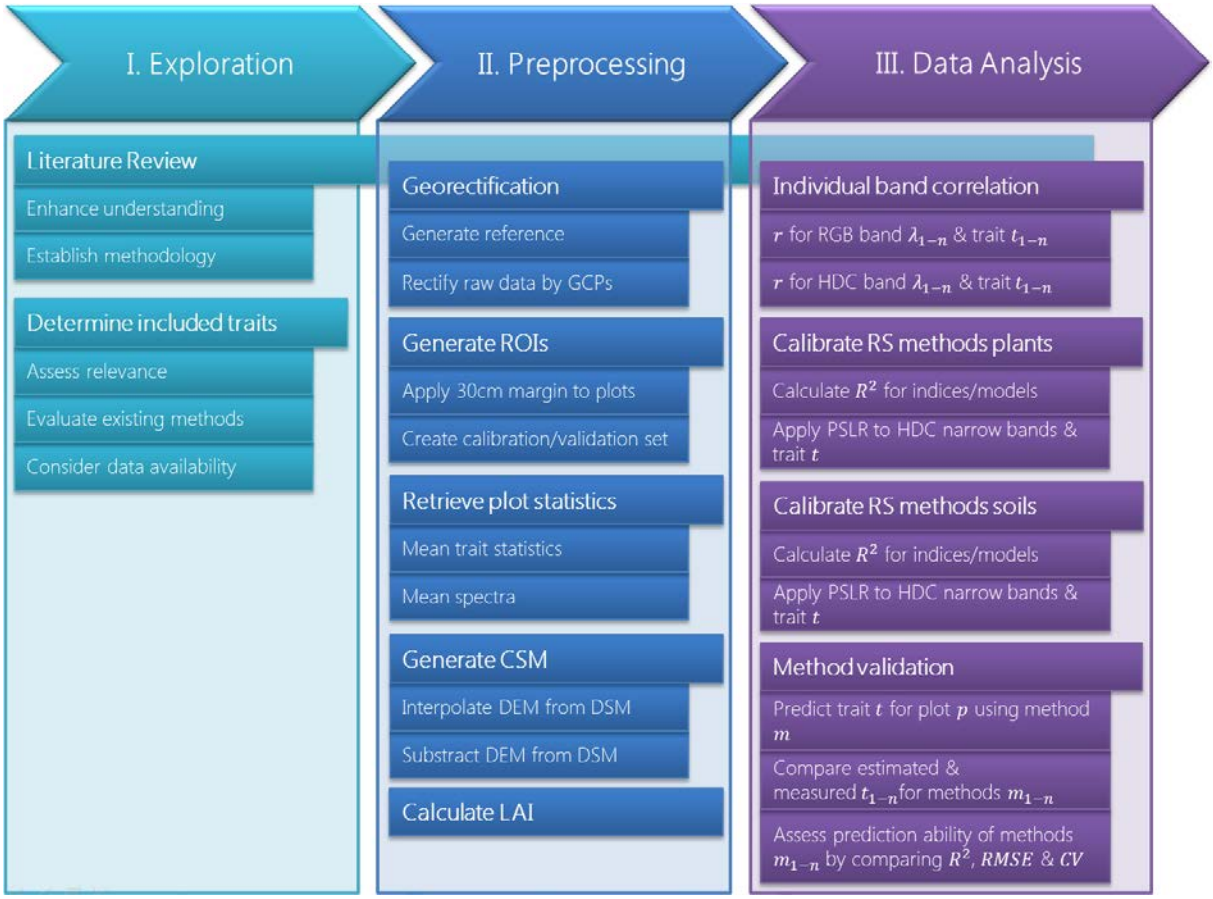

Figure 6.1: Analysis scheme depicting the research' three overarching stages and subsequent phases therein. Note that the Literature Review is an ongoing process that follows through all three stages.

6.1 Exploration (I)

6.1.1. Literature review

The research commenced with an extensive literature review. This phase is especially significant considering my personal relative lack of knowledge and experience within related fields such as (hyperspectral) remote sensing, UAVs, precision agriculture and plant phenology (chapters 2-5). Therefore, the initial exploration was primarily geared towards enhancing the understanding of relevant developments, theories, operations, concepts, constructs and jargon. This phase was additionally used to examine (partially) similar and relevant studies, in order to develop a general idea of the state-of-the-art of the field, methodological deliberations and research requirements. A significant portion of the findings distilled from this phase have already been covered in the theoretical contextual chapters preceding this. Additional findings, however, will continue to be presented throughout this report from here onwards. Similarly, the literature review is largely situated in the early phases of the research, although it remained in effect throughout the remainder of the process.

6.1.2. Determination of traits

Subsequently, the research focused on determination of relevant plant traits to be further investigated. In the past, a large variety of different biophysical and/or biochemical crop attributes have been studied, to various extends and for different purposes. Given the time and data constraints inherent to this research, this phase is primarily oriented at deciding upon relevant traits to be incorporated, and justification thereof. These decisions are ultimately based on a combination of literature reviewing, expertise of experts and availability of data, respectively.

In addition to enhancing understanding of relevant topics, the literature review was initially focused on determination of relevant biophysical and biochemical plant traits from an agronomical and remote sensing perspective, respectively. It has been indicated that although some of these distinct characteristics are considered relevant and studied within both fields, some are only recurring within one or the other. Here it is investigated why specific traits are typified as being relevant, i.e. which agricultural parameters (e.g. yield prognosis, crop health status) and practices (e.g. application of fertilizers) they are considered appropriate indicators for. Besides, the literature review was utilized to explore which crops and associated plant traits were retrieved in previous research, by what remote sensing methods, and requiring exactly which input data (chapter 4 and appendix C). Eventually, a list of potential trait variables was presented that served as input for subsequent selection procedures. The experts in this instance are represented by the thesis supervisor dr. ir. L. Kooistra and associate professor dr. ir. G. de Deyn from the WUR department of Soil Quality. The latter is primarily associated with the overarching field experiment mentioned before. Based on their expert opinion, the possibility and added value of incorporating distinct traits was evaluated to further narrow the initial selection.

Furthermore, availability in-situ measurements played an essential role as it ultimately determined which traits could (not) be incorporated into this research (paragraph 5.2). Assessment of the relationship between spectral reflectance data and distinct traits, as well as the evaluation of the acquired UAV data in regard to accuracy, inevitably requires ground measurements for calibration and validation. If ground-truth data of a specific parameter were unavailable, processing and evaluation of the aerial data for that trait is rendered impossible, and therefore abandoned. The provided UAV imagery represents an additional aspect of data availability for similar reasons (paragraph 7.4). It has been indicated in the preceding literature review

that there exists a multitude of varying data analysis methods one may utilize to identify, map and quantify traits of vegetation. Each methodology relies on distinct and different data input requirements with respect to sensor characteristics. Some require the incorporation of spectral data at specific spectral ranges that cannot be provided by the HYMSY platform being used here. Similarly, some methods rely on entirely different sensors, such as thermal, laser and/or microwave scanners. For obvious reasons, traits demanding such unavailable data as input were excluded early on in the process.

6.2 Data Preprocessing (II)

Prior to the phase in which the actual data analysis commenced, a data pre-processing phase was intercalated for various reasons. This is a vital prerequisite due to the notion that some of the provided data, once the post-flight processing chain had been completed (paragraph 5.4.2), was not yet fit for use. In the following paragraphs, the need and procedures for different forms of preprocessing are further elaborated on.

6.2.1 Georectification

6.2.1.1 Geometric errors in HYMSY acquired imagery

A selection of causes for geometric errors in the imagery used for this thesis was already (partially) accounted for by geometric correction procedures preceding this research, aided by the post-flight processing chain mentioned in paragraph 5.4.2. Regardless of these operations, artifacts of geometric distortions are still discernible in the HDC that was acquired. Some individual plots are randomly warped to different degrees and in different directions, resulting in different shapes and associated surface areas. The phase presented here aims to minimize the strength of these distortions through further georectification of the HDC. First, a brief overview of the principles of georectification principles is discussed, after which they are subsequently applied to the data.

6.2.1.2 Georectification methodologies

In order to deal with geometric errors and to georectify raw data accordingly, a variety of different models have been devised to transform data through use of mathematical functions (Toutin, 2004). In essence, these models depict the (mathematical) relationship between the image coordinate system and the target geographic coordinate system, respectively (Xie et al., 2008). Generally speaking, these models rely on image matching in which features in the acquired data are matched with the same feature as depicted in a rectified reference map, orthophoto or a DEM (Xiang & Tian, 2011). Traditional georeferencing by means of an externally acquired (i.e. global or regional) DEM, however, will induce too large errors due to the significant difference in resolutions of such a DEM and the UAV data, respectively (Suomalainen et al., 2014). The most common transformations are performed by means of polynomial methods, due to their relatively simple applicability and presence in a variety of different software packages (Rocchini & Rita, 2005). Polynomial functions come in different 'orders' and can accommodate either two or three dimensions. The latter incorporates z-terms to cover the third dimension of the terrain (Toutin, 2004). For relatively flat areas, however, such rigorous and computationally more intensive models do not necessarily yield better results (Rocchini & Rita, 2005). Therefore, given the hardly elevated study area, 3D polynomials are excluded here. The higher the function's order of 2D polynomials the more complex the distortion that can be corrected. First order (affine) transformations allow shifting, scaling and rotating of an image, whereas the second order can also handle torsion and convexity (Toutin, 2004). Even though third and higher order polynomials enable correction of even more complex distortions, they are also prone to introducing significant additional errors in in the process, and are therefore rarely applied (Rocchini & Rita, 2005). In all cases, however, 2D

polynomials should only be applied to images with limited distortions, a condition that is more easily met when images were acquired in nadir, when systematic errors have already been corrected for and/or when the image covers (relatively) flat terrain (Toutin, 2004). The final step in all of the geometric processing models comprises of image rectification, in which 1) the new cell coordinates in the original image and 2) the new values of pixels are computed by means of a geometric and radiometric operation, respectively. The latter operation, known as resampling, is an interpolation function based on values from the original image (Toutin, 2004).

6.2.1.3 Applying georectification to the HYMSY acquired hyperspectral imagery

A georeferenced map or orthophoto of the study area was nonexistent. Besides, the exact location in space of individual plots has not been measured and ground control points (GCPs) were not established. As a result, direct georectification through image matching was rendered impossible and therefore followed a different approach. The method primarily relies on the known geometric dimensions of the field experiment (spacing and plot size) and the coordinates of the field's outer corners. The known geometry enabled the generation of a digital figurative representation of the study area, including relative spatial dimensions of individual plots and plot spacing, similar to the actual field situation.

First, the original HDC flight line data was imported into ESRI's Arcmap. To enhance the hyperspectral imagery and allow discrimination of individual plots and shadows, the HDC was visualized in RGB through utilization of the appropriate bands (460_{nm}, 570_{nm}, 670_{nm}) and application of gamma stretching. Georectification inevitably lowers the resolution of the warped imagery. To accomplish the highest resolution for output datasets, the raw hyperspectral imagery with the highest original spatial resolution (13.4cm) was included. The reference map was then also imported, subsequently providing its corners with the in-situ measured coordinates. Hereafter, the reference was re-projected to bring its projected coordinate system in alignment with the spatial reference of the hyperspectral data. Then, GCPs were manually assigned to each of the four corners making up each plot and then linked to appropriate location in the reference accordingly (figure 6.2). As the imagery is solely utilized for analysis of oat plots, only these plots were incorporated into the process. The method for image rectification was based on quantitative (RMSE scores) and visual results provided for each type of transformation. A lower RMSE and output imagery that better aligned with the reference plots was considered best. A second order polynomial transformation yielded the lowest RMSE for both flight lines (0.25m and 0.29, respectively) and most adequate visual output, and was therefore selected. For resampling, or computing of new values of pixels, the nearest neighborhood algorithm was applied. This algorithm first locates the cell's center in the warped image in the original non-rectified data. Next, a nearest neighborhood is applied to retrieve the value of the nearest cell in the original data and assign this value to the output raster cell. The algorithm is specifically designed for resampling of discrete thematic or categorical data, such as radiometric values in remotely sensed imagery (Esri, 2015). Both HDC flight lines were resampled to a cell size of 14.0cm.

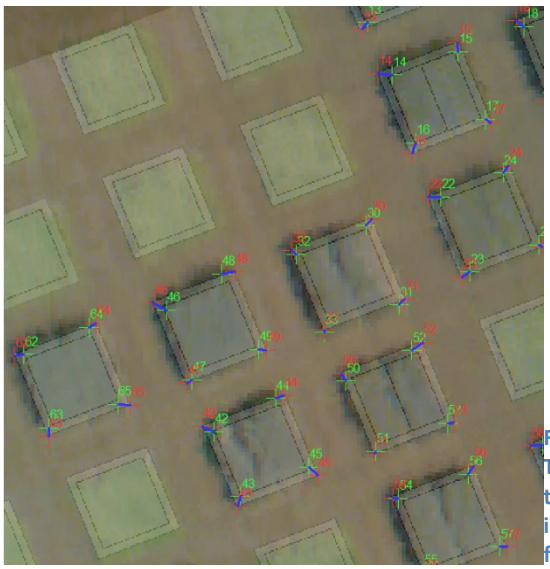

Figure 6.2: Snapshot of the georectification process in Esri Arcmap. The GCPs in the reference map (transparent top layer) are in red, the common GCP is depicted and located in the original HDC image in green. The latter are eventually rectified to the location of the first.

6.2.2 Generating Regions of Interest (ROIs)

Region Of Interest (ROI) vectors were generated for all left and right subplots for all oat plots. Each individual vector in polyculture plots, or two for monoculture plots, represents a single plot that allows for retrieval of zonal statistics of spectra and height data. These ROIs were established for the Crop Surface Model (paragraph 6.2.3) and HDC separately. Regardless of the incorporation of boresight calibrations in the geometric post-flight processing chain, the orthomosaic (from which the CSM was derived) and the HDC are still not perfectly aligned. Therefore, eventual retrieval of features from these datasets using identically shaped and located ROIs is considered questionable. In order to limit the influence of likely edge effects (e.g. shadowing), a 30cm margin between the vector's edges and the actual plot's edges was incorporated. An identical buffer is included with the respect to the plot's center line for monoculture accommodating two types of polyculture vegetation. During acquisition of the field data a similar trimming was adhered to, i.e. no samples were taken from within 30cm of the plot's edges. By applying an equally sized margin to the ROIs the zonal statistics are extracted from an area assumed relatively similar to the area in which field data was collected. Circumventing edge effects in this manner is common practice, as is demonstrated by (Bareth et al., 2014). The ROIs, or more specifically the zonal statistics retrieved from these shapes, are eventually used to calibrate different models and validate their accuracy at later stages.

Subsequently, the ROIs were randomly divided in a calibration and a validation set of equal size (50%/50%). In the overarching field experiment it is assumed that the variation of different plot treatments influences traits of current vegetation. Therefore, it was made sure that, prior to randomization, each set comprised of an equal number of plots having received a distinct treatment to minimize this potential effect. The first (calibration) set was used for developing functions that depict the mathematical relationship between spectral data (i.e. vegetation indices) and each trait studied (chapter 8). The validation set was hereafter used to validate the relationships, i.e. to assess the prediction ability and accuracy of each model, by comparing the actual field measurements with the values estimated by calibrated models (Li et al., 2014). The calibration and validation process is discussed in more detail in paragraphs 6.3.2 and 6.3.3, respectively.

6.2.3 Generating Crop Surface Model (CSM)

Although a DSM representing the surface height of the entire study area was derived, it does not contain data on the height of vegetation itself. Therefore, a new dataset was created to provide a rough estimation of the height of vegetation within each individual plot. This first required the generation of a Digital Terrain Model (DTM), representing the bare ground surface of the study area. This was accomplished by interpolating height values (derived from the DSM) of 90% of 13733 point locations, spaced 10cm apart, situated between the plots. It is assumed that the surface (bare soil) height of plots prior to cultivation does not (significantly) differ from the surrounding grounds, and a DTM covering of the entire study area can thus be approached by interpolation of nearby non-plot locations. Given the relatively stable elevation in the study area, the dense distribution of points and the goal to arrive at a smooth continuous terrain model, the spline method was applied for interpolation (Childs, 2004). A barrier polygon reaching slightly beyond the most outside plots was included to limit processing time. To assess the performance of the interpolation, the remaining 10% of 13733 points were used to calculate residuals in height between the original DSM and 'predicted' DTM (RMSE = -0.093 vertical mm). By subtracting the resultant DTM from the existing DSM, the latter representing the study area including vegetation cover, the height of plants within different plots was retrieved (figure 6.3 & Appendix B), as demonstrated by Tilly et al. (2014) for barley crops. From here onwards, the output dataset will be referred to as a CSM (Crop Surface Model).

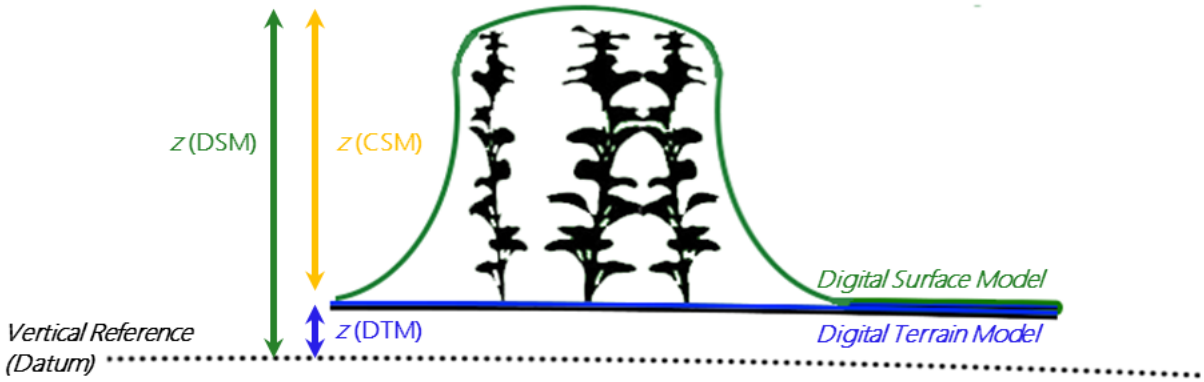

Figure 6.3: The relationships between the DSM, DTM and CSM. suggested here.

6.2.4 Retrieval of plot statistics

Figure 6.4 is a graphical representation of this segment of the data preprocessing and subsequent data analysis phases, and is considered a comprehensive addition. First, the ground measurements taken at selected locations in each plot with respect to distinct plant and soil traits were processed. For each plot, the values of individual measurements were stored, in addition to the associated standard deviation σ and coefficient of variation ε when multiple measurements were retrieved from a single plot. For traits where the latter was the case (i.e. leaf Chl content and plant height), the readings were averaged to arrive at a mean quantitative value $\hat{y}$ of trait x, representing each plot (figure 6.4A). For all traits, the (averaged) measured values were stored in a single spreadsheet.

In order to efficiently extract the (hyper)spectral data, a Python script was written to collect the reflectance values of all pixels that fall within an ROI dedicated to one plot (appendix N). The automated extraction was repeated for all wavelengths present in the HDC. Subsequently, the reflectance values of pixels were averaged for each separate band and ROI, resulting in a single spectral mean reflectance value ($\bar{R}$) representing that plot at each wavelength. Similarly, the height values stored in the CSM were extracted and then averaged using ROI vectors, resulting in an indication of the plot's average vegetation height (figure 6.4A). The resultant mean spectra are automatically stored in a spreadsheet.

During the subsequent data analysis calibration stage, the relationship between the mean of measured reflectance at individual bands, indices calculated from these values, and trait measurements, is assessed for each plot. At this point it is worth mentioning that utilizing reduced subplot size ROIs to allow retrieval of smaller scale statistics for calibration and validation, based on the exact location of individual samples, is ultimately preferred. In such an ideal situation the UAV imagery acquired at very high resolution could be more precisely related to point/zonal measurements of traits on the ground. Because the exact locations of ground-truth measurements are not known, and because remaining geometric distortions disallow accurate estimation of these locations, however, calibration and validation based on even more detailed ROIs is considered highly questionable and arbitrary. Therefore, the research relies on averaged zonal statistics for (spectral) UAV data. Working with plot averaged metrics is a practice that is frequently observed in related or comparable studies (Bareth et al. (2014), Kooistra et al. (2014), Yu et al. (2008).

6.3 Data Analysis (III)

Once the original data was preprocessed and considered fit for use the analysis commenced. This stage passes through a substantial number of consecutive phases majorly aimed at establishing of relationships between spectral data acquired by the UAV and field trait data by calibration, and assessment thereof through validation. At this point, the literature review has identified a variety of different reflectance oriented approaches (i.e. indices and other models) that have proven to be effective for estimation of the

selected biophysical and biochemical plant traits. These approaches vary in regard to data input requirements and the degree to which they have been able to successfully estimate distinct parameters (chapter 4 & appendix C). The field and aerial UAV data that was collected and examined before in chapter 5 has been stored in spreadsheets and serves as input for this stage. The diversity of (statistical) analyses presented below will be processed using both R and Microsoft Excel. The latter is most strictly employed due to its provision of extensive capabilities in regard to statistical analysis of sizable datasets (Maindonald & Braun, 2010). The use of Excel is primarily geared towards the eventual production of supportive figures, and retrieval of more basic statistics to a lesser degree.

6.3.1 Univariate band-trait correlation

This phase is focused on illuminating the relationship between spectra of individual bands present in the HDC and in-situ measurements of traits. Correlation coefficients (r) between individual band and distinct plant characteristic are generated by cross-correlation of average plot spectra and (mean) plot trait measurements. This is repeated for each individual band. The output comprises of graphs indicating univariate correlation coefficients at each narrow band, for each trait (Nguyen & Lee, 2006; Hansen & Schjoerring, 2003; Thenkabail et al., 2000). The graphs provide a visual means for enhancing understanding of how strongly and in which direction the variation of spectral values in distinct bands and trait metrics are (not) related (Zhao et al., 2014). Univariate bandwidths that are highly correlated are considered suitable indicators for the specific trait, and vice versa. Subsequently, such bands are expected to yield the best results during the gradual development of simple or more advanced (multiple) regression models for estimating biophysical and/or biochemical vegetation parameters in later stages (Bajwa & Kulkarni, 2012). In addition to the regressing of individual spectral bands with individual traits, this step will additionally evaluate the ability of the DSM to model actual plant heights within actual plots. For this purpose, the mean of in situ plant height measurements for each plot are regressed with the mean plant height as modelled by the CSM.

6.3.2 Calibrating UAV Data & Field Trait Data relationships

6.3.2.1 Univariate index-trait correlation

A selection of the available indices, as mentioned in chapter, will be applied to the processed spectral data present in the calibration set. Due to the utilization of different sensors in studies from which the methods were derived, some of the indices rely on distinct band centers that are different from those of the HYMSY platform. In order to approximate these models, the inputs will be replaced by HYMSY bands whose center is situated most nearby in the electromagnetic range. Each index is applied to each individual plot's mean spectral value at the designated wavelengths, resulting in a numerical index value representing that plot. Subsequently, the relationship between indices and the selected traits is assessed through regression between the observed index and trait values for each plot (figure 6.4B). The output comprises of a mathematical function (i.e. a model) that best describes the relationship using coefficients that minimize the sum of squares of residuals (Maindonald & Braun, 2010) (figure 6.4C). In addition, the coefficient of determination (R^2) associated with the function is provided, which displays the proportion of the total sum of squares about the mean that is explained by the model itself (Maindonald & Braun, 2010, p. 186). It provides a comprehensive indication of how adequately dependent variables (traits) can be explained by the model, while subsequently allowing comparison of models for and between different traits. (Kooistra et al., 2014; Blackburn, 1998). Only when the graphical output exhibits a clear non-linear relationship (e.g. exponential), alternative curve-fitting will be applied to assess whether this yields higher R^2 values.

6.3.2.2 Regression through contour plots

Considering that the interaction of plants and their constituents with incoming radiation is highly diversified for different crop species, their physical structure and developmental stage, among other factors, the existing indices tested here might effectively produce sub-optimal results (Freeman et al., 2007; Osborne et al., 2002). Consequently, it is argued worthwhile to explore the possibility of alternative band combinations within an index with respect to their ability to identify specific traits (more adequately). Therefore, for general indices based on only two bands (SRs, NDVIs & SDs), matrix contour plots indicating the coefficient of determination (R^2) for each possible combination of bands from 450nm to 915nnm with the trait studied will be generated. These plots will be generated by a self-written optimization algorithm script in R. From this optimized two-band indices that most strongly relate to the distinct traits (i.e. hotspots), and the associated function, can then be easily extracted (Nguyen & Lee, 2006; Thenkabail et al., 2000) (figure 6.4C).

6.3.2.3 Univariate PLS regression

Finally, univariate Partial Least Square Regression (PLSR) will be employed to all spectral bands in the HDC to produce a linear model (function) between the mean spectral values and (mean) trait values of each plot, incorporating an *x* number of narrow bands. Similar to the methodologies mentioned above, the adequacy of the resultant regression model with each trait is indicated by its value for the coefficient of determination R^2. PLSR finds an *x* number of latent variables which together maximize the amount of variation explained in the spectral data considered relevant for estimation of a single specific biophysical or biochemical trait (Alchanatis & Cohen, 2012; Bajwa & Kulkarni, 2012). PLSR, besides, reduces data dimensionality and model over-fitting by avoiding collinearity between (adjacent) bands, while also directly incorporating information of the response variable (trait) into the process (Mulla, 2013; Cho et al., 2007; Mevik & Wehrens, 2007). For this reason PLS regression has been frequently mentioned as a promising technique for analysis of extensive and highly dimensional hyperspectral data (Yu et al., 2014; Feilhauer et al., 2010). Even though alternative information extraction methods exist (e.g. Discriminant Analysis, PCA), PLSR is stated to perform better in vegetation monitoring applications and is therefore frequently applied in agricultural science (Bajwa & Kulkarni, 2012; Liu et al., 2007), as demonstrated by Yu et al. (2014), Cho et al. (2007) Nguyen & Lee (2006), Hansen & Schjoerring (2003) and Smith et al. (2002).

More specifically, and similar to utilization of PLS in most applications, a random PLS model based on leave-one-out-cross-validation will be built. Two types of PLS models will be calibrated for each trait, one incorporating only hyperspectral spectra, and a second in which the estimated plant in the CSM is added as an auxiliary variable. Using this approach, each observation is separately dropped from the set during the model building process, which is repeated for all samples in the calibration set. The (training) observations that remain are used to calibrate the PLS regression model which is subsequently used to predict the value of the left-out variable (e.g. the testing set) (Abdi, 2010). The PLS model quality, i.e. its precision and accuracy, will be evaluated internally according to the (cross-validated) R^2, RMSEP (Root Mean Square Error in Prediction) expressed in original units and REP (Relative Error of Prediction) expressed as a percentage, resulting from this cross validation (Appendix M). A higher value for the first, and lower values for the latter two, indicate a better model performance (Nguyen & Lee, 2006). During cross-validation, the number of latent variables to be included in the building of the model is increased by one after each repetition (Li et al., 2008).

In general, PLS model precision increases as the number of latent variables is increased (Yu et al., 2014). Due to the risk of model overfitting, however, this does not necessarily equal an increase in the prediction quality of random PLS models when a larger number of variables (or factor loadings) is included. Instead, the quality lowers momentarily once a certain number of variables has been included, i.e. the information useful to fit the observations from the learning set is no longer useful to fit new observations (Abdi, 2010, p. 101). In order to optimize the number of independent variables to be included in PLS model, i.e. to maximize performance while circumventing model overfitting, the PRESS statistic is employed (Nguyen & Lee, 2006). PRESS (Predicted Residual Error Sum of Squares) or Residual Y-variance is a measure commonly applied for the purpose of assessing whether inclusion of an additional latent variable significantly adds to the model (Yu et al., 2014; Esbensen et al., 2002). More specifically, loading additional variables is stopped once the minimum PRESS has been reached, and the PLS model producing the lowest PRESS value is considered the preferred and best performing model for each trait (Nguyen & Lee, 2006) (figure 6.4C). The resultant optimal PLS models will subsequently be used to predict the traits in the validation set, their quality will be assessed using the same indicators presented here (paragraph 6.3.3).

6.3.3 Validating UAV Data & Field Trait Data relationships

To assess the performance of different approaches, the validation phase is geared towards analyzing the ability of indices to predict distinct traits. For this purpose, only the data from the independent validation set is employed to validate the relationships found between indices and traits during calibration. First, a selection of the best performing (existing/optimized & PLS) indices/models, and their associated mathematical relationship, found in the preceding calibration phase are applied to each individual plot's mean reflectance value at the according wavelengths (figure 6.4D). The outcome is a quantified (average) trait estimate, for each individual trait, function and plot (figure 6.4E). Next, the trait prediction for each plot is cross-validated with the (mean of the) observed trait values, as measured previously in the field. The model's performances are then assessed through comparison of the resultant values for R^2 (coefficient of determination), RMSE (Root Mean Square Error) and the normalized CVRMSE (CV in %) for each trait (figure 6.4F). Lower values for the latter two and a higher R^2 indicate enhanced predictive capabilities and model adequacy, respectively (Li et al., 2014; Reddy, 2011; Nguyen & Lee, 2006). Assessing the performance of different models through validation, once the models are calibrated, is a common approach applied in multiple related studies (see for example: Li et al. 2014; Tian et al., 2011; Heiskanen, 2006; Nguyen & Lee 2006; Haboudane et al., 2004; Smith et al. 2002; Gong et al., 1995).

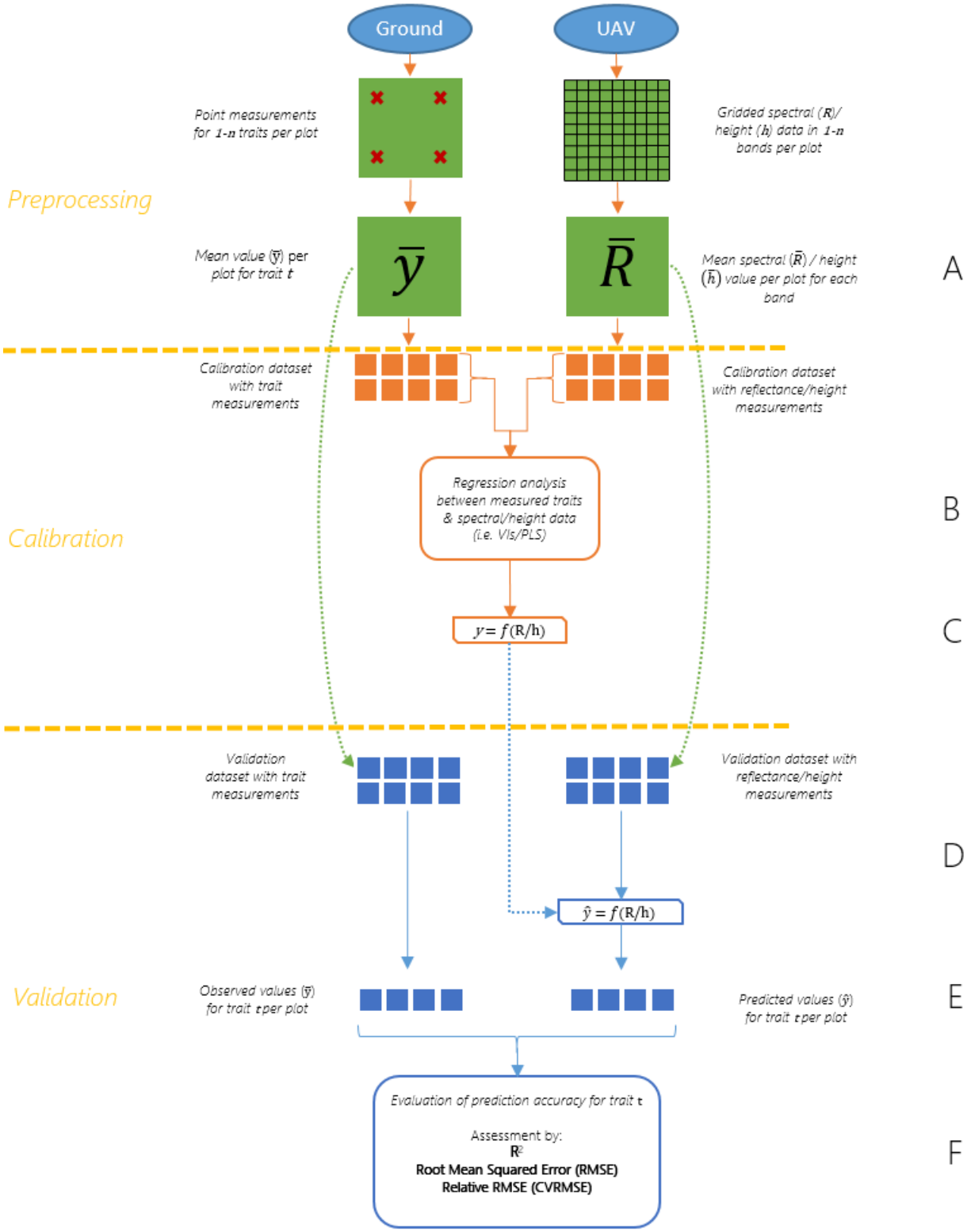

Figure 6.4: Graphical representation of part of the preprocessing operations and the subsequent calibration and validation phase.

7. Analyses & Results: Exploratory Data Analysis (EDA)

An initial inspection of the data was conducted prior to the subsequent analysis in order to enhance the understanding of the underlying data acquired either in the field and from the air. Below, a brief summary of relevant data and its main characteristics is presented in both a textual and graphical manner for calibration and validation data separately. As will be discussed shortly in paragraph 7.3, exploration of the data exposed various unexpected anomalies that were likely resulting from (sincere) within-plot physical heterogeneity. It was eventually decided to leave these individual plots out of the analysis, hence the explanation and figures presented hereafter are solely related to the dataset(s) after removal of these plots where both calibration and validation set comprise of 28 individual plots..

7.1 Average spectra

Average spectra were calculated for all plots combined at each wavelength (figure 7.1). For both the calibration and validation set, the figures adhere to the traditional spectral signature of vegetation. In the visible segment of the spectrum the diffusion among plots with different inter-seasonal treatments is relatively limited. The signature indicates a minor and varied decrease in (chlorophyll induced) absorption in the green (500-620 nm) compared to blue (450-500 nm) and red (620-700 nm) wavelengths. Considering only the visible part of the spectrum, the highest and lowest reflectance values are recorded at 555nm and 675nm, respectively. This is in agreement with these wavelengths frequently being identified as the chlorophyll absorption minimum and maximum, respectively (Vincini et al., 2007; Haboudane et al., 2004; Broge & Leblanc, 2000). The reflectance notably increases beyond the chlorophyll post-maxima (±700nm) throughout the red-edge and particularly at near-infrared wavelengths (>750 nm). At this point, the signatures for different treatment types gradually deviate along a vertical shift, i.e. the relative shapes remain largely identical. In the near-infrared, the reflectance of plots cultivated with *Lolium perenne* (Lp), *Trifolium repens* (Tr) or a combination of the two cover crop types consistently display lower reflectance's, and so are those plots left fallow. In contrast, plots cultivated with *Rapharus sativa* (Rs), *Vicia sativa* (Vs) or a combination of the two structurally indicate higher reflectance values. Variations in reflectance among individual plots adhere to a similar structure, indicated by marginal deviations in the blue and red resulting from increased chlorophyll absorption, and more diverging values throughout the green and near-infrared (not shown, see appendix D).

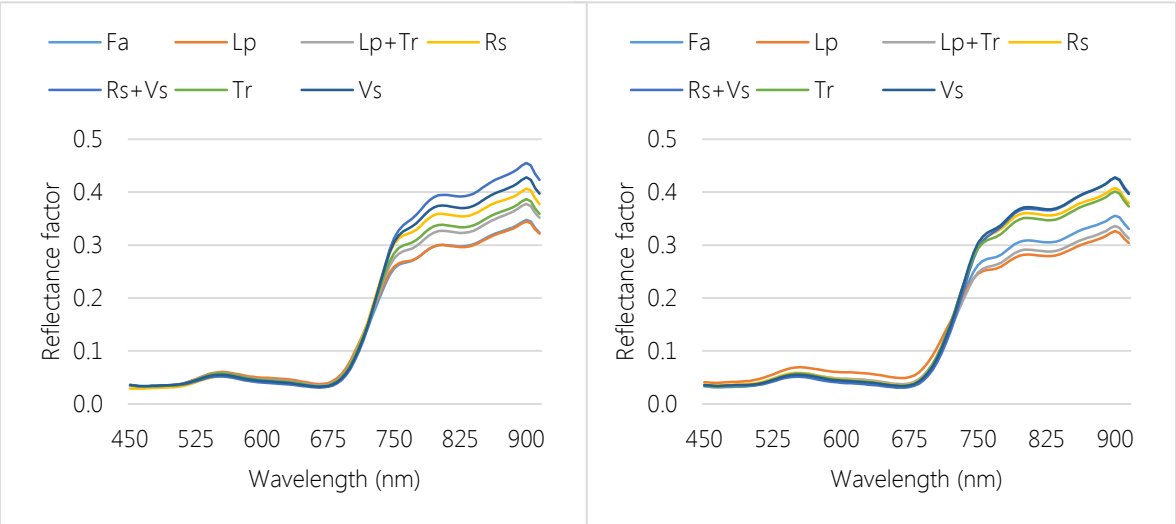

Figure 7.1: Average reflectance spectrum of the different experimental plots and their associated treatments for the calibration (n=28, left) and validation (n=28, right) set (Fa = fallowed, Lp = *Lolium perenne*, Rs = *Rapharus sativa*, Tr = *Trifolium repens*, Vs = *Vicia sativa*).

7.2 Summary statistics of crop traits

The experimental design of the study area and varied intra- and inter seasonal treatments of individual plots produced some variation within some of the different crop traits studied (table 7.1). The statistics for both input datasets are largely in accordance with one another, the maximum difference between mean values is 3% (C content). Some differences for minimum and maximum values are discernible, particularly for fresh biomass, C content and N content where the extreme low and/or high values in the validation set exceed the calibration set. Concentration and content of leaf chlorophyll and nitrogen content display the largest dispersion considering their associated coefficients of variation (CV). Besides, the dispersion for each trait is equal or larger within the validation set, except for both leaf chlorophyll measures and N concentration. In contrast, concentration of C hardly exhibits any variation, in accordance with the notion that carbon concentration in vegetation is a relative constant (Magnussen and Reed, 2004). A breakdown of these trait statistics for different treatments in validation plots is presented in paragraph 9.4.

Table 7.1: Summary statistics for all field trait measurements

Crop Trait	Unit	Calibration set (n=28)					Validation set (n=28)				
		Mean	*SD*	*CV*	*Min*	*Max*	*Mean*	*SD*	*CV*	*Min*	*Max*
Height	*cm*	91.26	10.04	0.11	72.50	112.50	89.67	9.92	0.11	72.50	108.88
Fresh BM	*kg m^{-2}*	3.54	0.86	0.24	2.19	5.41	3.47	1.04	0.30	1.67	5.77
Dry BM	*kg m^{-2}*	1.18	0.24	0.21	0.81	1.64	1.15	0.29	0.26	0.60	1.73
N concentration	*%*	0.76	0.16	0.22	0.54	1.16	0.77	0.16	0.21	0.53	1.15
N content	*g m^{-2}*	8.98	2.91	0.32	5.14	17.85	9.00	3.27	0.36	3.87	15.23
C concentration	*%*	45.26	0.36	0.01	44.20	45.80	45.22	0.44	0.01	43.90	45.80
C content	*g m^{-2}*	535.8	111.7	0.21	365.4	749.9	519.5	134.6	0.26	264.1	785.8
LC concentration	*mg kg^{-}*	5.08	2.08	0.41	2.37	9.75	4.82	1.70	0.35	2.57	8.91
LC content	*g m^{-2} PLA*	0.76	0.28	0.37	0.38	1.38	0.72	0.23	0.32	0.41	1.27

All traits are positively correlated with one another (figure 7.1). For the calibration set, the strongest correlations were found between leaf chlorophyll concentration and content, and between fresh and dry biomass, in addition to C content being a near-function of dry biomass ($r \approx 1.0$). The correlations between height and nitrogen content, fresh biomass and nitrogen content, nitrogen concentration and content and between nitrogen concentration and chlorophyll concentration/content are lower but still substantial ($r \approx 0.8$). Correlation coefficients for other combinations are lower and range between $r \approx 0.15$ (for dry biomass and chlorophyll concentration/content) and $r \approx 0.7$ (appendix E). Generation of correlation coefficients for the validation set yielded largely similar results with respect to distinct combinations of traits exhibiting relatively weak or strong relationships (not shown in main text, but presented in appendix E). The most notable deviations relate to lower correlation coefficients between nitrogen concentration and chlorophyll concentration/content ($r \approx 0.6$), relatively stronger relationships between various combinations of height and both types of biomass, and the very limited of interdependency between carbon content and leaf chlorophyll concentration/content.

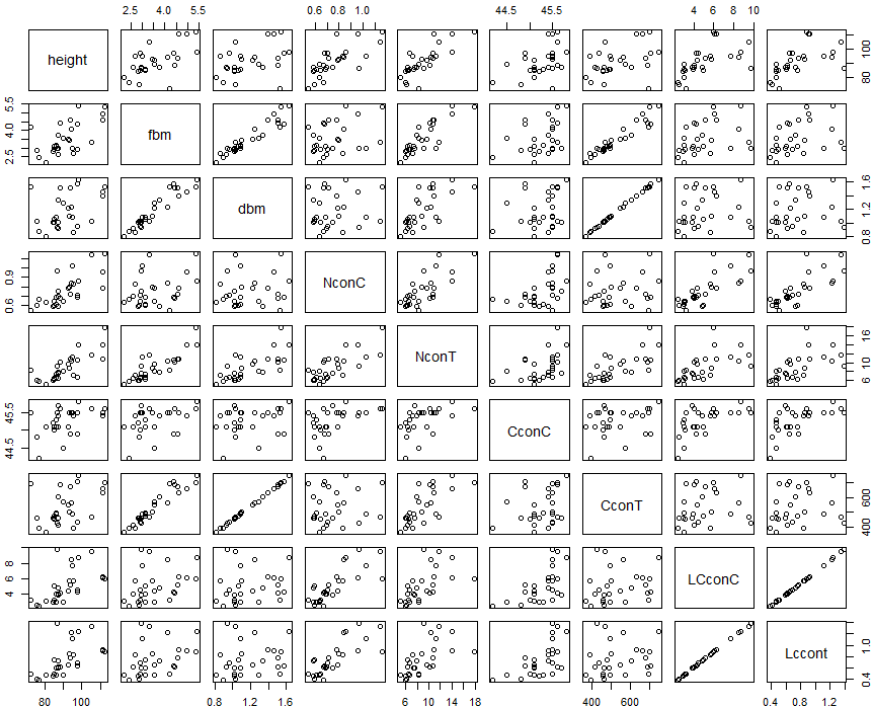

Figure 7.2: Scatterplots for all possible combinations of traits in the calibration set (n=28)

Please note that for N, C and leaf Chl, both concent and concentration values are provided in the above figures. Only the aerial metrics expressed by content, however, are incorporated in the description and calibration and validation procedures following hereafter. According to Chen et al. (2010), vegetation monitoring oriented research primarily focused on N content rather than N concentration. It was therefore decided to incorporate the former, as it is argued to allow for easier retrieval of existing indices and evaluation of the findings with respect to previous studies. C concentration was found to be rather invariable and to exhibit very limited variation. It was thus decided to incorporate only C content instead. Dry biomass was excluded from subsequent analysis for the same reason, considering that C content hardly deviates from dry biomass due to the derivation of the former from the latter through C concentration. Inclusion of both resultantly invokes redundancy, hence a single variable was selected. Finally, leaf Chl content and concentration were found to be relatively indifferent and produce largely overlapping correlations due to their deduction from the same SPAD readings. Consequently, only leaf Chl content was selected.

7.3 Correlation between crop trait and canopy reflectance over wavebands

Figure 7.3 below visualize univariate correlations coefficients (*r*) between separate plant traits and individual narrow bands. Prior to the removal of some plots, as was mentioned previously, univariate correlations for some of the traits exhibited vastly unanticipated values throughout the spectrum in comparison to findings in existing studies. Besides, the figures for the calibration and validation set were highly contrasting with respect to multiple traits. At this point further exploration of the data commenced, aimed at illuminating which plots' reflectance values and/or in-situ trait measurements most notably affected the assumingly flawed coefficients. It was reasoned that the anomalies were mostly likely ascribable to within-plot physical heterogeneity, i.e. smaller or larger sections of plots exhibiting poor or absent vegetation growth, and the different and inadequate spatial resolution at which input data was acquired. In order to minimize the influence of this complex notion on the output, it was decided to remove all plots from the dataset that exhibited clearly observable physical heterogeneity based on a visual inspection of the RGB orthomosaic. A more extensive elaboration on this matter including supportive figures can be found in Appendix F.

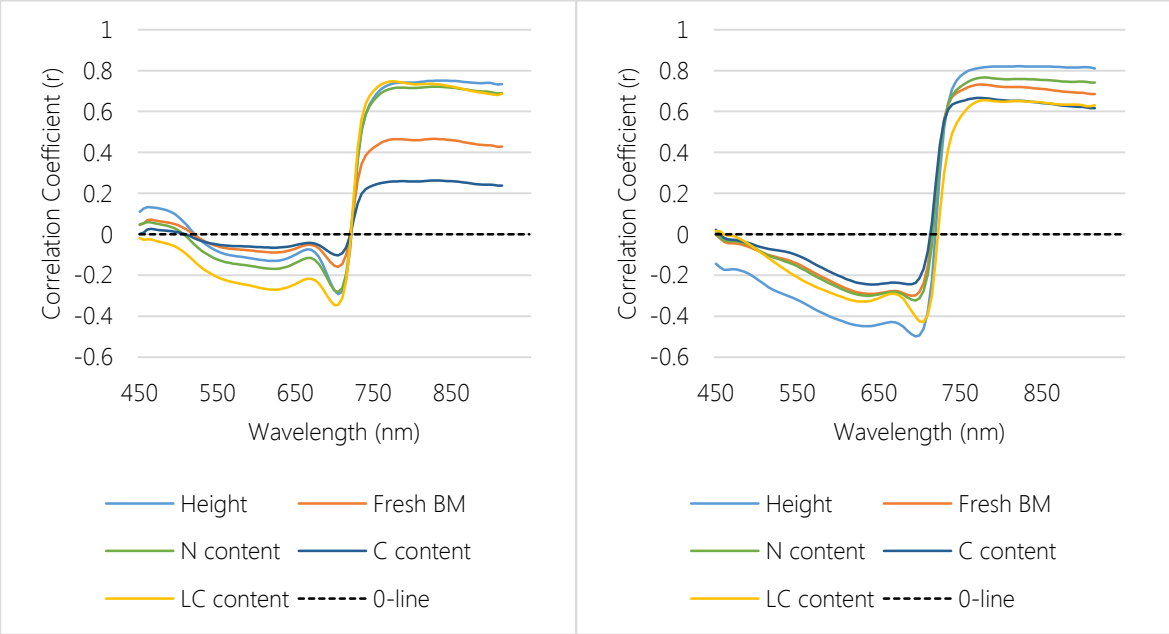

Figures 7.3 : Wavelength dependence of the correlation coefficient (r) based on a linear regression between average plot canopy reflectance and each crop trait studied for the calibration (left, n=28) and validation (right, n=28) set.

The coefficients of correlation (r) between measured canopy reflectance and individual traits diverge notably over different wavelengths, varying from mostly negative correlations in the visible range to positive correlations throughout the near-infrared. All of the traits indicate relatively comparable patterns with respect to wavelengths at which they exhibit positive or negative correlations, differences between traits most strictly relate to the strength of such correlations. Until approximately 500nm, *r* is minimal and pivots around the center line representing no correlation ($r \approx -0.1 <> 0.1$). From here onwards, the coefficient turns increasingly negative until the maximum negative r values are reached at approximately 640nm and at 695nm in the chlorophyll absorption post maxima, in agreement with Zhao et al. (2014, Nguyen & Lee (2006), Thenkabail et al. (2000). At approximately 675nm, the correlation's strength weakens due to a loss of sensitivity resulting from maximum chlorophyll absorption. Between 695nm and near-infrared wavelengths, *r* rather abruptly becomes positive, intersecting with the center line between 710-720nm for different traits, followed by a flattening at approximately 750nm (with $r \approx 0.6 <> 0.8$ for most traits). The relatively higher (negative) correlation coefficients surrounding 695nm in the red and (positive) coefficients in the near-infrared from 750-915nm suggest these narrow bands' relative importance with respect to prediction of distinct crop traits (Bajwa & Kulkarni, 2012).

Particularly striking, however, is the diffusion in the near-infrared among values of *r* for plant height (max. $r \approx 0.75$), fresh biomass (max. $r \approx 0.45$) and C content (max. $r \approx 0.25$) within the calibration set. The latter trait is an approximate function of dry biomass due to near-constant values for C concentration and the derivation of C content through dry biomass. It is commonly understood that plant height is positively and rather strongly correlated to plant biomass (Tilly et al., 2014; Fernandez et al., 2009; Niklas & Enquist, 2001). Therefore, relatively similar correlation coefficients at individual wavelengths were anticipated for these variables, as is the case for the validation set. These diverging patterns, however, follow from relatively poor univariate correlations among these variables for the calibration set, especially when compared to the results for the validation set (figure 7.2 and 7.4 & Appendix E).

Furthermore, the results are largely in accordance with the findings of, for example, Zhao et al. (2015), Fava et al. (2009), Nguyen & Lee (2006), Hansen & Schjoerring (2003) and Thenkabail et al. (2000) regarding some of the traits included here for different vegetation types. The strength of correlations

throughout the visible spectrum, however, is notably and consistently lower than was observed in these studies. Besides, minor anomalies in correlation coefficients, observed by Nguyen & Lee (2006) and Hansen & Schjoerring (2003) in the green near the chlorophyll peak at ±550nm and ±525nm, however, are not discernible in the figures above. It is argued that this may be ascribable to the lower spectral resolution provided by the sensor and resultant 'smoothed' dataset incorporated here (FWHM = 30nm) compared to the higher spectral resolution of the spectroradiometer's used by these studies (FWHM = 1.0 <> 1.55nm). On the other hand, such anomalies were also not observed by Zhao et al. (2015) for N content in oats, regardless of utilizing a similarly high spectral resolution spectrometer.

7.4 Correlation between crop trait and Crop Surface Model

Subsequently, in-situ measurements for all traits were individually correlated with the average crop height according to the crop surface model (CSM) (figure 7.4). Not surprisingly, the CSM most closely resembles the field measurements of height, resulting in correlation coefficients of 0.85 and 0.91 for calibration and validation data, respectively. Relative variations in CSM height are also significantly related to discrepancies observed between in situ measured height when broken down by different treatments for all (56) plots (figure 7.5). For both data sets, however, the CSM structurally underestimates the measured height, by 20cm on average. This may result from a certain degree of bias being present in the CSM. The remainder of traits exhibited a lower amount of correlation, judging from the coefficients ranging from 0.45 to 0.8. The values of *r* for validation plots are consistently higher than for calibration plots, although deviations between the datasets is marginal for height and N content (< -7.0%). The largest exceptions are observed for C content (-36%) and fresh biomass (-16.5%), in accordance with the deviations in univariate correlations observed for both traits in the previous paragraphs. In general, the observed interdependency confirm the associated relationships between vegetation height and variables such as growth rate, biomass and plant fertility/health, among others, expressed by Till et al. (2014) and Cornelissen et al. (2003).

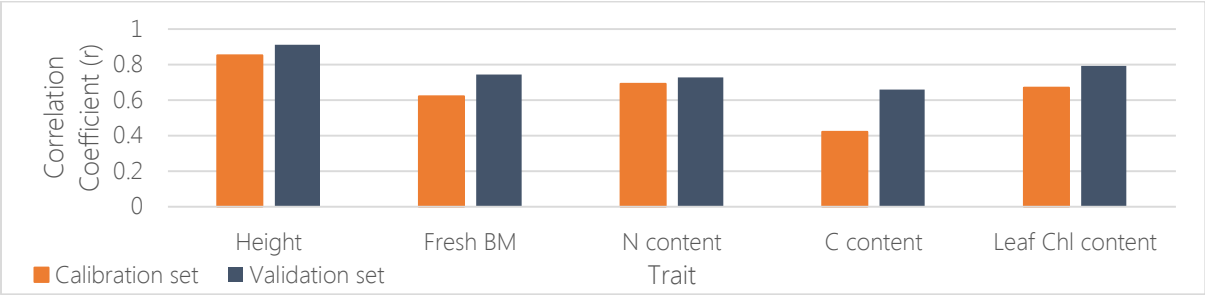

Figure 7.4: Correlation coefficients (r) based on a linear regression between average CSM plot height and each crop trait studied for the calibration (n=28) and validation set (n=28).

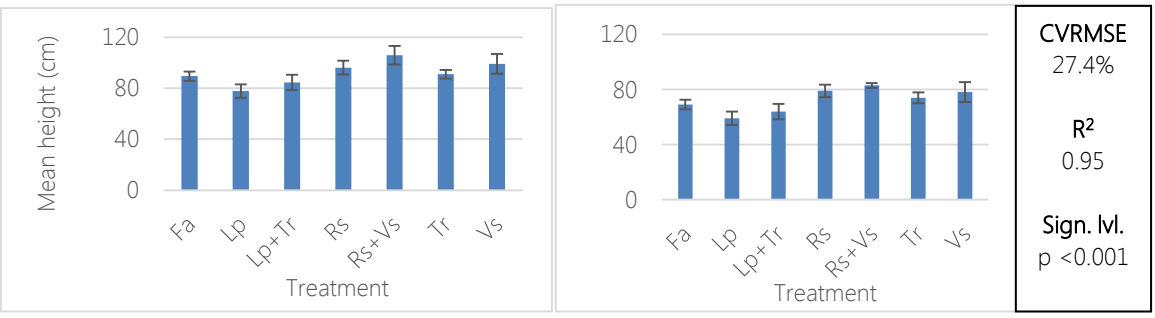

Figure 7.5: Mean and standard deviations of measured (left) and CSM (right) height values per treatment type for all plots (n=56). The statistics relate to statistical interferencing of the means of the two height estimates. (Fa = fallowed, Lp = *Lolium perenne*, Tr = *Trifolium repens*, Vs = *Vicia sativa*)

Figure 7.6 below display the univariate correlation coefficients between average CSM plot height and separate traits by different treatments for the calibration and validation set, respectively. Please note that the *Rapharus sativa* monoculture (Rs) and *Rapharus sativa/Vicia sativa* treatment (Rs+Vs) are excluded from both figures. After removal of some plots (paragraph 7.3 and appendix F), both treatments comprised of too few observations (1 <> 2) in either the calibration or validation set, or both, to allow for correlation analysis. The figures suggest notable deviations for different treatments within, and between, both datasets. Besides, the consistently positive correlations with traits displayed in figure 7.4 are not mirrored by similarly structural positive correlations for separate treatments. The strongest alignment is observed for the *Vs* treatment, indicating positive correlations for all traits other than leaf Chl content in both data sets. In contrast, the fallow treatment is highly varied, indicated by opposite (i.e. negative) correlations for height and leaf Chl content and, albeit to a far lesser degree, fresh biomass and C content. For *Lp*, the positive correlations for fresh biomass, N content and C content are largely overlapping between both datasets, although correlations for height and leaf Chl content are negative for the validation dataset, hereby conflicting with the positive correlations for calibration plots. Likewise, *Lp+Tr* only displays overlap for height and leaf Chl content, whereas correlations for the other traits are consistently either positive or negative for the calibration and validation set, respectively. Finally, *Tr* exhibits comparatively strong correlations with all traits in the validation set. In the calibration set this is only matched by height, leaf Chl content and N content to a lesser extent, whereas contrasting (negative) correlations are recorded for fresh biomass and C content.

It is troublesome to precisely elucidate what lies at the foundation of these discrepancies. It should be mentioned, however, that the treatments rely on a limited number of observations (4 <> 5) in both validation and calibration datasets, separately. Consequently, a single observation exerts relatively much leverage and influence on the direction and strength of resultant correlations. Besides, the CSM height metrics are extracted from a considerably larger section (i.e. the whole) of the plot compared to the trait samples (i.e. 1-4 sampling locations). Resultantly, considering the possibility of these samples not adequately representing the remainder of the plot and/or their expected (biochemical/biophysical) relation to plant height, unanticipated or contradicting correlations in the opposite direction may be invoked. The latter notion on the varied densities on which ground and aerial measurements are based is a recurring topic in this report and is discussed in more detail in paragraph 10.3

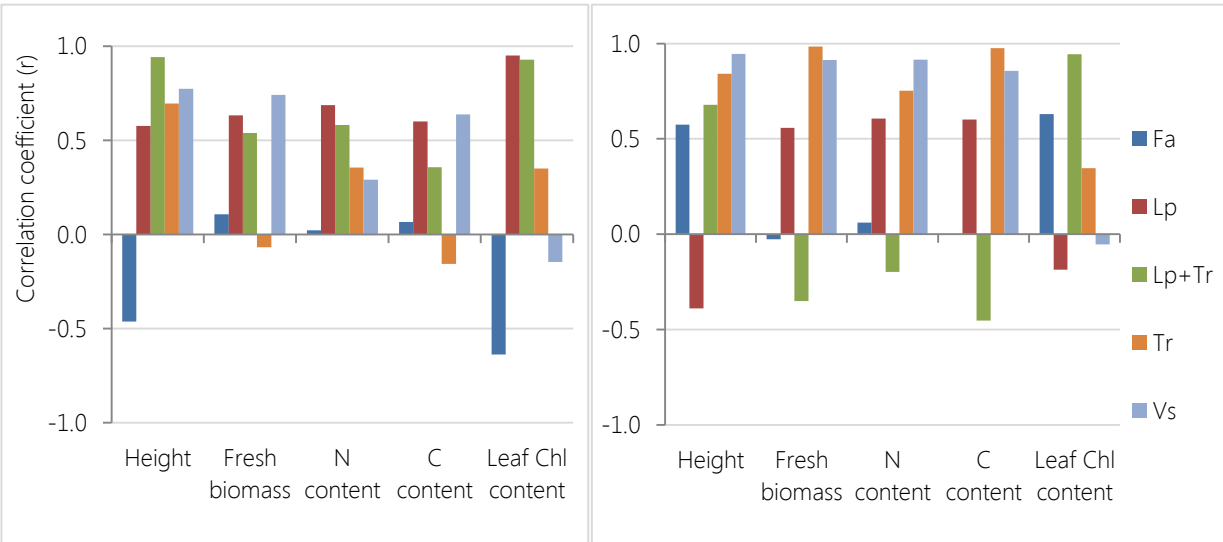

Figure 7.6: Correlation coefficients (r) based on a linear regression between average CSM plot height and each crop trait studied, broken down by treatment, for the calibration (left) and validation (right) set. (Fa = fallowed, Lp = *Lolium perenne*, Tr = *Trifolium repens*, Vs = *Vicia sativa*)

8. Analysis & Results: Calibration of the relationships between vegetation indices and crop traits

The following paragraphs discuss the regression analysis of crop traits and vegetation indices or PLS models, as well as the calibration of mathematical relationship functions based on these outcomes. First, the results of correlating previously found indices with individual traits are given. Subsequently, contour plots relating to all possible two-band combinations in SR, NDVI and SD indices are presented, allowing identification of potentially new spectral indices. Thirdly, the calibration of various PLS models is presented. For the best performing existing/optimized indices and PLS models, supportive figures of the regression are depicted in appendix G and I, respectively.

8.1 Correlation between crop trait and Vegetation Indices

Linear regression of all existing and previously mentioned vegetation indices (chapter 4) revealed highly varying results with respect to (the strength of) their relationship to all crop traits studied (table 8.1). For each trait, the three best performing indices are highlighted in bold. The highest coefficients of determination (R^2) were found for some of the more complex indices, i.e. REP and MTCI in particular. Existing two-band NDVI indices, especially NDVI_d, NDV_e and NDVI_f, consistently outperformed those based on a simple ratio formulation.

Table 8.1 Coefficients of determination (R^2) based on a linear regression between vegetation indices and each crop trait studied for the calibration. The three models producing the highest coefficients for each trait are displayed in bold.

	Height	Fresh biomass	N content	C content	Leaf Chl content
SR_a	0.050	**0.032**	**0.078**	**0.019**	**0.117**
SR_b	0.472	0.178	0.450	0.060	0.488
SR_c	0.147	0.067	0.175	0.028	0.231
SR_d	0.120	0.057	0.149	0.024	0.207
SR_e	0.337	0.132	0.326	0.049	0.412
MSR	0.335	0.130	0.332	0.048	0.398
NDVI_a	0.278	0.078	0.169	0.018	0.142
NDVI_b	0.354	0.105	0.215	0.023	0.220
NDVI_c	0.338	0.134	0.334	0.050	0.410
NDVI_d	0.566	**0.197**	**0.505**	0.063	**0.546**
NDVI_e	0.492	0.184	0.454	0.062	0.525
NDVI_f	0.533	0.191	0.477	**0.064**	0.514
NDVI_g	0.327	0.128	0.321	0.048	0.400
NDVI_h	0.039	0.024	0.063	0.013	0.119
NDVI_i	0.449	0.170	0.420	0.059	0.493
NDVI_j	0.125	0.061	0.153	0.027	0.227
NDVI_k	0.380	0.145	0.364	0.053	0.440
REP	**0.698**	**0.245**	**0.580**	**0.074**	**0.573**
MCARI_a	0.429	0.158	0.414	0.052	0.475
MCARI_b	0.477	0.174	0.454	0.057	0.510
TCARI/OSAVI	0.195	0.073	0.207	0.027	0.263
MCARI/OSAVI	0.195	0.073	0.207	0.027	0.263
MTCI	**0.679**	**0.245**	**0.599**	**0.079**	**0.583**
TGI	0.248	0.090	0.194	0.034	0.222
MCARI/MTVI2	**0.655**	0.183	0.459	0.047	0.463

From assessing the R^2 values on a trait by trait basis it follows that C content consistently exhibits the lowest coefficients of determination, followed by fresh biomass. This is in agreement with anticipations considering both traits were least strongly correlated with individual wavelengths, particularly in the near-infrared (figure 7.3). Likewise, higher univariate correlation coefficients with distinct wavelengths for height, N content and leaf Chl content are reflected by higher R^2 values for these traits with respect to the variety of indices presented here.

The tested indices were extracted from earlier studies, in which they were found to be relatively strongly correlated with one or more of the traits included in this research. The results presented here indicate that in some instances these indices do indeed produce relatively high R^2 values when regressed with distinct traits (e.g. SR_b, NDVI_f, REP for fresh biomass, MTCI, REP, NDVI_d, MCARI/MTVI2, NDVI_e, SR_b for N content, MTCI, REP, for C content, MTCI, REP, SR_b, MCARI, NDVI_i for leaf Chl content) (figure 8.1 & 8.2). Nonetheless, as can be discerned from table 8.1 above, a variety of new index/trait combinations exhibit similar or even higher coefficients of determination (e.g. MTCI, NDVI_d, NDVI_e for fresh biomass, NDVI_f, MCARI for N content, NDVI_d, NDVI_e, NDVI_f for C content and leaf Chl content). Finally, exploration of the tabular overview suggests that a selection of indices yielding relatively high R^2 values when correlated with a distinct trait are also rather strongly correlated to multiple or all other traits (e.g. SR_b, SR_e, NDVI_d, NDVI_e, NDVI_f, NDVI_i, NDVI_k, REP, MCARI, MTCI, MCARI/MTVI2). These notions logically follow from the earlier mentioned observation that univariate trait-wavelength correlation patterns (figure 7.3) are relatively similar in shape and diverge most strongly regarding the strength of such correlations. Consequently, indices performing relatively well in explaining the variation of a single trait potentially yield similarly high R^2 values for other traits due to their reliance on distinct wavelengths multiple other crop traits were also strongly correlated with.

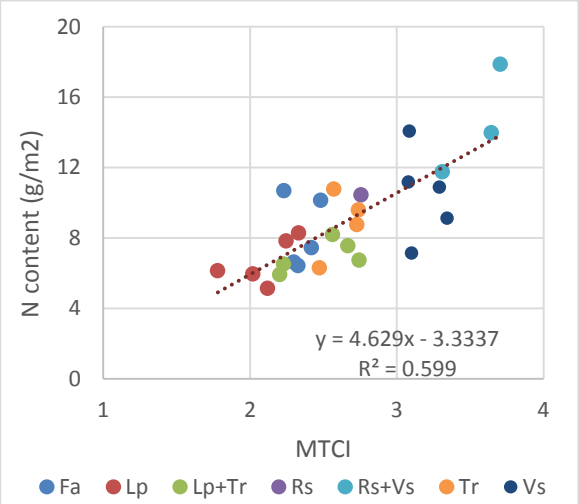

Figure 8.1: Relation between in-situ measured N content and index MTCI. (Fa = fallowed, Lp = *Lolium perenne*, Rs = *Rapharus sativa*, Tr = *Trifolium repens*, Vs = *Vicia sativa*).

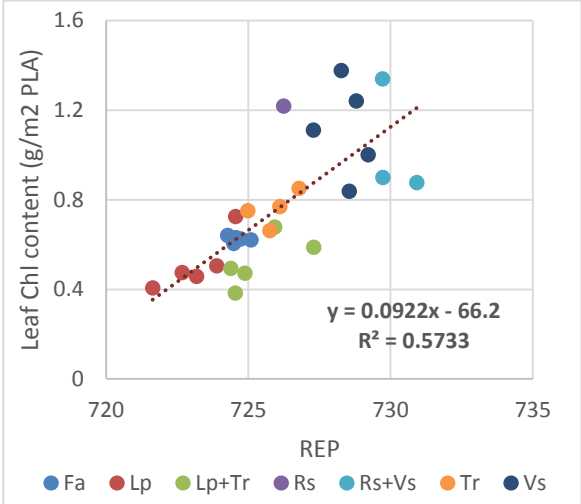

Figure 8.2: Relation between in-situ measured leaf Chl content and index REP. (Fa = fallowed, Lp = *Lolium perenne*, Rs = *Rapharus sativa*, Tr = *Trifolium repens*, Vs = *Vicia sativa*, PLA = Projected Leaf Area)

Furthermore, it is revealed that the best performing SR (λ1/λ2) and NDV indices ((λ2- λ1)/(λ2+ λ1)), i.e. those producing comparatively high coefficients of determination for one or multiple traits, are based on a recurring combination of bands at distinct wavelengths (table 8.2). The indices borrow either from the near-infrared (>750nm) and the far red (±710nm), from the red-edge (710nm <> 750nm) and the far red, or solely from the red-edge. The highlighting of these wavelengths logically follows from the importance of these spectral regions with respect to changing interactions with incoming radiation and the resultant rapid alterations in reflectance of vegetation. Consequently, it is observed that the indices mentioned here are consistently based on a wavelength that is (strongly) positively correlated to one or multiple traits on the one hand, and a second that is either (strongly) negatively or not correlated in figure 7.3 on the other. The REP and MTCI indices employ relatively similar wavelengths in the far red, the red-edge and onset of the near-infrared. Additionally, both indices exploit a distinct region in the visible part of the spectrum where absorption of chlorophyll reaches its peak (i.e. ±675nm), shortly prior to the sharp increase in reflectance and sensitivity from the red-edge onwards (Gitelson, 2012; Dash & Curran, 2007; Mutanga & Skidmore, 2007; Lichtenthaler et al., 1996). In contrast, existing indices performing relatively weak are found to be primarily based on (green (i.e. ±550nm) and blue) wavelengths for which differences in measured reflectance and sensitivities are minimal and which are subsequently largely poorly correlated. This disallows such indices to effectively exploit vast differences in reflectance and sensitivities, due to the relative absence of the latter. Revision of the studies that some of these indices were retrieved from confirmed their foundation on univariate wavelength correlations that are minimally, but highly relevantly, different from the figures (i.e. notably stronger, particularly in the visible spectrum) found for the oat plots. This renders such indices plausibly valuable for these studies, but rather sub-optimal for the case study, crop type, development stage, hardware and/or resultant dataset, among other relevant parameters, adhered to here. The indices compensating for soil background noise (i.e. TCARI/OSAVI & MCARI/OSAVI) were not found to display better results than their non-compensating counterparts. It is argued that this may follow from the advanced vegetative stage of the crops and the resultant dense canopy cover, rendering the possible appearance and influence of soil background largely absent (Thenkabail et al., 2000).

Index	λ1	λ2	Λ3	Λ4
SR_b	780	710		
SR_e	705	755		
MSR	750	705		
NDVI_d	735	750		
NDVI_e	715	770		
NDVI_f	720	820		
NDVI_i	710	780		
NDVI_k	710	750		
MTCI	755	710	680	
REP	780	700	670	740

Table 8.2: Best performing indices and their wavelength dependency

8.2 Contour plots: hotspot identification and optimal index selection

Next, contour plots or correlation matrices were generated for all 8.836 two-band combinations within the 450-915nm range. Figure 8.3 and 8.4 below, in addition to those presented in appendix H, represent the resultant graphs displaying R^2 values for all possible formulations of a simple ratio (SR) form λ1/λ2, normalized difference vegetation index (NDV) form (λ2-λ1)/(λ2+λ1) and simple difference (SD) form λ1-λ2, and their relationship with all traits. This is a relevant process considering that the performance of individual wavelengths and indices with respect to modelling variation in crop parameters varies with different types of vegetation, crop development stage, sampling dates, among other variables (Freeman et al., 2007; Osborne et al., 2002). Consequently, indices derived from existing studies as presented in chapter 4 and appendix C are not guaranteed to provide optimal performance with respect to this specific case study.

The range of R^2 values indicates that, for all traits, alternative band combinations exist that are better able to explain the variation of in-situ trait measurements than the existing two-band indices included in this study. When also considering the best performing more complex indices (i.e. MTCI and REP in particular), improvements were only observed for C content and leaf Chl content and SR/NDVI/SD indices, and only for SD indices for fresh biomass and N content. The importance of the red-edge and near-infrared are confirmed for each index and trait other than C content. The relatively consistent overlap of hotspots for different indices follows from similarly strong interdependencies between field measurements thereof (paragraph 7.2), comparable correlations over wavebands (figure 7.3), and indirect biochemical relationships between height, leaf Chl content, N content and, to a lesser degree, fresh biomass. Subsequently, considering intra and inter trait comparisons, differences in the graphs are mostly related to the maximum coefficients of determination, and the spread of values throughout the graph to a lesser degree. Following from the lower univariate wavelength correlations observed for fresh biomass and C content, all of the indices tested here display reduced maximum coefficients of determination compared to the other traits. The hotspots for new SR, NDVI and, to a lesser extent, SD indices are majorly focused on the same region in the electromagnetic spectrum on which the best performing existing indices were based, i.e. the far red(-edge) (>720nm) and the onset of the near-infrared. This notion is in accordance with the findings of Aasen et al. (2014), Yu et al. (2012), Müller et al. (2008) and Hansen & Schjoerring (2003) who performed a similar optimization algorithm plots for some of the traits included here, for different crop species. In contrast to additional findings in these studies, however, indices fully oriented at the visible spectrum or, alternatively, indices exploiting the red-edge/near-infrared and visible (i.e. the green at ±550nm) wavelengths, are found to be less strongly related to variations to in situ measurements of all traits than was anticipated. The latter type of index in particular is found to yield low coefficients of determination for SR and NDVI indices, and SD indices to a lesser degree.

In agreement with the findings of Yu et al. (2012), instances of SRs where $\lambda1 > \lambda2$ (below diagonal), or where $\lambda1 < \lambda2$ (above diagonal), generate different values for R^2. SRs where $\lambda1 > \lambda2$, however, generally exhibit larger 'hotspots' with slightly higher coefficients of determination. Likewise, such variation for both cases ($\lambda1 > \lambda2$ or $\lambda1 < \lambda2$) in correlation strength is not discernible for NDVIs or SDs where each side of the diagonal mirrors the other. The discrepancy for SRs, however, is much lower than was observed by Yu et al. (2012). The hotspots identified for SRs below fully align with those found for all possible combinations for NDVIs and traits, although values for R^2 vary marginally (± 0.01) (table 8.3). Hotspots and coefficients of determination for SD indices are more, albeit still rather limitedly, varied.

8.2.1 New indices for height

The hotspot for height pivots around band combinations from 725nm onwards until longer near-infrared wavelengths, although the relationship weakens for combinations incorporating longer wavelengths. The highest R^2 values (=0.70) are obtained for an SR/NDVI index where $\lambda1$ is in the near-infrared at 795nm (± Δ20nm) and $\lambda2$ at the end of the red-edge at 755nm (± Δ10nm) (figure 8.3), or a largely similar SD index where $\lambda1$ is at 785nm (+ Δ30nm) and $\lambda2$ at 760nm (- Δ10nm) (R^2 = 0.69). These wavelengths at (the onset of) the near-infrared were also identified to exhibit good correlations with crop height by Wolfgang et al. (2010), Thenkabail (2001) and Senay et al. (2000). As expressed by Wang et al. (2011), a direct physical relationship between height of a canopy on the one hand and the reflective behavior of that canopy on the other is nonexistent. Alternative structural parameters of vegetation such as LAI, fractional canopy and the associated structure and biomass, however, are related to both height and reflectance. Generally speaking, as the growing season progresses and plant height increases, so do LAI, biomass and fractional cover. Consequently, Raper et al. (2013) found strong correlations between measured values of a red/near-infrared

NDVI index and LAI, and relatedly height, of crops throughout the growing season. The red band dependency, which was also found to be a good predictor of plant height/LAI in various crops by Thenkabail et al. (2000), however, is negligible according to any of the generated contour plots. It is argued that this may be related to the developmental stage of the oat crops studied and the resultant fractional vegetation cover nearing the 100% marker. Traditional red/near-infrared indices for estimation of biophysical crop characteristics ultimately exploit the red region with respect to its sensitivity to dynamic and gradually increasing covering of background soils as crops develop, although this sensitivity is rapidly lost once the canopy is increasingly densified and fractional cover reaches its maximum (Carlson & Ripley, 1997). The reliance on the near-infrared relates to the notion that reflectance continues to increase as additional leaves are disclosed that further enhance scattering at these wavelengths. As a canopy becomes more dense and the influence of background soils is lessened, the vastly different rates at which interaction with incoming radiation is altered and reflected at these wavelengths invokes an imbalance, rendering the index largely insensitive (Mutanga & Skidmore, 2004). It is consequently argued that, considering the advanced growth stage of oat crops, indices become more reliant on longer (red-edge) wavelengths, similar to what was found for densified canopies and estimating of biomass thereof (Mutanga & Skidmore, 2004) (paragraph 8.2.2).

Besides, the rate at which the preceding rapid increase of reflectance gradually flattens in this particular spectral region is strongly and positively related to chlorophyll content and yields higher reflectance for healthy vegetation containing higher levels of chlorophyll, in accordance with Lamb et al. (2002). Considering the associated biochemical relationship between the enhancement of vegetation health/fertility, photosynthetic capacity, growth rate, plant height, and chlorophyll content (Cornelissen et al., 2003; Gopal et al., 2002), this may explain the higher correlations for these band combinations as chlorophyll related wavelengths serve as a proxy for plant height. This associated relation was also discernible from the comparatively strong positive univariate correlations between both field and CSM height and measured leaf Chl content. The inclusion of a band at approximately 720nm, stated to be frequently employed within crop growth studies by Gitelson (2012), produces comparatively less performance, indicated by lower coefficients of determination at the edges of the hotspot. Besides, the assumingly effective pairing of near-infrared (±845nm) and red (±682nm) for estimation of biophysical crop attributes such as plant height (Thenkabail et al., 2012a), is not discernible in any of the contour plots for height.

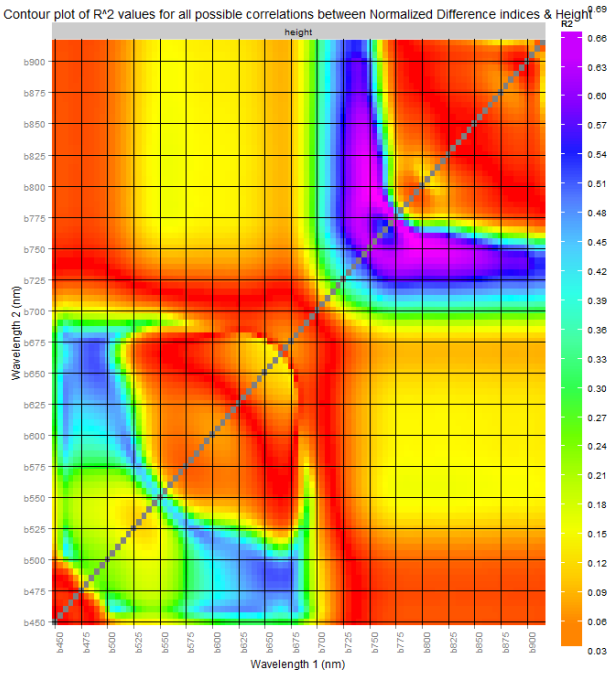

Figure 8.3: Contour plot showing the coefficient of determination (R^2) between in-situ measured crop height and narrow band SR indices for 94 bands spread across λ1 (450nm to 915nm) and λ2 (450nm to 915nm). The different hotspots, indicating regions with relatively high R^2 values, are depicted in pink and subsequently used to retrieve the best combinations of bands from.

8.2.2 New indices for fresh biomass and C content

The hotspot for fresh biomass near perfectly overlaps with the hotspot found for plant height, although exploiting of longer near-infrared wavelengths invokes a lowering of the coefficient of determination more rapidly than is the case for the latter trait. This concise overlap is in agreement with the demonstrated strong relationship between both plant height and biomass in various earlier studies (i.e. Tilly et al., 2014; Fernandez et al., 2009; Niklas & Enquist, 2001). Relatedly, the optimum SR/NDVI indices locate λ1 in the near-infrared at 790nm (± Δ10nm) and λ2 at the onset thereof at 755nm (± Δ5nm) ($R^2 \approx 0.24$). One of the two hotspots found for fresh biomass based on an SD index yields a slightly higher R^2 (≈ 0.26) and borrows from approximately the same spectral region with λ1 at 780nm (+ Δ10nm) and λ2 at 760nm (+ Δ5nm). Each index exploits distinct wavelengths close to those that were previously found to be good estimators of leaf mass (Cho et al., 2007). Likewise, the near-infrared is ultimately related to biomass and canopy structure, i.e. an increase in near-infrared reflectance suggests enhanced production mass or increased densification of the vegetative canopy as scattering in this region is increased (Christenson et al., 2013; Clevers & Kooistra, 2012). It is observed that the optimal band combinations for explaining the variation in measured biomass are relatively adjacent, in agreement with the findings of Cho et al. (2007) and Hansen & Schjoerring (2003). Relatedly, Mutanga & Skidmore (2004) demonstrated that relatively adjacent bands positioned on the steep linear red-edge shift and/or short near-infrared wavelengths are a more accurate estimator of biomass related traits in dense vegetation (e.g. (full-grown) oats) than more traditional SRs or NDVIs based on the red and near-infrared as was mentioned in paragraph 8.1.1. A combination of very adjacent bands in approximately the same spectral region (746-757nm) was also identified to exhibit a relatively strong correlation with biomass in rice across different growth stages using contour plots by Aasen et al. (2014), although none of the growth stages coincides with the mature stage of oats studied here. The comparatively low coefficients of determination may be, in addition to the comparatively lower univariate correlations over wavelengths (figure 7.3), related to the notion that the correlation between biomass and indices generally saturates at higher levels of biomass (> 100mg/m2) for different plant species (Goswami et al., 2015; Hunt et al., 2005). Crops reach full canopy closure during the mid-vegetative phase, after which biomass and plant height continue to accumulate while not (proportionally) effecting the spectral appearance of its canopy (Thenkabail et al., 2000). The vegetation in all plots structurally exceeds this value (significantly), hereby potentially explaining the reduced capability of spectral indices to discriminate and quantify different levels of biomass adequately.

A very small second hotspot for SD indices, producing a further enhancement of the coefficient of determination (≈ 0.27), is observed for fresh biomass at longer near-infrared wavelengths with λ1 positioned at 875nm (± Δ5nm) and λ2 at 915nm (± Δ5nm). The optimum SR/NDVI ($R^2 \approx 0.12$) and SD ($R^2 \approx 0.13$) indices for C content exploit a largely similar spectral region at these longer wavelengths, utilizing 885nm (λ1, ± Δ5nm) and 875nm (λ2, ± Δ5nm), and 875nm (λ1) and 915nm (λ2, ± Δ5nm), respectively. Considering the near-perfect alignment (conceptually and statistically) between fresh biomass and C content (through dry biomass and carbon concentration), the considerable overlap in relevant wavelengths may be explained, although the red-edge/near-infrared hotspot observed for fresh biomass is only very marginally discernible for C content. All three indices are reliant on distinct regions in the near-infrared shoulder that are commonly referred to as the *near-infrared prepeak* (±885nm) and *near-infrared peak* (±915nm), respectively (Gnyp et al., 2014). Both are stated to be frequently employed to estimate biophysyical parameters such as fresh and dry biomass, although the notion that these wavelengths are often paired with a red band at 682nm for these purposes cannot be distilled from the contour plots (Thenkabail et al., 2012a/b; Thenkabail et al., 2004).

More than is the case for any of the other traits studied, a variety of SR/NDVI indices exploiting solely the visible segment of the electromagnetic spectrum is identified for biomass, although the R^2 values (≈ 0.19) remain significantly lower than for red-edge/near-infrared oriented indices. It is argued that this region may be particularly relevant with respect to the mature and final growth stage of the oat crops, in which plant senescing and ripening within (some) plots has commenced (Thorsted et al., 2002). For various crop types, including oats, biomass rapidly accumulates throughout the growing season, while stagnating during later stages when maximum biomass is reached (Malhi et al., 2006). Instead, biomass is being increasingly displaced at later growth stages prior to harvest (Dixon, 2007). During senescence, stocks of biomass (and N) are gradually re-allocated to seeds or grains, in addition to photosynthetic capacity of leaves decreasing due to this relocation, hereby causing leaves and the vegetation's canopy appearance to color yellowish/brownish (figure 10.2). Likewise, as plant decay starts to set in, the opposite of canopy closure (i.e. diminishing) is observed, hereby likely invoking the influence of additional factors such as soils in the background and within-plot shadowing effects (Murphy & Murray, 2003; Thenkabail, 2000). Consequently, the differences in reflectance between yellowish senescing (biomass maxima) and greener (biomass pre-maxima) vegetation are particularly pronounced at these visible wavelengths, in agreement with Huete & Jackson (1987).

8.2.3 New indices for N content

Although the hotspots found for N content are again largely overlapping with those mentioned previously for other traits, a minor shift to shorter wavelengths is observable, starting from approximately 705nm at the shortest red-edge wavelengths. The best results, however, are still obtained from band combinations exploiting longer wavelengths. Likewise, similar to the height, the hotspot found is more elongated than for fresh biomass and carries through to longer near-infrared wavelengths. The highest R^2 values for SR/NDVI indices are found for λ1 at 790nm (± Δ15nm) and λ2 at 745nm (± Δ10nm) (R^2 ≈ 0.58). The optimum wavelengths for SD indices exploit approximately the same red-edge/near-infrared region, but are more closely spaced with λ1 at 780nm (± Δ10nm) and λ2 at 765nm (± Δ5nm) besides producing a slightly higher coefficient of determination (R^2 ≈ 0.61).

Each index type exploits a distinct red-edge and near-infrared wavelength that was also found to be strongly correlated to N in oat cultivars, i.e. 741nm and 760nm, respectively (Zhao et al., 2014). The 745nm wavelength dependency besides approximates the red-edge band at 740nm that was found by Thenkabail et al. (2012a) to be highly sensitive to accumulation of nitrogen in corn leafs. Identification of these wavelengths is also in relative agreement with some of the best two-band indices for predicting N content in wheat according to Hansen & Schjoerring (2003), i.e. relying on wavelengths situated at the red-edge and onset of the near-infrared. These specific wavelengths (>760nm) were also accredited with the largest factor loadings in the first latent variable during the construction of a PLS model aimed at estimating N content in rice cultivars by Nguyen & Lee (2006). The inclusion of a red-edge band in particular relates to the biochemical interdependency between chlorophylls and nitrogen. The red-edge was identified as a (direct) function of absorption by chlorophylls by Zhao et al. (2014) and subsequently exhibits considerable sensitivity to accumulation of nitrogen according to Thenkabail et al. (2012a). The optimum SD index more strictly utilizes the spectral region in which the rapid reflectance increase over red-edge wavelengths gradually stabilizes at the onset of the near-infrared. The rate at which this flattening occurs is highly varied and ends at higher maximum reflectance values for increased levels of chlorophyll (Lamb et al., 2002), arguably induced by similarly higher N content values considering the vast biochemical relationship between the two variables (Inoue et al., 2012).

It was found by Freeman et al. (2007), among others, that an (NDV) index employing the red and near-infrared segment of the spectrum was ultimately able to discriminate between different levels of N content in corn crops, again resulting from the demonstrated influence of N on chlorophyll content, and the resultant sensitivity to differences in variation of chlorophyll content and N stress at red wavelengths. This reasoning was not confirmed by the contour plots for SR/NDVI ($R^2 \approx 0.2 <> 0.3$) indices in particular or for SD indices to a lesser degree ($R^2 \approx 0.45$), indicated by notably lower R^2 values for this wavelength compared to the red-edge/near-infrared. Similarly, the notion that, at later growth stages, N content can be more effectively estimated using blue wavelengths in particular (Alchanatis & Cohen, 2012) was not confirmed for oats. It is, however, reasoned that this relative undervaluation of visible wavelengths may be related to the developmental stage of the oat crops under study, as will be discussed in more detail in paragraph 10.4.

8.2.4 New indices for leaf chlorophyll (Chl) content

In accordance with the previously mentioned strong biochemical interdependency between chlorophylls and nitrogen in vegetation (Zhao et al., 2014; Homolová et al., 2013; Clevers & Kooistra, 2012; Smith et al., 2002 Weiss et al., 2001), the hotspots observed for leaf Chl content are overlapping with those of N content to a large degree. Similarly, in contrast to contour plots for other traits, the hotspot area exhibits a minor shift to shorter (red-edge) wavelengths. In contrast to N content, however, the hotspots for SR/NDVI indices do not venture as far into the near-infrared and are primarily reliant on adjacent shorter wave narrow bands situated in the red-edge/near-infrared, or solely in the red-edge to a lesser degree. The best performance is provided by SR/NDVI/SD indices where λ1 is located at 760nm (± Δ10nm) and λ2 at 740nm (± Δ10nm). The best SD index yields a marginally better R^2 (≈ 0.61) than its SR or NDVI counterparts (≈ 0.59). Even more than was the case for N content, a relatively large area is observable in the contour plot for SD indices that relates to band combinations utilizing shorter near-infrared wavelengths (760nm <>800nm) on the one hand, and visible (particularly green and red) on the other, that are found to exhibit sub-optimal coefficients of determination (≈ <0.54).

The optimum index exploits a distinct wavelength at the onset of the near-infrared (760nm) where chlorophylls in leafs hardly exhibit absorption features while simultaneously exerting a relatively strong correlation between variations in chlorophyll and reflectance compared to other near-infrared wavelengths (Blackburn, 1998). In contrast, the 740nm band is positioned at the steep linear-shift of the red-edge and exploits the spectral region in between vast absorption of chlorophylls in the red and scattering in the near-infrared. Reliance of indices on this distinct spectral region avoids saturation effects while preserving sensitivity to varied levels of chlorophyll contents (Gitelson, 2012). A comparable index borrowing entirely from adjacent red-edge bands was also identified as the best estimator of chlorophyll content in wheat cultivars by Hansen & Schjoerring (2003), although combinations of shorter red-edge wavelengths yielded marginally stronger

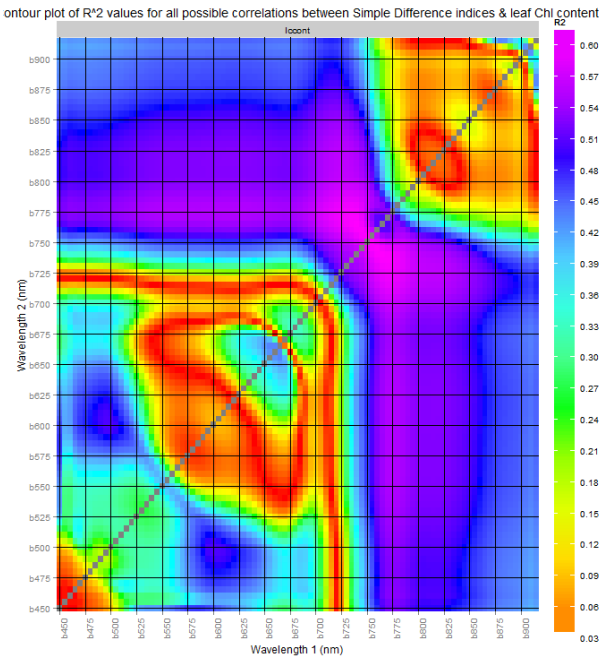

Figure 8.4: Contour plot showing the coefficient of determination (R^2) between in-situ measured leaf Chl content and narrow band SD indices for 94 bands spread across λ1 (450nm to 915nm) and λ2 (450nm to 915nm).

relationships than those based on longer wavelengths. The latter notion, however, may be related to the advanced developmental stage of the oat crops studied. Various studies have demonstrated that the lapse of the red-edge and the associated inflection point thereof shift to longer wavelengths as LAI (i.e. indirectly related to growth stage and plant height), chlorophyll content, availability of nitrogen, among other factors, are increased (Clevers & Kooistra, 2012; Yang & Li, 2012; Mutanga & Skidmore, 2007; Mutanga & Skidmore, 2004). Consequently, it is argued that optimum band combinations may similarly move to slightly longer wavelengths.

Although SD indices exploiting shorter near-infrared wavelengths (750nm <> 800nm) and visible bands yield lower R^2 values than their red-edge/near-infrared counterparts it is argued that the observed pattern may not go unnoticed. Various earlier studies have suggested the use of the visible spectrum for estimating chlorophyll in vegetation, due to the inherent interchange of different levels of chlorophyll pigment induced absorption features throughout this region. The blue and red region represent the chlorophyll absorption maxima at which there exists a relative sensitivity to change in chlorophylls (Alchantis & Cohen, 2012; Thenkabail et al., 2012a; Thenkabail et al., 2012b). Contrastingly, the green region at approximately 555nm is known as the chlorophyll or green peak. Here, reflectance of vegetation in the visible notably increases in comparison to blue and red wavelengths, but especially for lower chlorophyll levels (Gitelson, 2012; Thenkabail et al., 2004; Gitelson et al., 2003b; Yoder & Pettigrew-Crosby, 1995). In addition to the red-edge region, reliance on this spectral region is therefore stated to mitigate saturation issues while maintaining relative sensitivity to chlorophyll levels. Consequently, Gitelson (2012) noted that the green and red-edge spectral regions are the only ones sensitive to highly varied levels of chlorophyll levels. Reliance on the former region, however, does only marginally show from the different contour plots. The differences between coefficients of determination of indices employing either a green or red band are negligible, as are the differences between green and blue band oriented indices, albeit to a lesser degree. Besides, the anticipated and frequently demonstrated relevance of the chlorophyll peak at 555nm for estimating chlorophyll does not stand out compared to adjacent green or other visible wavelengths. As will be discussed in more detail in paragraph 10.4, however, this may again be related to the developmental stage of the oats crops studied and the associated implications thereof to (reduced) photosynthetic capacity of plants and the dynamic interplay between different (influential) other pigments.

Table 8.3: Tabular overview of optimized indices for different traits and their wavelength dependency

Index	λ1 (nm)	λ2 (nm)	Height	FBM	N content	C content	Leaf Chl content
SR's							
SR_i	795	755	X				
SR_ii	790	755		X			
SR_iii	790	745			X		
SR_iv	885	875				X	
SR_v	760	740					X
NDVI's							
NDVI_i	795	755	X				
NDVI_ii	790	755		X			
NDVI_iii	790	745			X		
NDVI_iv	885	875				X	
NDVI_v	760	740					x
SD's							
SD_i	785	760	X				
SD_ii	875	915		X			
SD_iii	780	760		X			
SD_iv	780	765			X		
SD_v	875	915				X	
SD_vi	760	740					X

8.3 PLS

Two PLS models were built for each of the five traits studied, solely utilizing data from the calibration set. Models of the first type are entirely based on the average reflectance measurements for each plot (explanatory (x) variables) and the in-situ measurements of traits (dependent (y) variables). For the second PLS model the plot height values as were estimated by the crop surface model (CSM) were added as an additional explanatory variable in the model building process.

The optimal number of latent variables to be included in each model was determined by assessment of multiple statistical parameters of the (leave-one-out) cross validation process, being the highest values for cross-validated R^2, and lowest values for RMSEP, REP and PRESS statistics. A more extensive tabular overview resulting from PLS calibration for models with different numbers of latent variables is given in appendix I. The preferred number of variables ranged from 11 to 1 for PLS models of the first type to predict N content, and fresh biomass and C content, respectively (table 8.3). The optimal PLS model for leaf Chl content employs 5 latent variables; the model for height includes 3. Once CSM height was included as an auxiliary variable, the number of latent variables in order to predict height increased to 5, while thereafter the PLS model for N content relied on only 2 variables (table 8.4). The number of included latent variables for fresh biomass, C content and leaf Chl content remained unchanged. The precision of the models varies significantly, judging from the cross-validated R^2 estimate ranging from -0.09 to 0.65 and from 0.06 to 0.81 for both PLS model types, respectively. As was anticipated, the precision is comparatively good for height, leaf Chl content and N content, and less so for C content and fresh biomass. The model's accuracies are equally diverging, indicated by the relative error of prediction (REP) ranging from ±6% for height to approximately 20-24% for the other traits in both PLS models. Inclusion of the (CSM) estimated within plot height enhanced PLS model performance for height, fresh biomass and C content. For N content and leaf Chl content, however, no (significant) improvements were observed.

Subsequently, the PLS fitted values were regressed with the actual response variable values to retrieve the coefficient of determination for the resultant fit. These were consequently compared to the R^2 values of the best existing or new index presented in paragraphs 8.1 and 8.2. The reflectance oriented PLS model increased the R^2 for height, leaf Chl content and N content by 0.05, 0.18 and 0.32, respectively. Not surprisingly, when the CSM was added as an additional explanatory variable, the performance of the PLS model increased in particular for height fresh biomass and C content, further increasing the R^2 by 0.13, 0.18 and 0.12, respectively. In contrast to the performance of PLS models of the first type, the second PLS model outperforms the best selected existing and/or new indices for both fresh biomass and C content.

Table 8.4: Statistical parameters of the PLS calibration (only reflectance values included as explanatory variables)

Crop trait	NLV	Cross-validation statistics				R^2 (FV)
		R^2 (CV)	RMSEP	REP(%)	PRESS	
Height	3	0.65	5.909	6.47%	982.5438	0.75
Fresh biomass	1	0.06	0.8352	23.57%	19.58553	0.20
N content	11	0.49	2.054	22.88%	120.7543	0.93
C content	1	-0.09	116.9	21.82%	383674.2	0.06
Leaf Chl content	5	0.63	0.1681	22.43%	0.79723	0.79

(NLV = Number of Latent Variables (components), R^2 = coefficient of determination, CV = Cross-Validation, RMSEP = Root Mean Square Error of Prediction, REP = Relative Error of Prediction, PRESS = Predicted Residual Sum of Squares, FV = Fitted Values)

Table 8.5: Statistical parameters of the PLS calibration (reflectance and CSM values included as explanatory variables)

Crop trait	NLV	Cross-validation statistics				R^2 (FV)
		R^2 (CV)	RMSEP	REP(%)	PRESS	
Height	5	0.81	4.377	4.80%	540.3332	0.88
Fresh biomass	1	0.29	0.7268	20.51%	14.82958	0.39
N content	2	0.47	2.127	23.69%	127.1302	0.58
C content	1	0.06	108.5	20.25%	330691.2	0.18
Leaf Chl content	5	0.62	0.1709	22.81%	0.829131	0.76

The factor loadings indicate how the (1…*n*) latent variables in different PLS trait models have been established. Consequently, the loading weight graphs provide a comprehensive means for distilling the explanatory variables (i.e. wavebands) that are most important for each individual component (Appendix I). Higher loading values attribute comparatively high influence in contrast to lower values. It is observed for all traits that the first latent variable, in PLS models borrowing entirely from reflectance values, ascribes significant loadings weights to near-infrared wavebands, and to red-edge positioned bands to a lesser degree (similar to univariate correlations in figure 7.3). The second component generates the highest loading weights in the onset of the red-edge at ±710nm for leaf Chl content, and near the green peak at ±560nm for N content and height. For height it was found that the wavebands accredited with the largest PLS loading weights in the second latent variable are near-perfectly aligning with the wavebands included in the best performing four band OMNBR model to estimate plant height in corn crops by Thenkabail (2000).

Once CSM height is included in the model building process it is assigned the maximum loading weight in the first latent variable for all traits. Hereafter, the second latent variable for height, N content and leaf Chl content is again majorly borrowing from red-edge and near-infrared wavelengths. Likewise, loading weights of the third latent variable for leaf Chl content and height approximate the second latent variable of the first PLS model type, with loading value peaks at identical wavelengths. For C content and fresh biomass PLS models of the second type comprise only of one latent variable. Therefore the resultant model is merely a linear function of CSM height rather than of reflectance, following from larger univariate correlations observed between the CSM and both traits than over separate wavelengths.

9. Analysis & Results: Validation of the relationships between vegetation indices and crop traits

Finally, the relationships between different indices and crop traits found in the preceding calibration phase are validated. In order to reduce processing time, only the three best performing existing indices, one or optimized index (i.e. 'hotspots') identified by the contour plots for each index formulation, and PLS models of both types were included in the validation for each trait. Resultantly, the total number of uniquely included indices is 31, although plural use of various indices for different traits brings the total number of validations to 41. Except for one outcome, all of the relationships to be discussed below are highly significant at the 0.01 or higher probability level(s), in agreement with the level of significance deemed required for supporting adjusting of farming practices according to Maindonald & Braun (2010).

9.1 Validation of the best selected indices and PLS models

Generally speaking, the best selected existing indices exhibit a performance that is relatively comparable to the best selected new indices or PLS models, indicated by limitedly deviating RMSE's, CV's, and coefficients of determination (R^2) (table 9.1 & appendix J). For height and leaf Chl content the best existing index (MTCI and REP, respectively) outperforms both PLS models and all of the new indices, whereas the latter two type of models provide enhanced performance with respect to predicting of the remaining traits. The dispersion of predictions varies significantly, i.e. the coefficient of variation ranges from the lowest values observed for height (± 5.0% <> 7.0%) to as high as ±23.0% for N content, fresh biomass and C content. The prediction capability of existing indices with respect to leaf Chl content is slightly better, considering the associated CV's ranging between 15.0% and 21.0%. The ability of the calibrated relationships to explain the variance of observed values for the response variables is equally varied. The highest R^2 values were noted for height and leaf Chl content (± 0.79), followed by N content (± 0.63) and fresh biomass (± 0.49). The explained variance for C content ($R^2 \approx 0.35$) was the lowest.

Considering the best performing existing indices, utilization of new optimized indices covering all possible combinations in various two-band indices resulted in lowering of the RMSE/CV and increments in R^2 values for all traits other than height and leaf Chl content. Furthermore, improvements are only observed for the optimized SD indices, i.e. performance of new SR/NDVI indices largely overlaps with the predicting capabilities of selected existing indices other than the best one. The RMSE of predictions for C content is lowered the most by at least 9.3%, the strongest enhancement was observed for $SD_{[875\text{-}915nm]}$ (R^2 + 0.05). No improvements are recorded for the optimized SR/NDVI[885-875nm] indices. With respect to fresh biomass, the selected $SD_{[875\text{-}915nm]}$ index invokes a lowering of the RMSE of 6.7% (R^2 + 0.07) or more compared to validated existing indices. The enhancement provided by $SD_{[780\text{-}760nm]}$ is marginal (RMSE – 1.6%, R^2 +0.07), and absent for $SR/NDVI_{[790\text{-}755]}$ indices. Regarding N content, the newly devised $SD_{[780\text{-}765nm]}$ index brings about a lowering of the RMSE by at least 4.9% (R^2 + 0.05) compared to the best existing index. Again, no notable improvements are observed for the $SR/NDVI_{[790\text{-}745nm]}$ indices. The latter notion may be related to the findings of Freeman et al. (2007), who demonstrated better performance of NDVI with respect to N content at early growth stages, but reduced correlations at later stages. As was mentioned, none of the new indices displays a mentionable increase in predictive accuracy for height or leaf Chl content, indicated by similar or worse values for RMSE, (CV)RMSE and R^2 statistics to different degrees (figure 9.1).

At last, the results of the best performing previously mentioned indices are compared to the results of validation of the calibrated PLS models. The outcomes suggest that PLS regression only improves the predictive accuracy for fresh biomass, albeit marginally (RMSE -2.7%, R^2 ± 0.0) and only regarding the second PLS model type. The PLS model of the second type for fresh biomass, however, comprises of a

single latent variable allocating maximum weight to the CSM data, and therefore equals a linear regression of CSM height measurements rather than an actual multi-dimensional PLS model. It was found that for leaf Chl content, and to a lesser degree N content, partial least square regression yielded no significant improvement compared to (some of) the existing and/or new indices discussed in the previous paragraphs. This is in agreement with the findings of Hansen & Schjoerring, 2003). Predictions of height and C content based on PLS modelling are also outperformed by (some of) those relying on existing and/or optimized indices. For all these traits, PLS modelling is only found to exhibit minor improvements when comparing the results with either existing or newly optimized indices other than the best one(s).

Except for height, the coefficients of determination (R^2) for PLS models of the second type are consistently similar or higher than observed for the second type of PLS model including CSM data. Consequently, the PLS' models predictive accuracies speak in favor of the second model type, indicated by lower (CV)RMSEs for all traits other than height. These latter notions are in conflict with earlier findings during PLS model calibration, as well as those presented in figure 7.4, both of which demonstrated a relatively strong correlation between in situ measured height and CSM modelled height.

Table 9.1: Overview of validation statistics for the best selected existing/optimized indices and both PLS models. All results are significant at the 0.0001 probability level, unless the asterisks indicate otherwise (*** < 0.001, ** < 0.01, * < 0.1). For each trait, the model with the highest predictive accuracy is displayed in green contours.

Traits / Index	Height			Fresh biomass			N content			C content			Leaf Chl content		
Existing indices	*RMSE*	*CV*	*R2*	*RMSE*	*CV*	*R2*	*RMSE*	*CV*	*R2*	*RMSE*	*CV*	*R2*	*RMSE*	*CV*	*R2*
NDVI_d				0.82	23.55%	0.437***	2.26	25.11%	0.53				0.15	21.18%	0.61
NDVI_f										120.9	23.27%	0.301**			
REP	4.70	5.24%	0.78	0.794	22.89%	0.494	2.04	22.61%	0.63	119.7	23.04%	0.354***	0.11	14.50%	0.794
MTCI	4.59	5.12%	0.79	0.797	22.96%	0.472	2.12	23.58%	0.585	119.2	22.95%	0.339**	0.13	17.73%	0.71
MCARI/MTVI2	6.984	7.79%	0.565												
New indices	*RMSE*	*CV*	*R2*	*RMSE*	*CV*	*R2*	*RMSE*	*CV*	*R2*	*RMSE*	*CV*	*R2*	*RMSE*	*CV*	*R2*
SR_i	5.19	5.79%	0.74												
SR_ii				0.83	23.91%	0.455									
SR_iii							2.06	22.83%	0.628						
SR_iv										121.3	23.34%	0.301**			
SR_v													0.12	17.16%	0.728
NDVI_i	5.16	5.75%	0.75												
NDVI_ii				0.828	23.80%	0.458									
NDVI_iii							2.05	22.78%	0.629						
NDVI_iv										121.3	23.35%	0.248			
NDVI_v													0.13	17.36%	0.725
SD_i	4.81	5.37%	0.77												
SD_ii				0.741	21.37%	0.56									
SD_iii				0.78	22.52%	0.56									
SD_iv							1.94	21.60%	0.68						
SD_v										108.1	20.81%	0.521			
SD_vi													0.16	21.72%	0.61
PLS models	*RMSE*	*CV*	*R2*	*RMSE*	*CV*	*R2*	*RMSE*	*CV*	*R2*	*RMSE*	*CV*	*R2*	*RMSE*	*CV*	*R2*
PLS 1	4.84	5.39%	0.78	0.77	22.31%	0.50	3.81	42.34%	0.242*	116.1	22.34%	0.413***	0.17	23.82%	0.57
PLS 2	5.30	5.91%	0.74	0.72	20.78%	0.56	2.05	22.82%	0.62	109.2	21.03%	0.434***	0.16	21.63%	0.64

9.2 Into the models' prediction accuracy & sources of error

Considering that RMSE penalizes large prediction errors more than small prediction errors, it is worth identifying which observations (e.g. plots) exert relatively much influence on the outcome. It was observed that, in general, observations exhibiting relatively large prediction errors (positive or negative) do so consistently (appendix K) for the majority or all other indices validated, regardless of them relying on (significantly) different wavelengths. Similarly, medium or low prediction residuals observed for individual observations using distinct indices exhibit relatively comparable degrees of errors for other indices. The relative influence of even the largest residuals is particularly low for height, which is subsequently reflected in comparatively low overall (CV)RMSE values. Except for leaf Chl content, a largely overlapping vector of unique plots is recurrently observed to contribute relatively much to the (CV)RMSE, although the relative degree of influence varies for different traits. This observation logically follows from the strong univariate correlations between the measured values for these traits ($r \approx 0.8 <> 1.0$, paragraph 7.2) and the biophysical interdependency between height, and biomass (≈ C content) (Tilly et al., 2014; Fernandez et al., 2009; Machado et al., 2002; Niklas & Enquist, 2001). More specifically, plots 40a, 40b, 104 and 116a were structurally allocated comparatively high positive residuals (i.e. over estimation of the response variable). In contrast, plots 41, 78, 91b and 117 were identified to exert the opposite effect relatively strongly (i.e. negative residuals/underestimation). The importance of these plots is reflected in significant lowering of the (CV)RMSE of predictions for the best performing indices when all eight plots are omitted; to 3.03% (-2.09%) for height, 14.43% (-6.35%) for fresh biomass, 15.49% (-6.11%) and to 13.68% (-7.13%) for C content. When extending the number of plots with either comparatively high or low residuals an even larger number of plots are consistently found to exert relatively similar influential behavior for prediction of these traits.

9.2.1 Within plot heterogeneity and sampling density

Acknowledging the recurrent identification of these plots as influential, for a variable number of indices and wavebands as well as different traits, it is suggested that the deviations may not be solely ascribed to (inconsistencies in) the spectral data. Consequently, a variety of different deliberations believed to be potentially causing such prediction errors are considered here. Listing the plots with the largest prediction errors and their type of treatment in between the previous and current growing season provided no indisputable results, indicated by each treatment type being represented approximately equally frequently. Instead, it is reasoned that the first and foremost explanation of inadequate predictions is related to within plot variability with respect to the distribution of biophysical and biochemical parameters on the one hand, and the density and location of in-situ samples on the other. For fresh biomass, C content and, N content to a lesser degree, a relatively consistent pattern was observed when predicted values of these traits were overlaid with the field measurements for crop height (figure 9.1). The latter measurements were taken on four locations, one in each plot's sub quadrant (NW, SW, NE, SE). In contrast, the sampling for fresh biomass, C content and N content relied on a single location in one of the two northern sub quadrants in monoculture plots (NW or NE), or both northern quadrants in polyculture plots (NW for side a, NE for side b) (figure 5.2). It was found that for the negative residuals regarding prediction of any of the three traits, the sampling location was frequently located in the plot's quadrant in which the (second) highest height was recorded. In contrast, for instances in which the largest positive residuals were noted the opposite is observed, i.e. samples were located in quadrants in which comparatively low height measurements were taken. Relatedly, the highest measured values for biomass were found in plots for which the samples were retrieved from comparatively elevated vegetation, and vice versa. Considering that plant height is positively correlated to traits such as biomass it is reasonably assumed that observed within plot variability of measured height partially equals similar within plot heterogeneity of biomass, of which the latter is not

reflected adequately in the calibration/validation data due to limited sampling of biomass (Tilly et al., 2014; Fernandez et al., 2009; Machado et al., 2002 Niklas & Enquist, 2001). Resultantly, it is argued here that residuals may be partially ascribed to measurements of biomass not adequately representing the remainder of the plot; i.e. plots in which low proportions of biomass were recorded are (severely) overestimated if comparatively higher height values, assumed to reflect increased biomass and cause different spectral behavior, were retrieved from the remainder of the plot and vice versa.

This notion has been visualized below in figure 9.1. One should take note that the discussion presented above is not applicable to all of the 28 validation plots, i.e. for eight plots the opposite is observed. For an additional three plots no difference in height was recorded, but residuals were noted for these plots nonetheless. Furthermore, the severity of residuals is only (dis)proportionally related to the degree of observed height differences, i.e. relatively large differences in in situ measured height does not necessarily equal large prediction residuals, or and vice versa. Consequently, the potential cause discussed here may only explain some of the prediction (in)accuracies, but not all.

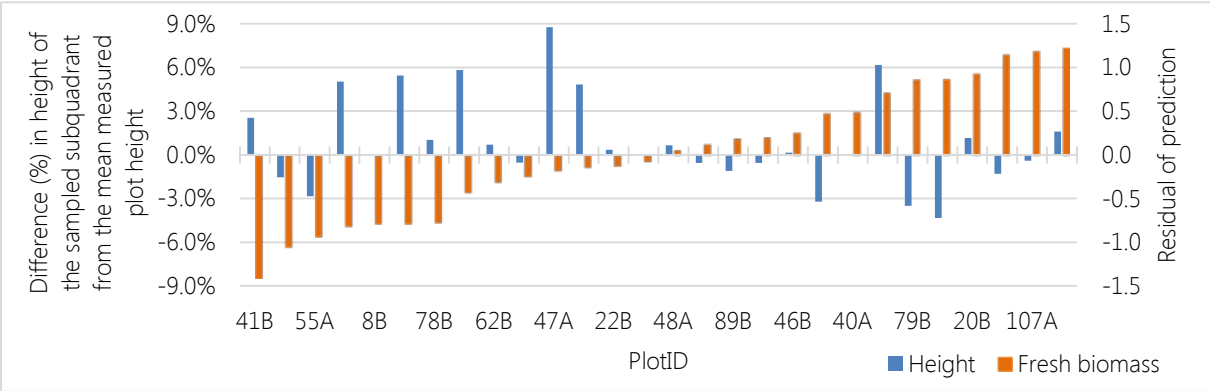

Figure 9.1: Within plot height measured variability versus residuals of fresh biomass prediction

Remarkably, a different selection of plots with comparatively large prediction residuals is identified for leaf Chl content, although some overlap with the previously mentioned traits is discernible. It is, however, reasoned that the higher sampling density of SPAD measurements has plausibly resulted in calibration of more representative and adequate models, while reducing the possibility of potential within plot variability to intrude and (significantly) affect the predictions. Relatedly, for leaf Chl content, the largest residuals (positive or negative) were located in monoculture plots. Polyculture plots exhibited comparatively limited prediction errors. This notion is important considering the relatively higher density of SPAD measurements in polyculture plots (four measurements per 4.5m^2) compared to monoculture plots (four measurements per 4.5m^2). Consequently, these findings may be used to justify increasing of the sampling density for traits, to allow calibration and validation of more adequate models. For leaf Chl content, two plots in particular display relatively large residuals for the majority of indices and PLS models, namely 15 (underestimation) and 55 (overestimation) (appendix K). No explanation, however, was found for these observations.

9.2.2 Model adequacy and extreme values

Although some exceptions are discernible, a weak pattern in which the largest negative residuals (underestimation) are observed for plots with relatively high (observed) leaf Chl content values and vice versa, is discernible for the best performing index ($R^2 \approx 0.15$). Although the plots for which this was identified differs, a similar and stronger pattern was also observed for height ($R^2 \approx 0.23$), fresh biomass ($R^2 \approx 0.72$), N content ($R^2 \approx 0.59$) and C content ($R^2 \approx 0.92$); i.e. overestimation of predicted values is generally more persistent and stronger for plots for plots in which a relatively lower measurement of the dependent variable

(trait) was recorded, and vice versa (appendix K). Given the relatively limited size of both the calibration and validation dataset, and the related limited range of potential y values, it is not unlikely that prediction errors become larger towards both ends of the range of in-situ measured trait values, due to a lower density of observations within a similar range of values during calibration. In addition, the range of y values covered by either the calibration and validation separately does not entirely overlap, with minimum and/or maximum values being (notably) lower or higher for some of the traits in the validation set (figure 7.1). Consequently, it is observed that the pattern of inadequate estimation of 'extreme' values is stronger for traits of which the range of values in the validation set is relatively larger than in calibration data. It is, however, complicated to assess the actual validity and influence of this deliberation, again due to the notions of sampling density and potential within plot variability. With respect to traits based on a single sample location (fresh biomass, N content, C content) in particular, extreme values recorded at one location may not necessarily equal the presence of similarly extreme values elsewhere throughout the plot.

9.2.3 Radiometric inconsistencies

Next, upon closer inspection of the raw HDC a region of abruptly changing reflectance values was identified in the south east of the study area (appendix A). Even though this region is majorly represented by endive plots not included in this study, severe levels of spectral anomalies are also observed to coincide with plots 104, 116 and, to a lesser extent, plots 117 and 79. A similar but spatially less extensive area of distortion was identified in the far south western corner, intersecting with plot 12. A number of series of black pixels (NoData), albeit limited in size, are also discernible in a demarcated section of the HDC acquired during the second flight line. A single of these clumps of errored pixels is found to overlap with the ROI of an oat plot, namely plot 69a. It is remarkable that the radiometric diversions are most frequent and severe in a relatively localized area towards the end of the second flight line. It cannot be indisputably precluded what is causing these radiometric inconsistencies, although abrupt and temporal in-flight distortions are considered a plausible explanation acknowledging the relative overall susceptibility of low-weight UAV platforms and the hyperspectral sensor's push broom technology being prone to the striping effect (Hardin & Jensen, 2015; Gómez-Chova et al., 2008). It was identified that each of these (partially) radiometrically distorted plots exerts comparatively large residuals with respect to the prediction of all traits, except for leaf Chl content, to different extents. Considering the consistency of this pattern it is argued that, in addition to the deliberations mentioned above, radiometric inconsistencies may be reasonably believed to negatively influence the predictions to some degree as well. Alternatively, such anomalies may be related to the opening angle of the sensor rendering different reflectance values (i.e. vignetting) and associated estimates for plots captured under nadir or oblique viewing angles (Retzlaff et al., 2014; Lelong et al., 2008).

9.3 Evaluating within-plot variability of predictions

The above mentioned notion of possible within-plot variability in the distribution of biophysical or biochemical crop traits was further explored using prediction maps. Based on the lowest RMSE, the best performing (existing or optimized) index, and the associated mathematical relationship, were utilized to generate a prediction map for each trait separately (figure 10.2 and appendix L). Subsequently, the variability or within-plot heterogeneity of predictions was assessed through evaluation of the coefficient of variation (CV) of predicted values within the ROIs only. It is observed that the largest intra-plot variability of predictions is ascribed to leaf fresh biomass (CV_{mean} = 0.35). In contrast, predictions of height are prone to the least amount of variation (CV_{mean} = 0.03), followed by leaf Chl content (CV_{mean} = 0.16), N content (CV_{mean} = 0.18) and C content (CV_{mean} = 0.20).

Some individual plots presented with large residuals for the prediction of observed response variables (appendix K) do indeed overlap with plots exhibiting relatively substantial variability in within plot predictions. Nonetheless, no indisputable correlations between the two variables could be established for any of the traits, indicated by poor or even contradicting relationships between the two variables for some other plots. Considering the possible presence of actual within plot heterogeneity of trait parameters, however, such vast variability does not necessarily translate into prediction errors of similar strength if the sample(s) are located at 'average' locations with respect to (significant) anomalies elsewhere within the plot. With respect to the variation in plot specific in-situ SPAD measurements, a positive relationship was observed with the within-plot variability of leaf Chl content predictions ($r \approx 0.35$), i.e. larger variations in plot specific SPAD measurements were conducted in plots with relatively larger variations in predictions in the prediction maps, and vice versa. Although the correlation is relatively weak, it may at least partially lay the foundations for the assumption that within plot variability in predictions may be caused by the actual distribution of biophysical and/or biochemical plant properties not being homogenous within plots after all.

Even though an incontestable association between within plot variation of predictions and plot specific prediction residuals, potentially confirming the implications of within plot heterogeneity for (inadequate) model predictions, could not be established, other valuable comments may be distilled from the prediction maps. Upon visual inspection of the prediction maps it is identified that variabilities follow non-uniform patterns, displaying notable heterogeneity between western and eastern sides of plots and/or deviations along the norther/western direction. For leaf Chl content, height and N content, variability between western and eastern plot sides is particularly strong for polyculture plots and, as is to be anticipated, less for monoculture cultivars. The observed variability follows a relatively gradual pattern over individual plots, showing only limitedly changing values between adjacent pixels. Except for C and leaf Chl content, all inter-trait correlations of variability in predictions are positive, i.e. larger deviations in predictions for one trait are reflected in relatively large predictive variability for other traits, although their strength is vastly deviating. The strongest correlations are, not surprisingly, observed between fresh biomass and C content ($r \approx 0.8$), followed by N content and fresh biomass/C content ($r \approx 0.6$), and height/fresh biomass ($r \approx 0.4$) and height/C content ($r \approx 0.25$). Again, the pattern for leaf Chl content is slightly different, indicated by relatively low correlations with C content, fresh biomass, height and N content ($r \approx -0.03 <> 0.14$). These figures largely follow the variations in strength of univariate correlations between field measurements of trait mentioned in paragraph 7.2 and appendix E. Subsequently, considering variation in single plots only, the highest variations are again found for fresh biomass ($CV_{max} = 0.49$), followed by leaf Chl content ($CV_{max} = 0.43$), N content ($CV_{max} = 0.37$), C content ($CV_{max} = 0.28$) and height ($CV_{max} = 0.07$).

Particularly interesting is the relationship between the average within-plot variability of predictions in prediction maps, the total (CV)RMSE of resultant predictions and the relative differences in sampling density for different traits. Leaf Chl content is observed to exhibit a comparable degree of variability ($CV_{mean} = 0.16$) in the prediction maps compared to both N ($CV_{mean} = 0.18$) and C content ($CV_{mean} = 0.20$). The maximum observed variability is even higher for leaf Chl content ($CV_{max} = 0.43$) than for N ($CV_{max} = 0.37$) and C content ($CV_{max} = 0.28$). The best performing index for each trait, however, displayed a notably higher predictive accuracy for leaf Chl content ($(CV)RMSE_{min} = 14.5\%$) compared to C/N content ($(CV)RMSE_{min} = 20.0\% <> 21.0\%$), despite of the similar degrees of variability in predictions. Besides, the lowest degree of within plot prediction variabilities are found for height ($CV_{mean} = 0.03$) and leaf Chl content, happening to be traits for which field samples were conducted at a higher density. Both deliberations are believed to further substantiate the reasonability of assuming that within plot heterogeneity of biophysical and biochemical crop traits is persistent within (some) plots. This variability may be more adequately modeled and predicted for

traits relying on a multitude of different measurement locations (i.e. leaf Chl content and height) compared to those based on only a single sampling location (i.e. fresh biomass, N content and C content).

Despite of these deliberations, it remains both challenging and questionable to assume or quantify persistent and varying levels of heterogeneity in the distribution of biophysical and biochemical crop traits within individual plots. Considering the rather limitedly convincing and sometimes contradicting findings one cannot evidently ascertain what the various degrees of observed variation in the prediction maps or residuals of prediction models are caused by. On the one hand they may possibly result from anomalies in the spectral data incorrectly matching/representing the distribution of biophysical or biochemical properties, the latter being ultimately homogeneous after all. In contrast, the option that the distribution of these properties is indeed variable to different degrees, while being only partially respected and reflected by the various in-situ sampling densities (resulting in calibration and validation of inadequate and sub-optimal relations), remains another possible explanation at the other end of the spectrum. Both are likely and reasonable explanations for which some degree of supporting evidence was provided in this report, such as the notion of various levels of radiometric errors examined in paragraph 9.2.3, as well as the persistence of vast and demonstrated highly influential physical within plot heterogeneity mentioned in paragraph 7.3 and appendix F. Additional research is required to assess the likelihood, validity and magnitude of these causes with respect to their associated implications for the calibration of spectral models and the predictive abilities thereof.

9.4 Discrimination of traits by different treatments

At last, the ability to distinguish differences in traits with respect to the different treatments plots have undergone will be presented below. This is in line with the agronomic hypothesis and associated ambition of the overarching field experiment where in this study has been conducted. The former states that historical vegetation and intermediate treatments of cultivars, and the legacies thereof, affect the development and associated traits of vegetation planted hereafter. Consequently, the question remains to which extent quantitative differences observed for different plots and their historical treatment through field sampling may be distilled from remotely sensed data acquired by an UAV. Figure 9.2 displays the mean and standard deviation values of observed and predicted traits, according to the best performing model for each trait, for unique treatments in the validation set.

It is suggested that the majority of traits can be reasonably discriminated with respect to the different treatments, albeit to varying degrees. The discrimination is most successful and significant for height and leaf Chl content. Relative and, to a lesser extent, absolute quantitative differences follow a near perfectly aligning pattern across the different treatments and show comparatively low errors (table 9.2). Except for discriminating between *Rs* and *Rs+Vs*, absolute and relative differentiating between treatments is also relatively successful for N content. Predicted values for the former regimes have interchanged notably compared to in situ measurements, hereby exerting vast leverage on lowering of the CVRMSE. Compared to the other treatments and due to the removal of some plots, however, *Rs* and *Rs+*Vs are significantly underrepresented. The discrimination for fresh biomass is less conclusive, indicated by a lower level of significance and larger errors, in agreement with the overall prediction error mentioned in paragraph 9.1. Although the treatments with the lowest measured biomass (*Fa, Lp, Lp+Tr*) are successfully distinguished from remaining cultivars for which higher quantities were observed, the measured dissimilarities within the latter group are less explicitly and partially contradictory modelled by predictions. It is argued that this follows from the demonstrated inability of models to predict more extreme (low/high) values of biomass

(paragraph 9.2.2), resulting in levelling and reduced variation in predicted values compared to observations. The discrimination for C content can hardly be considered successful, relatively nor absolutely.

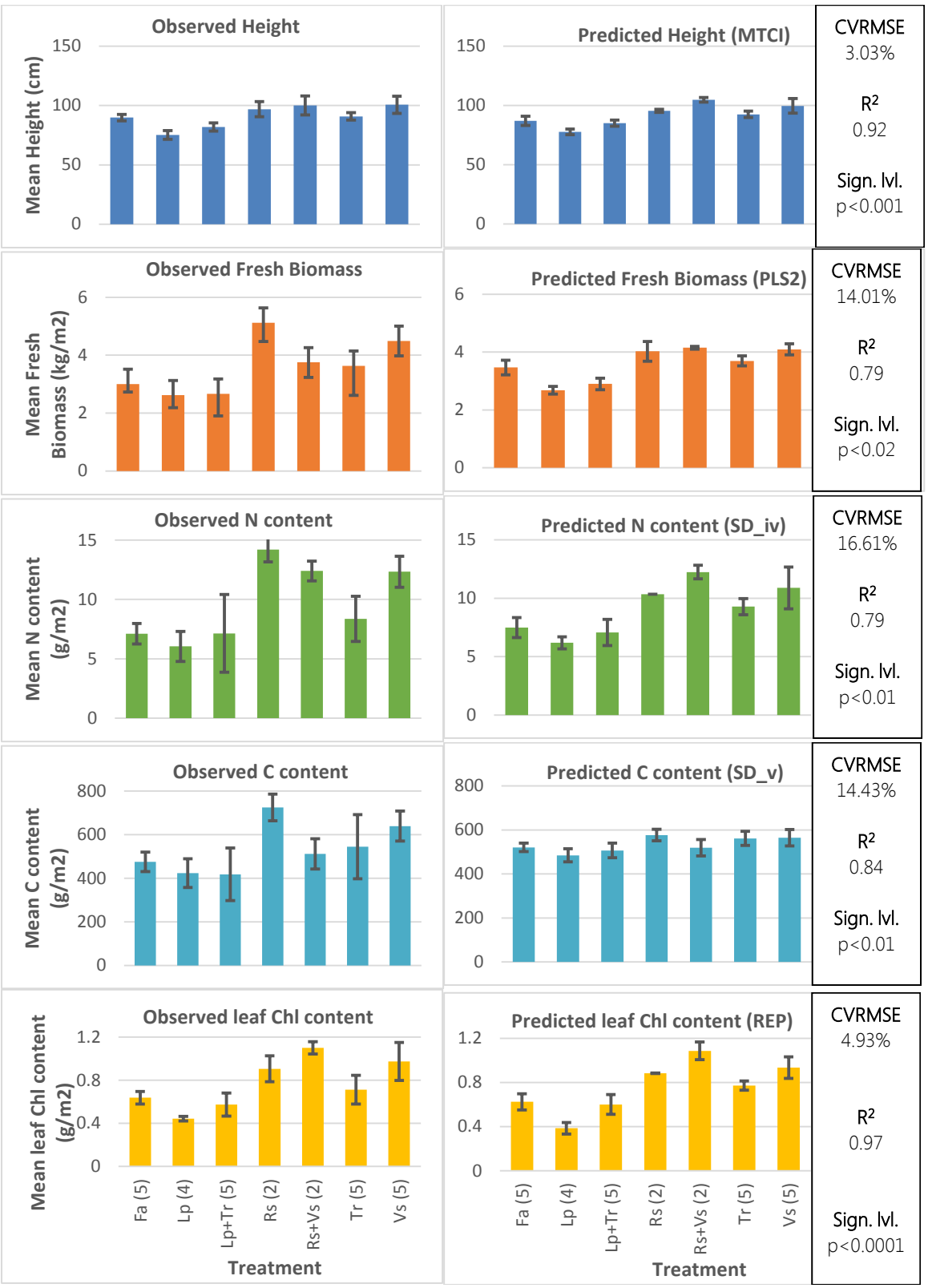

Figure 9.2: Mean and standard deviations of observed and predicted trait values per treatment type for validation plots (n=28). The statistics relate to statistical interference of the means of observed and predicted values. (Fa = fallowed, Lp = *Lolium perenne*, Rs = *Rapharus sativa*, Tr = *Trifolium repens*, Vs = *Vicia sativa*, CVRMSE = Coefficient of Variation of the Root Mean Square Error, R^2 = Coefficient of Determination, Sign. lvl. = Significance level).

9.5 Putting the models prediction capability into perspective

As could be distilled from the deliberations described in the preceding chapters and those presented in the succeeding reflective chapter, the interpretation of (CV)RMSE and R^2 values found during validation is a far from straight-forward process. Below, the findings of the best performing indices are elaborated on with respect to those in a selection of alternative studies, relating to one or more traits incorporated into this research, as a means for comparison and perspective.

Vegetative studies oriented at estimating heights of crops are relatively scarce, although a larger number of studies incorporate height as an (potential) explanatory variable for other traits (Freeman et al., 2007; Lisiwska et al., 2006). Nonetheless, the findings for height displayed amongst the highest values for R^2 ($R^2_{VI} \approx 0.79$, $R^2_{PLS} \approx 0.78$) and lowest prediction inaccuracies (CV ≈ 5.12%) for all traits, far exceeding the coefficient of determination of estimating height of corn and wheat crops using narrow band NDVI (0.31 and 0.34, resp.) and optimized four-band models (0.66 and 0.46, resp.) by Thenkabail et al. (2000) and Xavier et al. (2006), respectively. Besides, these findings were based solely on one-sided regression and excluded from independent validation. In contrast, the coefficients of determination were consistently lower for oats than those demonstrated by (Anderson et al., 2004) for estimating height of corn crops using visible, NIR and/or SWIR aerial and satellite data (R^2 = >0.93). The relative prediction error demonstrated here for oats, however, was significantly lower (CV = >11%). Higher R^2 values were also found for estimation of forest canopy height (0.9) and height of barley crops (0.8) using aerial (St-Onge & Achaichia, 2001) and tractor-mounted (Tilly et al., 2014) laser scanning equipment, respectively.

In comparison to height, significantly lower maximum coefficients of determination ($R^2_{VI} \approx$ <0.56, $R^2_{PLS} \approx 0.56$) and larger prediction inaccuracies (CV ≈ 21.0%) were observed during validation of fresh biomass predictions. Linear regression of the best performing narrow band NDV indices with measured biomass in various growth stages of winter wheat (maturation stage was excluded) yielded notably higher R^2 values (≈ >0.75) according to Hansen & Schjoerring (2003). In agreement with the same study, PLS regression improved prediction accuracy although differences remained substantial. The same notion was observed by Cho et al. (2007) for grass/herbs, although validated prediction errors for both optimized NDV indices (34%) and PLS regressions (26%) were higher. Optimized four band models (R^2 = 0.78) and narrow band NDV indices (R^2 = 0.71) also explained more of the variation in biomass of corn crops in a study by Thenkabail (2000). Higher R^2 values were also found by Heiskanen (2006) and Mutanga & Skidmore for estimating biomass of mountain birch forests (≈0.85) and dense grass canopies (≈0.8), respectively. The relative prediction error of validation found by the former study (CV = 41%), however, was notably lower for oats. The prediction accuracy for biomass estimation of oats was also higher than was observed for rice in both tillering and elongation phases (CV ≈ 33%), based on three or four band OMNBR models using (raw and first derivatives of) ground measured reflectance's (Gnyp, 2014). Construction of a linear model incorporating only CSM measurements through PLS regression yielded the lowest prediction inaccuracies and highest coefficients of determination (table 9.1). This latter finding underlines those of Tilly et al. (2014) with respect to demonstrating the relevance of laser-scanned barley crop height for predicting fresh (R^2 = 0.8) and dry biomass (R^2 = 0.77) thereof.

Validation for estimating N content yielded relatively varied results, ranging from lowest R^2 values and higher prediction errors for existing indices to enhanced performance for new optimized indices, the simple difference index in particular ($R^2_{VI} \approx 0.68$, CV ≈ 21.6%). For oats at jointing and heading stage, Zhao et al. (2014) found that a first derivative of reflectance based index and the red-edge position, in addition to some raw reflectance ratio indices, yielded the highest coefficients of determination ($R^2 \approx 0.78$ <> 0.94). Higher values for R^2 with respect to the prediction of N content in grassland and potato fields were also

found by Clevers & Kooistra (2012) using a variety of indices, although the differences are less elaborate. Albeit (significantly) higher than the values found in this study, no validation of the relationships was conducted in either of the studies, thereby disallowing comparison of the actual predictive capabilities of resultant models. The R^2 values for all tested indices and models were also outperformed by PLS regression for estimating N content in rice plants (0.84) by Nguyen & Lee (2006), although the predictions for oats were shown to exhibit a better accuracy (25.6%). The similar notion applies to efforts of Li et al. (2014) to estimate N content in maize crops using ground reflectance measurements, displaying even worse prediction accuracies during validation (>31%). For estimating N content in wheat crops, employing both optimized two-band indices and PLS modelling ($R^2 \approx 0.7$), largely aligning results were presented by Hansen & Schjoerring (2003). Similar to this study, prediction accuracies found (CV = 22%) are majorly overlapping and PLS regression did not yield (notable) improvements in the prediction of N content.

As was to be anticipated due to lower univariate VIS-NIR correlations and limited range of values in the calibration dataset, validation of models for prediction of C content within oats were found to exhibit the lowest performance ($R^2_{VI} \approx <0.52$, $R^2_{PLS} \approx 0.43$, CV ≈ 21%). This (in)directly followed from sincere discrepancies observed between univariate correlations over wavebands in both the calibration and validation set. These results, however, are also not entirely inexplicable considering that sensors are still unable to directly measure carbon in plant biomass and estimations therefore remain reliant on (sub optimal) proxies as chlorophyll content, dry matter/biomass and production and assimilation rates of carbon (Brewer et al., 2011; Tucker et al., 1981). Tucker et al. (1981) found strong correlations ($R^2 > 0.8$) between ground measured near-infrared and red spectra oriented SR and NDVI indices and accumulation of dry matter in winter wheat. This relationship, however, was only persistent during the stem elongation, booting and anthesis stage. In the final month prior to harvesting this correlation rapidly decreased, reaching comparable or even lower values for R^2 (≈ 0.0 <> 0.6) than observed here for oats. Peng et al. (2011) and Wu et al. (2009) assessed the ability of the product of (chlorophyll oriented) spectral indices with data on incoming photosynthetically active radiation (PAR) to assess production of carbon by maize and wheat crops, respectively. Highly varying coefficients of determination were found for, ranging between 0.45 and 0.75 for wheat crops to as high as 0.82-0.93 for maize. Validation on maize crops across multiple years, besides, exhibited a higher accuracy for prediction of carbon prediction (CV = 14-20%) than was observed for the prediction of carbon itself in oats (Peng et al., 2011). Alternative approaches exploited the association between fPAR, i.e. the fraction of Photosynthetically Active Radiation absorbed by a vegetation's canopy, and carbon stocks in plants. Consequently, based on satellite spectral data, Namayanga (2002) demonstrated relatively poor performance of an NDVI/fPAR oriented index to explain the variation ($R^2 \approx 0.38$) of in-situ measurements of carbon in various woody vegetation types. Hall et al. (1992) found stronger correlations between spectral measurements incorporated into a near-infrared/visible NDVI index and measured fPAR in a grassland field experiment, although multispectral sensor measurements by helicopter ($R^2 = -0.7$) yielded exhibited performance than ground measurements $R^2 = 0.57$).

After height, prediction of leaf Chl content in the oat crops studied demonstrated the strongest correlation and highest prediction, particularly for the existing REP index accuracies ($R^2_{VI} \approx <0.79$, CV ≈ 14.5%). In accordance with the findings of Hansen & Schjoerring (2003), PLS regression of including all individual spectra did not improve performance of predictions ($R^2_{PLS} \approx 0.64$, CV ≈ 22%). The results for the REP and MTCI indices, as well as some of the best performing new indices, largely align with those found for alternative optimized indices by Yu et al. (2012) with respect to predicting of chlorophyll in leafs of various species of barley crops ($R^2 \approx 0.74$). The same applies to Sims & Gamon (2002), who demonstrated comparable model performance to predict leaf chlorophyll content in various types of vegetation with different leaf structures, indicated by R2 values ranging from 0.61 to 0.83 for different red and near-infrared

based SR indices. None of these studies, however, included independent validation, rendering comparison of relative prediction (in)accuracies impossible. Both calibration and validation was conducted by Datt (1998) for estimation of chlorophyll content in eucalyptus leaves using a selection of NDVI and SR indices. During validation, the best performing model yielded a coefficient of determination of 0.83, hereby slightly outperforming the best model found for oats (SEP = 0.0068 mg/cm^2, (CV)RMSE not provided). A number of existing indices were optimized for the estimation of leaf chlorophyll content with the PROSPECT model by Wu et al. (2008). Optimization resulted in notable improvement of these models, displaying R^2 values ranging from 0.88 to 0.94 and from 0.67 to 0.76 when being validated on Hyperion spectral data for wheat and corn crops, respectively. An optimized and soil adjusted vegetation index (TCARI/OSAVI) calibrated through modelling and validated using airborne hyperspectral data on corn crops by Haboudane et al. (2002) yielded similar results, indicated by an R2 of 0.8. In a greenhouse experiment incorporating various crop species and ground spectroradiometer measurements, an optimized NDVI index generated even higher R^2 value (≈ 0.87) compared to the findings presented here. The relative prediction error (CV ≈ 22%), however, was higher compared to what was found for chlorophyll in leafs of oat crops

10. Discussion and directions for future research

Both UAV based remote sensing and, to a lesser extent, precision agriculture are two fields of expertise that are growingly but still limitedly practiced. Likewise, research into each is still not voluminous or self-evident, although it is gradually substantiating in recent years. Both fields are believed to exhibit substantial opportunities with respect to the future development of the other, for which the findings of this study represent just a mere example. In this chapter, the main findings of this research are reflected upon with respect to their strengths and limitations. Consequently, it is anticipated that repeated, continued and auxiliary research into (partially) overlapping and novel directions, respectively, are called for in the years to come. Below, following from the discussion itself or other commentary referred to throughout this report, a list of suggestions for these directions is presented.

10.1 Accuracy and acceptability of plant trait predictions

At the very beginning of this research it was questioned to which extent (hyperspectral) optical sensors on board of an UAV platform are able to retrieve quantified measures of various biophysical and biochemical crop attributes. After an extensive process of spectral data calibration and validation mixed results, indicating varied levels of prediction (in)accuracies, have been presented in the previous chapters. Prediction accuracies of the best performing models range from 5% for height to approximately 21% for fresh biomass, C content and N content, followed by leaf Chl content at 15% (figure 10.1). Subsequently, precision of predictions were similarly diverse, varying from highest R^2 values for height and leaf Chl content (0.80) to lowest values recorded for C content (R^2 = 0.52). Calibration of new indices using an optimization algorithm enhanced the prediction accuracy and precision for all traits other than height and leaf Chl content. Partial least square regression modelling further increased prediction accuracies only for fresh biomass. Comparison of these findings with outcomes presented in similarly oriented studies in paragraph 9.4 displayed blended results, indicated by prediction capabilities being similar, better or worse

The results for this specific study, however, should ultimately be considered and evaluated with respect to their applicability and value for the Wageningen field-experiment for which the study was initially executed. Consequently, a meeting was convened with the responsible person of the field-experiment itself to discuss and evaluate the outcomes presented here with respect to their (non-) applicability to the experiment itself. It is argued that there likely exist different degrees of variability in the distribution of various plant parameters within individual plots. Resultantly, it is not implausible that in-situ measurements for these traits exhibit comparable or even larger deviations with respect to their (non-) representability of the entirety of plots to different degrees. This renders destructive sampling as a similar or worse proxy, respectively. The plausibility of such plot heterogeneity is also discernible within the in-situ measurements for traits based on more than one sampling location (i.e. crop height and leaf Chl content). The within plot variation (CV) of field measurements for these two traits suggests that the assumption of complete within plot homogeneity does not entirely hold for all plots, to different degrees (height: CV_{max} = 6.04%, CV_{mean} = 3.07% / leaf Chl content: CV_{max} = 20.0% CV_{mean} = 9.0%). Consequently, trait prediction related deviations such as plot specific residuals of predictions and pixel-based within plot variability of predicted values (i.e. in prediction maps) may not be solely ascribed to inadequate and/or incorrect data acquisition by the UAV and its sensor, and potential limitations thereof. Instead, it is argued that they may at least partially result from actual heterogeneity in the distribution of such biophysical and biochemical crop attributes in the plots itself not being fully reflected in the field samples after all. Therefore, this notion is reasoned to be particularly valid for plant traits which were measured in the field at a single location only (i.e. fresh biomass, nitrogen (N) content and carbon (C) content) and for which potential and reasonably credible within plot variability is not adequately and comparatively less well accounted for (paragraph 10.3).

Additional quantitative and qualitative factors that one should also consider in this practical context are auxiliary benefits of UAV crop monitoring campaigns with respect to, for example, enabling of repeated crop inspection, reduced investments of time, labor and possibly finances, as well as avoidance of the need to require in situ samples in a destructive and environmentally harmful manner. It is subsequently argued that is worth considering that the potential, albeit not indisputably endorsed/ascertained, loss in accuracy invoked by crop monitoring by means of an UAV compared to field samples may be taken for granted considering the assumed advantages such campaigns offer to other practicalities of interest. The diversified and both quantitative and qualitative nature of these decisive factors, renders it both complicated and questionable to pronounce a definitive appraisal, although these ingoing efforts may be considered with respect to practicing monitoring studies such as the field-experiment covered here.

Overall it is argued that the findings presented in this report are promising at least for the majority or all traits studied with respect to prediction of their quantities and discrimination thereof across different cultivar treatments. Following from the upcoming paragraphs, there are some influential factors, not all being directly ascribable to (in)capabilities provided by the UAV platform and its associated sensor(s) (e.g. sampling procedures), that have potentially impacted the results. Hence it is believed that future research and a more elaborate research setup, incorporating at least some of the suggestions following hereafter, may further improve the accuracy and precision of predicting various crop traits under study by means of remotely sensed reflectance.

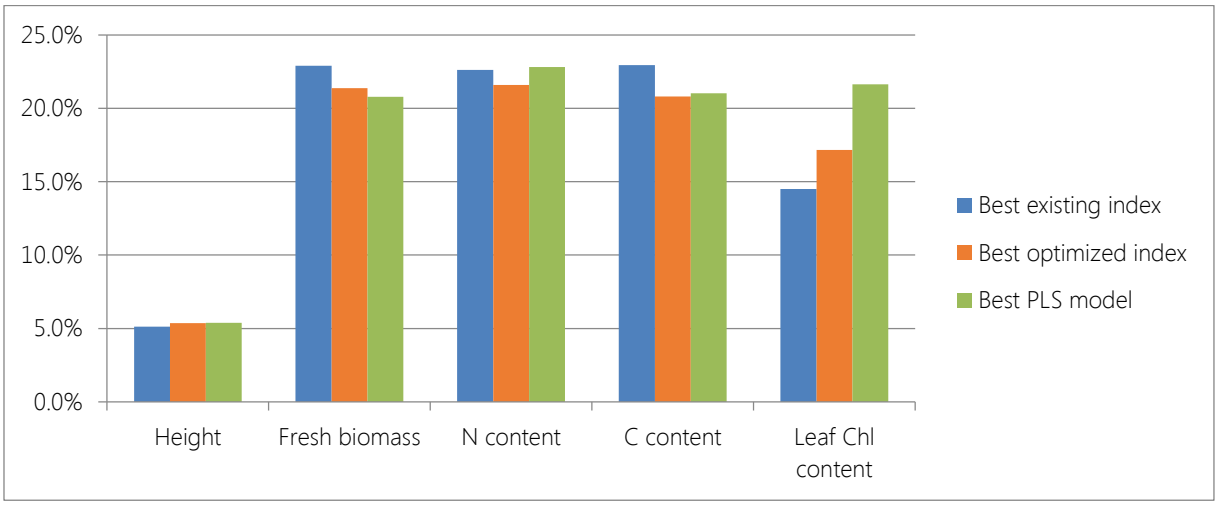

Figure 10.1: Relative predictions errors (CVRMSE's) in percentages (%) of the best performing indices/PLS models with regard to predicting each trait.

10.2 General applicability of findings

As was to be reasonably anticipated, the research presented here found highly varied and sub-optimal relationships between in-situ field measurements and reflectance data captured by the UAV platform. A multitude of reasons lay at the foundation of these findings, some of which may be directly ascribable to the capabilities and limitations of the platform and sensor(s) used, while some others are not. In this respect, factors such as platform and sensor characteristics/limitations, the viewing geometry, growth stage of crops, differentiation of plant architecture, within-plot trait heterogeneity thereof, sampling density, sampling date(s) sampling errors, among others, are worth mentioning. The data used in this study was only acquired at a single moment in time at a distinct crop development stage, for one location and crop species, using the same viewing angle. Given the current research setup, however, it is impossible to ascribe a certain influence or weight to (some of) these factors with respect to the extent to which they impact(ed) the

outcomes. In short, more extensive research is recommended to improve the precision and accuracy of the models prior to their practical application.

For example, it is evident that specific wavelengths or indices for estimating traits such as biomass, N, yield and chlorophyll change with growth stage of crops, sampling dates and differentiation of plant structures (e.g. planophile vs. erectophile), among other factors (Freeman et al., 2007; Osborne et al., 2002). The notion related to the developmental stage of crops is discussed in more detail later on this chapter (paragraph 10.4). Therefore, the relationships found in this research are not necessarily suitable when applied at other moments during the season, or to other crop types. Additional research is both required and recommended to explore whether the relationships with individual spectra and spectral indices are valid for other phases of crop development as the composition and architecture of vegetation changes, although previous studies suggest this is not (necessarily) the case (e.g. Zhao et al., 2014; Freeman et al., 2007; Xavier et al., 2006; Haboudane et al., 2004; Scotford & Miller, 2004; Osborne et al., 2002; Yang & Miller, 1985). Ideally, future research should comprise of repeated intra seasonal field measurements and UAV campaigns, not only to evaluate the validity and robustness of the relationships found here, but rather to explore whether different relations at alternative growth stages exhibit other (better) prediction capabilities. Similarly, Retzlaff et al. (2014) assessed the ability of a UAV based multispectral system to quantify different plant traits, and the importance of the platform/sensor's viewing angle in particular. It was demonstrated that a 45° oblique viewing direction significantly enhanced discrimination and quantification abilities (of soil modalities and leaf Chl content) using spectral data, due to the visibility of a larger fraction of canopy in angled imagery. Consequently, collection of the spectral data under different viewing angles could have been conducted to assess the importance of this variable in (in)accurately predicting distinct plant traits. Even though a brief examination (not shown) of the location of plots exhibiting relatively large prediction errors and their associated (angled) orientation towards the sensor yielded no indisputable patterns as such, more elaborate exploration is required to precisely weigh out and quantify such external influences. Factors relating to field sampling are also argued to be valid and of influence for this particular study, although this notion will be discussed separately in the following paragraph.

Considering the practical applicability of findings to precision agriculture (PA) it is worth mentioning that the latter is generally stated to comprise of four overarching phases (paragraph 3.3.1). This research, however, solely covered the second phase, relating to mapping in-field variability, and parts of the first phase (data collection) during data pre-processing. Ideally, regarding the actual practical implications of this research' findings to practitioners of precision agriculture, the latter two stages (decision-making and variably adjusting crop management) should also be considered prior to implementation. As is stated by Rango et al. (2009), operationalization and practicing of UAV based agricultural monitoring requires comprehensive and readily available data analysis and interpretation procedures to end users. Regardless of anticipated perks often ascribed to (UAV based) remote sensing for agricultural monitoring, farmers still frequently lack the appropriate knowledge and practical skills to effectively utilize such technologies and interpret the data it brings about (Seelan et al., 2003). Such issues relating to image interpretation, data extraction and integration of expert data, among others, are also stated to limit the effective implementation of remote sensing in precision agriculture according to Zhang & Kovacs (2012). It is believed that the output as presented in this report may be off a level and density too complicated to be effectively comprehended and subsequently put in practice by practitioners in the field. Rather than a variety of different prediction maps, translation of such findings, possibly combined with external (i.e. climatic or ground sensor) data, into (nutrient) prescription, task, or variable rate application maps may better align with the specific needs of practitioners. Relatedly, the time-span over which the research was conducted, and its results retrieved, is off a too coarse temporal resolution to allow adequate adjusting of intervening practices in a timely manner.

Consequently, it is argued to be similarly important to take into consideration how findings of studies as these can be effectively delivered to those in need, in a timely and user-friendly manner, hereby strictly aligning with the specific needs and (in)capabilities of its eventual (end) users. Even though these deliberations were clearly and purposefully not the focal point of this study, it is argued that auxiliary research into practical implementation of this technology is worthwhile to enhance its eventual success and durability thereof.

At last, only univariate relations between wavebands, indices and PLS models were established in this study to evaluate their ability to predict different plant parameters. According to Mulla (2013), however, there is a growing demand for the generation of more all-embracing models that are able to predict quantifiable measures for different plant traits simultaneously at once. Subsequently, exploration of such multivariate models with multiple depending trait (y) variables is recommended from both a scientific and application perspective. Relatedly, the performance of such models should be effectively compared to univariate models presented in this and many other studies.

10.3 In-situ sampling

Monitoring of vegetation properties and calibration of models for such purposes is ultimately constrained by both the quality and quantity of ground truth data (Michaelsen et. al., 1994, p. 673). The field measurements of different traits were conducted on various spatial scales or densities that, for some traits, were further varied for monoculture and polyculture plots (figure 5.2). For example, biomass measurements (including measurements of N and C), were based on a single sample for both monoculture and polyculture plots. Besides, the samples were taken by means of a 25x25cm quadrant, that was put in a plot's (left or right) sub quadrant representing ¼ of a monoculture plots area, and ½ of polyculture plots. In contrast, a single height measurement was taken from each plot's sub quadrant, regardless of monoculture or polyculture plots. Average measured height for monoculture plots is thus based on four measurements, and only on two measurements for polyculture plots, although the surface area for each plot type is varied proportionally to this. Furthermore four SPAD readings (for leaf Chl content measures) were acquired from each plot, regardless of plot type. Consequently, the SPAD readings have a denser spatial resolution for polyculture plots (4 per 4.5m^2) than for monoculture plots (4 per 9m^2), due the same number of readings within a smaller area. Spectral reflectance is based on an average over the entire plot (minus the 30cm edge effect), or ½ plots for polyculture plots. Subsequently, the calibrated and validated models are based on the latter (mean reflectance), and (non-)averaged field samples for a distinct trait. This is where potential deviations may occur. Field measurements may in fact be representative for the specific scale at which they were conducted but, due to potentially and observable within plot heterogeneity, they may not necessarily be extrapolated to the remainder of the plot.

Regardless of the actual adequacy of indices and their associated relationship to one or more traits as were calibrated, various degrees of within plot variability in measured reflectance is observed over separate wavebands. Consequently, this heterogeneity is also discernible in the various index and trait prediction maps, which are both based on the spectral data at unique wavelengths. On the one hand, these anomalies might be the results of certain technical limitations imposed by the distinct sensor/platform combination used here (i.e. signal-to-noise errors). Such anomalies might invoke variability of reflectance measurements within plots that may instead be homogenous with respect to the spatial distribution of various biophysical and/or biochemical vegetation traits, resulting in inadequate relationships during calibration. On the other hand, however, the distribution of traits within plots may not be homogeneous after all, hereby (partially) explaining the observed variability for reflectance values. In both situations, these notions invoke inadequate and incorrect calibration and validation of relationships between plot averaged

spectra and in-situ trait measurements relating to only one or a limited number of demarcated locations. The latter notion with respect to within plot heterogeneity cannot be indisputably confirmed to persist, other than the clearly visible physical variability observed for some plots prior to removal thereof (paragraph 7.3, appendix F). It has been regularly elaborated on within this report, however, that a certain degree of within plot differences and the associated implications for calibration and validation procedures can be reasonably assumed to be present.

With respect to sampling procedures it is worth mentioning that the eventual UAV flight campaign was initially envisaged relatively ad-hoc, being more of a spontaneously pronounced opportunity rather than a well thought-out and extensively prepared operation in which both the experiment and UAV campaign were strictly aligned well in advance. Consequently, it is argued that studies such as these may notably benefit from a different, extensive and more homogenous density of in-situ sampling. Alternatively, one may consider making sample areas more easily recognizable from the aerial data through placement of markers to allow more precise alignment of the area from which spectra and field measurements are retrieved, as was already mentioned in paragraph 6.2.4. A more extensive sampling density, on the one hand, likely enhances the calibration and validation of relationships that are more representative of the area from which the spectral data is retrieved. On the other hand, a more homogenous sampling density enables a more adequate evaluation and sensible intra-comparison of the predictive accuracy for different plant traits.

10.4 Implications of the developmental stage of crops

The development stage of the oat crops at the time of field and data acquisition should be mentioned, for a variety of reasons. Both the field and UAV data acquisition campaigns were conducted relatively late in the crop's growing season, only a few weeks prior to harvesting when the crops were at a mature stage. The near simultaneous acquisition of field and UAV data renders the research rather relevant considering the field experiment specifically, enabling evaluation of the extent to which the aerial data can be effectively employed to estimate attributes of crops that are otherwise retrieved destructively in the field itself.

This notion, however, is increasingly important from both the perspective of UAV based crop monitoring for application in precision agriculture, as well as the implications for spectral analysis. Regarding the application for precision agriculture practices, the studying of relatively mature crops may be considered less appropriate or valuable than of crops in a preceding growth stage. This deliberation is especially valid considering the assumed advantage of UAV based crop monitoring for enhancing retrieval of (near-) real time parameters on the status of crops and the associated ability to adjust crop management practices in a timely manner (Anderson & Gaston, 2013; Mulla, 2013; Rango et al., 2009; Dobermann et al., 2004). The oats crops studied are in such a full-grown stage shortly prior to the actual harvesting thereof that application of additional nutrients to influence future development will be rather ineffective. To raise effectiveness of such intervening practices, the predictions of traits should ideally be based on spectral data acquired at a preceding critical stage to make adjustment of practices more worthwhile. Unless the calibrated models and their associated accuracy evaluated in this research are comparatively effective during other growth stages, which is questionable (Freeman et al., 2007; Osborne et al., 2002), analysis of the ability to predict crop traits during a critical foregoing development stage may be more relevant from the viewpoint of farming practices.

With respect to the implications for spectral analysis, it should be mentioned that the biochemistry within crops is consistently changing throughout the growing season, up to and including the final stage. Nitrogen, for example, is known to be highly mobile and being constantly relocated between different plant

components based on absorption and desorption in soils and the atmosphere. The presence of N within wheat crops was found to be particularly high during the early vegetative phase, after which it was structurally reduced throughout succeeding phases. As vegetation reaches the maturity stage, nitrogen was demonstrated to be increasingly relocated from leaves to grains and from stems and soils to a lesser extent (Dixon, 2007; Peinetti et al., 2001; Harper et al., 1960). Resultantly, Zhao et al. (2014) and Freeman et al. (2007) found that N content in oats and corn, respectively, could be more accurately predicted at early growth stages than during later stages. Relatedly, deviations in N content may only be effectively utilized to discriminate crop status given that all crops in different plots are in the same growth stage. This follows from N content being the product of N concentration and dry biomass, both variables are prone to variations across different developmental phases. Assessing whether the oat crops in different plots are indeed aligning with respect to their vegetative growth process, however, is challenging as available N and soil conditions are potentially varied for each plot resulting from historical treatments of such plots (Chen et al., 2010). The results, however, suggest that a distinction of varied levels of N content across cultivars with different treatments can be established with a reasonable precision and accuracy (figure 9.2). The same notion of remobilization at later (mature) growth stages also applies to biomass which, during senescence, is increasingly transported to seeds of plants to be available during the next generation (Murphy & Murray, 2003). As the seeds of crops are filled, turning brown when water is subdued, remote estimation of biomass is prone to larger inaccuracies than is the case for earlier developmental stages (Yang & Miller, 1985). Relatedly, chlorophylls in a vegetation's canopy accumulate throughout the season, after which it is gradually reduced during reproductive and senescing phases (Ciganda et al., 2009). Therefore, canopy reflectance and the associated correlation with chlorophyll content were found to be highly varied both in strength and direction across different growing stages (Sun et al., 2010). Senescing leaves gradually reveal a yellowish/brownish appearance as chlorophyll content within these leaves decays and energy is increasingly relocated to grains, hereby exposing other plant pigments already priory present, such as carotenoids (Murphy & Murray, 2003) (figure 10.2). The latter were found to significantly influence, and therefore potentially distort, adequate discrimination and quantification of chlorophylls at specific wavelengths by Gitelson (2012). It is besides argued that the resultant loss of photosynthetic capacity as vegetation matures may partially explain the reduced importance of visible (particularly red) wavelengths in existing and new indices, as absorption at these wavelengths may become less pronounced than is the case for preceding growth stages (Gitelson, 2012; Murphy & Murray, 2003). Significant implications of the development stage were also demonstrated by Xavier et al. (2006) and Scotford & Miller (2004) for estimating plant height, indicated by significantly lower coefficients for univariate and multivariate correlations between spectra/VIs and height at the tillering and maturation phase of wheat. Instead, variations in height were found to be especially discernible during rapid crop development at booting and heading stage, whereas this was not the case during maturation when variations in height became less pronounced due to comparatively lower levels of green biomass.

The senescence process in mature stages of vegetation, however, is an ultimately complex organ-wide process that is further influenced by additional factors such as hormones, environmental factors, and nutrients, among others, which are not all properly understood or recorded for the dataset (Murphy & Murray, 2003; Gan & Amasino, 1997). Besides, based on a visual inspection of the RGB orthomosaic, hyperspectral data and ground photography it is suggested that some plots are in a different stage of senescing than others, if at all (figure 10.2). All such deliberations further complicate the process of adequately calibrating relationships between measured reflectance and in-situ measurements of traits. This deliberation may also (partially) justify the relative underperformance that was observed for some of the existing indices during calibration in general, and the relatively small hotspots for two-band indices identified

by the optimization algorithm. Considering that the majority of these existing indices were once found and eventually calibrated based on spectral data acquired during a preceding crop development stage, their limited applicability to the growth stage of the oat crops included in this study is not entirely inexplicable. It also challenges the sensible comparison of coefficients of determination and prediction (in)accuracies with those found in such studies, as certain traits may be effectively better estimated during a given growth stage than during another.

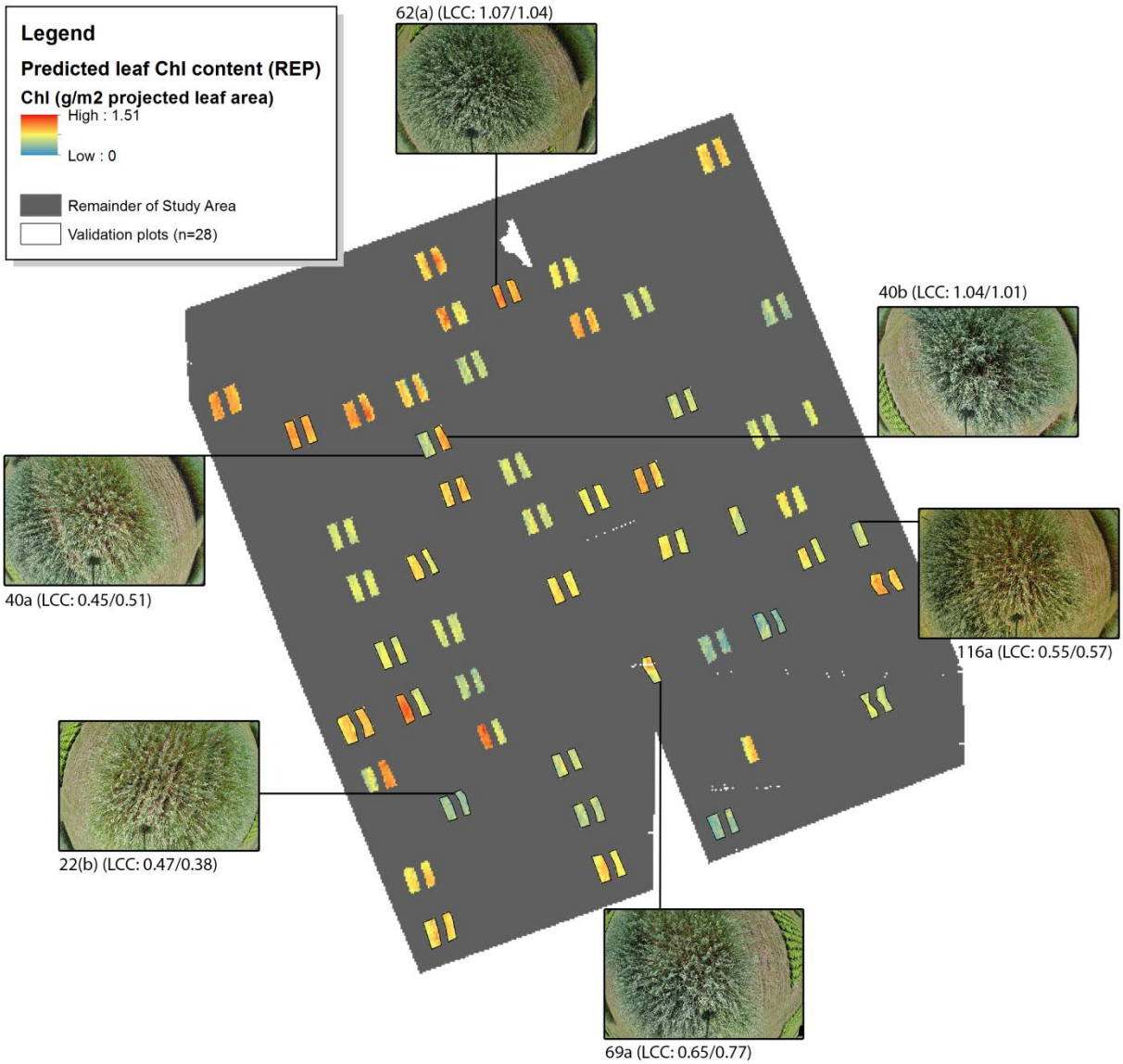

Figure 10.2: The prediction map for leaf Chl content based on the best performing index (REP). For a selection of plots, with varying levels of measured and predicted leaf Chl content, the associated Digital Hemispherical Photographs are provided. Both the UAV data and photographs were acquired on the same day. For each photograph, both the plot number and side (a = west, b = east) are given. The values in parentheses relate to the mean in situ measured leaf Chl content and (REP) predicted leaf Chl content, respectively. Differences in leaf coloring and their linking to comparatively lower (yellow/brownish) or higher (greener) chlorophyll contents, as well as plot architecture (e.g. density), likely suggesting different crop development (i.e. senescing) stages, are clearly discernible.

10.5 Ascribing (in)capabilities to the UAV platform and sensing system(s)

For this research, reflectance measurements were only retrieved by means of an UAV. In an ideal research oriented situation the reflectance of the plots was not only measured in this way, but also by a spectrometer in the field to record ground 'truth' measurements to serve as a reference. Both measurements can subsequently be correlated with distinct traits. More importantly, however, this would have effectively allowed comparing of spectra measured by both sensor platforms, or more specifically to evaluate to which extent remotely sensed UAV data acquired by the HYMSY setup (does not) compare to the higher resolution data acquired by a more stable sensing platform (Suomalainen et al., 2014). A similar set up is common practice in various other studies in which the applicability of UAV based remote sensing for monitoring vegetation is assessed (e.g. Bareth et al., 2014; Tattaris et al., 2014). As has been mentioned it is very well possible that limited performance of one or multiple indices is not necessarily or entirely caused by unsuitability of the UAV platform/sensor combination, but rather the result of inadequate or insufficient ground sampling practices. If ground spectral data was also available it would have been possible to more accurately identify and explain such anomalies.

Relatedly, the vegetation indices incorporated into this study were largely retrieved from existing research. Even though the focus was purposefully on spectral analysis of other cereal crops, the majority of indices evaluated were in fact assessed for crops other than oats. As is the case for the effect of measuring at different growth stages of vegetation, differences in plant species and their associated structures are also likely to influence the performance of one or multiple indices with respect to estimating distinct traits. Consequently, poor performance of distinct existing indices may not be necessarily ascribable to inabilities of the UAV platform or its sensor, but rather to the notion that the index itself is not as effective for estimating a trait in these oat plats as it is for estimating the same trait in another cereal crop in another development stage. The importance of this notion was confirmed by the exploration of alternative indices using an optimization algorithm to extract other combinations of bands. During index calibration, it was observed for the majority of traits that exploration of auxiliary band combinations and/or PLS modelling is well worth the effort, indicated by (further) improvements in the resultant model adequacy.

Finally, potential limitations invoked by the PLS modelling procedure are elaborated on with respect to parsimony and plausible overfitting. As was mentioned previously in paragraph 6.3.2.3, the PRESS statistic was employed during calibration in order to select the ideal parsimonious (i.e. simplest, incorporating the least latent variables) PLS models with the optimum number of latent variables. Selecting a PLS model based on the (lowest) resultant PRESS model is a methodology that is frequently utilized to minimize risks of model overfitting (Yu et al., 2014; Nguyen & Lee, 2006; Esbensen et al., 2002). According to some authors, however, reliance on the PRESS statistic is not entirely free from errors and may still provoke a certain, albeit marginal, degree of overfitting. Consequently, Haaland & Thomas (1988) propose an alternative approach through which a model with fewer latent variables (i.e. a more parsimonious model) is selected, given that its associated PRESS statistic value is not significantly higher than the lowest PRESS statistic. Relatedly, Sawatky et al. (2015) state that relying on the *van der Voet's statistic* yields more adequate and parsimonious models. This criterium selects the model with the fewest latent variables for which the residuals are insignificantly larger than the residuals of the model with the lowest PRESS value. Compared to reliance on individual PRESS statistics, Abdi (2010) suggests a more elaborate approach in which the ratio between the PRESS statistic of a PLS model with a x number of variables and a model with $x-1$ variables are compared with some arbitrary value to evaluate when the preferred number of latent variables has been reached. Following from the tabular overviews of PLS model calibration presented in appendix I it is observed that, for some traits, alternative PLS models incorporating fewer latent variables were found to exhibit PRESS values only

marginally lower than the lowest possible PRESS statistic. More specifically, this relates to N content for PLS models of the first type and plant height for the second type of PLS model incorporating CSM height. Alternatively, these more parsimonious substitute models could have been calibrated, validated and evaluated with respect to changing performances instead.

10.6 Sensors, resolution and geometry

The manual generation of ROIs, especially for the HDC, is likely to have invoked certain inconsistencies. Due to the HDC's resolution and geometric errors resulting from its pushbroom scanner mechanics, identifying the correct demarcation of vegetation/plots was a complicated process. Regardless of extensive georectification during pre-processing, various degrees of geometric errors remained persistent in the dataset. The presence of significant and highly varying amounts of shadows further complicated the process of ROI generation. This is exemplified by the diverse geometry of ROIs and their surface areas (mean = 1.62m^2, std = 0.26m^2, min = 1.1m^2 , max = 2.5m^2). From an application point of view, such time consuming georectification endeavors are ideally gotten rid of to reduce the total processing time and allow adjustments of intervening (farming) practices more adequately shortly after the remote measurements. Besides, consistent absolute geometric accuracies are considered highly important when applied in multi-temporal (repeated) flight campaigns over the same study area, to allow re-utilization of the same ROI dataset over and over again. From the view point of spectral analysis in this study this notion is relevant considering the varied and inevitably sub-optimal alignment of ROIs with the actual area of plots considered for in-situ field measurements, potentially distorting adequate calibration of the relationship between measurements and average spectra over wavebands. Multiple solutions to (potentially) mitigate these necessities exist. Hyperspectral scanning equipment such as the one used in this research are prone to some limitations with respect to mapping a given area geometrically adequate, particularly when the platform they are mounted on or the object under study are abruptly and/or rapidly moving as is the case for UAV systems (Hardin & Jensen, 2015; Jung et al., 2013a; Schowengerdt,, 2012; Bajwa et al., 2004). Given this research as a point of departure, it is therefore suggested to evaluate the performance of hyperspectral frame cameras and/or miniaturized gyro stabilized gimbal mechanics that are now gradually finding their way to the UAV market (Whitehead & Hugenholtz, 2014; Jung et al., 2013b). Instead (or additionally), the inclusion of a larger number of ground control points (GCPs) across the study area may be considered to allow for a more adequate georectification of the resultant dataset. For the latter option, however, the additional workload associated with in-field placement of these markers is to be taken into account, particularly with respect to the anticipated time savings accrued by reduced georectification in post-flight processing.

The spectral capabilities of the sensor are similarly worth mentioning. Initially, the raw HDC data was used for this research. This raw data comprised of a HDC with a very low FWHM of only 9nm. This low FWHM is important, because it fits the recommendation to adhere to a bandwidth between 5-10$_{nm}$. Narrower bandwidths most likely provoke signal noise issues, whereas broader widths tend to obstruct identification of distinct biophysical and biochemical properties studied (Thenkabail et al., 2012b). At some point, however it was decided to utilize a secondary level data product instead (due persistence noise errors present in the raw HDC), being an alternative HDC with a FWHM of 30nm. This fortunately did resolve most of the noise issues, however, it potentially reduced the ability to detect small spectral anomalies, which could be effectively utilized to identify distinct traits. Nguyen & Lee (2006) and Hansen & Schjoerring (2003), for example identified small scale anomalies in univariate correlations of traits over individual wavebands throughout the visible spectrum utilizing a much higher spectral resolution (± 1nm) spectroradiometer. Subsequently, some of the eventually calibrated VIs and PLS models relied on these discrepancies to various

degrees. Due to the absence of such deviations in the HDC, plausibly resulting from smoothing of spectra due to the larger FWHM, optimal indices relied less heavily on these spectral regions, if at all. Consequently, it is considered worthwhile to explore what is underlying the vast spectral noise in the original dataset in order to reduce its severity, while expectantly enhancing the possibility to exploit the spectra more accurately with respect to the prediction of relevant plant traits.

10.7 Extent, composition and reliability of calibration and validation data sets

The calibration of relationships between reflectance data and crop traits was conducted using a relatively limited dataset, comprising of only 28 individual observations. The same notion applies to the validation phase and the associated data set. This respectful size was purposely decided on to arrive at two sets of an acceptable size that are, albeit marginally, still large enough to consider as independent and fit for use in statistical analysis. It may be reasonably expected that the use of a larger (calibration) dataset would have resulted in more accurate and/or robust relationships with enhanced predictive capabilities. Similarly, to evaluate both the resultant robustness and applicability of these relationships, a larger validation is ideally recommended (Li et al., 2014). The significance and potential implications of adhering to relatively small datasets was most clearly illustrated prior to the removal of plots dealing with observable physical heterogeneity (appendix F). During the exploration of what could possibly be causing the anomalies and unanticipated univariate correlation between traits and wavebands, it was observed that even a single plot was able to exert highly significant and influential power on the correlations. Even minor errors in individual plots, possibly related to field measurements and/or spectral inconsistencies, among other causes, may thus be able to notably distort relations and affect the results given these datasets of a limited size

The discrepancies observed between the calibration and validation set with respect to univariate correlations over wavebands should be mentioned here again. Although both traits followed a relatively comparable (horizontal) pattern of correlations over individual wavebands, the correlation coefficient values diverged notably (vertically) in between both data sets. Consequently, it is believed that the (random) definition of one set as a calibration set, and the other as a validation set, has had its implications on calibration and validation procedures for these two traits in particular. Given the largely comparable horizontal pattern of univariate correlations over different wavebands in both data sets, reallocating the calibration set to validation and vice versa would not necessarily have resulted in the identification of (notably) different bands (combinations) through plotting of correlation matrices or PLS regression. In contrast, it is however plausible that such a turnaround will result in different coefficients of determination during calibration, as well as values for R^2, RMSE and (CV)RMSE differing from those currently found during validation.

An alternative form of statistical analysis that is possibly able to reduce or mitigate the intrusion of such external effects is bootstrapping. Bootstrapping requires letting go of the current depiction of an independent calibration set that is subsequently validated externally by means of an entirely new (validation) dataset. Instead, in bootstrapping, the full data set is used for both training (calibration), testing (validation) and retrieval of prediction (in)accuracy statistics internally (Gude et al., 2009). A random sample is acquired from the entire dataset for calibration and to calculate the desired statistic(s) of interest (Mutanga & Skidmore, 2007). This step is then repeated for a defined number of replications, each exploiting different combinations of observations, to arrive at a vector of *n* statistics (i.e. errors) which can then be averaged to arrive at a measure of precision and robustness of relationships found (Boves Harrington, 2006). Relatedly, Souza et al. (2010) stated that bootstrapping may be a more preferable technique in situations when the number of observations is relatively limited. Considering the objecting univariate correlations of fresh biomass and C content in particular, the primal benefit of employing bootstrapping relates to the notion that

statistical interferences exploit the distribution of a proxy sample acquired from the data itself rather than a sample retrieved from a population that is not yet properly understood (Mutanga & Skidmore, 2004). Additionally, such internal validation may be advantageous to alternative (i.e. external) validation procedures as it allows the defining of limits for the values that may be expected (Steyerberg & Harrell, n.a.). The latter may be of particular importance considering that, for some traits, the measured values in the validation set exceed the range measured for calibration data in either or both directions.

10.8 Prediction of plant traits from reflectance and plant height

Various existing studies have explored and demonstrated the enhanced predictive accuracy of indices and/or (in situ) field measurements of vegetation height for different plant traits (e.g. Tilly et al., 2014; Swatantran et al., 2011; Anderson et al., 2008; Freeman et al., 2007). It was demonstrated in this study that, alternatively, one is able to extract relatively accurate and representative plant height measurements through the extraction of a CSM from affordable optical (RGB) sensors. Consequently, future research may illuminate if and to what extent combining of CSM height and spectral (index) data, both of which were shown to be collectable simultaneously from an UAV platform, improves the accuracy and precision of trait predictions. Due to time constraints, exploration of the added value of CSM measures was only considered for PLS model calibration and yielded mixed results. It is not unlikely, however, that CSM data can effectively improve the performance of indices with respect to the prediction of one or more traits.

11. Concluding remarks

The results presented in the preceding chapters illuminated that a variety of biophysical and biophysical traits present in oat crops can be predicted in a quantifiable manner with different levels of precision and accuracy (figure 9.1). Besides, the outcomes suggest that, for some traits, predictions may be effectively further discriminated for different cultivars and their associated treatments (figure 9.2). Exploitation of new indices enhanced the prediction ability for both N and C content, as well as fresh biomass. For the latter trait prediction accuracy was further increased through PLS regression, no improvements were recorded for the remainder of traits through such modelling. It was also observed that crop height data, retrieved by a traditional RGB camera mounted on board of the UAV simultaneously with the hyperspectral sensor, is a similarly good predictor of fresh biomass, and C content to a lesser degree, than individual wavelengths and/or indices. Only considering the best performing models, crop height was indicated with the highest prediction accuracy (CVRMSE = 5.12%), followed by leaf Chl content (CVRMSE = 14.5%) Prediction of fresh biomass (CVRMSE = 20.78%), C content (CVRMSE = 20.81%), and N content (CVRMSE = 21.6%) displayed larger but comparable discrepancies in prediction. Band combinations borrowing from the red-edge and (lower) near-infrared wavelengths were consistently identified to yield the best prediction accuracies for the different crop traits under study other than C content. In most instances the bands incorporated into distinct indices exhibiting the best performance were closely spaced in the electromagnetic spectrum, hereby effectively exploiting the strictly skewed shift in reflectance between visible (red) and short near-infrared wavelengths, or the flattening thereof. For C content and, alternatively for fresh biomass, an (sub-)optimal relationship was found for indices borrowing from longer near-infrared wavelengths close to the near-infrared peak at approximately 915nm.

Except for crop height and leaf Chl content to a lesser degree, both accredited with the highest prediction accuracies, the remainder of traits did not show significantly deviating (CV)RMSEs. The anomalies observed for univariate correlations of fresh biomass and C content in the calibration and validation set do at least suggest that prediction of these traits may be more problematic. Due to the current research setup it remains troublesome, however, to indisputably assess or quantify to which extent a distinct crop attribute can be more accurately predicted than another by UAV based remote sensing. It is reasoned that this notion is most strongly influenced by significantly different densities at which in-situ measurements were retrieved, varying both among different traits and between monoculture and polyculture plots, and were subsequently used to calibrate and eventually validate prediction models. It is plausible that a more homogenous, thought-out and prepared field sampling campaign, explicitly considering the analysis of remotely sensed data by a UAV platform a priori, yields different, potentially more stable and less strongly varying results within and between traits. In addition to sampling procedures, supplementary variables that have possibly influenced the results of this study in either direction have been suggested in the previous chapter. It requires additional research to assess the importance of each with respect to their potential influencing of the predictive ability of different models for various traits tested here.

Nonetheless, it is believed that this research displayed promising results to various extents with respect to the possible application of UAV based remote sensing in monitoring of crops for various purposes, indicated by prediction accuracies largely comparable or better with regard to existing studies for height, N content and leaf Chl content. Findings for both fresh biomass and C content were consistently lower and outperformed by a multitude of existing studies. Some remarks on the causes thereof, in addition to several suggestions to potentially mitigate these causes, have been put forward throughout in this report. Additional research, however, is essential to assess the validity and robustness of these findings for application on alternative crop types, and in preceding growth stages. Besides, it is both required and

recommended to further explore and optimize the precision of the technology used, preferably incorporating one or multiple recommendations presented in the previous chapter, prior to exercising UAV based monitoring practices on a large scale. This deliberation remains particularly relevant considering the current momentum of the development of Unmanned Aerial Vehicles, the miniaturization of compatible sensor systems and the growing number of industries articulating to be willing to explore the added value of this technology for diversified applications.

12. References

Aasen, H., Gnyp, M. L., Miao, Y. & Bareth, G. (2014). Automated Hyperspectral Vegetation Index Retrieval from Multiple Correlation Matrices with Hypercor. *Photogrammetric Engineering & Remote Sensing,* 80(8), pp. 61-71.

Alchanatis, V. & Cohen, Y. (2012). Spectral and Spatial Methods of Hyperspectral Image Analysis for Estimation of Biophysical and Biochemical Properties of Agricultural Crops. In P. S. Thenkabail, J. G. Lyon, & A. Huete (Eds.), *Hyperspectral Remote sensing of vegetation* (pp. 289-308). New York: CRC Press.

Allan, J. A. (2013). Sensors, Platforms and Applications; Acquiring and Managing Remotely Sensed Data. In M. D. Steven & J. A. Clark (Eds.), *Applications of Remote Sensing in Agriculture* (pp. 3-18). London, UK: Butterworths.

Anderson, K. & Gaston, K. J. (2013). Lightweight unmanned aerial vehicles will revolutionize spatial ecology. *Frontiers in Ecology and the Environment,* 11(3), pp. 138-146.

Anderson, J. E., Ploure, L. C., Martin, M. E., Braswell, B. H., Smith, M., Dubayah, R. O., Hofton, M. A. & Blair, J. B. (2008). Integrating waveform lidar with hyperspectral imagery for inventory of a northern temperate forest. *Remote Sensing of Environment,* 112, pp. 1856-1870).

Anderson, M. C., Neale, C. M. U., Li, F., Norman, J. M., Kustas, W. P., Jayanthi, H. & Chavez, J. (2004). Upscaling ground observations of vegetation water content, canopy height, and leaf area index during SMEX02 using aircraft and Landsat imagery. *Remote Sensing of Environment,* 92, pp. 447-464.

Arnó, J., Martínez-Casasnovas, J. A., Ribes-Dasi, M. & Rosell, J. R. (2009). Review. Precision Viticulture. Research topics, challenges and opportunities in site-specific vineyard management. *Spanish Journal of Agricultural Research,* 7(4), pp. 779-790.

Bajwa, S. G. & Kulkarni, S. S. (2012). Hyperspectral Data Mining. In P. S. Thenkabail, J. G. Lyon, & A. Huete (Eds.), *Hyperspectral Remote sensing of vegetation* (pp. 93-120). New York: CRC Press.

Bajwa, S. G., Bajcsy, P., Groves, P. & Tian, L. F. (2004). Hyperspectral Image Data Mining for Band Selection in Agricultural Applications. *Transactions of the ASAE,* 47(3), pp. 895-907.

Barber, J. & Baker, N. R. (1985). *Photosynthetic Mechanisms and The Environment, Topics in Photosynthesis,* vol 6. Elsevier: Amsterdam.

Bareth, G., Aasen, H., Bendig, J., Gnyp, M. L., Bolten, A., Jung, A., Michels, R. & Soukkamäki, J. (2014). Spectral Comparison of Low-Weight and UAV-based Hyperspectral Frame Cameras with Portable Spectroradiometer Measurements. In J. Bendig, & G. Bareth (Eds.), *Proceedings of the Workshop on UAV-based Remote Sensing Methods for Monitoring Vegetation* (pp. 1-6). Cologne: Kölner Geographische Arbeiten, 94.

Barnes, E. M., Clarke, T. R., Richards, S. E., Colaizzi, P. D., Haberland, J., Kostrewski, M., Waller, PL, Choi, C., Riley, E., Tompson, T., Lascano, R. J., Li, H. & Moran, M.S. (2000). Coincident detection of crop water stress, nitrogen status and canopy density using ground-based multispectral data. In: Proceedings of the 5th International Conference on Precision Agriculture. Bloomington, MN, USA.

Barrett, E. C. & Curtis, L. F. (1999). *Introduction to Environmental Remote Sensing*. United Kingdom: Stanley Thornes Ltd.

Bellvert, J., Zarco-Tejada, P. J., Girona & Feres, E. (2014). Mapping crop water stress index in a 'Pinot-noir' vineyard: comparing ground measurements with thermal remote sensing imagery from an unmanned aerial vehicle. *Precision Agriculture,* 15, pp. 361-376.

Bendig, J. & Bareth, G. (2014). *Proceedings of the Workshop on UAV-based Remote Sensing Methods for Monitoring Vegetation.* Cologne: Kölner Geographische Arbeiten, 94.

Bendig, J., Bolten, A. & Bareth, G. (2013). UAV-based Imaging for Multi-Temporal, very high Resolution Crop Surface Models to monitor Crop Growth Variability. *Photogrammetrie-Fernerkundung-Geoinformation*, 6, pp. 551-562.

Bento, M. D. F. (2008). Unmanned Aerial Vehicles: An Overview. *InsideGNSS,* pp. 54-61.

Berni, J. A. J., Zarco-Tejada, P. J., Suárez, L., González-Dugo, V. & Fereres, E. (2009). Remote sensing of vegetation from UAV platforms using lightweight multispectral and thermal imaging sensors. *International Archive of Photogrammetry, Remote Sensing and Spatial Information Sciences,* 38(6).

Blackburn, G. A. (1998). Quantifying Chlorophylls and Carotenoids at Leaf and Canopy Scales: An Evaluation of Some Hyperspectral Approaches. *Remote Sensing of Environment,* 66, pp. 273-285.

Van Blyenburgh, P. (2013). *2013-2014 RPAS Yearbook: Remotely Piloted Aircraft Systems: The Global Perspective.* Paris: Blyenburgh & Co.

Boves Harrington, P. de (2006). Statistical validation of classification and calibration models using bootstrapped Latin partitions. *Trends in Analytical Chemistry,* 25(11), pp. 1112-1124.

Bradbury, R. B., Hill, R. A., Mason, D. C., Hinsley, S. A., Wilson, J. D., Balzter, H., Anderson, G. Q. A., Whittingham, M. J., Davenport, I. J. & Bellamy, P. E. (2005). Modelling relationships between birds and vegetation structure using airborne LiDAR data: a review with case studies from agricultural and woodland environments. *Ibis,* 147, pp. 443-452.

Brewer, C. K., Monty, J., Johnson, A., Evans, D. & Fisk, H. (2011). Forest carbon monitoring: A review of selected remote sensing and carbon measurement tools for REDD+ RSAC-10018-RPT1. *Department of Agriculture, Forest Service, Remote Sensing Applications Center.* Salt Lake City, U.S.

Broge, N. H. & Leblanc, E. (2000). Comparing prediction power and stability of broadband and hyperspectral vegetation indices for estimation of green leaf area index and canopy chlorophyll density. *Remote Sensing of Environment,* 76, pp. 156-172.

Calderón, D., Navas-Cortés, J. A., Lucena, C. & Zarco-Tejada, P. J. (2014). High-resolution hyperspectral and thermal imagery acquired from UAV platforms for early detection of Verticillium wilt using fluorescence, temperature and narrow-band indices In J. Bendig, & G. Bareth (Eds.), *Proceedings of the Workshop on UAV-based Remote Sensing Methods for Monitoring Vegetation* (pp. 7-14). Cologne: Kölner Geographische Arbeiten, 94.

Campbell, J. B. & Wynne, R. H. (2002). *Introduction to Remote Sensing.* New York: The Guildford Press.

Caris, M. & Stanko, S. (2014). Millimeter Wave SAR for UAV-based Remote Sensing. In J. Bendig, & G. Bareth (Eds.), *Proceedings of the Workshop on UAV-based Remote Sensing Methods for Monitoring Vegetation* (pp. 15-19). Cologne: Kölner Geographische Arbeiten, 94.

Carlson, T. N. & Ripley, D. A. (1997). On the Relation between NDVI, Fractional Vegetation Cover, and Leaf Area Index. *Remote Sensing of the Environment,* 62, pp. 241-252.

Carrivick, J. L., Smth, M. W., Quincey, D. J. & Carver, S. J. (2013). Developments in budget remote sensing for the geosciences. *Geology Today,* 29(4), pp. 138-143.

Casadesús, J., Y. Kaya, J. Bort, M.M. Nachit, J.L. Araus, S. Amor, G. Ferrazzano, F. Maalouf, M. Maccaferri, V. Martos, H. Ouabbou & D. Villegas (2007). Using vegetation indices derived from conventional digital

cameras as selection criteria for wheat breeding in water-limited environments. *Annals of Applied Biology*, 150, pp. 227-236

Centre for Remote Imaging, Sensing & Processing (CRISP) (2015). http://www.crisp.nus.edu.sg/~research/tutorial/image.htm [retrieved on September 10th 2015].

Chen, P., Haboudane, D., Tremblay, N., Wang, J., Vigneault, P. & Li, B. (2010). New spectral indicator assessing the efficiency of crop nitrogen treatment in corn and wheat. *Remote Sensing of Environment,* 114, pp. 1987-1997.

Chen, Z., Li, S., Ren, J., Gong, P., Zhang, M., Wang, L., Xiao, S. & Jiang, D. (2008). Monitoring and Management of Agriculture with Remote Sensing. In S. Liang (Eds.), *Advances in Land Remote Sensing* (pp. 397-421). USA: Springer

Childs, C. (2004). Interpolating Surfaces in ArcGIS Spatial Analyst. *ArcUser July-September,* pp. 32-35.

Cho, M. A., Skidmore, A., Corsi, F., Wieren, S. E. van & Sobhan, I. (2007). Estimation of green grass/herb biomass from airborne hyperspectral imagery using spectral indices and partial least squares regression. *International Journal of Applied Earth Observation and Geoinformation,* 9, pp. 414-424.

Christenson, B., Schapaugh, W. T. Jr., An, N., Price, K. P. & Fritz, A. K. (2013). Characterizing Changes in Soybean Spectral Response Curves with Breeding Advancements. *Crop Science,* 54, pp. 1585-1597.

Chuvieco, E. (2011). *Fundamentals of Satellite Remote Sensing*. New York: CRC Press

Ciganda, V., Gitelson, A. & Schepers, J. (2009). Non-destructive determination of maize leaf and canopy chlorophyll content. *Journal of Plant Physiology,* 166, pp. 157-167.

Clevers, J. G. P. W. & Kooistra, L. (2012). Using Hyperspectral Remote Sensing Data for Retrieving Canopy Chlorophyll and Nitrogen Content. *IEEE Journal of Selected Topics in Applied Earth Observations and Remote Sensing,* 5(2), pp. 574-583.

Colomina, I. & Molina, P. (2014). Unmanned aerial systems for photogrammetry and remote sensing: A review. *ISPRS Journal of Photogrammetry and Remote Sensing,* 92, pp. 79-97.

Congalton, R. G., Fenstermaker, L., McGwire, K. C. & Tinney, L. (1991). Remote sensing and geographic information systems: Error sources and research issues. *Photogrammetric Engineering and Remote Sensing,* 57(6), pp. 677-687.

Cornelissen, J. H. C., Lavorel, S., Garnier, E., Diaz, S., Buchmann, N., Gurvich, D. E., Reich, P. B., Steege, H. ter, Morgan, H. D., Heijden, M. G. A. van der, Pausas, J. G. & Poorter, H. (2003). A handbook of protocols for standardized and easy measurement of plant functional traits worldwide. *Australian Journal of Botany,* 51, pp. 335-380.

Cracknell, A. P. & Hayes, L. (2007). *Introduction to Remote Sensing*. Boca Raton: CRC Press.

Cure, J. D. & Acock, B. (1986). Crop Responses to Carbon Dioxide Doubling: A Literature Survey. *Agricultural and Forest Meteorology,* 38, pp. 127-145.

Daughtry, C. S. T., Walthall, C. L., Kim, M. S., Brown de Colstoun, E. & McMurtrey, J. E. (2000). Estimating Corn Leaf Chlorophyll Concentration from Leaf and Canopy Reflectance. *Remote Sensing of Environment,*

Delécolle, R., Maas, S. J., Guérif, M. & Baret, F. (1992). Remote sensing and crop production models: present trends. *ISPRS Journal of Photogrammetry and Remote Sensing,* 47, pp. 145-161.

Murphy, D. J. & Murray, B. G. (2003). *Encyclopedia of Aplied Plant Sciences, Three-Volume Set.* Academic Press.

Dash, J. & Curran, P. J. (2007). Evaluation of the MERIS terrestrial chlorophyll index (MTCI). *Advances in Space Research,* 39, pp. 100-104.

Datt, B. (1999). Remote Sensing of Chlorophyll a, Chlorophyll b, Chlorophyll a+b, and Total Carotenoid Content in Eucalyptus Leaves. *Remote Sensing of Environment,* 66(2), pp. 111-121.

Dobermann, A., Blackmore, S., Cook, S. E. & Adamchuk, V. I. (2004). Precision Farming: Challenges and Future Directions. *Proceedings of the 4th International Crop Science Congress*. Brisbana, Australia.

Dixon, G. R. (2007). *Vegetable Brassicas and Related Crucifers*. Oxfordshire, UK: CABI

Drauschke, M., Bartelsen, J. & Reidelstürz, P. (2014). Towards UAV-based Forest Monitoring. In J. Bendig, & G. Bareth (Eds.), Proceedings of the Workshop on UAV-based Remote Sensing Methods for Monitoring Vegetation (pp. 21-32). Cologne: Kölner Geographische Arbeiten, 94.

Ehlert, D., Horn, H. & Adamek, R. (2008). Measuring crop biomass density by laser triangulation. *Computers and Electronics in Agriculture,* 61, pp. 117-125.

Elachi, C. & Zyl, J. van (2007). *Introduction To The Physics and Techniques of Remote Sensing*. New York: John Wiley & Sons, Inc.

Eling, C., Klingbeil, L. & Kuhlmann (2014). A Precise Direct Georeferencing Systems for UAVs. In J. Bendig, & G. Bareth (Eds.), *Proceedings of the Workshop on UAV-based Remote Sensing Methods for Monitoring Vegetation* (pp. 33-41). Cologne: Kölner Geographische Arbeiten, 94.

Esbensen, K. H., Guyot, D., Westad, F. & Houmoller, L. P. (2010). Multivariate Data Analaysis – in Practice: An Introduction to Multivariate Data Analysis and Experimental Design. *Multivariate Data Analysis.*

Esri (2015). Gis Dictionary > nearest neighbor resampling. http://support.esri.com/en/knowledgebase/GISDictionary/term/nearest%20neighbor%20resampling [retrieved on September 30th 2015].

Everaerts, J. (2009). NEWPLATFORMS – Unconventional Platforms (Unmanned Aircraft Systems) for Remote Sensing. *Technical Report 56*. European Spatial Data Research (EuroSDR).

Everaerts, J. (2008). The use of Unmanned Aerial Vehicles (UAVs) for Remote Sensing and Mapping. *The International Archives of the Photogrammetry, Remote Sensing and Spatial Information Sciences,* 37, pp. 1187-1192.

Feilhauer, H., Asner, G. P., Martin, R. E. & Schmidtlein, S. (2010). Brightness-normalized Partial Least Squares Regression for hyperspectral data. *Journal of Quantitative Spectroscopy & Radiative Transfer,* 111, pp. 1947-1957.

Fernandez, M. G. S., Becraft, P. W., Yin, Y. & Lübberstedt, T. (2009). From dwarves to giants? Plant height manipulation for biomass yield. *Trends in Plant Science,* 14(8), pp. 454-461.

Flemming, K. L., Westfall, D. G., Wiens, D. W. & Brodahl, M. C. (2000). Evaluating Farmer Defined Management Zone Maps for Variable Rate Fertilizer Application. *Precision Agriculture,* 2, pp. 201-215.

Fiorani, F. & Schurr, U. (2013). Future Scenarios for Plant Phenotyping. *Annual Review of Plant Biology*, 64, pp. 267-291.

Foody, G. M., Warner, T. A. & Nellis, M. D. (2009). A Look to the Future. In T. A. Warner, M. D. Nellis & G. M. Foody (Eds.), *The SAGE Handbook of Remote Sensing* (pp. 475-481). London, UK: SAGE Publications Ltd.

Franklin, S. E. (2001). *Remote Sensing for Sustainable Forest Management*. New York: CRC Press.

Freeman, K. W., Girma, K., Arnall, D. B., Mullen, R. W., Martin, K. L., Teal, R. K., & Raun, W. R. (2007). By-plant prediction of corn forage biomass and nitrogen uptake at various growth stages using remote sensing and plant height. *Agronomy Journal*, 99(2), pp. 530-536.

Gan, S. & Amasino, R. M. (1997). Making Sense of Senescence. *Plant Physiology,* 113, pp. 313-319.

Gitelson, A. A. (2012). Nondestructive Estimation of Foliar Pigment (Chlorophylls, Carotenoids, and Anthocyanin) Contents: Evaluating a Semianalytical Three-Band Model. In P. S. Thenkabail, J. G. Lyon, & A. Huete (Eds.), *Hyperspectral Remote sensing of vegetation* (pp. 141-166). New York: CRC Press.

Gitelson, A. A., Viña, A., Verma, S. B., Rundquist, D. C., Arkebauer, T. J., Keydan, G., Leavitt, B., Ciganda, V., Burba, G. G. & Suyker, A. E. (2006). Relationship between gross primary production and chlorophyll content in crops: Implications for the synoptic monitoring of vegetation productivity. *Journal of Geophysical Research,* 111, pp. 1-13.

Gitelson, A. A., Viña, A., Ciganda, V., Rundquist, D. C. & Arkebauer, T. J. (2005). Remote estimation of canopy chlorophyll content in crops. *Geophyiscal Research Letters,* 32(8), pp. 1-4.

Gitelson, A. A., Viña, A., Arkebauer, T. J., Rundquist, D. C., Keydan, G. & Leavitt, B. (2003a). Remote estimation of leaf area index and green leaf biomass in maize canopies. *Geographysical Research Letters,* 30(5), pp. 52-55.

Glenn, E. P., Huete, A. R., Nagler, P. L. & Nelson, S. G. (2008). Relationship Between Remote-sensed Vegetation Indices, Canopy Attributes and Plant Physiological Processes: What Vegetation Indices Can and Cannot Tell Us About the Landscape. *Sensors,* 8(4), pp. 2136-2160.

Gnyp, M. L., Miao, Y., Yuan, F., Yu, K., Yao, Y., Huang, S. & Bareth, G. (2014a). Derivative analysis to improve rice biomass estimation at early growth stages. In JBendig, & G. Bareth (Eds.), Proceedings of the Workshop on UAV-based Remote Sensing Methods for Monitoring Vegetation (pp. 43-50). Cologne: Kölner Geographische Arbeiten, 94.

Gnyp, M. L., Bareth, G., Li, F., Lenz-Wiedemann, V. I. S., Koppe, W., Miao, Y., Hennig, S. D., Jia, Liangliang, Laudien, R., Chen, X. & Zhang, F. (2014b). Development and implementation of a multiscale biomass model using hyperspectral vegetation indices for winter wheat in the North China Plain. *International Journal of Applied Earth Observation and Geoinformation,* 33, pp. 232-242.

Gómez-Chova, L., Alonso, L., Guanter, L., Camps-Valls, G., Calpe, J. & Moreno, J. (2008). Correction of systematic spatial noise in push-broom hyperspectral sensors: application to CHRIS/PROBA images. *Applied Optics,* 47, pp. F46-F60.

Gong, P., Pu, R. & Miller, J. R. (1995). Confierous Forest Leaf Area Index Estimation along the Oregon Transect Using Compact Airborne pictographic Imager Data. *Photogrammetric Engineering & Remote Sensing,* 61(9), pp. 1107-1117.

Gopal, R., Mishra, K. B., Zeeshan, M., Prasad, S. M. & Joshi, M. M. (2002). Laser-induced chlorophyll fluroesence spectra of mung plants growing under nickel stress. *Current Science,* 83(7), pp. 880-884.

Gopi, S., Sathikumar, R. & Madhu, N. (2008). *Advanced Surveying: Total Station, GIS and Remote Sensing*. India: Dorling Kindersley.

Goswami, A., Gamon, J. A., Vargas, S. & Tweedie C. E. (2015). Relationship of NDVI, biomass, and Leaf Area Index (LAI) for six key plant species in Barrow, Alaska. *PeerJ PrePrints 3:e1127* https://dx.doi.org/10.7287/peerj.preprints.913v1

Govender, M., Chetty, K. & Bulcock, H. (2007). A review of hyperspectral remote sensing and its application in vegetation and water resource studies. *Water SA,* 33(2), pp. 145-152.

Gude, J. A., Mitchell, M. S., Ausband, D. E., Sime, C. A. & Bangs, E. E. (2009). Internal validation of predictive logistic regression models for decision-making in wildlife management. *Wildlife Biology,* 15, pp. 352-369.

Guyot, G. (2013). Optical Properties of Vegetation Canopies. In M. D. Steven & J. A. Clark (Eds.), *Applications of Remote Sensing in Agriculture* (pp. 19-44). London, UK: Butterworths.

Haaland, D. M. & Thomas, E. V. (1988). Partial Least-Squares Methods for Spectral Analyses. 1. Relation to Other Quantitative Calibration Methods and the Extraction of Qualitative Information. *Analytical Chemistry,* 60(11), pp. 1193-1202.

Haboudane, D., Miller, J. R., Tremblay, N., Zarco-Tejada, P. J. & Dextraze, L. (2002). Integrated narrow-band vegetation índices for prediction of crop chlorophyll content for application to precision agriculture. *Remote Sensing of Environment,* 81, pp. 416-426.

Hall, A., Lamb, D. W., Holzapfel, B. & Louis, J. (2002) Optical remote sensing applications in viticulture – a review. *Australian Journal of Grape and Wine Research,* 8(1), pp. 36-47.

Hansen, P. M. & Schjoerring, J. K. (2003). Reflectance measurement of canopy biomass and nitrogen status in wheat crops using normalized difference vegetation indices and partial least squares regression. *Remote Sensing of Environment,* 86, pp. 542-553.

Harper, L. A., Sharpe, R. R., Langdale, G. W. & Giddens, J. E. (1960). Nitrogen Cycling in a Wheat Crop: Soil, Plant, and Aerial Nitrogen Transport. *Agronomy Journal,* 79(6), pp. 965-973.

Heiskanen, J. (2006). Estimating aboveground tree biomass and leaf area index in a mountain birch forest using ASTER satellite data. *International Journal of Remote Sensing,* 6(20), pp. 1135-1158.

Abdi, H. (2010). Partial least squares regression and projection on latent structure regression (PLS Regression). *Wiley Interdisciplinary Reviews: Computational Statistics 2.1,* pp. 97-106.

Herwitz, S. R., Johnson, L. F., Dunagan, S. E., Higgins, R. G., Sullivan, D. V., Zheng, J., Lobitz, B. M., Leung, J. G., Gallmeyer, B. A., Aoyagi, M., Slye, R. E. & Brass, J. A. (2004). Imaging from an unmanned aerial vehicle: agricultural surveillance and decision support. *Computers and Electronics in Agriculture,* 44, pp. 49-61.

Hilker, T., Coops, N. C., Wulde, M. A., Black, T. A. & Guy, R. D. (2008). The use of remote sensing in light use efficiency based models of gross primary production: A review of current status and future requirements. *Science of the Total Environment,* 404, pp. 411-423.

Hirano, A., Madden, M. & Welch, R. (2003). Hyperspectral Image Data for Mapping Wetland Vegetation. *Wetlands,* 23(2), pp. 436-448.

Homolová, L., Malenovský, Z., Clevers, J. G. P. W., García-Santos, G. & Schaepman, M. E. (2013). *Ecological Complexity,* 15, pp. 1-16.

Honkavaara, E., Saari, H., Kaivosoja, J., Pölönen, I., Hakala, T., Litkey, P., Mäkynen, J. & Pesonen, L. (2013). Processing and Assessment of Spectrometric, Stereoscopic Imagery Collected Using a Lightweight UAV Spectral Camera for Precision Agriculture. *Remote Sensing,* 5(10), pp. 5006-5039.

Houborg, R., Anderson, M. & Daughtry, C. (2009). Utility of an image-based canopy reflectance modeling tool for remote sensing of LAI and leaf chlorophyll content at the field scale. *Remote Sensing of Environment,* 113, pp. 259-274.

Hruska, R., Mitchell, J., Anderson, M. & Glenn, N. F. (2012). Radiometric and Geometric Analysis of Hyperspectral Imagery Acquired from an Unmanned Aerial Vehicle. *Remote Sensing,* 4(9), pp. 2736-2752.

Huang, Y., Thomson, S. J., Hoffmann, W. C., Lan, Y. & Fritz, B. K. (2013). Development and prospect of unmanned aerial vehicle technologies for agricultural production management. *International Journal of Agricultural and Biological Engineering*, 6(3), pp. 1-10.

Hunt, E. R. Jr., Doraiswamy, P. C., McMurtrey, J. E., Daughtry, C. S. T. & Perry, E. M. (2013). A visible band index for remote sensing leaf chlorophyll content at the canopy scale. *International Journal of Applied Earth Observation and Geoinformation,* 21, pp. 103-112.

Hunt, E. A. Jr., Hively, W. D., Fujikawa, S. J., Linden, D. S., Daughtry, C. S. T. & McCarty, G. W. (2010). Acquisition of NIR-Green-Blue Digital Photographs from Unmanned Aircraft for Crop Monitoring. *Remote Sensing,* 2, pp. 290-305.

Hunt, E. R. Jr., Cavigelli, M., Daughtry, C. S. T., McMurtrey, J. & Walthall, C. (2005). Evaluation of Digital Photography from Model Aircraft for Remote Sensing of Crop Biomass and Nitrogen Status. *Precision Agriculture,* 6, pp. 359-378.

Huete, A. R. & Jackson, R. D. (1987). Suitability of Spectral Indices for Evaluating Vegetation Characteristics on Arid Rangelands. *Remote Sensing of Environment,* 23, pp. 213-232.

Inoue, Y., Sakaiya, E., Zhu, Y. & Takahasdi, W. (2012). Diagnostic mapping of canopy nitrogen content in rice based on hyperspectral measurements. *Remote Sensing of Environment,* 126, pp. 210-221.

Michaelson, J., Schimel, D. S., Friedl, M. A., Davis, F. W. & Dubayah, R. C. (1994). Regression Tree Analysis of satellite and terrain data to guide vegetation sampling and surveys. *Journal of Vegetation Science,* 5, pp. 673/686.

Jones, H. G. & Vaughan, R. A. (2010). *Remote Sensing of Vegetation: Principles, Techniques, and Applications.* UK: Oxford University Press.

Jung, A., Michels, R. & Graser, R. (2013a). Non-scanning Hyperspectral Imaging and Spectral Video Technique for Object Documentation. In: Proposer to the COST Action TD1201 Colour and Space in Cultural Heritage (COSCH): Working Group Meetings. Mainz, Germany.

Jung, A., Michels, R. & Graser, R. (2013b). Non-scanning Hyperspectral Imaging Camera for UAS Platforms (Nichtscannende hyperspektrale Kamera für UAS Plattformen). *In: Proceedings of 19th CBA Workshop and 2nd UAS Workshop.* Berlin, Germany.

Kerekes, J. P. & Schott, J. R. (2007). Hyperspectral Imaging Systems. In Chang, C. I. (Eds.), *Hyperspectral Remote sensing of vegetation* (pp. 19-46). New York: John Wiley & Sons, Inc.

Khosla, R., Fleming, K., Delgado, J. A., Shaver, T. M. & Westfall, D. G. (2002). Use of site-specific management zones to improve nitrogen management for precision agriculture. *Journal of Soil and Water Conservation,* 57(6), pp. 513-518.

Knipling, E. B. (1970). Physical and physiological basis for the reflectance of visible and near-infrared radiation from vegetation. *Remote Sensing of Environment,* 1(3), pp. 155-159.

Kooistra, L., Suomalainen, J., Iqbal, S., Franke, J., Wenting, Ph., Bartholomeus, H., Mücher, S. & Becker (2014). Crop Monitoring Using a Light-Weight Hyperspectral Mapping System for Unmanned Aerial Vehicles: First Results for the 2013 Season. In J. Bendig, & G. Bareth (Eds.), Proceedings of the Workshop on UAV-based Remote Sensing Methods for Monitoring Vegetation (pp. 51-58). Cologne: Kölner Geographische Arbeiten, 94.

Kumar, S. (2005). Basics of Remote Sensing and GIS. *Firewall Media.* India: New Delhi.

Lamb, D. W., Steyn-Ross, M., Schaare, P., Hanna, M. M., Silvester, W. & Steyn-Ross, A. (2002). Estimating leaf nitrogen concentration in ryegrass (Lolium spp.) pasture using the chlorophyll red-edge: Theoretical modelling and experimental observations. *International Journal of Remote Sensing,* 23(18), pp. 3619-3648.

Lamb, D. W. & Brown, R. B. (2001). PA-Precision Agriculture: Remote-Sensing and Mapping of Weeds in Crops. *Journal of Agricultural Engineering Research*, 78(2), pp. 117-125.

Lelong, C. C. D., Burger, P., Jubelin, G., Roux, B., Labbé, S. & Baret, F. (2008). Assessment of Unmanned Aerial Vehicles Imagery for Quantitative Monitoring of Wheat Crop in Small Plots. *Sensors,* 8, pp. 357-3585.

Li, F., Miao, Y. & Chen, X. (2014). Using Area-Based Spectral Indices to Estimate Aerial N Uptake of Maize. In J. Bendig, & G. Bareth (Eds.), *Proceedings of the Workshop on UAV-based Remote Sensing Methods for Monitoring Vegetation* (pp. 59-65). Cologne: Kölner Geographische Arbeiten, 94.

Li, L., Cheng, Y., Ustin, S., Hu, X., & Riaño (2008). Retrieval of vegetation equivalent water thickness from reflectance using genetic algorithm (GA)-partial least squares (PLS) regression. *Advances in Space Research,* 41, pp. 1755-1763.

Liang, .S, Li, X. & Wang, J. (2012). *Advanced Remote Sensing: Terrestrial Information Extraction and Applications*. USA: Academic Press.

Liang, S. (2008). Recent Advances in Land Remote Sensing: An Overview: In S. Liang (Eds.), *Advances in Land Remote Sensing* (pp. 1-6). USA: Springer

Lichtenthaler, H. K., Gitelson, A. & Lang, M. (1996). Non-Destructuive Determination of Chlorophyll Content of Leaves of a Green and an Aurea Mutant of Tobacco by Reflectance Measurements. *Journal of Plant Psysiology,* 148, pp. 483-493.

Lieth, H. (1963). The Role of Vegetation in the Carbon Dioxide Content of the Atmosphere. *Journal of Geophysical Research,* 68(13), pp. 3887-3898.

Lillesand, T., Kiefer, R. W. & Chipman, J. (2014). *Remote Sensing and Image Interpretation*. New York John Wiley & Sons, Inc.

Lisiewska, Z., Kmiecik, W. & Korus, A. (2006). Content of vitamin C, carotenoids, chlorophylls and polyphenols in Green parts of dill (*Anethum graveolens* L.) depending on plant height. *Journal of Food Composition and Analysis,* 19, 134-140.

Liu, Z., Huang, J., Shi, J., Tao, R., Zhou, W. & Zhang, L. (2007). Characterizing and estimating rice Brown spot disease severity using stepwise regression, principal component regression and partial least-square regression. *Journal of Zhejiang University Science B,* 8(10), PP. 738-744.

Lobell, D. B., Asner, G. P., Otiz-Monasterio, J. I. & Benning, T. L. (2003). Remote sensing of regional crop prdouction the Yaqui Vallye, Mexico: estimates and uncertainties. *Agriculture, Ecosystems and Environment,* 94, pp. 205-220.

López-Granados, F., Jurado-Expósito, M., Peña-Barragán & García-Torres, L. (2005). Using geostatistical and remote sensing approaches for mapping soil properties. *European Journal of Agronomy*, 23, pp. 279-289.

Maas, H. G. (2008). Close range photogrammetry. In: Li, Z., Chen, J. & Baltsavias, E. (eds.), *Advances in Photogrammetry, Remote Sensing and Spatial Information Sciencies* (pp. 63-72). Londen: Taylor & Francis

Machado, S., Bynum Jr., E. D., Archer, T. L., Lascano, R. J., Wilson, L. T., Bordovsky, J., Segarra, E., Bronson, K., Nesmith, D. M. & Wu, X. (2002). Spatial and temporal variability of corn growth and grain yield: Implications for site-specific farming. *Crop Science,* 42, pp. 1564-1576.

Magnussen, S. & Reed, D. (2004). Modeling for estimation and monitoring. *National Forest Assessment.*

Malhi, S. S., Johnston, A. M., Schoenau, J. J., Wang, Z. L. & Vera, C. L. (2006). Seasonal biomass accumulation and nutrient uptake of wheat, barley and oat on a Black Chernozem Soil in Saskatchewan. *Canadian Journal of Plant Science,* 86(4), pp. 1005-1014.

Martin, S., Bange, J. & Beyrich, F. (2011). Meteorological profiling of the lower troposphere using the research UAV "M2AV Carolo". *Atmospheric Measurement Techniques,* 4, pp. 705-716.

McBratney, A., Whelan, B. & Ancev, T. (2005). Future Directions of Precision Agriculture. *Precision Agriculture,* 6, pp. 7-23.

Maindonald, J. & Braun, W. J. (2010). *Data Analysis and Graphics Using R: An Example-Based Approach*. UK: Cambridge University Press.

Mevik, B. & Wehrens, R. (2007). The pls Package: Principal Component and Partial Least Squares Regression in R. *Journal of Statistical Software,* 18(2), pp. 1-24.

Moran, M. S., Inoue, Y. & Barnes, E. M. (1997). Opportunities and Limitations for Image-Based Remote Sensing in Precision Crop Management. *Remote Sensing of Environment,* 61, pp. 319-346.

Mulder, V. L., Bruin, S. De, Schaepman, M. E. & Mayr, T. R. (2011). The use of remote sensing in soil and terrain mapping – A review. *Geoderma,* 162, pp. 1-19.

Mulla, D. J. (2013). Twenty five years of remote sensing in precision agriculture: Key advances and remaining knowledge gaps. *Biosystems Engineering,* 114, pp. 358-371.

Müller, K., Böttcher, U., Meyer-Schatz, F. & Kage, H. (2008). Analysis of vegetation indices derived from hyperspectral reflection measurements for estimating crop canopy parameters of oilseed rape (Brassica napus L.). *Biosystems Engineering,* 101, pp. 172-182.

Mutanga, O. & Skidmore, A. K. (2007). Red edge shift and biochemical content in grass canopies. *ISPRS Journal of Photogrammetry & Remote Sensing,* 62, pp. 34-42.

Mutanga, O. & Skidmore, A. K. (2004). Narrow band vegetation indices overcome the saturation problem in biomass estimation. *International Journal of Remote Sensing,* 25(19), pp. 3999-4014.

Najib, N. & Hamel, T. (2007). A UAV for bridge inspection: Visual servoing control law with orientation limits. *Automation in Construction,* 17, pp. 3-10.

Namayanga, L. N. (2002). Estimating Terrestrial Carbon Sequestered in Aboveground Woody Biomass from Remotely Sensed Data. *International Institute for Geo-information Science and Earth Observation, the Netherlands.*

NASA (2016). Reflected near-infrared waves. http://missionscience.nasa.gov/ems/08_nearinfraredwaves.html [cited on January 23rd 2016].

National Research Council (NRC): Committee on Remote Sensing for Agricultural Purposes (1970). *Remote Sensing: With Special References to Agriculture and Forestry.* Washington: National Academy of Sciences.

Natural Resources Canada (NRCan) (2013). Radiometric Resolution. http://www.nrcan.gc.ca/earth-sciences/geomatics/satellite-imagery-air-photos/satellite-imagery-products/educational-resources/9379.

Nebiker, S., Annen, A., Scherrer, M. & Oesch, D. (2008). A Light-Weight Multispectral sensor for Micro UAV – Opportunities for Very High resolution Airborne Remote Sensing. *The International Archives of the Photogrammetry, Remote Sensing and Spatial Information Sciences,* 37, pp. 1193-1199.

Neeland, H. & Kraft, M. (2014). Construction and Measurement Technology of the ThünoCopter for Contactless Inspection of Crop Canopies: First measurements with a Low-Cost Image Analyzing System. In J. Bendig, & G. Bareth (Eds.), *Proceedings of the Workshop on UAV-based Remote Sensing Methods for Monitoring Vegetation* (pp. 67-74). Cologne: Kölner Geographische Arbeiten, 94.

Nellis, M. D., Price, K. P. & Rundquist, D. R. (2009), Remote Sensing of Cropland Agriculture. In T. A. Warner, M. D. Nellis & G. M. Foody (Eds.), *The SAGE Handbook of Remote Sensing* (pp. 368-380). London, UK: SAGE Publications Ltd.

Netto, A. T., Campostrini, E., Gonçalves, O., J. de & Bressan-Smith, R. E. (2005). Photosynthetic pigments, nitrogen, chlorophyll *a* fluorescence and SPAD-502 readings in coffee leaves. *Scientia Horticulturae,* 104, pp. 199-209.

Niethammer, U., James, M. R., Rothmund, S., Travelletti, J. & Joswig, M. (2012). UAV-based remote sensing of the Super-Sauze landslide: Evaluation and results. *Engineering Geology,* 128, pp. 2-11.

Niklas, K. J. & Enquist, B. J. (2001). Invariant scaling relationships for interspecific plant biomass production rates and body size. *Proceedings of the National Academy of Sciences of the United States of America,* 98(5), pp. 2922-2927.

Nguyen, H. T. & Lee, B. (2006). Assessment of rice leaf growth and nitrogen status by hyperspectral canopy reflectance and partial least square regression. *European Journal of Agronomy*, 24(4), pp. 349-356.

Nuvalur, K. (2007). *Multispectral Image Analysis Using the Objected-Oriented Paradigm.* New York: CRC Press.

Odido, D. & Madara, D. (2013). Emerging Technologies: Use of Unmanned Aerial Systems in the Realisation of Vision 2030 Goals in the Counties. *International Journal of Applied Science and Technology,* 3(8), pp. 107-127.

Ortenberg, F. (2012). Hyperspectral Sensor Characteristics: Airborne, Spaceborne, Hand-Held, and Truck-Mounted; Integration of Hyperspectral Data with LIDAR. In P. S. Thenkabail, J. G. Lyon, & A. Huete (Eds.), *Hyperspectral Remote sensing of vegetation* (pp. 39-68). New York: CRC Press.

Osborne, S. L., Schepers, J. S., Francis. D. D. & Schlemmer, M. R. (2002). Detection of Phosphorus and Nitrogen Deficiencies in Corn Using Spectral Radiance Measurements. *Agronomy Journal, i94, pp. 1215-1221.*

Peinetti, H. R., Menezes, R. S. C. & Coughenour, M. B. (2001). Changes induced by elk browsing in the aboveground biomass production and distribution of willow (Salix monticola Bebb): their relationships with plant water, carbon, and nitrogen dynamics. *Oecologia,* 127, pp. 334-342.

Peng, Y., Gitelson, A. A., Keydan, G., Rundquist, D. C. & Moses, W. (2011). Remote estimation of gross primary production in maize and support for a new paradigm based on total crop chlorophyll content. *Remote Sensing of Environment,* 115, pp. 978-989.

Peter, K. D., d'Oleire-Oltmanns, S., Ries, J. B., Marzolff, I. & Hssaine, A. A. (2014). Soil erosion in gully catchments affected by land-levelling measures in the Souss Basis, Morocco, analysed by rainfall simulation and UAV remote sensing data. *Catena,* 113, pp. 24-40.

Pinter, P. J. Jr., Hathfield, J. L., Schepers, J. S., Barnes, E. M., Moran, M. S., Daughtry, C. S. T. & Upchurch, D. R. (2003). Remote Sensing for Crop Management. *Photogrammetric Engineering & Remote Sensing,* 69(6), pp. 647-664.

Pohl, C. & Genderen, J. L. van (1998). Multisensor image fusion in remote sensing: concept, methods and applications. *International Journal of Remote Sensing,* 19(5), pp. 823-854.

Prasad, R., Dixit, A., Malhotra, P. K. & Gupta, V. K. (2007). Geoinformatics in Precision Farming: An Overview. In A. K. Singh (Eds.), *Geoinformatics Applications in Agriculture* (pp. 39-78). India: New India Publishing Agency.

Primicerio, J., Filippo Di Gennaro, S., Fiorillo, E., Genesio, L., Lugato, E., Matese, A. & Vaccari, F. P. (2012). A flexible unmanned aerial vehicle for precision agriculture. *Precision Agriculture,* 13, pp. 517-523.

Pudelko, R., Stuczynski, T. & Borzecka-Walker, M. (2012). The suitability of an unmanned aerial vehicle (UAV) for the evaluation of experimental fields and crops. *Agriculture,* 99(4), pp. 431-436.

Qi, J., Inoue, Y. & Wiangwang, N. (2012). Hyperspectral Remote Sensing in Global Change Studies. In P. S. Thenkabail, J. G. Lyon, & A. Huete (Eds.), *Hyperspectral Remote sensing of vegetation* (pp. 70-89). New York: CRC Press.

Quattrochi, D. A. & Goodchild, M. F. (1997). *Scale in Remote Sensing and GIS*. New York: CRC Press

Rango, A., Laliberte, A., Herrick, J. E., Winters, C., Havstad, K., Steele, C. & Browning, D. (2009). Unmanned aerial vehicle-based remote sensing for rangeland assessment, monitoring, and management. *Journal of Applied Remote Sensing,* 3(1), pp. 1-15.

Raper, T. B., Varco, J. J. & Hubbard, K. J. (2013). Canopy-Based Normalized Difference Vegetation Index Sensors for Monitoring Cotton Nitrogen Status. *Agronomic Journal,* 105, pp. 1345-1354.

Rascher, U., Blossfeld, S., Fiorani, F., Jahnke, S., Jansen, M., Kuhn, A. J., Matsubara, S., Märtin, L. L. A., Merchant, A., Metzner, R., Müller-Linow, M., Nagel, K. A., Pieruschka, R., Pinto, F., Schreiber, C. M., Temperton, V. M., Thorpe, M. R., Dusschoten, D. van, Volkenburgh, E. van, Windt, C. W. & Schurr, U. (2011). Non-invasive approaches for phenotyping of enhanced performance traits in bean. *Functional Plant Biology,* 38, pp. 968-983.

Rasmussen, J., Nielsen, J., Garcia-Ruiz, F., Christensen, S. & Streibig, J. C. (2013). Potential uses of small unmanned aircraft systems (UAS) in weed research. *European Weed Research Society,* 53, pp. 242-248.

Reddy, T. A. (2011). *Applied Data Analysis and Modeling for Energy Engineers and Scientists.* New York: Springer

Rees, W. G. (2013). *Physical Principles of Remote Sensing*. UK: Cambridge University Press

Retzlaff, R., Molitor, D., Behr, M., Wantzenrieder, T., Hoffman, L., Evers, D. & Udelhoven (2014). Assessment of grapevine leaf and canopy vigour properties by quadrocopter-carried VIS/NIR multispectral camera. In J.

Bendig, & G. Bareth (Eds.), *Proceedings of the Workshop on UAV-based Remote Sensing Methods for Monitoring Vegetation* (pp. 75-82). Cologne: Kölner Geographische Arbeiten, 94.

Rocchini, D. & Rita, A. D. (2005). Relief effects on aerial photos geometric correction. *Applied Geography,* 25, pp. 159-168.

Roujean, J. & Breon, F. (1994). Estimating PAR Absorbed by Vegetation from Bidirectional Reflectance Measurements. *Remote Sensing of Environment,* 51, pp. 375-384.

Sahu, K. C. (2008). *Textbook of Remote Sensing and Geographical Information Systems*. India: Atlantic Publishers & Distributors Ltd.

Sawatsky, M. L., Clyde, M. & Meek, F. (2015). Partial Least Squares Regression in the Social Sciences. *The Quantitative Methods for Psychology*, 11(2), pp. 52-61.

Schenk, H. J., Callaway, R. M. & Mahall, B. E. (1999). Spatial Root Segregation: Are Plants Territorial? *Advances in Ecological Research,* 28, pp. 145-180.

Schimel, D. S. (1995). Terrestrial Biogeochemical Cycles: Global Estimates with Remote Sensing. *Remote Sensing of Environment,* 51, pp. 49-56.

Schowengerdt, R. A. (2012). *Remote Sensing: Models and Methods for Image Processing.* California, USA: Academic Press.

Scotford, I. M. & Miller, P. C. H. (2004). Combination of Spectral Reflectance and Ultrasonic Sensing to monitor the Growth of Winter Wheat. *Biosystems Engineering,* 87(1), pp. 27-38.

Seelan, S. K., Laguette, S., Casady, G. M. & Seielstad, G. A. (2003). Remote sensing applications for precision agriculture: A learning community approach. *Remote Sensing of Environment,* 88, pp. 157-169.

Sellers, P. J., Berry, J. A., Collatz, G. J., Field, C. B. & Hall, F. G. (1992). Canopy Reflectance, Photosynthesis and Transpiration. III. A Reanalysis Using Improved leaf Models and a New Canopy Integration Scheme. *Remote Sensing of Environment,* 42, pp. 187-216.

Sellers, P. (1985). Canopy reflectance, photosynthesis and transpiration. *International Journal of Remote Sensing,* 6, pp. 1335-1372.

Selige, T., Bohner, J. & Schmidhalter, U. (2006). High resolution topsoil mapping using hyperspectral image and field data in multivariate regression modeling procedures. *Geoderma,* 136, pp. 235-244.

Senay, G. B., Lyon, J. G., Ward, A. D. & Nokes, S. E. (2000). Using High Spatila Resolution Multispectral Data to Classify Corn and Soybean Crops. *Photogrammetric Engineering & Remote Sensing,* 66(3), pp. 319-327.

SEOS (2015). Supplement 1.2: Remote Sensing Instruments Used in Marine Pollution Monitoring. http://lms.seos-project.eu/learning_modules/marinepollution/marinepollution-c01-s02-p01.html [retrieved on October 21st 2015].

Shaw, G. A. & Burke, H. K. (2003). Spectral Imaging for Remote Sensing. *Lincoln Laboratory Journal,* 14(1), pp. 3-28.

Shippert, P. (2004). Why use hyperspectral imagery? *Photogrammetric engineering and remote sensing,* 70(4), pp. 377-396.

Sims, D. A. & Gamon, J. A. (2002). Relationships between leaf pigment content and spectral reflectance across a wide range of species, leaf structures and developmental stages. *Remote Sensing of Environment,* 81, pp. 337-354.

Smith, M., Ollinger, S. V., Martin, M. E., Aber, J. D., Hallett, R. A. & Goodale, C. L. (2002). Direct Estimation of Aboveground Forest Productivity through Hyperspectral Remote Sensing of Canopy Nitrogen. *Ecological Applications,* 12(5), pp. 1286-1302.

Souza, A. A., Galvão, L. S. & Santos, J. R. (2010). Relationships between Hyperion-derived vegetation indices, biophysical parameters, and elevation data in a Brazilian savannah environment. *Remote Sensing Letters,* 1(1), pp. 55-64.

Stehr, N. J. (2015). Drones: The Newest Technology for Precision Agriculture. *Natural Sciences Education,* 44,(1), pp. 89-91.

Steyerberg, E. W. & Harrell, F. E. (n.a.). *Validation of predictive regression models*. Erasmus University Medical Center Rotterdam.

St-Onge, B. A. & Achaichia, N. (2001). Measuring Forest Canopy Height Using a Combination of Lidar AND Aerial Photography Data. *Proceedings of the Workshop on land surface mapping and characterization using laser altimetry,* Annapolis, Maryland.

Stuart, M. & Friedland, C. J. (2011). A survey of Unmanned Aerial Vehicle (UAV) usage for imagery collection in Disaster Research and Management. In *Proceedings of the 9th International Workshop on Remote Sensing for Disaster Response, California*.

Sugiura, R., Noguchi, N. & Ishii, K. (2005). Remote-sensing Technology for Vegetation Monitoring using an Unmanned Helicopter. *Biosystems Engineering,* 90(4), pp. 369-379.

Suomalainen, J., Anders, N., Iqbal, S., Roerink, G., Franke, J., Wenting, P. Hünninge, D., Bartholomeus, H., Becker, R. & Kooistra, L. (2014). A Lightweight Hyperspectral Mapping System and Photogrammetric Processing Chain for Unmanned Aerial Vehicles. *Remote Sensing,* 6, pp. 11013-11030.

Sun, H., Li, M. Z., Zhao, Y., Zhang, Y. E., Wang, X. M. & Li, X. H. (2010). The spectral characteristics and chlorophyll content at winter wheat growth stages. *Guang Pu Xue Yu Guang Pu Fen Xi,* 30(1), pp. 192-196.

Swatantran, A., Dubayah, R., Roberts, D., Hofton, M. & Blair, J. B. (2011). Mapping biomass and stress in the Sierra Nevada using lidar and hyperspectral data fusion. *Remote Sensing of Environment,* 115(11), pp. 2917-2930.

Tattaris, M., Reynolds, M., Pietragalla, J., Molero, G., Cossani, M. C. & Ellis, M. (2014). In J. Bendig, & G. Bareth (Eds.), *Proceedings of the Workshop on UAV-based Remote Sensing Methods for Monitoring Vegetation* (pp. 125-136). Cologne: Kölner Geographische Arbeiten, 94.

Teillet, P. M., Staenz, K. & Williams, D. J. (1997). Effects of Spectral, Spatial, and Radiometric Characteristics on Remote Sensing Vegetation Indices of Foretsed Regions. *Remote Sensing of Environment,* 61, pp. 139-149.

Thenkabail, P. S., Lyon, J. G. & Huete, A. (2012a). Advances in Hyperspectral Remote Sensing of Vegetation and Agricultural Croplands. In P. S. Thenkabail, J. G. Lyon, & A. Huete (Eds.), *Hyperspectral Remote sensing of vegetation* (pp. 3-33). New York: CRC Press.

Thenkabail, P. S., Lyon, J. G. & Huete, A. (2012b). Hyperspectral Remote Sensing of Vegetation and Agricultural Crops: Knowledge Gain and Knowledge Gap After 40 Years of Resarch (2012). In P. S. Thenkabail, J. G. Lyon, & A. Huete (Eds.), *Hyperspectral Remote sensing of vegetation* (pp. 3-38). New York: CRC Press.

Thenkabail, P. S., Enclona, E. A., Ashton, M. S. & Meer, van der B. (2004). Accuracy assessments of hyperspectral waveband performance for vegetation analysis applications. *Remote Sensing of Environment,* 91, pp. 354-376.

Thenkabail, P. S., Smith, R. B. & Pauw, E. de (2000). Hyperspectral Vegetation Indices and Their Relationships with Agricultural Crop Characteristics.

Thorp, K. R. & Tian, L. F. (2004). A Review on Remote Sensing of Weeds in Agriculture. *Precision Agriculture,* 5, pp. 477-508.

Thorsted, M. D., Olesen, J. E. & Koefoed, N. (2002). Effects of white clover cultivars on biomass and yield in oat/clover intercrops. *Journal of Agricultural Science,* 138, pp. 261-267.

Tian, Y. C., Yao, .X, Yang, J., Cao, W. X., Hannaway, D. B. & Zhu, Y. (2011). Assessing newly developed and published vegetation indices for estimating rice leaf nitrogen concentration with ground- and space-based hyperspectral reflectance. *Field Crops Research,* 120, pp. 299-310.

Tilly, N., Hoffmeister, D., Aasen, H., Brands, J. & Bareth, G. (2014). Multi-Temporal Crop Surface Model derived from Terrestrial Laser Scanning for Accurate Plant Height Measurement and Biomass estimation of Barley. In J. Bendig, & G. Bareth (Eds.), *Proceedings of the Workshop on UAV-based Remote Sensing Methods for Monitoring Vegetation* (pp. 83-91). Cologne: Kölner Geographische Arbeiten, 94.

Toutin, T. (2004). Review article: Geometric processing of remote sensing images: models, algorithms and methods. *International Journal of Remote Sensing,* 25(10), pp. 1893-1924.

Tucker, C. J., Holben, B. N., Elgin, J. H. & McMurtrey, J. E. (1981). Remote sensing of total dry-matter accumulation in winter wheat. *Remote Sensing of Environment,* 11, pp. 171-189.

Turner, D., Lucieer, A. & Watson, C. (2012). An Automated Technique for Generating Georectified Mosaics from Ultra-High Resolution Unmanned Aerial Vehicle (UAV) Imagery, Based on Structure from Motion (SfM) Point Clouds. *Remote Sensing,* 4, pp. 1392-1410.

Uddling, J., Gelang-Alfredsson, J., Piikki, K. & Pleijel, H. (2007). Evaluating the relationship between leaf chlorophyll concentration and SPAD-502 chlorophyll meter readings. *Photosynthesis Research,* 91, pp. 37-46.

Urbahs, A. & Jonaite, I. (2013). Features of the use of unmanned aerial vehicles for agriculture applications. *Aviation,* 17(4), pp. 170-175.

Ustin, S. & Gamon, J. A. (2010). Remote sensing of plant functional types. *New Phytologist,* 186, pp. 795-816.

Verbyla, D. L. (1995). *Satellite Remote Sensing of Natural Resources*. New York: CRC Press

Veroustraete, F., Patyn, J. & Myneni, R. B. (1996). Estimating Net Ecosystem Exchange of Carbon Using the Normalized Difference Vegetation Index and an Ecosystem Model. *Remote Sensing of Environment,* 58, pp. 115-130.

Vincini, M., Frazzi, E. & Alessio, P. (2007). Comparison of narrow-band and broad-band vegetation indices for canopy chlorophyll density estimation in sugar beet. In: Stafford, J. V., *Precision agriculture '07* (pp. 189-196). Wageningen Academic Publishers: the Netherlands.

Wallace, L., Lucieer, A., Watson, C. & Turner, D. (2012). Development of a UAV-LiDAR system with application to forest inventory. *Remote Sensing*, 4, pp. 1519-1543.

Waller, S. S., Brown, M. A. & Lewis, J. K. (1981). Factors Involved in Estimating Green Biomass by Canopy Spectroeflectance Measurements. *Journal of Range Management,* 34(2), pp. 105-108.

Walter, V. (2004). Object-based classification of remote sensing data for change detection. *ISPRS Journal of Photogrammetry & Remote Sensing,* 58, pp. 225-238.

Wang, Z., Schaaf, C. B., Lewis, P., Knyazikhin, Y., Schull, M. A., Strahler, A. H., Yao, T., Myneni, R. B., Chopping, M. J. & Blair, B. J. (2011). Retrieval of canopy height using moderate-resolution imaging spectroradiometer (MODIS) data. *Remote Sensing of Environment,* 115, pp. 1595-1601.

Warner, T. A., Nellis, M. D. & Foody, G. M. (2009). The SAGE Handbook of Remote Sensing. London, UK: SAGE Publications Ltd.

Watts, A. C., Ambrosia, V. G. & Hinkley, E. A. (2012). Unmanned Aircraft Systems in Remote Sensing and Scientific Research: Classification and Considerations of use. *Remote Sensing,* 4(6), pp. 1671-1692.

Weiss, M., Troufleau, D., Baret, F., Chauki, H., Prévot, L., Olioso, A., Bruguier, N. & Brisson, N. (2001). Coupling canopy functioning and radiative transfer models for remote sensing data assimilation. *Agricultural and Forest Meteorology,* 108, pp. 113-128.

Whelan, B. M. & McBratney, A. B. (2000). The "Null Hypothesis" of Precision Agriculture Management. *Precision Agriculture,* 2, pp. 265-279.

Whitehead, K. & Hugenholtz, C. H. (2014). Remote sensing of the environment with small unmanned aircraft systems (UASs), part 1: A review of progress and challenges 1. *Journal of Unmanned Vehicle Systems,* 2, pp. 69-85.

Wolfgang, K., Fei, L., Gnyp, M. L., Miao, Y., Jia, L., Chen, X., Zhang, F. & Bareth, G. (2010). Evaluating Multispectral and Hyperspectral Satellite REMOTE Sensing for Estimating Winter Wheat Growth Parameters at Regional Scale in the North China Plain. *Photogrammetrie, Fernerkundung, Geoinformation,* 3, pp. 167-178.

Wu, B. & Meng, J. (2013). Remote Sensing Applications on Crop Monitoring and Prediction. In G. Wang & Q. Weng (Eds). *Remote Sensing of Natural Resources* (pp. 315-332). New York: CRC Press

Wu, .C, Niu, Z., Tang, Q., Huang, W., Rivard, B. & Feng, J. (2009). Remote estimation of gross primary production in wheat using chlorophyll-related vegetation indices. *Agricultural and Forest Meteorology,* 149, pp. 1015-1021.

Wu, C., Niu, Z., Tang, Q. & Huang, W. (2008). Estimating chlorophyll content from hyperspectral vegetation indices: Modeling and validation. *Agricultural and Forest Meteorology,* 148, pp. 1230-1241.

Wu, J., Wang, D. & Bauer, M. (2005). Image-based atmospheric correction of QuickBird imagery of Minnesota cropland. *Remote Sensing of Environment,* 99(3), pp. 315-325.

Wulder, M. A., White, J. C., Coops, N. C. & Ortlepp, S. (2009). Remote Sensing for Studies of Vegetation Condition: Theory and Application. In T. A. Warner, M. D. Nellis & G. M. Foody (Eds.), *The SAGE Handbook of Remote Sensing* (pp. 357-380). London, UK: SAGE Publications Ltd.

Xavier, A., C., Rudorff, B. F. T., Moreira, M. A., Alvarenga, B. S., Freitas, J. G. de & Salomon, M. C. (2006). Hyperspectral Field Reflectance Measurements to Estimate Wheat Grain Yield and Plant Height. *Science of Agriculture,* 63(2), pp. 130-138.

Xian, H. & Tian, L. (2012). Development of a low-cost agricultural remote sensing system based on an autonomous unmanned aerial vehicle (UAV). *Biosystems Engineering*, 108, pp. 174-190.

Xian, H. & Tian, L. (2011). Method for automatic georeferencing aerial remote sensing (RS) images from an unmanned aerial vehicle (UAV) platform. *Biosystems Engineering,* 108, pp. 104-113.

Xie, Y., Sha, Z. & Yu, M. (2008). Remote sensing imagery in vegetation mapping: a review. *Journal of Plant Ecology,* 1(1), pp. 9-23.

Yang, X. & Li, J. (2012). *Advances in Mapping from Remote Sensor Imagery: Techniques & Applications.* New York: CRC Press

Yang, Y.-K. & Miller, L.-D. (1985). Correlations of Rice Grain Yields to Radiometric Estimates of Canopy Biomass as a Function of Growth Stage. *Korean Journal of Remote Sensing,* 1(1), pp. 63-87.

Yao, H. & Huang, J. (2013). Remote Sensing Applications to Precision Farming. In G. Wang & Q. Weng (Eds). *Remote Sensing of Natural Resources* (pp. 333-352). New York: CRC Press

Yao, H., Tang, L., Tian, L., Brown, R. L., Bhatnagar, D. & Cleveland, T. E. (2012). Using Hyperspectral Data in recision Farming Applications. In P. S. Thenkabail, J. G. Lyon, & A. Huete (Eds.), *Hyperspectral Remote sensing of vegetation* (pp. 591-611). New York: CRC Press.

Yoder, B. J. & Pettigrew-Crosby, R. E. (1995). Predicting Nitrogen and Chlorophyll Content and Concentrations from Reflectance Spectra (400-2500 nm) at Leaf and Canopy Scales. *Remote Sensing of Environment,* 53, pp. 199-211.

Yu, K., Gnyp, M. L., Gao, J., Miao, Y., Chen, X. & Bareth, G. (2014). Using Partial Least Squares (PLS) to Estimate Canopy Nitrogen and Biomass of Paddy Rice in China's Sanjiang Plain. In: J. Bendig, & G. Bareth (Eds.), *Proceedings of the Workshop on UAV-based Remote Sensing Methods for Monitoring Vegetation* (pp. 99-103). Cologne: Kölner Geographische Arbeiten, 94.

Yu, K., Lenz-Wiedemann, V., Leufen, G., Hunsche, M., Noga, G., Chen, X. & Bareth, G. (2012). Assessing Hyperspectral Vegetation Indices for Estimating Leaf Chlorophyll Concentration of Summer Barley. *ISPRS Annals of the Photogrammetry, Remote Sensing and Spatial Information Sciences,* I-7, PP. 89-94.

Zarco-Tejada, P. J., González-Dugo, V. & Berni, J. A. J. (2012). Flurescence, temperature and narrow-band indices acquired from a UAV platform for water stress detection using a micro-hyperspectral imager and a thermal camera. *Remote Sensing of Environment,* 117, pp. 322-337.

Zarco-Tejada, P. J., Berni, J. A., Suárez, L. & Fereres (2008). A new era in remote sensing of crops with unmanned robots. *SPIE Newsroom.*

Zecha, C. W., Link, J. & Claupein, W. (2013). Mobile sensor platforms: categorization and research applications in precision farming. *Journal of Sensors and Sensor Systems,* 2, pp. 51-72.

Zhang, C. & Kovacs, J. M. (2012). The application of small unmanned aerial systems for precision agriculture: a review. *Precision Agriculture*, 13, pp. 693-712

Zhang, J. (2010). Multi-source remote sensing data fusion: status and trends. *International Journal of Image and Data Fusion,* 1, pp. 5-24.

Zhang, Y., Chen, J. M., Miller, J. R. & Noland, T. L. (2008). Leaf chlorophyll content retrieval from airborne hyperspectral remote sensing imagery. *Remote Sensing of Environment,* 112, pp. 3234-3247.

Zhang, X., Friedl, M. A., Schaaf, C. B., Strahler, A. H., Hodges, J. C. F., Gao, F., Reed, B. C. & Heute, A. (2003). Monitoring vegetation phenology using MODIS. *Remote Sensing of Environment,* 84, pp. 471-475.

Zhang, N., Wang, M. & Wang, N. (2002). Precision agriculture—a worldwide overview. *Computers and Electronics in Agriculture,* 36, pp. 113-132.

Zhao, B., Ma, B., Hu, Y. & Liu, J. (2014). Characterization of nitrogen and water status in oat leaves using optical sensing approach. *Journal of the Science of Food and Agriculture,* 95, pp. 367-378.

Appendices

Appendix A: Large scale representations of input RGB Orthomosaic, HDC & DSM

RGB Orthomosaic (1.5cm resolution)

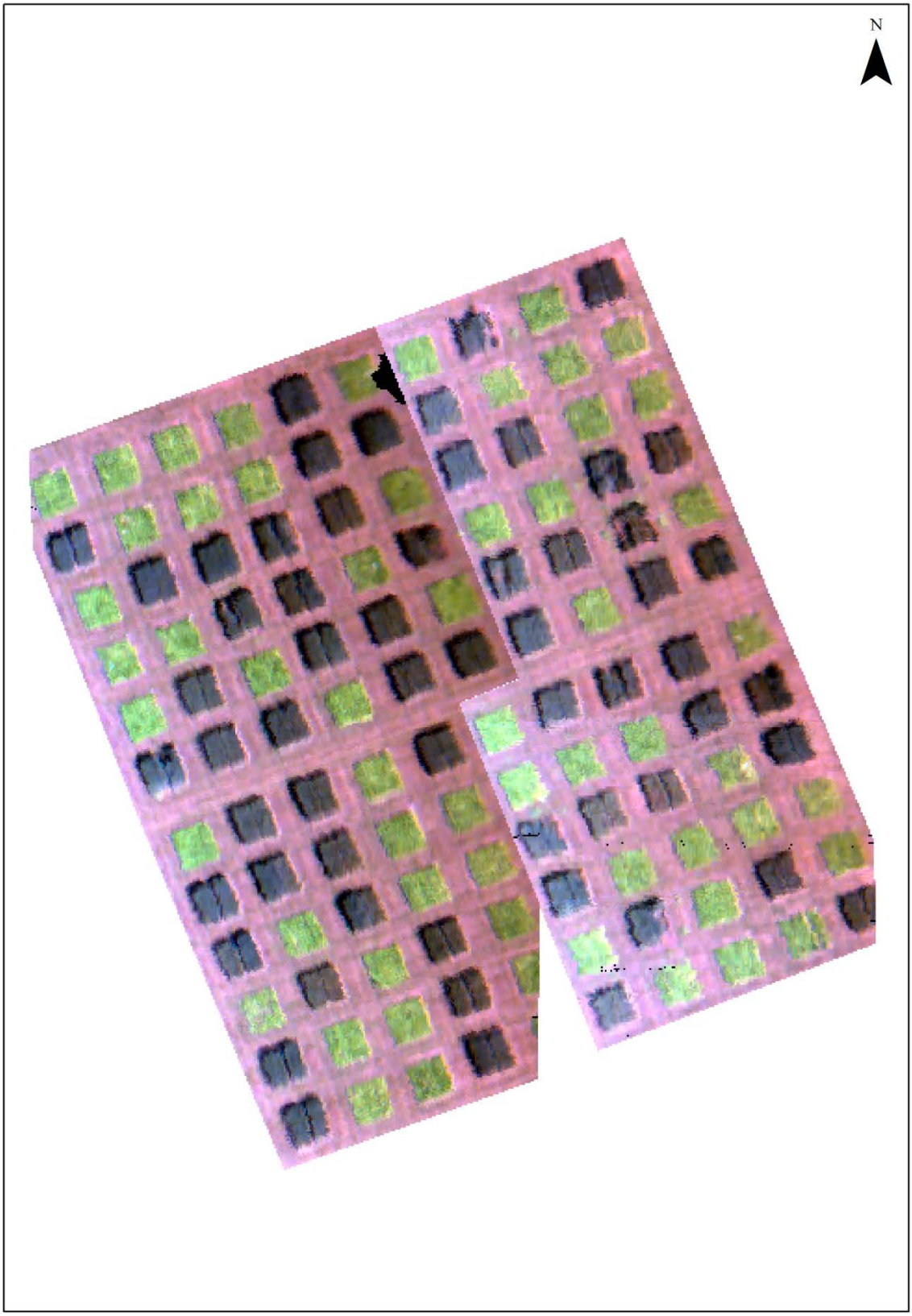

Hyperspectral Data Cube (14cm resolution) visualized as follows: Red = 660nm, Green = 550nm, Blue = 480nm

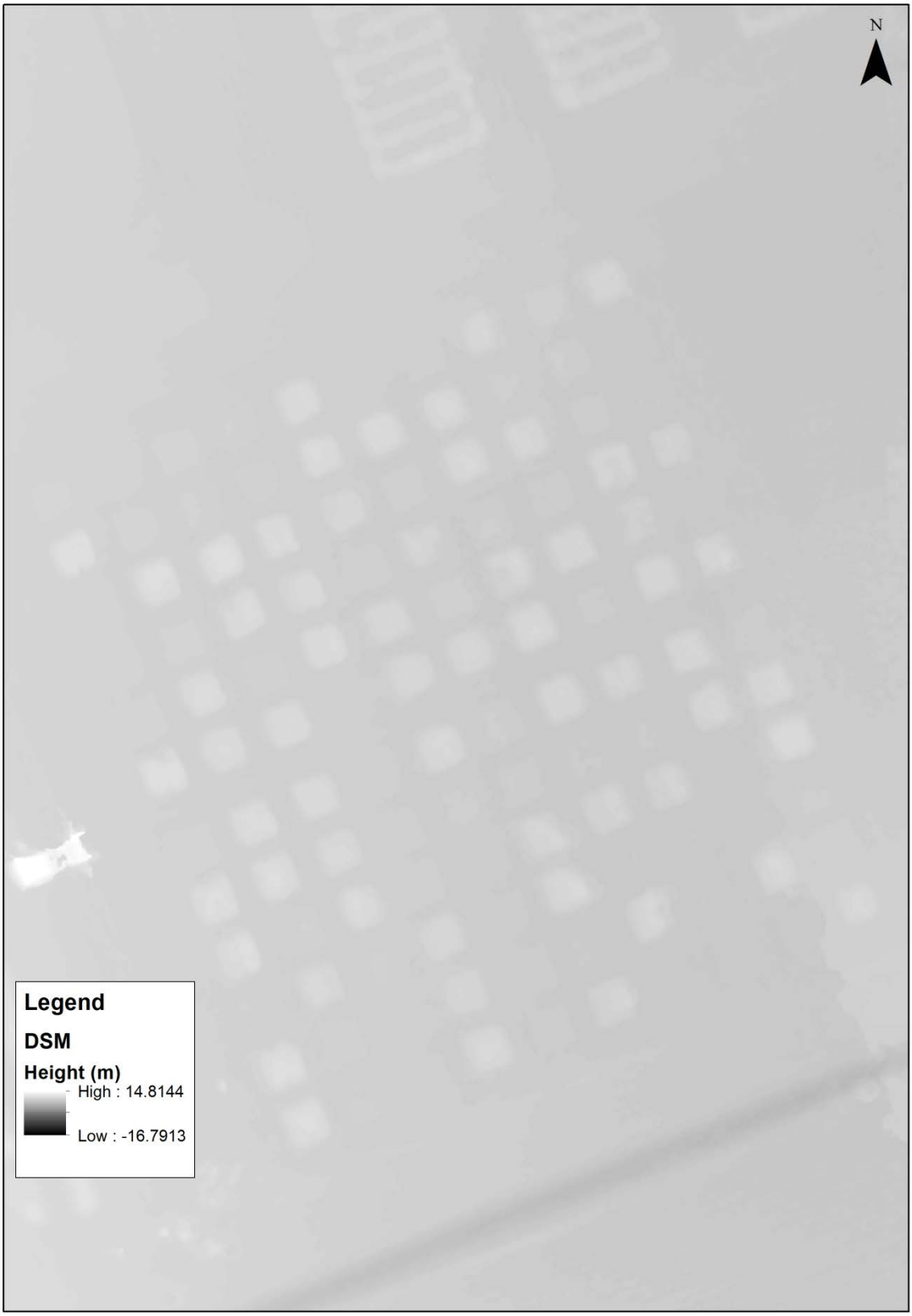

Digital Surface Model (2.9cm resolution)

Appendix B: Visual representation of deriving the CSM from the raw DSM

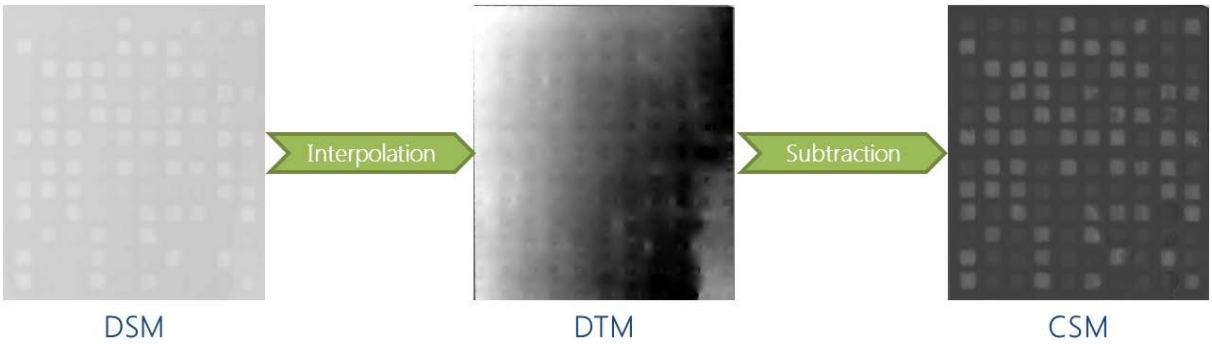

Input (DSM), intermediate output (DTM) and final output of the process to arrive at a Crop Surface Model (CSM).

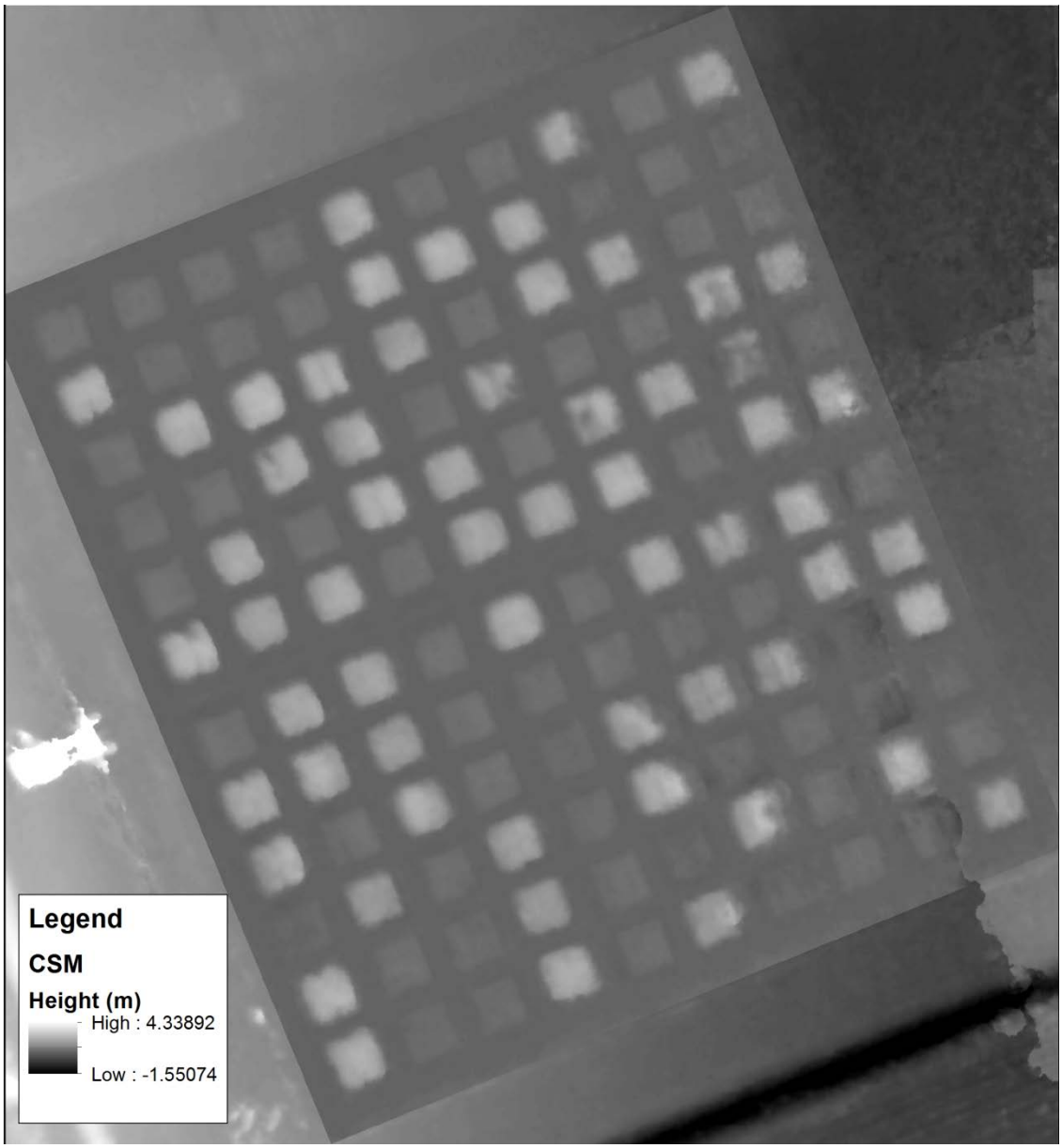

Resultant Crop Surface Modle (2.9cm resolution)

Appendix C: Textual elaboration on the existing indices used in this study

What follows below is a textual explanation with respect to the existing indices that were used in this study during calibration and subsequent validation. For each separate trait, previous studies that have employed one or more indices for these traits's derivation are elaborated on briefly. A tabular summary of the indices, their formulation and extraction from existing literature has been presented previously in chapter 4, in tables 4.1 and 4.2 specifically.

Biophysical plant traits

Fresh biomass (FBM)

Approaches to estimate above ground biomass of vegetation using spectral reflectance of plants were developed from the 1970s onwards, and have yielded various additional methodologies ever since (Waller et al., 1981). Existing research has highlighted the relationship between various VI's and green biomass, respectively (Pinter et al., 2003). In previous research, various formulations of the normalized difference vegetation index (NDVI) have been successfully correlated with biomass measures of different types of vegetation. More specifically, Thenkabail et al. (2000) demonstrated that a NDVI model incorporating a narrow red-edge band (λ1 at 720_{nm}) and a narrow NIR band (λ2 at 820_{nm}) provided the highest linear correlations with biomass in corn crops. Hunt et al. (2005) found that the NGRD index was linearly correlated to biomass of corn, alfalfa and soybeans at low biomass levels, although the correlation weakened for increased levels. The latter saturation effect was also observed by Goswami et al. (2015) for the relationship between NDVI and biomass in different vascular plants. In order to circumvent the saturation at high canopy cover, Mutanga & Skidmore (2004) developed a closely spaced red-edge/near-infrared narrow band NDVI and demonstrated its enhanced performance for higher canopy cover for grass. A simple ratio index incorporating narrow bands at 706_{nm} and 755_{nm}, however, yielded even higher coefficient of determination (R^2). Hansen & Schjoerring (2003) plotted a two-dimensional contour map depicting all hyperspectral two-band combinations (range $438\text{-}884_{nm}$) in a NDVI and the resultant coefficient of determination R^2 when linearly regressed with in-situ measurements of green biomass in wheat crops. Results revealed that the NDVI most strongly correlated to GBM was generated using λ1 in the green at 521_{nm} and λ2 in the red-edge at 689_{nm}. Applying PLSR further enhanced the prediction of GBM and resulted in lowering of the RMSE by 22%.

Furthermore, according to Cho et al (2007), wet biomass estimation based on the linearly interpolated red-edge position index (REP) is advantageous compared to NDVI based estimates, due to its enhanced resistance to influential soil and atmospheric conditions. Finally, Gnyp et al. (2014) performed a study in which estimation of rice biomass by means of OMNBR (Optimized Multiple Narrow Band Reflectivity) analysis based on raw reflectance (RR) was compared with the same model based on first derivative of reflectance's (FDR). The model with 1-4 variables was applied to rice in different growth stages and indicated that as the number of variables included increased, so did the model's sensitivity to GBM. More importantly, however, it was revealed that the model's accuracy was further increased when FDR rather than RR values were included when only two variables were used. Red-edge and short infrared wavelengths in particular recurred most frequently in these optimized models, although some exploited red or longer infrared wavelengths to some degree as well (Gnyp et al., 2014). Besides, Swatantran et al. (2011) and Anderson et al. (2008) demonstrated that combining hyperspectral reflectance data with plant height metrics effectively enhanced their model's ability to measure vegetation traits, such as above ground green biomass. Biomass, however, was found to frequently produce spectral response behavior relatively similar to LAI

(Heiskanen, 2006), i.e. univariate correlation of discrete narrow bands yield partially comparable results for both traits (Alchanatis & Cohen, 2012, and may therefore be more complicated to discriminate.

Alternatively, Casadesús & Villegas (2012), demonstrated that imagery captured by relatively simple and low cost digital consumer cameras may be effectively utilized to estimate biomass of plants. By counting the percentage of pixels in pictures within a certain segment of the hue histogram, between 60 and 120 or 80 and 120, the indices Green Area (GA) and Greener Area (GGA) were calculated, respectively. In essence, they relate to what percentage of soil is covered by green(er) canopy. It was found that in some cases these indices were correlated to biomass variables, such as grain yield, although saturation was witnessed for higher levels of LAI.

Plant height

In order to map height of vegetation (plant or canopy), Light Detection And Ranging (LiDAR), and SAR (Synthetic Aperture RADAR) to a lesser extent, have proved to provide the most accurate assessment in various studies (Homolová et al., 2013). Such altimetry equipment, however, is absent on the HYMSY platform utilized for this research and LiDAR will thus not be included in this elaboration. Thenkabail et al. (2000) assessed the heights of different crops using different hyperspectral models (OMNBR & narrow band NDVI's). Two band OMNBR models structurally outperformed single band OMNBR models, while four band OMNBR yielded even better results, but the relationships varied considerably. These findings are in accordance with Xavier et al. (2006). As little as 66% of the height variability of corn crops was explained by the latter model, whereas this value reached as high as 92% for soybeans. Besides, each of the models incorporated different (green, red, red-edge and/or near-infrared) hyperspectral bands to acquire the best result, some of which are not covered by the HYMSY platform. Similarly, the best narrow band NDVI's (bandwidths not provided) invariably outperformed those based on broad bands, but the R^2 for cotton (0.52), potato (0.77), soybean (0.78) and corn crops (0.31) differed notably (Thenkabail et al., 2000). Besides, due to the indirect relationship between plant height and LAI, Scotford & Miller (2004) observed that NDVI measurements for measuring plant height are only effective during early growth stages of plants, i.e. the index tends to saturate at later stages when plant height increases whereas NDVI does not necessarily or disproportionally.

Alternatively, in addition to laser, microwave and spectral oriented approaches, (digital) stereo photogrammetry provides an auxiliary means for retrieval of vegetation height (Bradbury et al., 2005). In essence, this relates to reconstruction of a three-dimensional scene from images by relatively orienting each to one or multiple others by identification of similar points of interest in different photographs (Drauschke et al., 2014). Aerial photographs and the camera orientations associated with each capture are imported into a photogrammetric software package. Next, the data is processed by a photogrammetric algorithm (e.g. Structure from Motion) to estimate unknown camera positions, eventually resulting in a surface model of the study area (DSM) through block bundle adjustments (Suomalainen et al., 2014; Bendig et al., 2013). Subsequently, when measurements prior to cultivation are available or the bare earth is visible in the photographs, a DEM representing the bare earth surface may be created, and then differenced with the DSM to arrive at a CSM (Crop Surface Model) depicting plant height (Tilly et al., 2014; Bendig et al., 2013). Stereo photogrammetry, however, is prone to errors in vast and dense (forested) environments where bare soil is hardly visible, rendering the retrieval of a ground plane reference practically impossible (St-Onge & Achaichia, 2001).

Biochemical plant traits

Chlorophyll (Chl) content

According to Qi et al. (2012), plant pigments such as chlorophyll, can only be effectively detected with hyperspectral optics. The spectral sensitivity to varying levels of chlorophyll content is relatively high in the green and red-edge region of the spectrum, whereas relative insensitivity in the blue and red region rapidly provokes saturation (Wu et al., 2008; Gitselson et al., 2003b). Likewise, traditional NDVI was found to be only sensitive to low levels of chlorophyll content (<1.5g/m2) in maize crops. Saturation beyond moderate levels (>2.0m/m2) notably lowered the sensitivity (Peng et al., 2011). As a result, chlorophyll content oriented models most frequently incorporate spectra in the green and/or red-edge region, hereby effectively circumventing saturation issues (Gitelson, 2012). Wu et al. (2008) evaluated relatively traditional indices and their slightly adjusted counterparts for leaf chlorophyll estimation in wheat crops, such as $NDVI_{[705-750]}$, $MSR_{[705-750]}$, $MCARI_{[705-750]}$, $TCARI/OSAVI_{[705-750]}$ and $MCARI/OSAVI_{[705-750]}$. The original TCARI/OSAVI index was developed by Haboudane et al. (2002) for leaf chlorophyll estimation in corn crops and expresses the ratio between two individual indices that are sensitive to chlorophyll and minimize soil background noise, respectively. Previous results indicated that the ratio index performed better than TCARI itself for a larger variation of LAI values, while maintaining the desired sensitivity to chlorophyll content (Qi et al., 2012). In all instances, the traditional indices demonstrated relative non-linearity and saturation at higher chlorophyll levels, whereas the proposed replacements notably improved the linearity of their relationship to chlorophyll content (Wu et al., 2008).

Yu et al. (2012) generated new simple ratio's (SRs) and NDVI indices using correlation matrix analysis. It was demonstrated that, across a variety of barley crops, SRs based on a pairing of bands from the red-edge at 734_{nm} (λ1) and red region at 629_{nm} (λ2) outperformed existing SRs for estimating leaf chlorophyll in a variety of different varieties combined. Subsequently, a NDVI incorporating 667_{nm} (λ1) in the red and 740_{nm} (λ2) from the red-edge outperformed NDVI indices established in previous studies. The newly computed SRs, however, yielded the best results when comparing all four new/existing SRs and NDVIs (Yu et al., 2012). It should be mentioned, however, that the adherence to these wavelengths yielded the best results when measurements for multiple barley crop varieties were combined and correlated simultaneously. For estimating chlorophyll in separate varieties, the best performing NDVIs frequently incorporated wavelengths in the VIS, especially in the ultraviolet and blue not accommodated for by the HYMSY setup. In contrast, a NDVI relying on 717_{nm} for λ1 and 732_{nm} for λ2, both in the red-edge, was found to be most strongly related to chlorophyll content in wheat crops according to Hansen & Schjoerring (2003).

Subsequently, Gitelson (2012) observed that the reflectance behavior of different pigments, each displaying different reflective capacities in different spectra, in plants is interrelated. For example, reflectance in the green region depends both on anthocyanins, carotenoids and chlorophylls, while reflectance in the red-edge varied notably depending on the ratio between the latter two pigments and the practically absent absorption of carotenoids in this region. Acquiring information on a single pigment from spectra is therefore ultimately challenged, and hence a distinct three-band model for each specific pigment was developed. It was calculated that for anthocyanin-free leaves, CI_{green} and $CI_{red-edge}$ are optimal indices, whereas only the latter applies to anthocyanin-containing leaves. In subsequent model performance analysis, it was demonstrated that the two models outperformed other models (e.g. $SR_{[800-680]}$, $NDVI_{[800-680]}$, EVI2, NDVIred-edge and $ECI_{[860-708-550]}$ when considering their sensitivity to a variety of different levels of chlorophyll content for different crop types, including maize (Gitelson, 2012).

Kooistra et al. (2014) assessed the performance of various VIs in regard to estimating of chlorophyll content in potato crops, by comparing the R^2 values of resultant linear estimators. It was found that the majority of indices studied, $CI_{red\text{-}edge}$, CI_{green}, NDRE and TCARI/OSAVI are differently but ultimately strongly related to chlorophyll content, in that particular order. $CI_{red\text{-}edge}$ and CI_{green} were developed by Gitelson (2003b) and were demonstrated to be stronger related to chlorophyll content than existing indices. The relationship between NDRE and chlorophyll content was also evaluated by Hunt Jr. et al. (2013) for maize crops and was found to be strongly correlated. In addition to some of the indices measured here, Clevers & Kooistra (2012) evaluated the suitability of MCARI/OSAVI, REP, MTCI and previously mentioned variations of the MCARI/OSAVI, TCARI/OSAVI and $CI_{red\text{-}edge}$ indices for predicting chlorophyll content. It was found that the adjusted indices outperformed traditional ones, all yielded R^2 values exceeded 0.90. This notion was in accordance with the findings of Wu et al. (2008). REP was only strong correlated with chlorophyll content when regressed in a non-linear fashion, a linear relationship was only found valid over a limit range due to saturation effects (Clevers & Kooistra, 2012).

An alternative model relying solely on reflectance in the VIS spectrum was developed by Hunt Jr. et al. (2013), i.e. Triangular Greenness Index or TGI. It estimates chlorophyll content based on the area of a triangle, in which each corner stone represents a wavelength in the blue (480_{nm}), green (550_{nm}) and red (670_{nm}), respectively. These wavelengths follow from the chlorophyll absorption maxima and the chlorophyll peak in the green, respectively. For analysis of chlorophyll content in maize crops, TGI showed a higher correlation than indices using a band in the NIR spectrum, and performed approximately similar when compared to indices using a wavelength in the red-edge region. Besides, it was indicated that TGI is a relatively robust index that was not affected by higher LAI values. A final benefit of TGI relates to the notion that the index is relatively independent of the sensor's spectral resolution and can be computed using spectral data acquired by low-cost broad band sensors such as digital cameras (Hunt Jr. et al., 2013).

Nitrogen (N) content

Considering the importance of N in agronomy, it is not surprising that a multitude of studies have been conducted to estimate nitrogen in crops through remote sensing practices in the past. The majority of research, however, focused on estimation of N content (on an aerial basis) rather than N concentration (Chen et al., 2010). Likewise, an extensive library of different indices has been established over time, some of which are overlapping with chlorophyll oriented indices due to the inherent relationship between the two traits (Homolová et al., 2013).

Zhao et al. (2014) assessed the ability to quantify N content in oat leaves at various growing stages in a laboratory setting using various SRs and (derivative) indices in the VIS-NIR segment of the spectrum. Considering univariate correlation between N content and narrow bands, the strongest (negative) correlations were found for the majority of the visible spectrum, but especially in the 525-650nm range, and at 705nm in the far red. The region around 696_{nm} and 705_{nm} are defined as the chlorophyll absorption post maxima and a function of chlorophyll concentration by Zhao et al. (2014), respectively. Due to the inherent interdependency between N and chlorophyll, alterations in the latter provide sensitivity for measuring the other in this spectral region specifically (Wu et al., 2008). From approximately this region onwards the correlation turns positive and gradually increases in strength throughout the NIR. This contrasting difference in reflectance-N dependency in the VIS and NIR was also identified by Nguyen & Lee (2006) for N in rice. The reflectance behavior, however, differed slightly for different growth stages and levels of water stress. Subsequently, $SR_{[760\text{-}550]}$ and $NDVI_{[760\text{-}550]}$ showed relatively strong relationships with leaf N compared to other indices tested. This is not surprising considering these indices' adherence to specific wavelengths that were highly (univariate) related to N (Zhao et al., 2014). The importance of these specific wavelengths for

estimating N was also demonstrated by Clevers & Kooistra (2012). Linearly regressing N content measurements in two potato fields with narrow band hyperspectral data resulted in the identification of REP, $CI_{green[780-550]}$, $CI_{red-edge[780-710]}$ and MTCI indices as most suitable for accurately measuring N. All rely on pairing of bands at largely similar wavelengths in the near-infrared (high positive correlation) with others in the visible (reduced negative correlation).

Hansen & Schjoerring (2003) linearly correlated all narrow band NDVI combinations in the 438_{nm}-883_{nm} range with N content for wheat crops. Mostly similar to the findings of Zhao et al. (2014) and Nguyen & Lee (2006) mentioned above, the strongest negative univariate correlations were found in the VIS (438-690_{nm}) spectrum. Likewise, high positive correlations were identified in the 750-883_{nm} range beyond the red-edge in the near-infrared. Relatedly, the best NDVI indices, according to Hansen & Schjoerring (2003), for measuring N included narrow bands in the red-edge range at 734_{nm} (λ1) and 750_{nm} (λ2), or alternatively at 770_{nm} in the NIR (λ2) and at 717_{nm} in the red-edge for λ1. When an exponential fit was applied to the optimal linear NDVIs, an small increase in performance was displayed. In a final assessment, a PLS model was loaded with all individual narrow bands, subsequently allowing comparison with the best NDVI indices. Estimation of N concentration saw the most significant improvement of R^2 and RMSE compared to the best linear and exponential NDVI model. Compared to the original best NDVI models for measuring N content, however, the improved performance of the resultant PLS model was negligible (Hansen & Schjoerring, 2003).

More recently, Tian et al. (2011) evaluated all possible two band combinations for simple ratios (SR), normalized difference (vegetation) indices (NDVIs) and simple difference indices (SD) and their relation to N in rice leafs. Besides, some existing three-band indices were evaluated. As far the assessment of the latter is concerned, MTCI performed best, similar to the findings of Clevers & Kooistra (2012). Finally, Chen et al. (2010) analyzed the relationship between a variety of indices frequently used for estimating nitrogen or chlorophyll concentrations and/or content in corn and wheat. It was found that especially the combined index MCARI/MTVI2 performed well for both crop types, whereas TCARI/OSAVI was only strongly correlated to N status of corn.

Carbon (C) content

Given the inherent and relatively constant linkage between biomass and carbon content of a given vegetation's canopy (Magnussen & Reed, 2004), some of the indices do at least partially overlap with those presented with regard to estimation of biomass itself. This observation also follows from the notion that sensors are currently unable to directly measure or estimate the amount of carbon stored as above ground plant biomass, and thus relies on using assumingly related proxies (Brewer et al., 2011; Tucker et al. 1981).

Peng et al. (2011) evaluated the ability to estimate the Gross Primary Production (GPP) of maize crops (gCarbon/m^{-2}/$time^{-1}$) using the broadband counterparts of indices that are frequently used to estimate chlorophyll status of vegetation, including CI_{green}, $CI_{red-edge}$, $SR_{[NIR-rededge]}$, EVI2 and NDVI. It was reasoned and demonstrated that chlorophyll is ultimately related to nitrogen status and photosynthetic capacity, and therefore to the capacity (i.e. GPP) of crops to convert photosynthetic active radiation (PAR) into dry carbon biomass. It was found that the product of a distinct index and in situ measured PAR produced a stronger relationship with GPP then the indices separately, although indices alone were also evidently related to GPP by themselves. Multiplication of each index with real-time PAR measurements was done to correct for high frequency deviations of incoming PAR, and thus allowing for more accurate estimation of GPP through time. A similar methodology was applied by Wu et al. (2009) for estimating GPP in wheat crops, using $NDVI_{[750-710]}$, $MCARI_{[705-750]}$ and MTCI, as well as the earlier mentioned $CI_{red-edge}$. Again, GPP and the product of each index

with measured PAR yielded clear relationships with different strengths. It was additionally demonstrated that, compared to other vegetation features, chlorophyll content is the main driver of GPP and the structure of plants is only of limited influence.

A second proxy worth mentioning is the assimilation/fixation of carbon, or fPAR, i.e. the fraction of Photosynthetically Active Radiation (PAR. $400\text{-}700_{nm}$) absorbed by the vegetation canopy. Assuming that various additional parameters are held constant, it has been demonstrated by various studies that dry matter (e.g. C content) is inherently related to fPAR (Namayanga, 2002). Consequently, assessment of fPAR provides a means to monitor inter-seasonal net vegetation productivity dynamics and temporal and spatial development of carbon stocks (Roujean & Breon, 1994). Since the 1980s, diversified evidence has been collected that there exists a notable relationship between fPAR and spectra in the visible (Red) and NIR (Hilker et al., 2008). Hall et al. (1992) indicated that NDVI is near linearly related to the latter variable for grasslands. It was, however, also found that the shape of the relationship was additionally affected by reflectance of the canopy substrate (e.g. soil and litter). These findings are in accordance with a study of Sellers (1985) using RTM. Relatedly, NDVI was also found to be near linearly related to $_{f}$PAR in relatively dense vegetation by Roujean & Breon (1994) based on RT simulations. NDVI performed notably weaker for less dense vegetation with reduced levels of LAI, especially when imagery is acquired in nadir view and the influence of background soil reflectance is increased. Therefore, an alternative (broad band) index that attempts to limit influence of soil reflectance (SAVI) was put forward and presented to yield a stronger linear relationship with only limited dispersion. Besides, Glenn et al. (2008) propose the use of the Enhanced Vegetation Index (EVI) for estimating $_{f}$PAR, due to reduced saturation behavior as demonstrated in various studies.

Appendix D: Reflectance plots

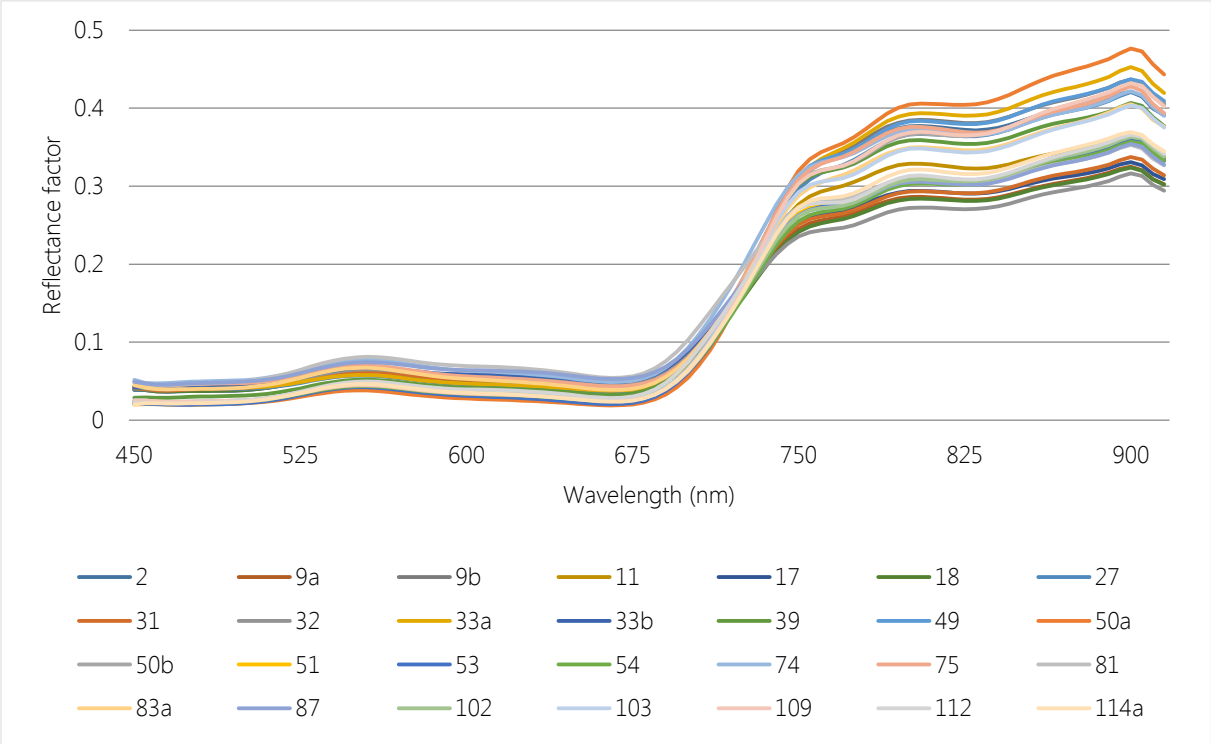

Average individual plot reflectance for the calibration set (n=28)

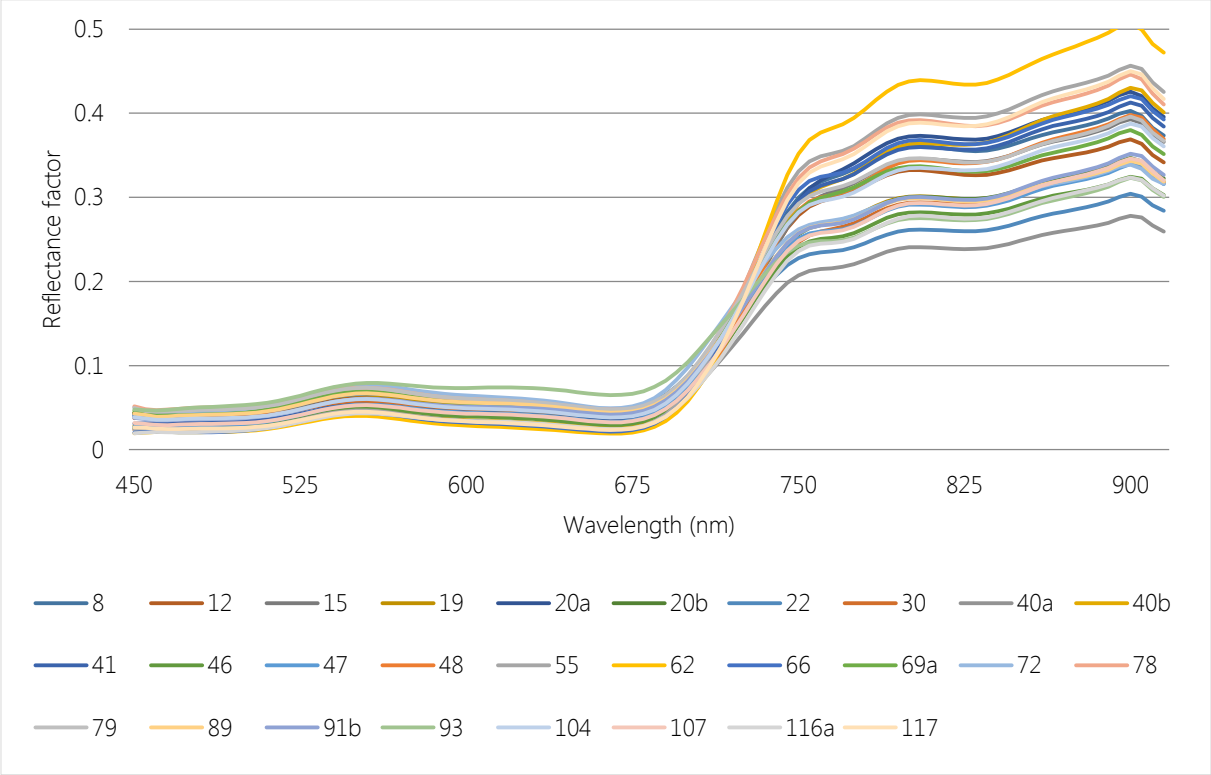

Average individual plot reflectance for the validation set (n=28)

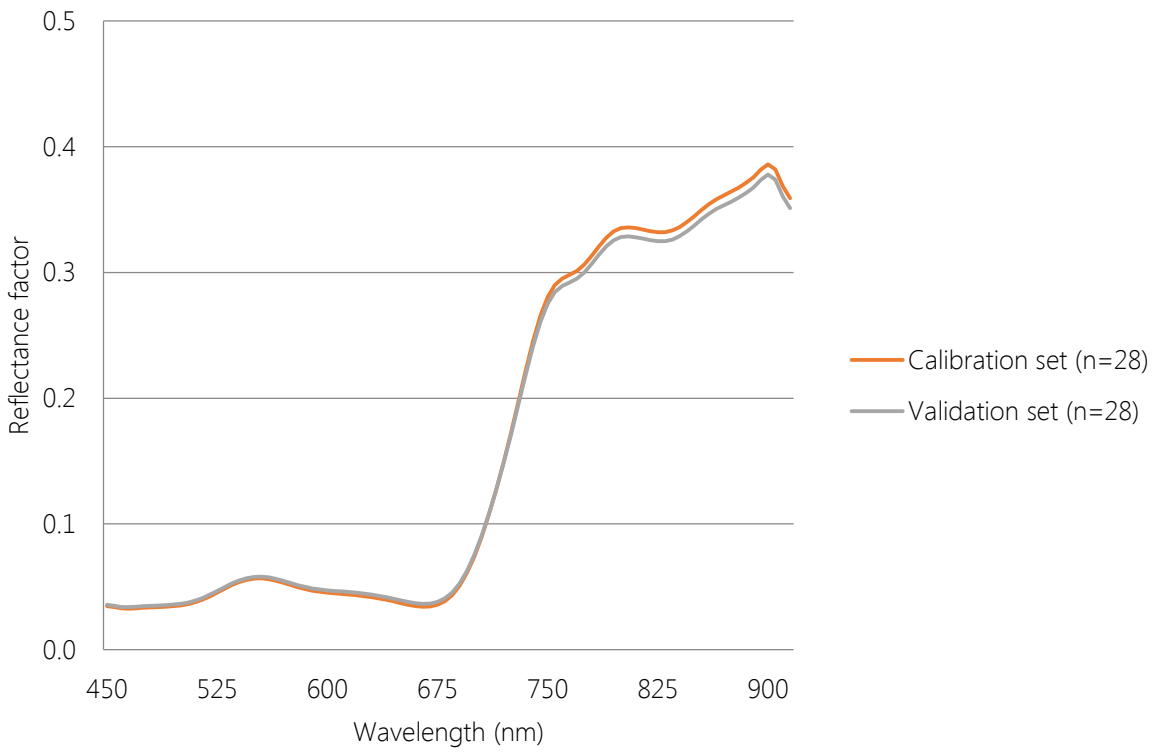

Average reflectance for all plots in either the calibration or validation set combined

Appendix E: Correlation coefficients among separate traits

Correlation coefficients (*r*) among individual trait (measurements) for the calibration set (n=28). (BM = biomass, N = nitrogen, C = carbon, LC = leaf chlorophyll, conC = concentration, conT = content)

	Height	Fresh BM	Dry BM	N conC	N conT	C conC	C conT	LC conC	LC conT
Height	-	0.60	0.41	0.73	0.79	0.44	0.42	0.59	0.60
Fresh BM	0.60	-	0.95	0.33	0.85	0.38	0.95	0.36	0.37
Dry BM	0.41	0.95	-	0.10	0.71	0.23	1.00	0.17	0.17
N conC	0.73	0.33	0.10	-	0.76	0.48	0.12	0.78	0.78
N conT	0.79	0.85	0.71	0.76	-	0.46	0.72	0.60	0.61
C conC	0.44	0.38	0.23	0.48	0.46	-	0.27	0.61	0.62
C conT	0.42	0.95	1.00	0.12	0.72	0.27	-	0.19	0.19
LC conC	0.59	0.36	0.17	0.78	0.60	0.61	0.19	1.00	1.00
LC conT	0.60	0.37	0.17	0.78	0.61	0.62	0.19	1.00	1.00

Correlation coefficients (*r*) among individual trait (measurements) for the calibration set (n=28). (BM = biomass, N = nitrogen, C = carbon, LC = leaf chlorophyll, conC = concentration, conT = content)

	Height	Fresh BM	Dry BM	N conC	N conT	C conC	C conT	LC conC	LC conT
Height	1.00	0.77	0.68	0.53	0.77	0.29	0.68	0.71	0.72
Fresh BM	0.77	1.00	0.98	0.40	0.90	0.25	0.98	0.58	0.58
Dry BM	0.68	0.98	1.00	0.29	0.84	0.24	1.00	0.48	0.48
N conC	0.53	0.40	0.29	1.00	0.75	0.03	0.29	0.59	0.59
N conT	0.77	0.90	0.84	0.75	1.00	0.21	0.85	0.64	0.65
C conC	0.29	0.25	0.24	0.03	0.21	1.00	0.28	0.10	0.10
C conT	0.68	0.98	1.00	0.29	0.85	0.28	1.00	0.48	0.48
LC conC	0.71	0.58	0.48	0.59	0.64	0.10	0.48	1.00	1.00
LC conT	0.72	0.58	0.48	0.59	0.65	0.10	0.48	1.00	1.00

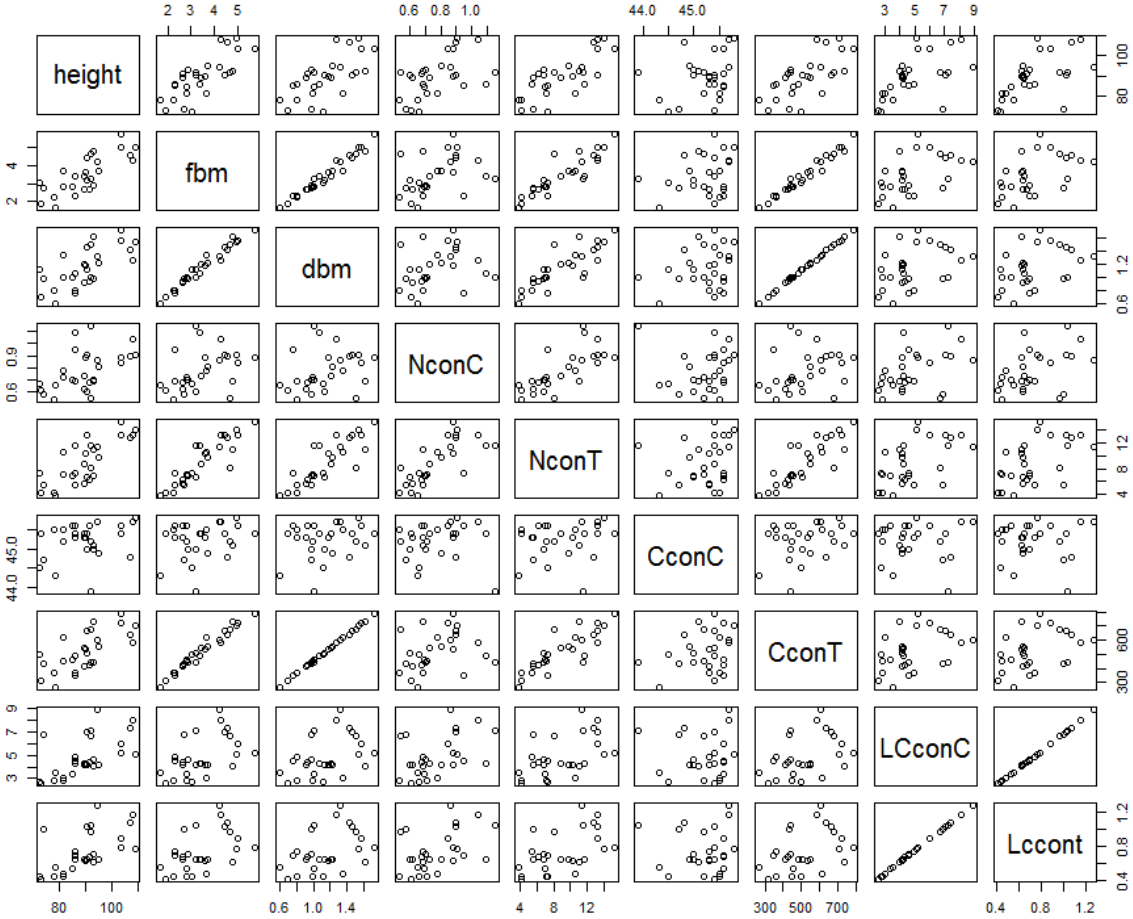
height
fbm
dbm
NconC
NconT
CconC
CconT
LCconC
Lccont

Appendix F: Textual elaboration on the removal of plots

The figures below, visualizing univariate correlation coefficients (r) between separate plant traits and individual narrow bands prior to removal of various plots, indicate notable differences between the calibration and validation dataset. More importantly, however, the shapes of the figures partially deviate (notably) from findings in previous research. The anomalies are most persistent within the calibration set and to a lesser extend in the validation set. Below, the findings of a thorough assessment on what lies at the foundation of such anomalies are presented through textual and figurative means. The exploration was conducted in a structured and systematic manner. First, the figures were compared with similar correlation figures as presented in multiple previous studies, apparent deviations at distinct wavelengths and/or generic spectral regions were then identified. Secondly, scatterplots and diagnostic correlation plots were generated using R to comprehensively identify individual plots exerting relatively substantial influence on the correlation coefficient found, i.e. to what extend it would change if the observation were omitted. This is indicated by an observation's Cook's distance value, which increases when large residuals are shown and/or when an observation's associated value is at an extreme end of the range of all values (Maindonald & Braun, 2010). Finally, the findings were related to visual inspections of the RGB orthomosaic and HDC in an attempt to find a plausible explanation for the anomalies.

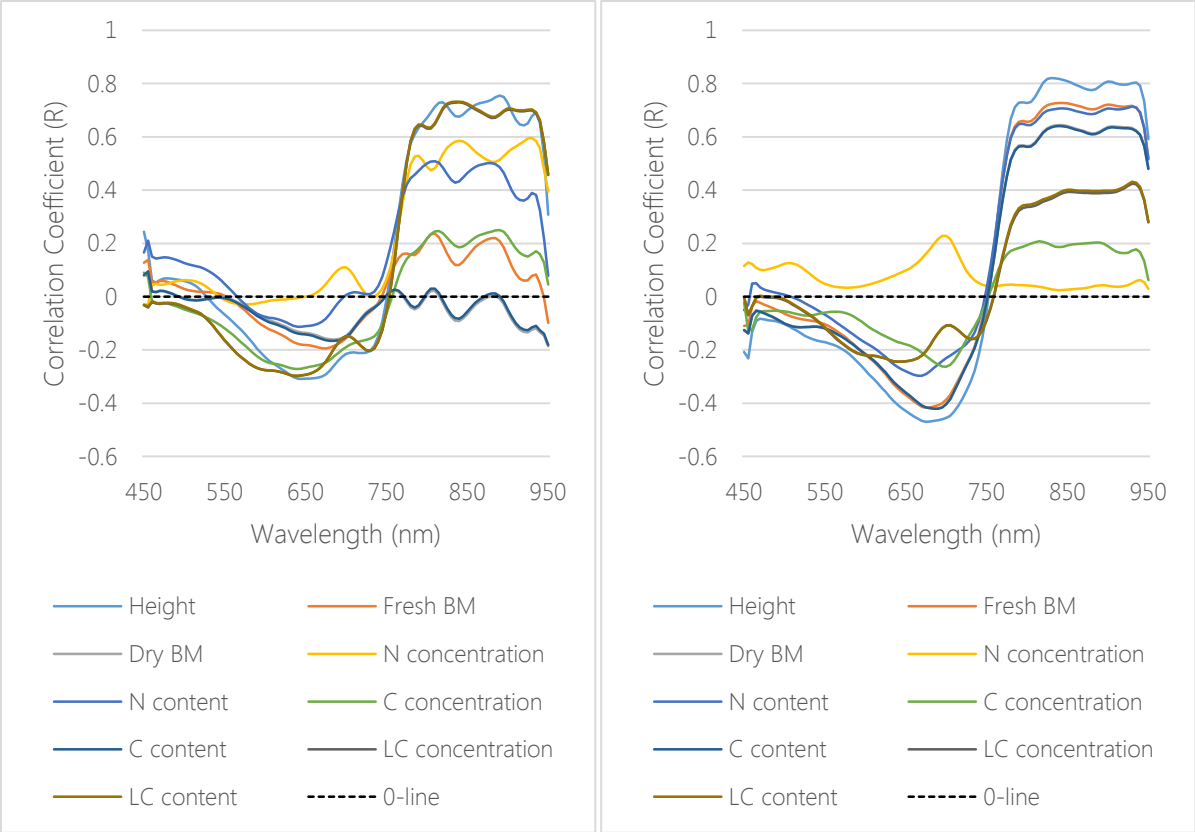

Wavelength dependence of the correlation coefficient (r) based on a linear regression between average plot canopy reflectance and each crop trait studied for the calibration (left, n=35) and validation (right, n=34) set prior to the removal of plots indicating within-plot structural heterogeneity.

The concentration of carbon is relatively constant for all plots, in accordance with the notion that this trait is only limitedly varied for different plant species and locations. Consequently, the correlation coefficients associated with this distinct trait are minimal at all wavelengths and practically identical for both calibration and validation plots.

Calibration set

Height, fresh biomass (fbm) and dry biomass (dbm)

As was stated in paragraph 7.3 previously, it is commonly understood that height is relatively strongly (positively) correlated to plant biomass (Tilly et al., 2014; Fernandez et al., 2009; Niklas & Enquist, 2001). Likewise, it may be reasonably expected that such traits indicate relatively similar correlations over wavebands (as is the case for the validation set). However, considerable diffusion in r values is discernible from the figures above, particularly in the near-infrared.

When fresh and dry biomass were both individually correlated with five equally spaced bands in the NIR (820-940nm), 114b consistently showed up as an influential observation with a cook's value averaging around 0.5 and nearing 1.0 at some wavelengths. Other plots were also identified to exert some influence (e.g. 77 and 100), but far less than was the case for 114b. Plot 114b was also a recurring band when measured height was individually correlated with fresh and dry biomass. In addition, plots 51, 77 and 100 were indicated as relatively influential. According to the field measurement data, plot 51 has the lowest (averaged) plant height. Contrastingly, however, its values for fresh and dry biomass are extremes at the high end of the range. Plots 114b, 100 and 77 represent plots with clearly the lowest values for fresh and dry biomass in the entire calibration set. However, the measured height in these plots is (above) average in comparison to all of the other calibration plots. Upon visual inspection of these plots it was identified that the (approximated) quadrant areas from which biomass samples were acquired are located on (or close to) poorly vegetated grounds, which potentially explains the low values for both forms of biomass. Height measurements, however, were conducted on four equally spaced locations in each plot, i.e. one in every plot's sub quadrant. Visual inspection indicates that these locations mostly represent seemingly successful vegetation, except for the one quadrant from which biomass was sampled and measured, hence the relatively higher measured mean height. This is also confirmed by the individual height values at each quadrant location prior to averaging, where only the measurement taken close to the biomass sample location stands out in the downwards direction. This explains the separated validity of both height and biomass measurements with respect to the sampling location, as well as the observed contradictions existing between both traits resulting from the different spatial scales at which each was measured and the within plot heterogeneity.

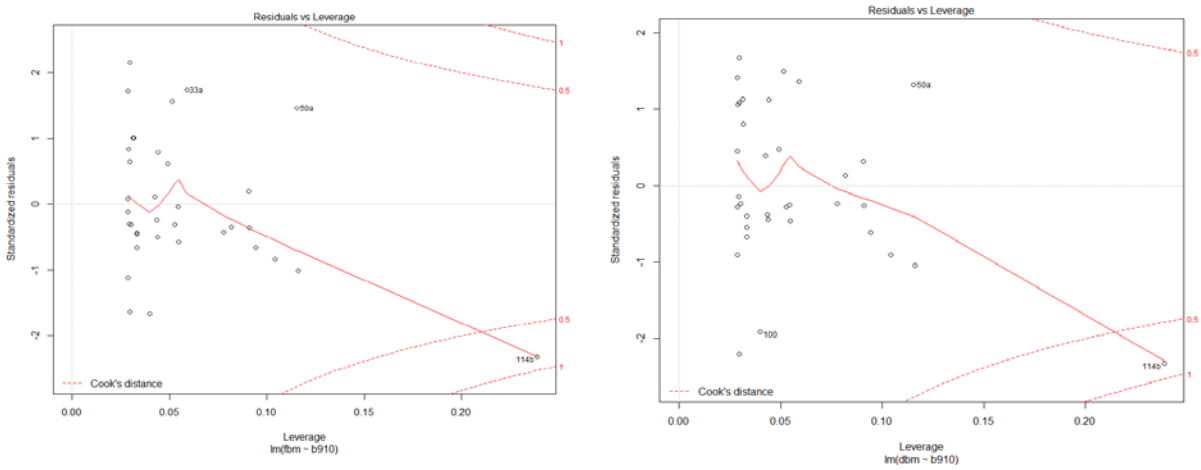

Diagnostic plot for correlation of fresh biomass (left) and dry biomass (right) with measured reflectance at 910nm.

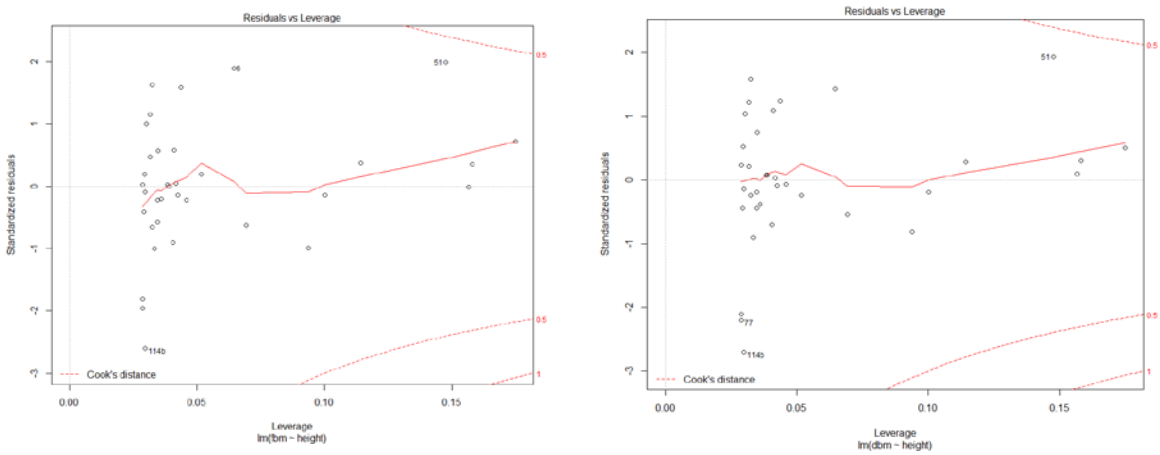

Diagnostic plot for correlation of fresh biomass (left) and dry biomass (right) with measured height

N concentration

The correlation coefficients for the concentration of N are plausible throughout the near-infrared, but the range of values between either low or positive correlations in the visible is not. The observed peak of positive correlation in the red at 690nm in particular, however, is not in accordance with findings in existing studies. A relatively strong negative correlation is to be expected in the red due to the negative relationship between concentration of N and reflectance in the red, i.e. increased N enhances production of chlorophylls, which subsequently absorb more at these wavelengths (Mulla, 2013; Daughtry et al., 2000). Generation of diagnostic plots of the correlation between the trait and spectra at 690nm revealed that plot 83b in particular exhibits significant leverage, in addition to above average residuals, far exceeding the leverage of any other plot in the calibration set. The latter results from the notion that the plot's reflectance at this wavelength is rather high and strongly deviating from any of the other plots. The value of N concentration associated with the plot, however, is comparatively and illogically high. In addition, plot 77 invokes notable influence on the value of *r* in the red, particularly due to the comparatively high values for both measured N concentration and the plot's reflectance at the 690 nm wavelength. The increased N concentrations may be explained by the notion that the samples were acquired on a location with limited vegetation. Decreased vegetation cover and increased spacing lowers competition between remaining individual plants and enhances their ability to absorb larger quantities of nutrients such as nitrogen (Schenk et al. 1999), and hence the seemingly striking observations for high N concentrations as well as relatively high red reflectance due to reduced vegetation cover. Plot 114b is also indicated to exhibit vast residuals with respect to the correlation and displays some sparse vegetation nearby the assumed sampling location, which relates to it being the plot assigned with the highest N concentration value. The majority of the remaining plot's area, however, is represented by vast vegetation cover which enhances limited reflectance in the red and therefore partially compensates for the high N concentration.

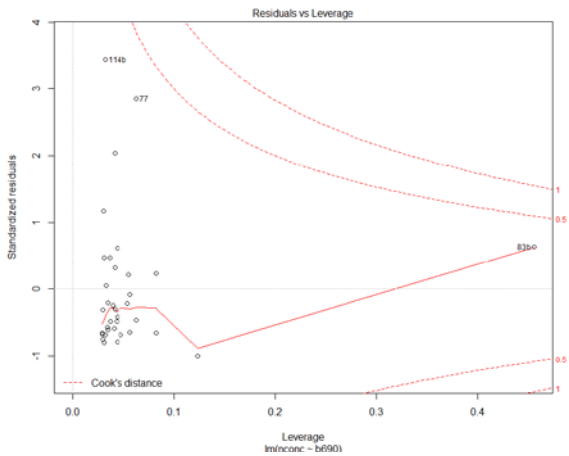

Diagnostic plot for correlation of N concentration with measured reflectance at 690nm.

N content

The peculiarities observed with respect to the correlation coefficients of N content are partially comparable those mentioned above for N concentration, which logically follows from the notion that the first is a function of the latter and dry biomass. Correlations in the blue are marginally positive and largely absent in the red, however, a stronger negative relationship is to be expected in both regions for reasons mentioned before. Generation of diagnostic plots of the correlation between the trait and spectra in the blue (480nm) and red (690nm) revealed that plots 6 and 83b, respectively, most strongly influence the unanticipated coefficients found in both spectral regions. One of the highest values for dry biomass was measured in plots 6, resulting in the highest N content value after multiplication with N concentration which only slightly exceeds the average. The latter notion relates to why plot 6 was not highlighted in diagnostic plots for N concentration, but why it was for N content once dry biomass measures were included. In contrast, the reflectance in the blue and red for plots 6 and 83b in particular consistently rank among the highest and resultantly invokes significant leverage on the resultant correlation coefficients in this region. In accordance with the findings for traits mentioned earlier, both plots display partial or significant areas of

limited vegetation cover and persistent penetration of the background soil, which may explain the deviating reflectance at these wavelengths.

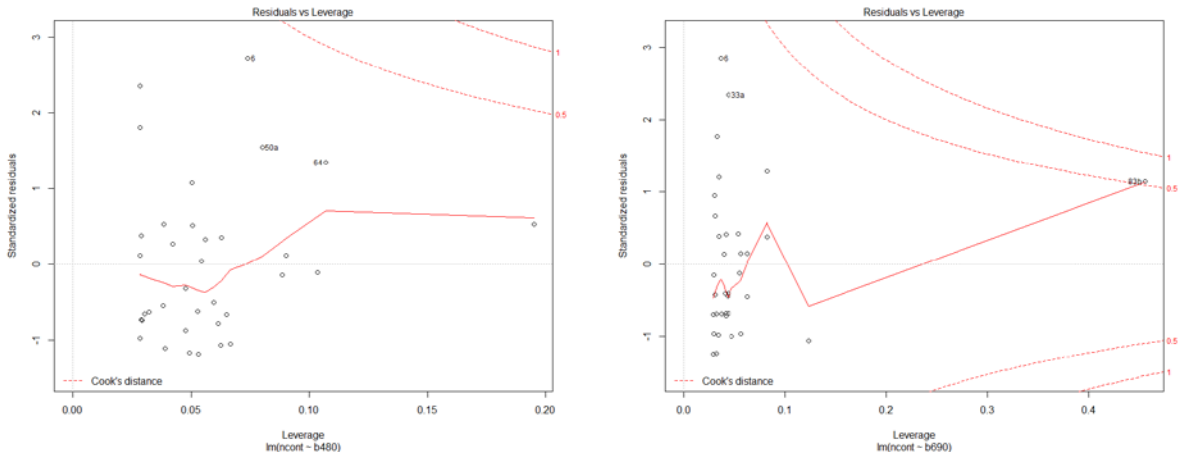

Diagnostic plot for correlation of N content with measured reflectance at 480nm (left) and 690nm (right).

Validation set

N concentration

The observed correlation coefficients for concentration of N are significantly deviating from findings in prior research, and also notably different in comparison to the calibration set. The positive correlation throughout the visible spectrum, the further increase in the red at 690nm, and the entire absence of correlations in the near-infrared are particularly striking in this respect. Diagnostic plots revealed plot 101 in particular invokes significant influence on the low correlation in the near-infrared, judging from its high Cook's value consistently exceeding 1.0 or resolving around 0.5 for different near-infrared wavelengths. Plots 91a, 69b and 85 all exert similar influences in the near-infrared, to a lesser degree. Diagnostic plots for the correlation of N concentration with blue wavelengths (480nm) and in the red (690nm) identified the same plots as highly influential. For all four plots, visual inspection indicates that samples from which N concentrations were calculated were retrieved from relatively poorly vegetated areas. This observation is confirmed by the notion that the dry biomass weighted in each sample is at the very low end of the spectrum. Besides, a large share of the remainder of plot 101 in particular, as well as of 91a, 69b and 85, is also scarcely covered with crops. Both notions combined potentially explain why the highest N concentrations were measured in these distinct plots. Relatedly, the lowered green cover substantially pulls the correlation coefficient in the downward direction throughout the near-infrared.

The unanticipated increased positive value of *r* in the red (690nm) is furthermore, and for a major part, also ascribable to plots 69b, 85, 101 and 91a, in that particular order. Measured N concentration in plots 101 and 91a represent the highest values of the validation's set range, while these plots measured reflectance in the red (and elsewhere in the visible) structurally exceeds the average reflectance of all plots. Subsequently, the averaged measured visible reflectance in plots 69b and 85 by far exceeds any of the other plot's reflectance, while measured N concentration is also at the far high end of the range. Measured N concentration and reflectance thus contradict findings in previous studies, although this logically follows from the different spatial scales at which each parameter was measured and the observed within plot heterogeneity. Besides, the uniquely high values for N concentration invoke significant leverage on the correlation coefficient in the visible that resultantly pushes the coefficient upwards.

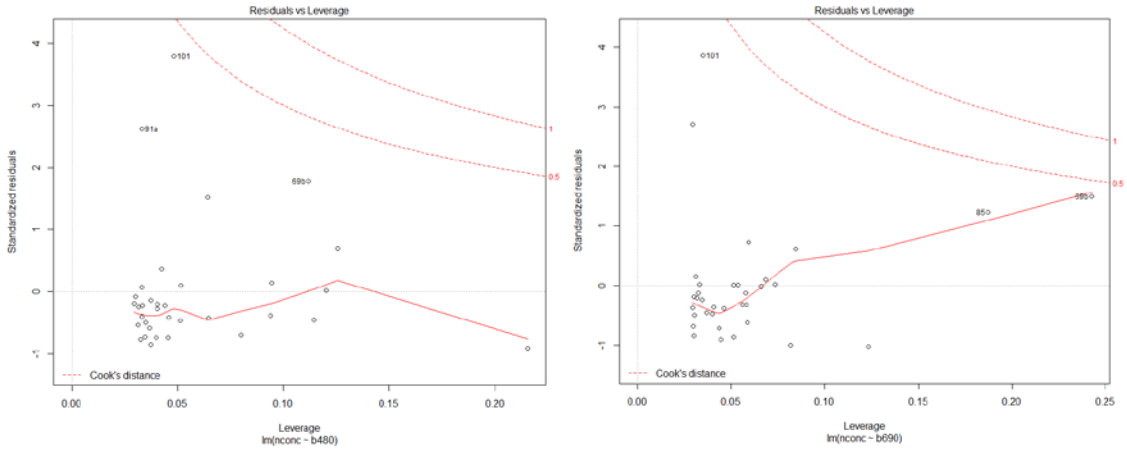

Diagnostic plot for correlation of N concentration with measured reflectance at 480nm (left) and 690nm (right).

Leaf Chl concentration/content

The correlation coefficients found for leaf Chl concentration and content are not necessarily remarkable with respect to findings in existing studies, i.e. the observed *r* values are (negative and) close to zero in the blue and green, increasingly lower in the red and positive beyond the red-edge in the near-infrared (Hansen & Schjoerring, 2003). More importantly, however, the coefficients of correlation in the near-infrared are relatively low ($r \approx 0.35$) and structurally lower compared to the calibration set ($r \approx 0.6$). Upon inspection of the data, plot 101 was again identified to exert significant influence in the near-infrared, judging from its Cook's value structurally exceeding 1.0. Plot 101 represents the plot with the highest value for leaf Chl concentration and, relatedly, leaf Chl content. This follows logically from the notion mentioned previously, namely that the highest N concentration was also measured within the same plot, and the indirect effect of increased N concentration on chlorophyll production (Homolová et al., 2013; Clevers & Kooistra, 2012). Due to very limited green cover and vast persistence of background soil within the plot, however, the increased chlorophyll concentration and content is not accompanied with increased near-infrared reflectance as is to be anticipated. These plausible but contradicting observations lie at the foundation of reduced correlations in the near-infrared, which are further exaggerated by the relatively large leverage due to the comparatively high values for both measures of leaf Chl.

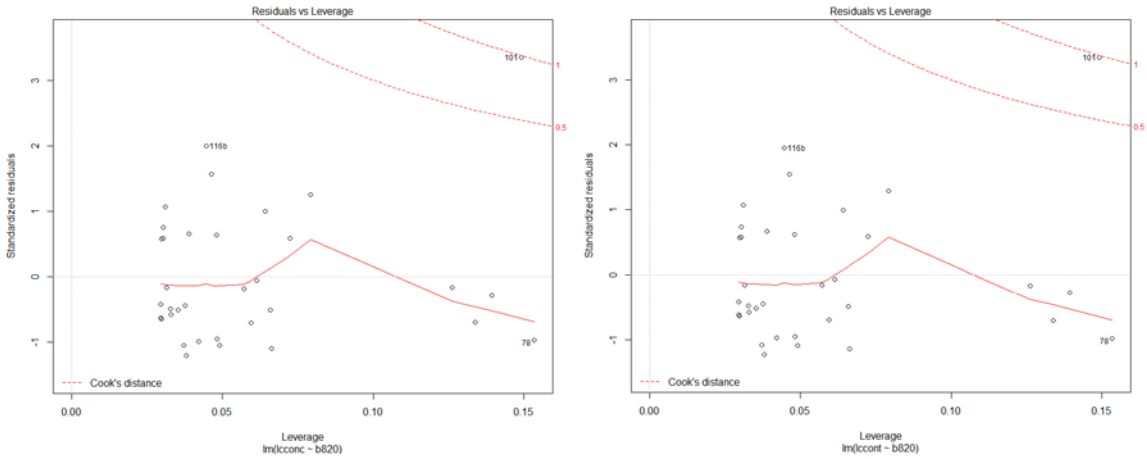

Diagnostic plot for correlation of leaf Chl concentration (left) and leaf Chl content (right) with measured reflectance at 820nm.

Summarizing

In short, the thorough assessment presented briefly above illuminated the likely but persistent influence of within plot heterogeneity relating to the plot's structure on the univariate correlation's results. More important, however, is this notion's relation to the scale difference of measurements for those metrics included in the univariate regression. More specifically, plot averaged reflectance and field trait measurements at 1, 2 or 4 locations in each plot, depending on the trait. The latter in particular is based on the assumption of relative within-plot homogeneity, and therefore on the notion that a small sample set sufficiently represents the whole of the plot. The sample locations, with respect to within-plot structural indifferences, produced trait measurement values that are indeed potentially valid by themselves, i.e. being representative for the areas in the close vicinity of the distinct sampling location. When regressed with plot averaged reflectance, however, non-sensible correlation coefficients were produced as a result from the assumption of homogeneity not being met sufficiently. This reasoning is further supported by the fact that anomalies were most numerous and influential for traits relying on a single sampling location (biomass, C & N). The severity of unanticipated correlations was less for traits relying on 2 (height in polyculture plots) or 4 samples (height in monoculture plots and leaf Chl), which by averaging are likely better able to correct for potential within-plot differences. Consequently, it was decided to remove all plots displaying small or extensive structural heterogeneity in one or multiple locations within the plot, for both the calibration (6, 28, 64, 77, 83b, 100 and 114b) and validation (69b, 70, 85, 91a, 101 and 116b) set, based on a visual inspection of the RGB orthomosaic and HDC (see also figure below).

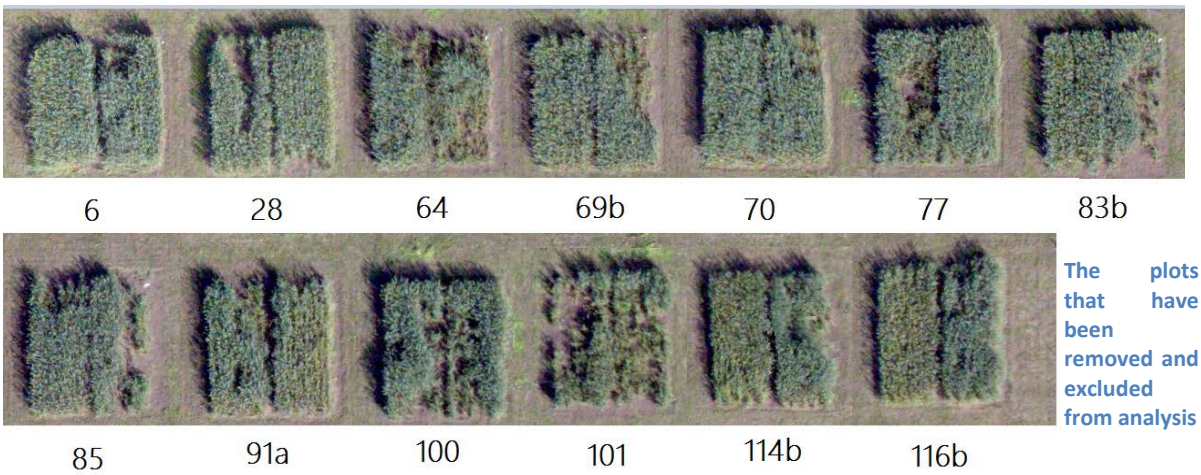

The plots that have been removed and excluded from analysis

The process of identifying individual plots with a certain degree of physical heterogeneity quickly revealed distinct pattern. Except for one, all of the identified plots received a treatment comprising of *Rapharus sativa* in a monoculture setting, or a polyculture setup in which the latter planting were combined with *Vicia sativa*. The latter was also observed by the researchers, monitoring the field experiment from the ground, soon after the first oat plants emerged. It is currently hypothesized that the heterogeneous and poor growth of oat plants in these plots may be directly related to the *Rapharus sativa* treatment, and the accumulation of pathogens and, to a lesser degree, nematodes that is believed to take off particularly well under this type of cover. It is subsequently argued that, during the deceasing of the *Rapharus sativa* treatment, unknown quantities of chemical phytotoxic substances have been released into the underlying soils. Hereafter the latter may have been able to affect the seedlings, either locally or zonally, and effectively slow down or entirely stall the subsequent development of oat plants.

During the course of the field experiment various soil samples have been collected and processed. The findings of this sampling at least partially underline the possibility of the hypothesis presented above,

although they are too inconclusive to provide irrefutable confirmation thereof. It has been found, for example, that nematodes have indeed accumulated relatively successfully under the *Rapharus sativa* treatment, although the increase is too limited to explain the whole. Likewise, the phytotoxic substances that were assumingly released during the dying of *Rapharus sativa* crops are glucosinolates that are believed to slay pathogens and nematodes to a certain degree, hereby potentially promoting the growth of oats plants rather than slowing it down. It is, however, not excluded that the nematodes found in the soil samples are factually less susceptible to such glucosinolates than is to be anticipated. Similarly important is the notion that the soil samples were acquired at the beginning of December prior to the introduction of the *Rapharus sativa* treatment. It is believed that the releasing of glucosinolates is highly varied across the different development stages of *Rapharus sativa* and, resultantly, the soil samples may not provide a valid representation of the soil conditions when the oats were sowed a few months later. Consequently, considering these influential deliberations, the cause(s) underlying the observed physical within plot heterogeneity can neither be confirmed nor precluded. Additional research is ultimately required to further assess the validity of the hypothesis. Regardless of the actual validity of the deliberations presented above, however, it is argued that the removal of this selection of plots can be justified for due to notion that the observed within plot physical heterogeneity is in conflict with the assumed plot homogeneity on which sampling procedures were initially grounded (paragraph 5.2).

Appendix G: Scatter plots indices –vs- traits (Calibration)

The below figures depict the scatter plots resulting from regression of index values and in situ measured trait values during calibration, on the horizontal and vertical axis, respectively. For each trait, the first three scatter plots relate to the best selected existing indices that were identified during calibration (table 8.1). Subsequently, these are followed by the three (four for fresh biomass) best performing new optimized indices as given in table 8.3. The scatter plots resulting from the regression of PLS models and measured traits values are presented separately in appendix I.

Height

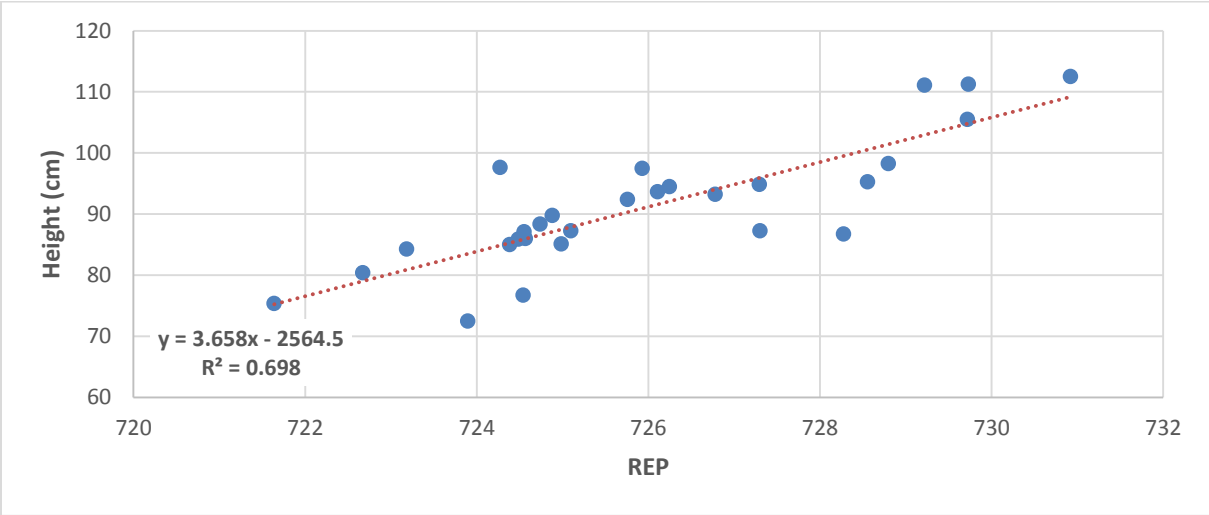

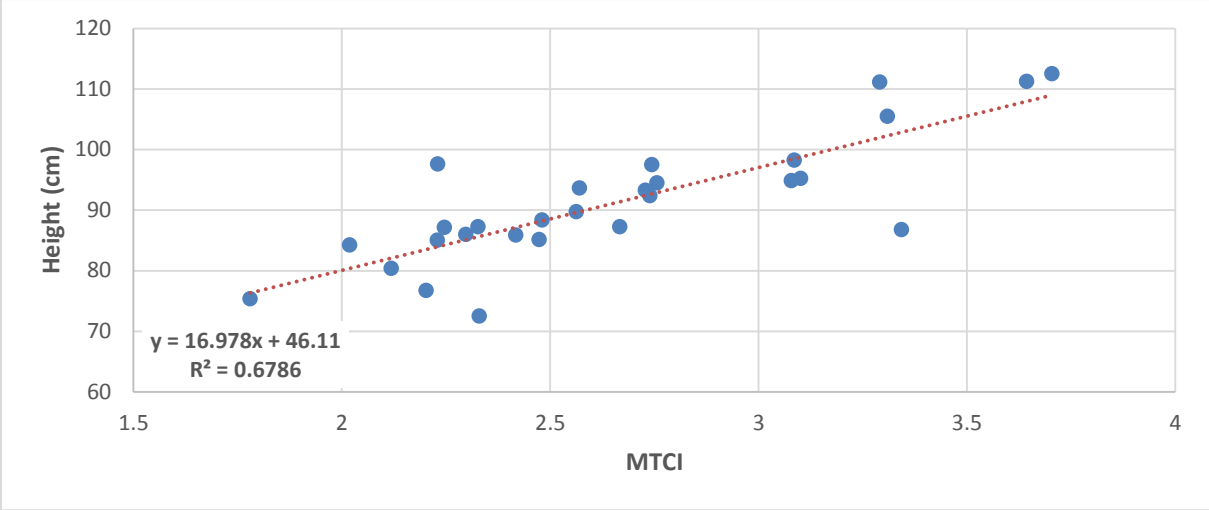

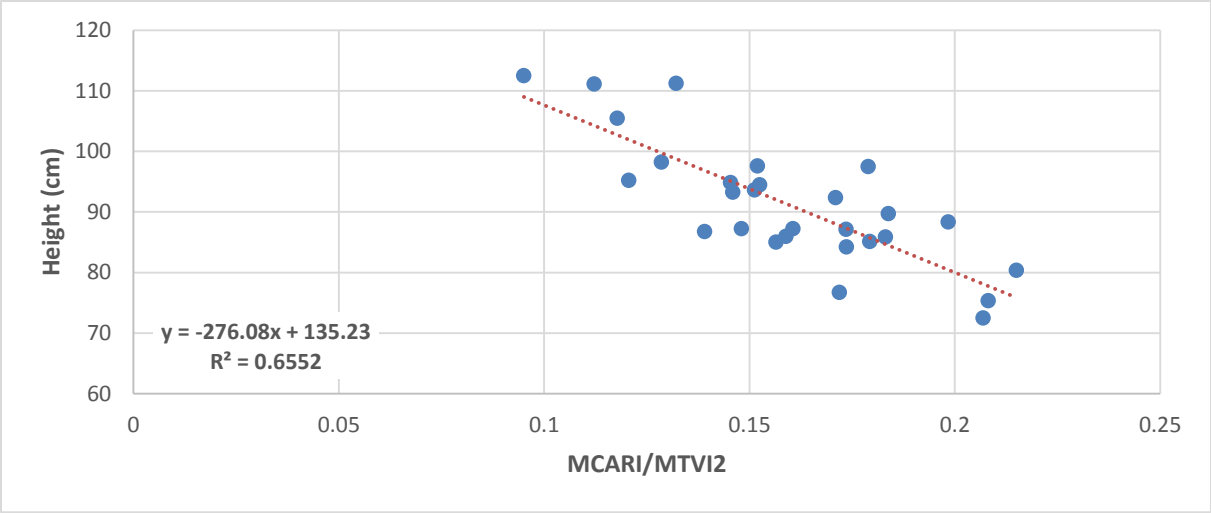
Height (cm)
MCARI/MTVI2
y = -276.08x + 135.23
R² = 0.6552

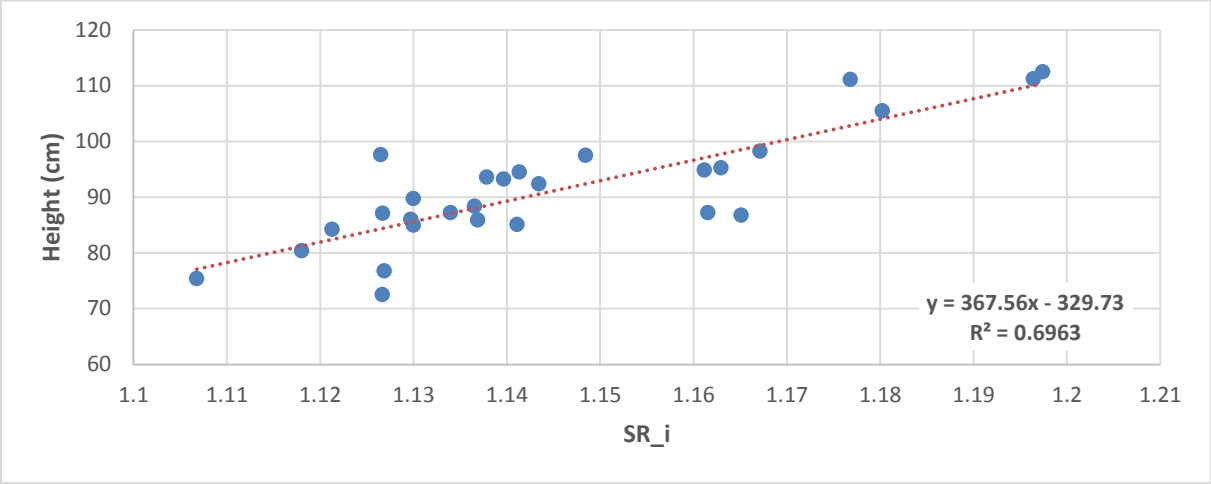
Height (cm)
SR_i
y = 367.56x - 329.73
R² = 0.6963

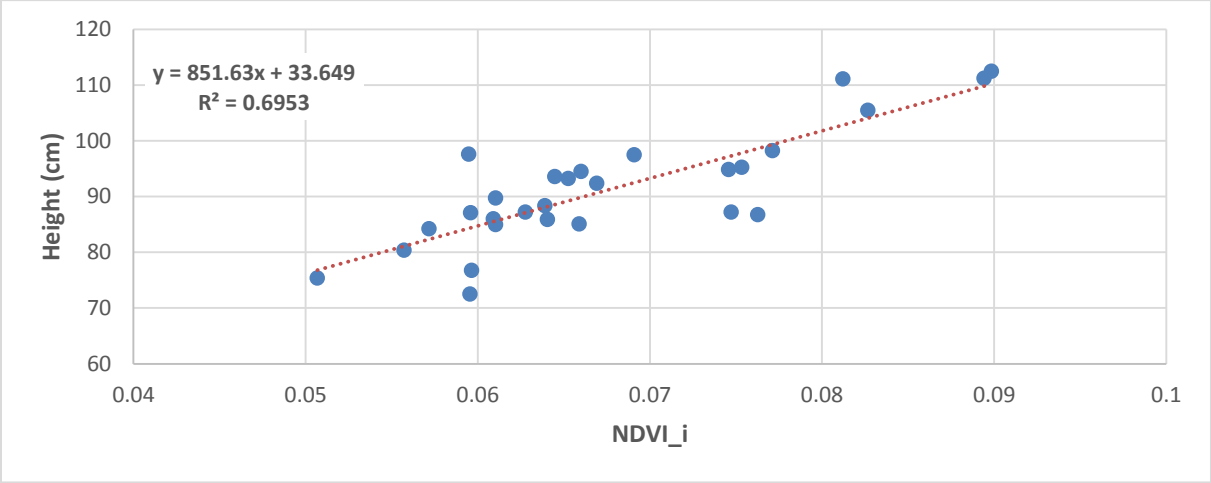
Height (cm)
NDVI_i
y = 851.63x + 33.649
R² = 0.6953

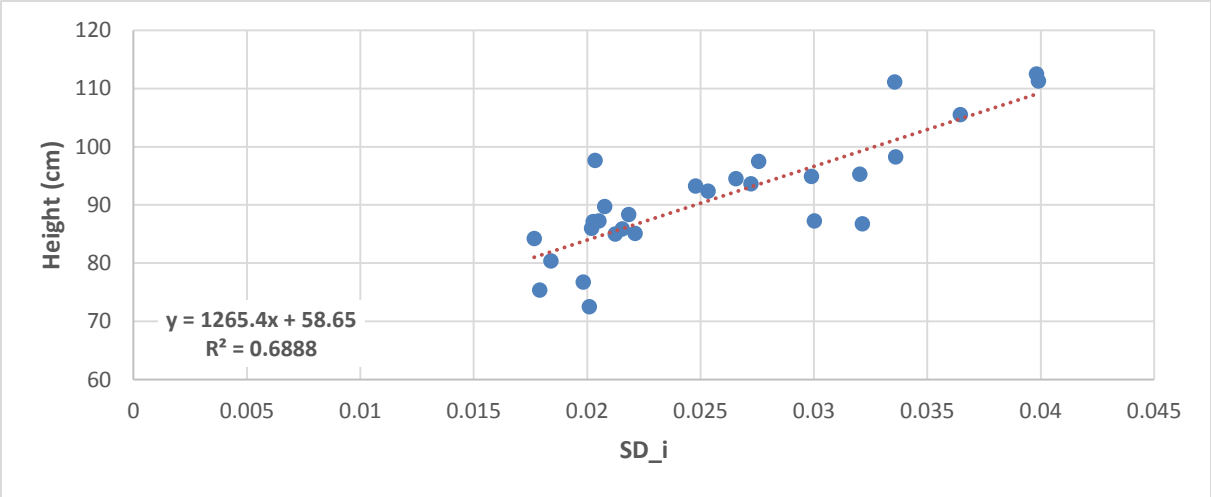
120
110
100
90
80
70
60
Height (cm)
y = 1265.4x + 58.65
R² = 0.6888
0
0.005
0.01
0.015
0.02
0.025
0.03
0.035
0.04
0.045
SD_i

Fresh biomass (FBM)

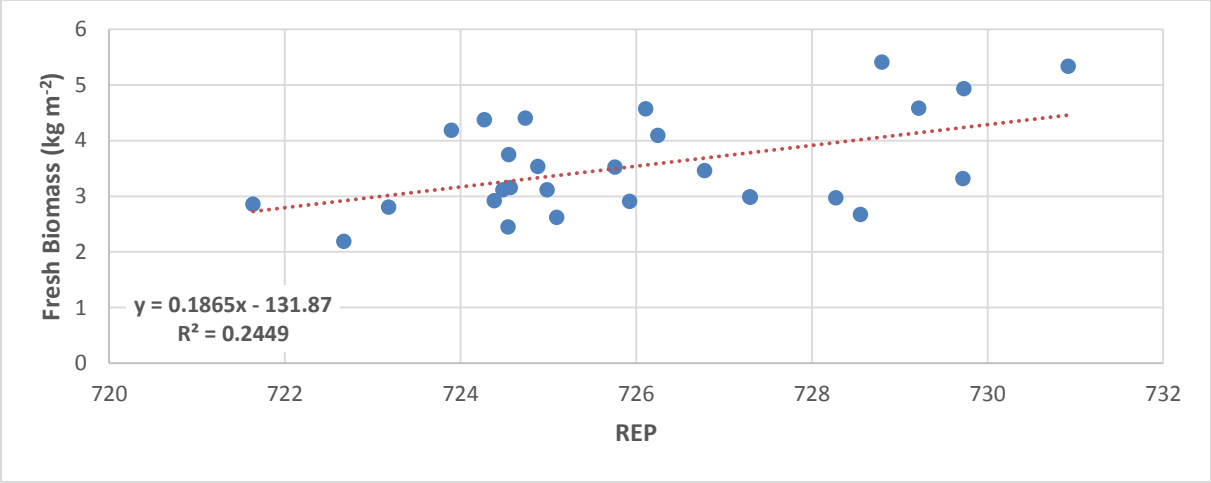

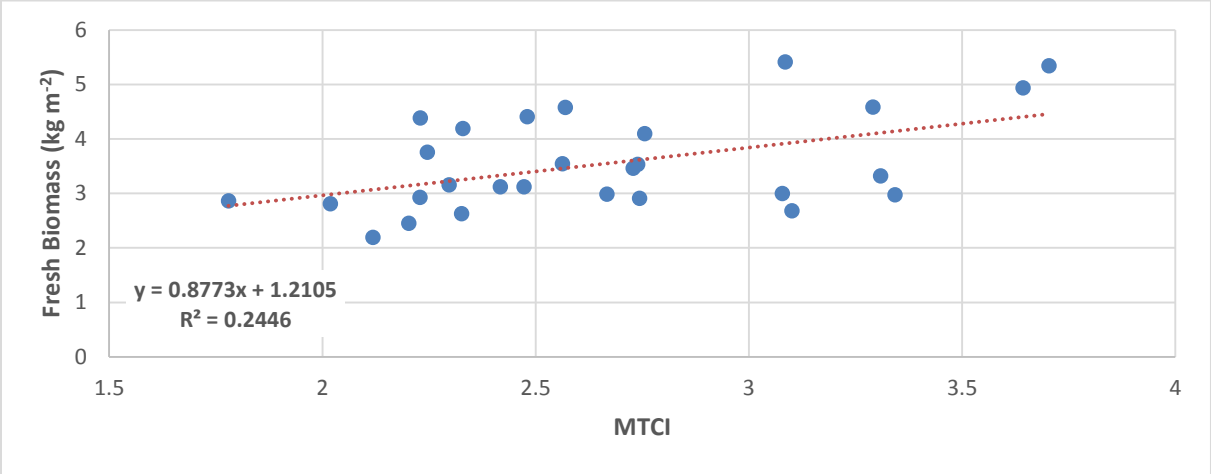

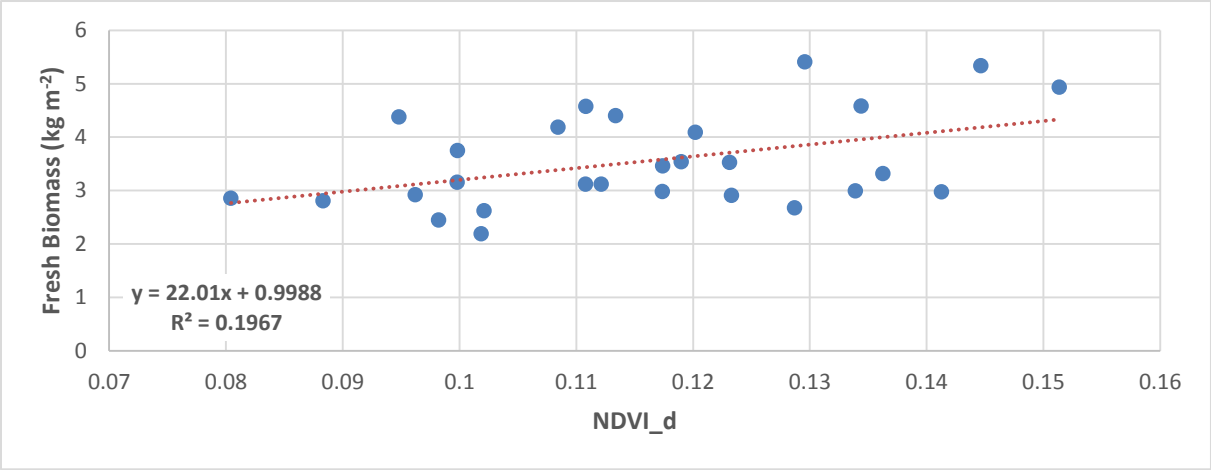

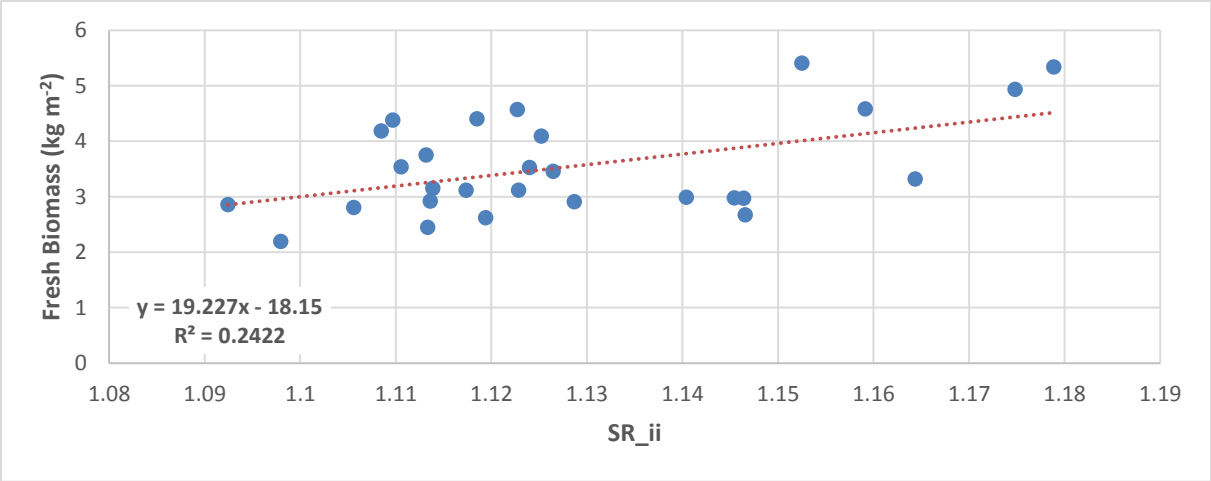
Fresh Biomass (kg m-2)
SR_ii
y = 19.227x - 18.15
R² = 0.2422
0
1
2
3
4
5
6
1.08
1.09
1.1
1.11
1.12
1.13
1.14
1.15
1.16
1.17
1.18
1.19

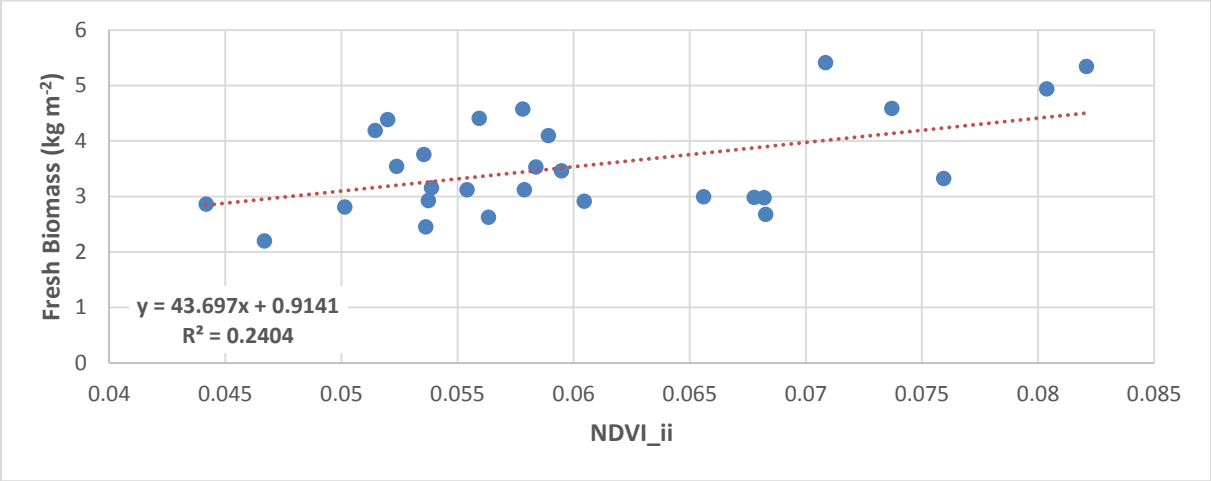
Fresh Biomass (kg m-2)
NDVI_ii
y = 43.697x + 0.9141
R² = 0.2404
0
1
2
3
4
5
6
0.04
0.045
0.05
0.055
0.06
0.065
0.07
0.075
0.08
0.085

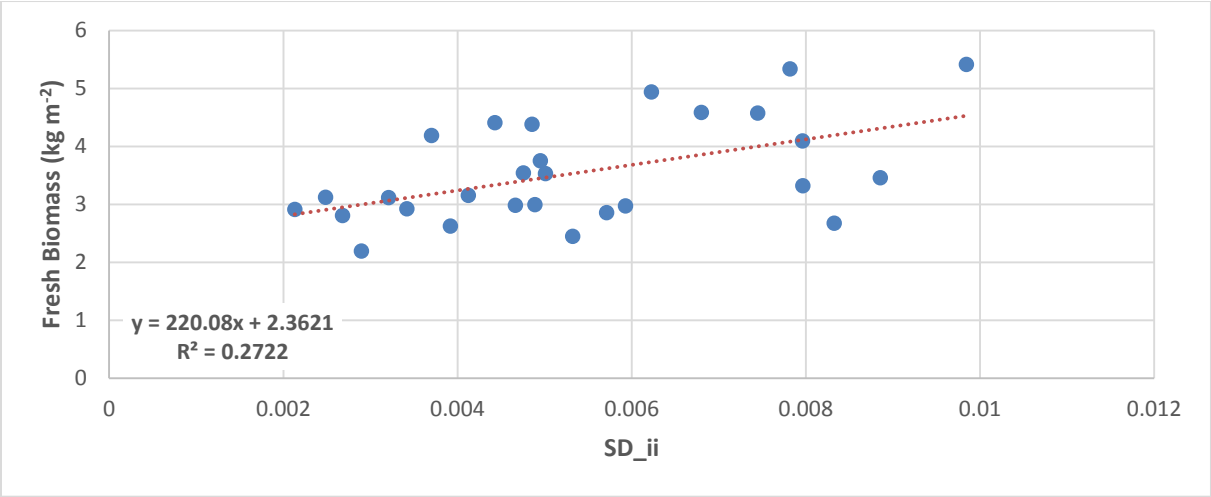
Fresh Biomass (kg m-2)
SD_ii
y = 220.08x + 2.3621
R² = 0.2722
0
1
2
3
4
5
6
0
0.002
0.004
0.006
0.008
0.01
0.012

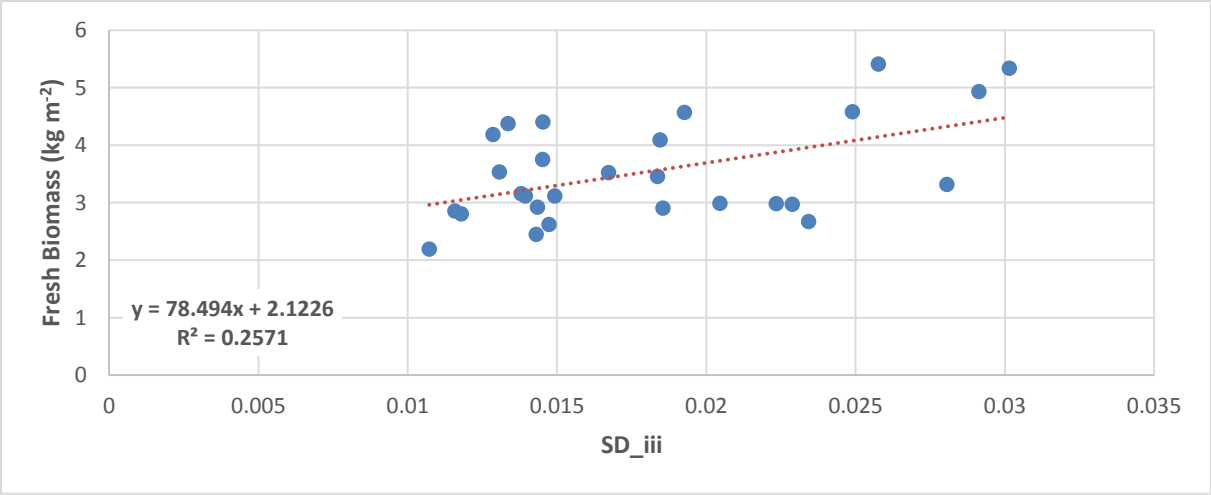
Fresh Biomass (kg m-2)
6
5
4
3
2
1
0
y = 78.494x + 2.1226
R² = 0.2571
0
0.005
0.01
0.015
0.02
0.025
0.03
0.035
SD_iii

Nitrogen content (N)

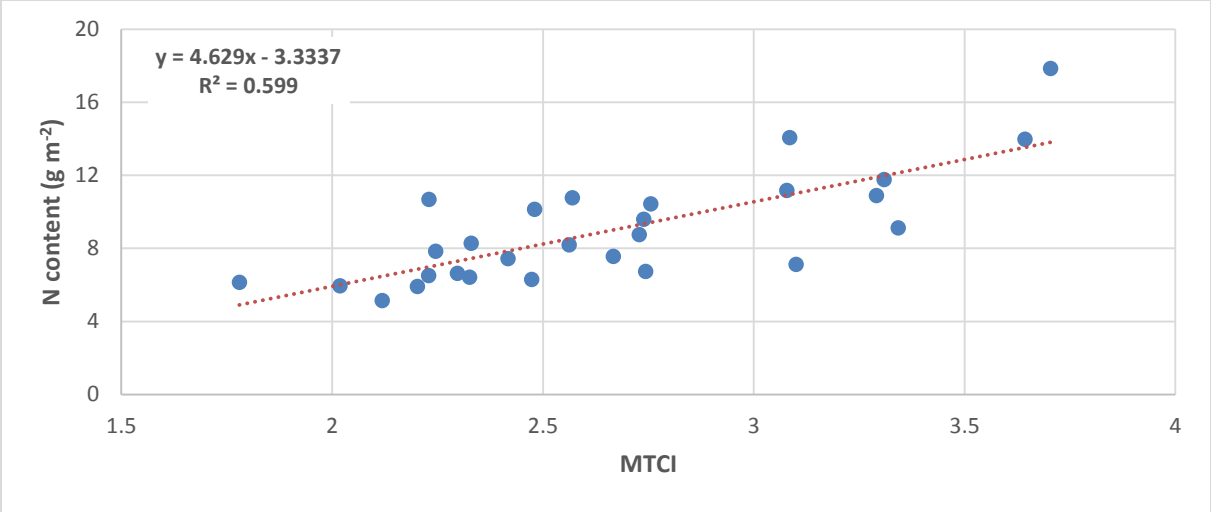

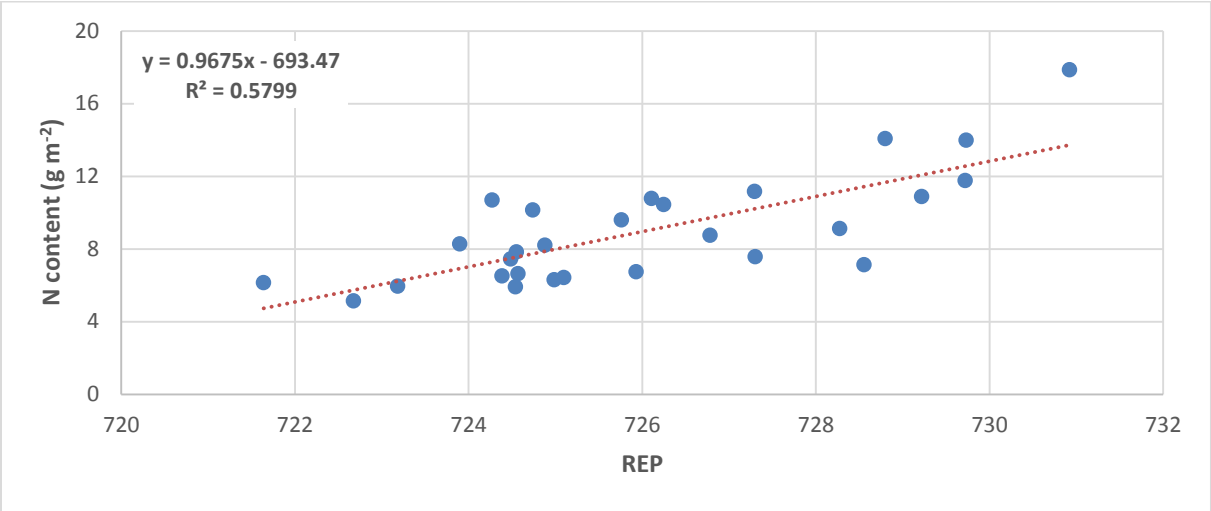

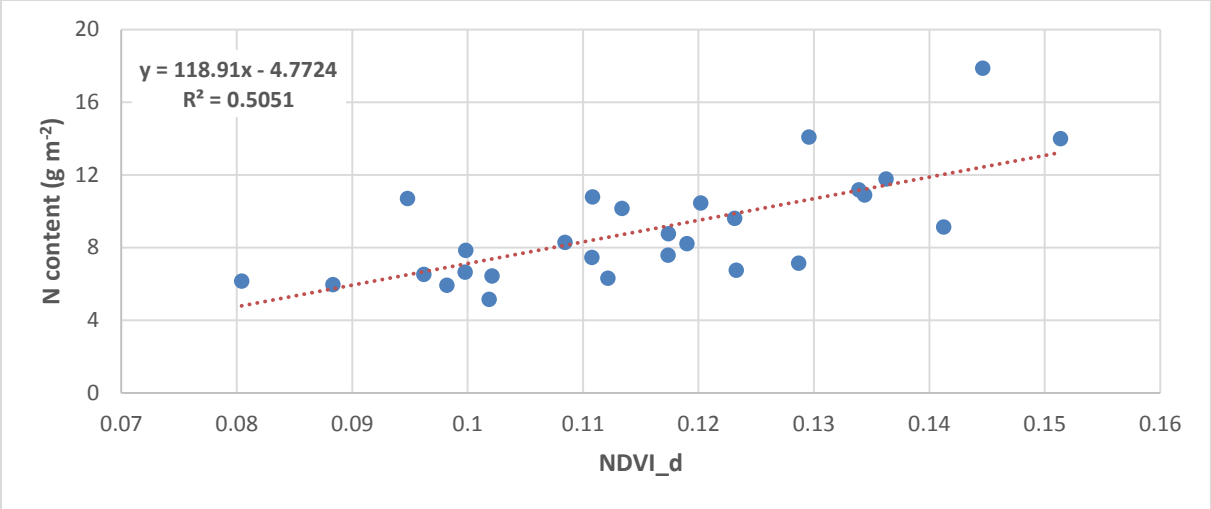

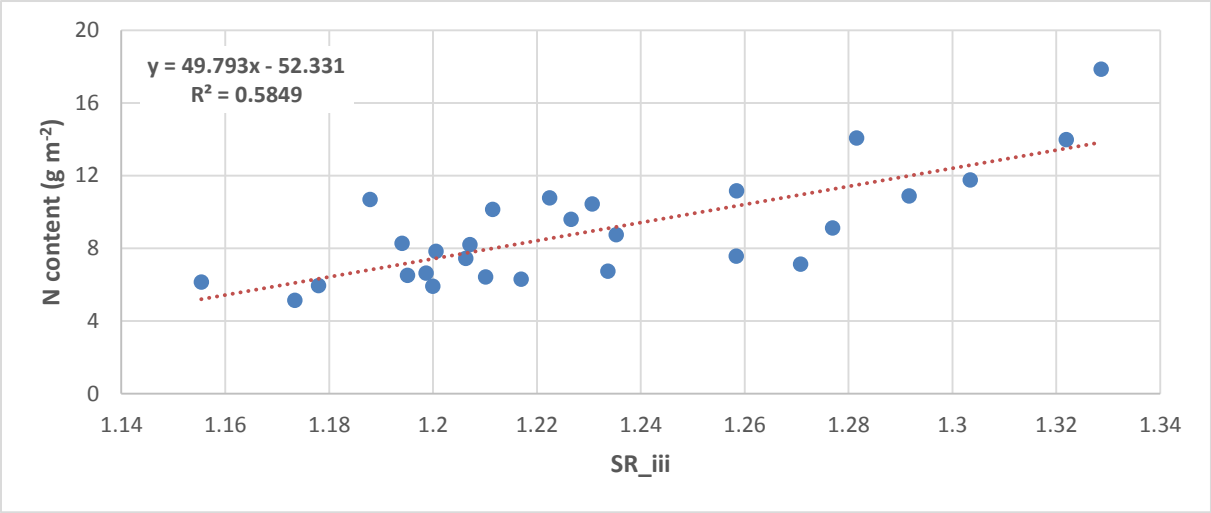
y = 49.793x - 52.331
R² = 0.5849
N content (g m-2)
SR_iii
0
4
8
12
16
20
1.14
1.16
1.18
1.2
1.22
1.24
1.26
1.28
1.3
1.32
1.34

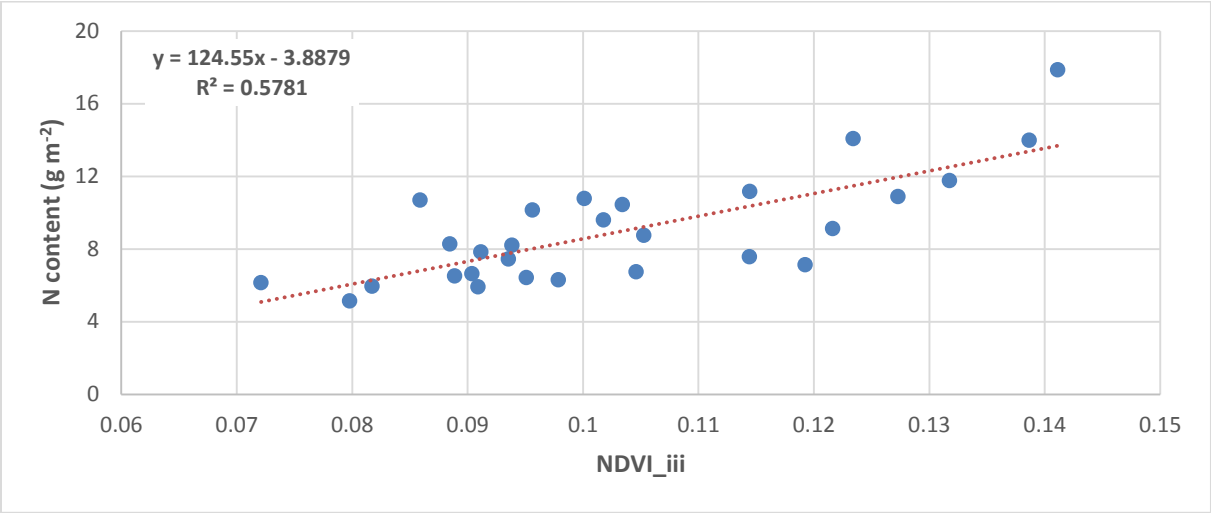
y = 124.55x - 3.8879
R² = 0.5781
N content (g m-2)
NDVI_iii
0
4
8
12
16
20
0.06
0.07
0.08
0.09
0.1
0.11
0.12
0.13
0.14
0.15

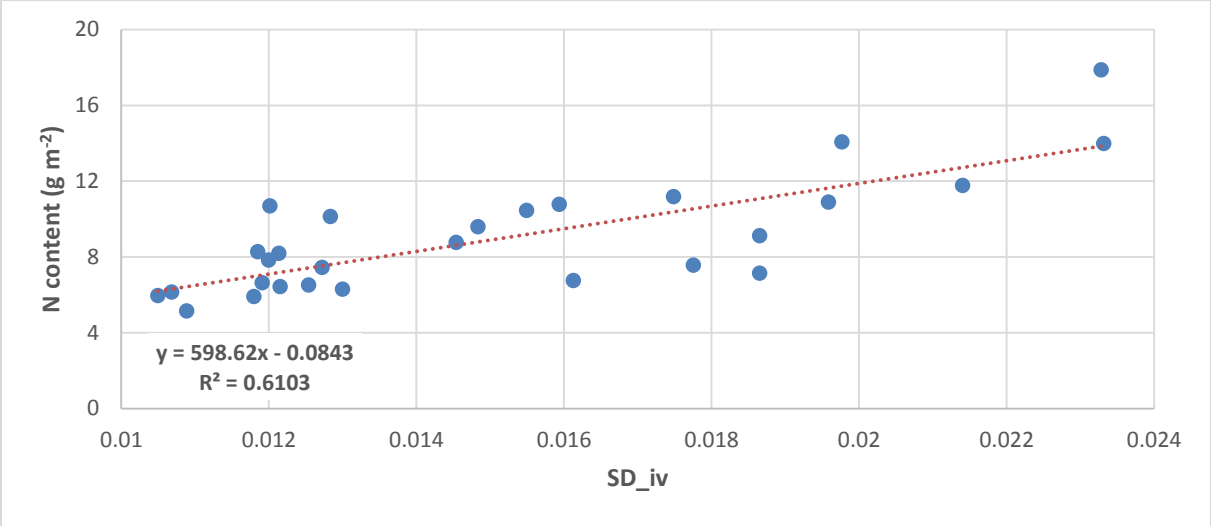
y = 598.62x - 0.0843
R² = 0.6103
N content (g m-2)
SD_iv
0
4
8
12
16
20
0.01
0.012
0.014
0.016
0.018
0.02
0.022
0.024

Carbon content (C)

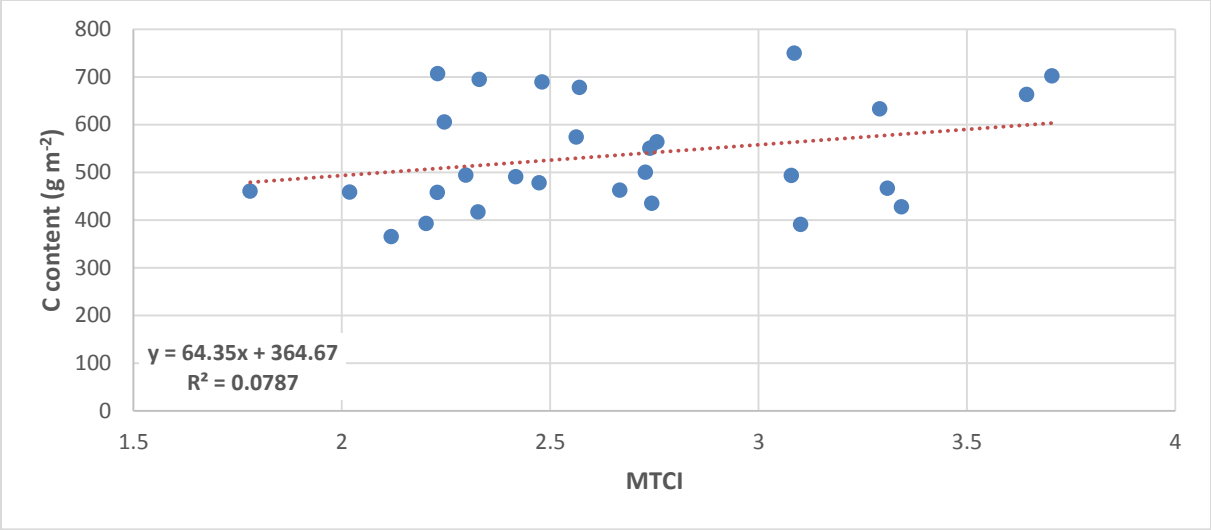

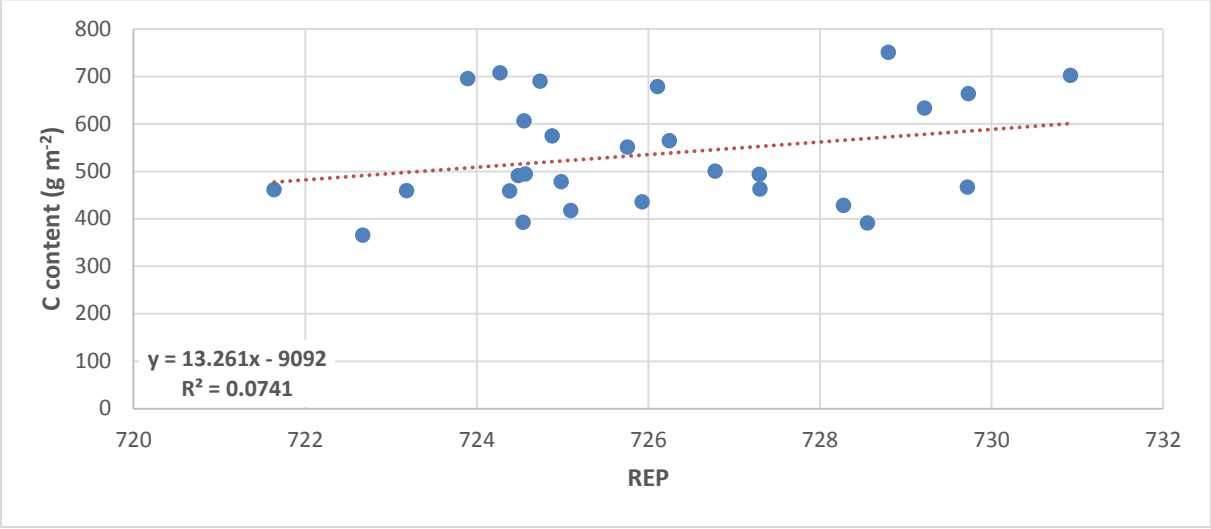

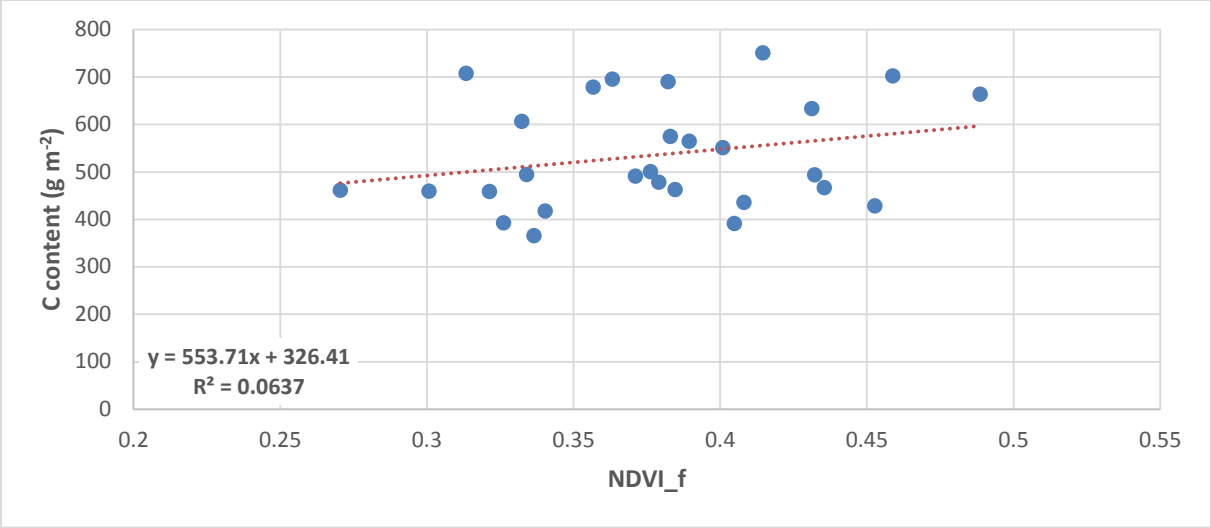

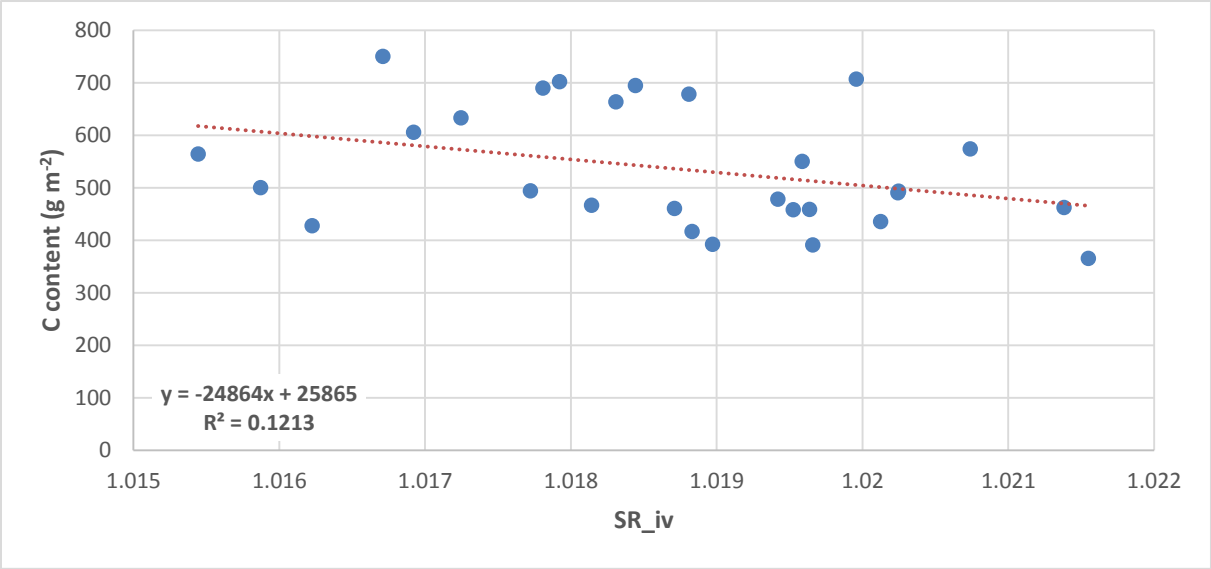
C content (g m-2)
800
700
600
500
400
300
200
100
0
y = -24864x + 25865
R² = 0.1213
1.015
1.016
1.017
1.018
1.019
1.02
1.021
1.022
SR_iv

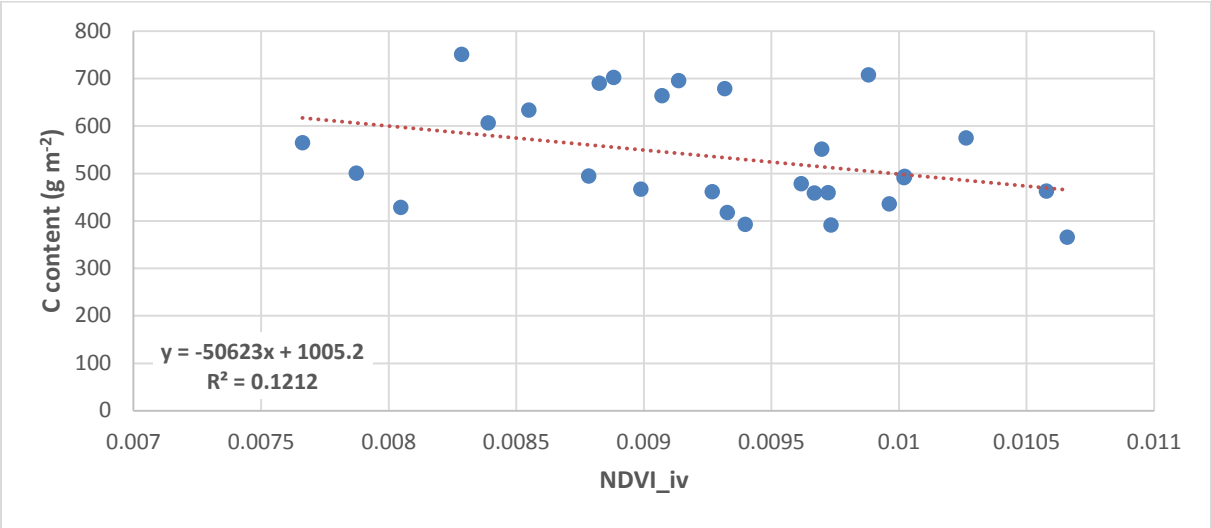
C content (g m-2)
800
700
600
500
400
300
200
100
0
y = -50623x + 1005.2
R² = 0.1212
0.007
0.0075
0.008
0.0085
0.009
0.0095
0.01
0.0105
0.011
NDVI_iv

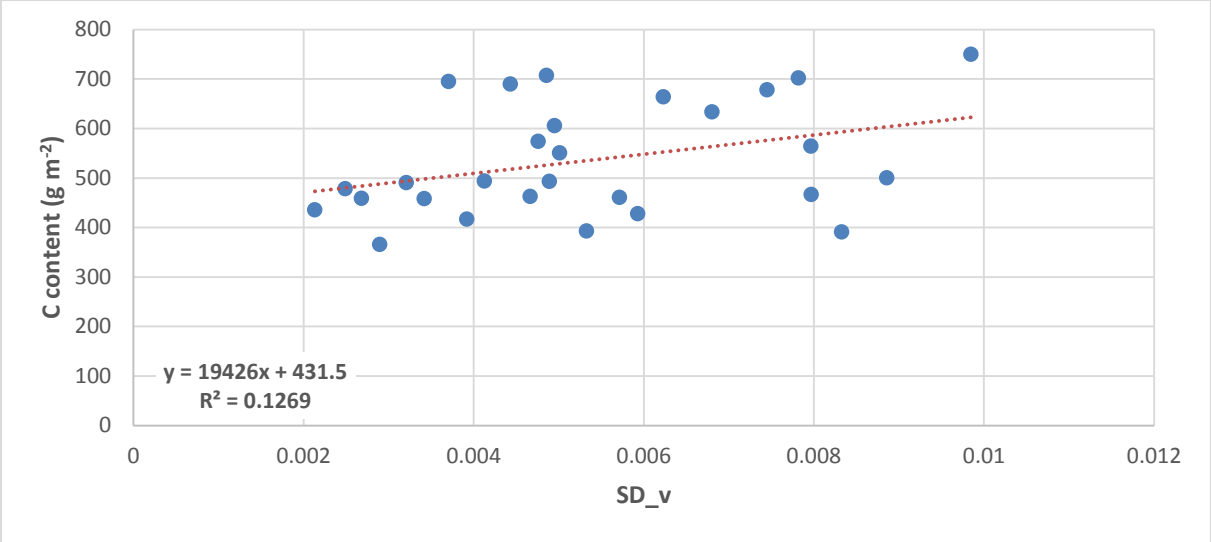
C content (g m-2)
800
700
600
500
400
300
200
100
0
y = 19426x + 431.5
R² = 0.1269
0
0.002
0.004
0.006
0.008
0.01
0.012
SD_v

Leaf Chl content (PLA = Projected Leaf Area)

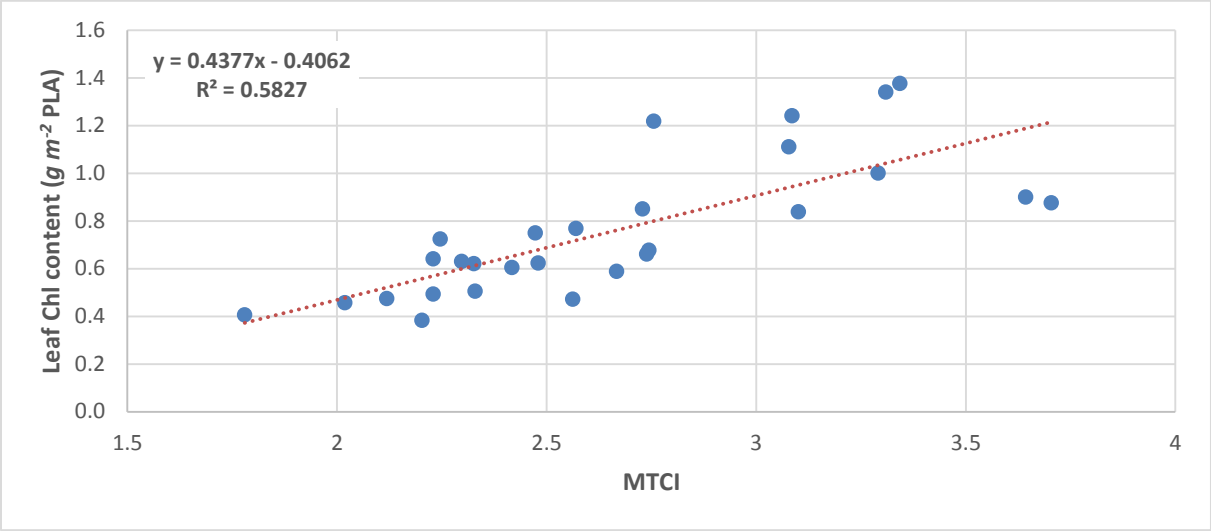

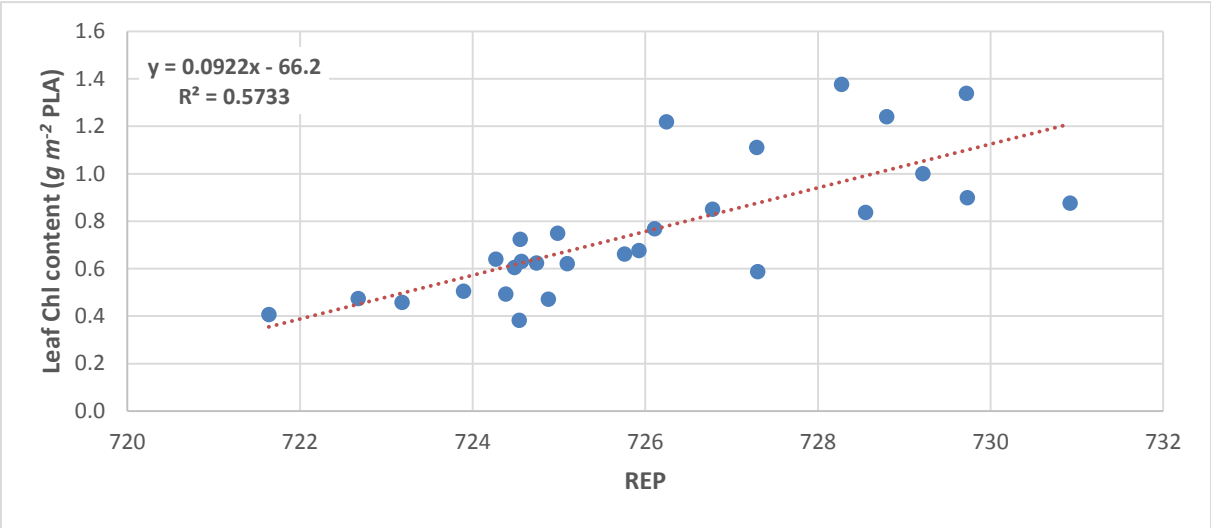

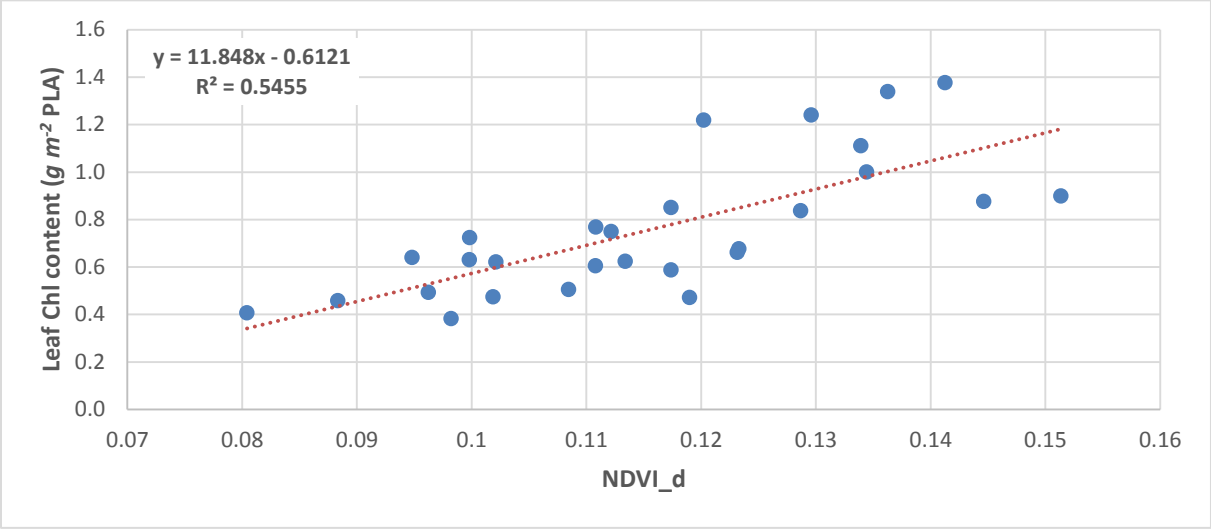

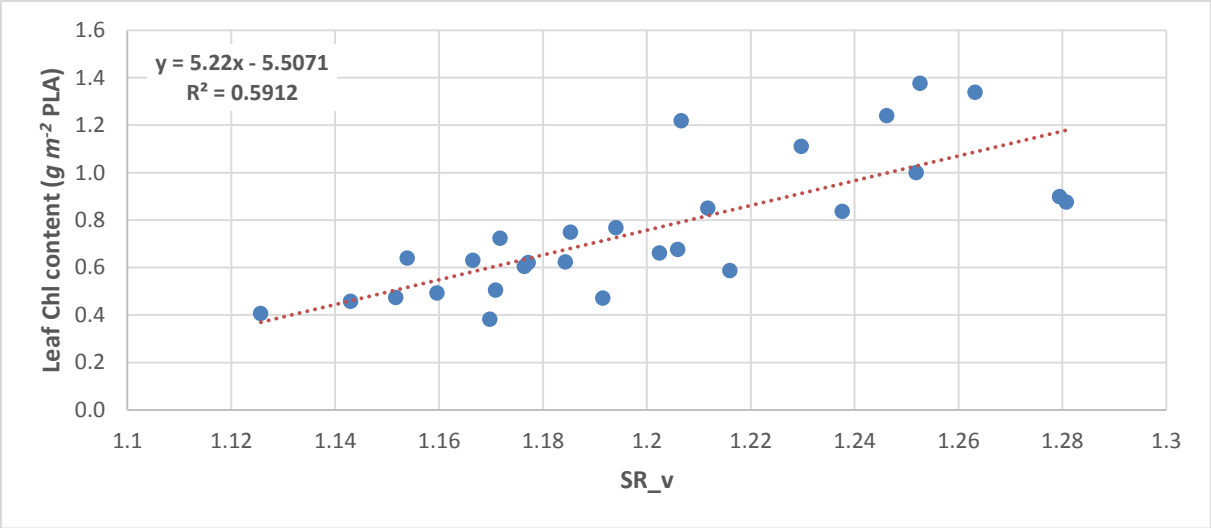
y = 5.22x - 5.5071
R² = 0.5912
Leaf Chl content (g m-2 PLA)
SR_v
1.6
1.4
1.2
1.0
0.8
0.6
0.4
0.2
0.0
1.1
1.12
1.14
1.16
1.18
1.2
1.22
1.24
1.26
1.28
1.3

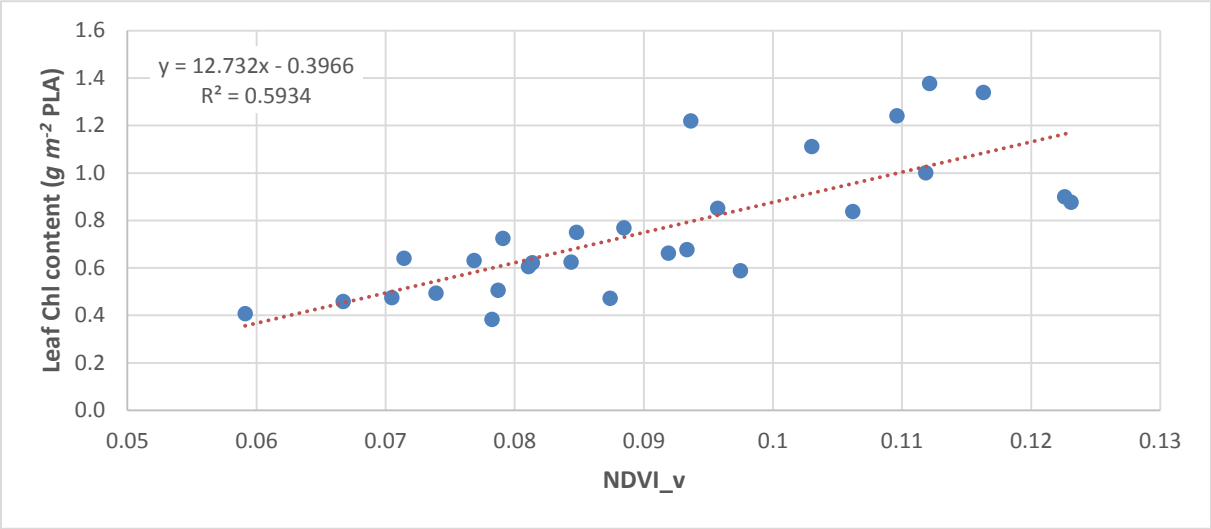
y = 12.732x - 0.3966
R² = 0.5934
Leaf Chl content (g m-2 PLA)
NDVI_v
1.6
1.4
1.2
1.0
0.8
0.6
0.4
0.2
0.0
0.05
0.06
0.07
0.08
0.09
0.1
0.11
0.12
0.13

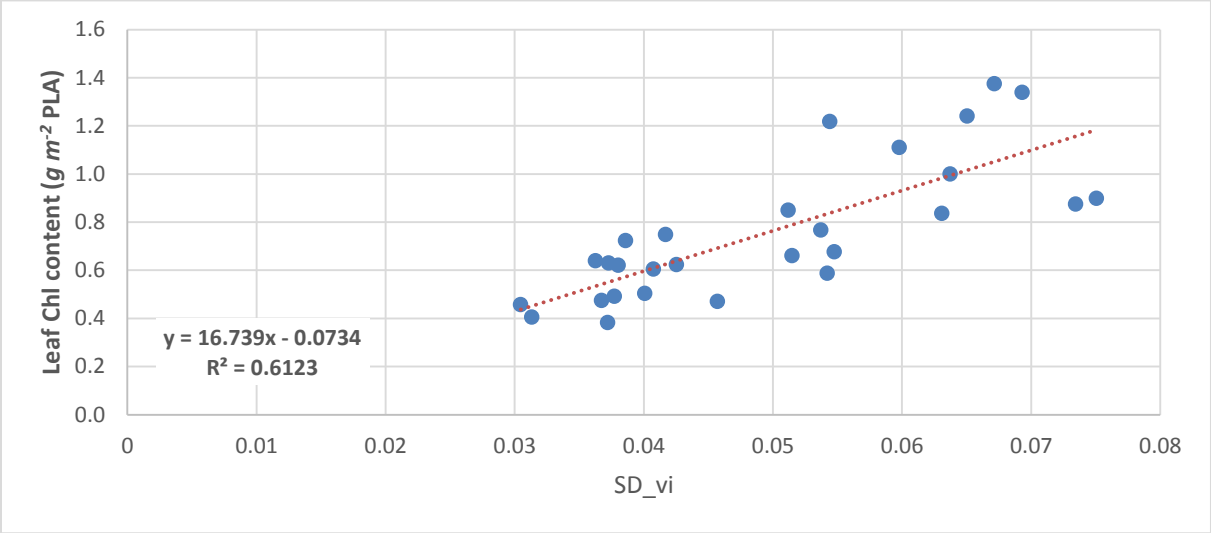
y = 16.739x - 0.0734
R² = 0.6123
Leaf Chl content (g m-2 PLA)
SD_vi
1.6
1.4
1.2
1.0
0.8
0.6
0.4
0.2
0.0
0
0.01
0.02
0.03
0.04
0.05
0.06
0.07
0.08

Appendix H: Contour plots (Calibration)

The below figures depict the contour plots resulting from regression of all possible band combinations in two-band SR/NDVI/SD indices with distinct traits. The presented colors render the coefficient of determination resulting from this regression for each possible index arrangement, of which the quantitative value may be distilled from the gradient legend on the right side of each plot.

Simple Ratio Indices: (λ1/λ2)

Height

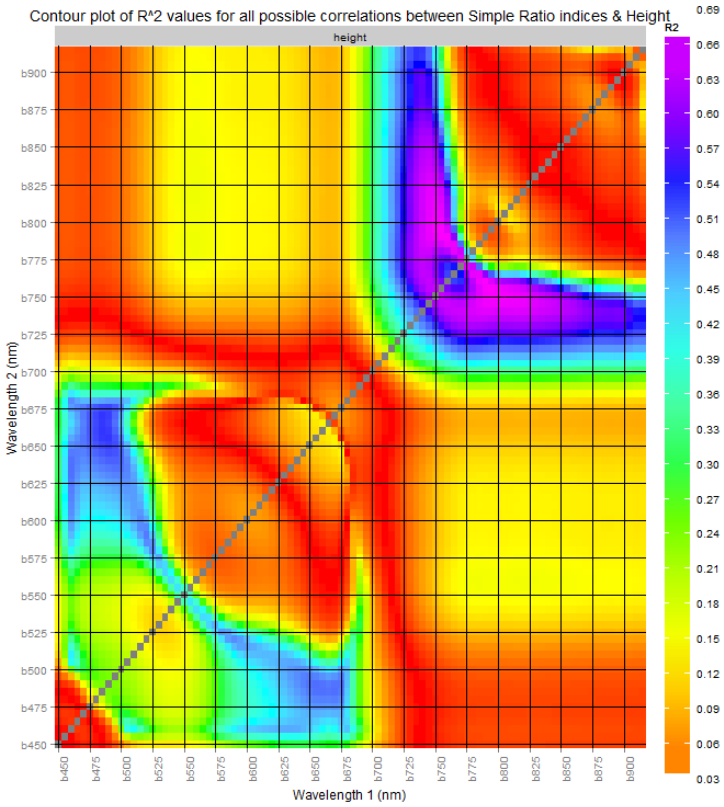

Fresh biomass (FBM)

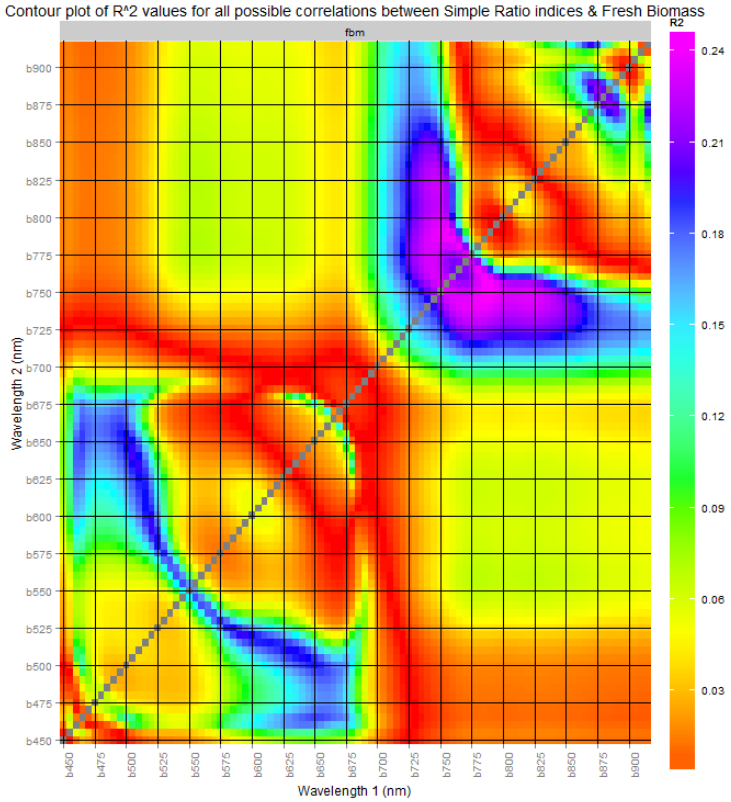

Nitrogen content (N)

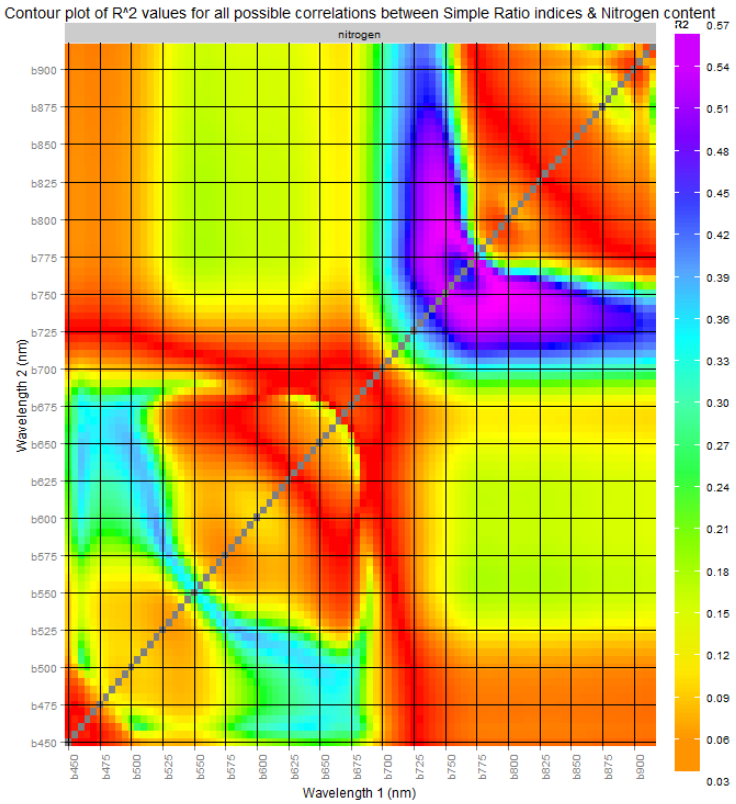

Carbon content (C)

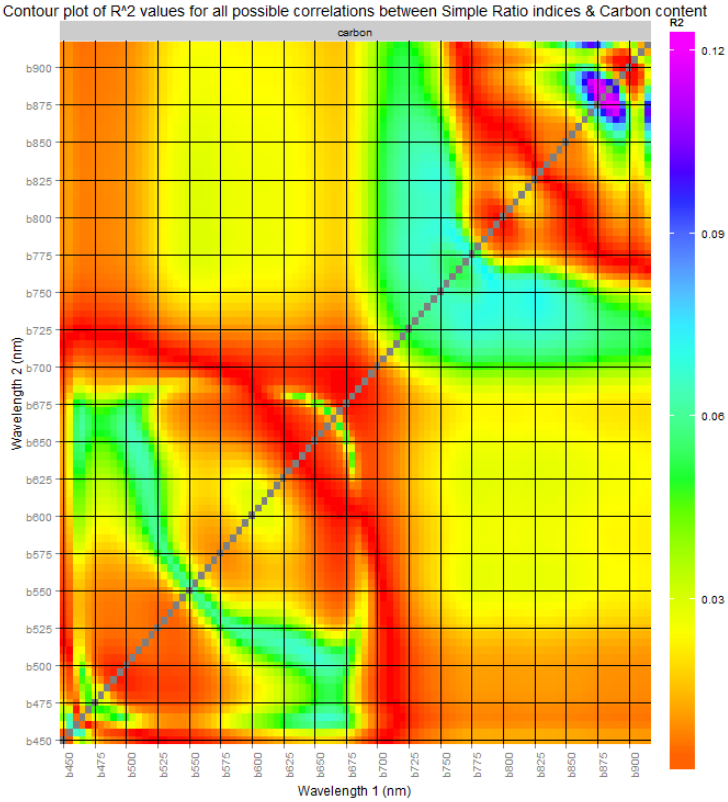

Leaf Chl content

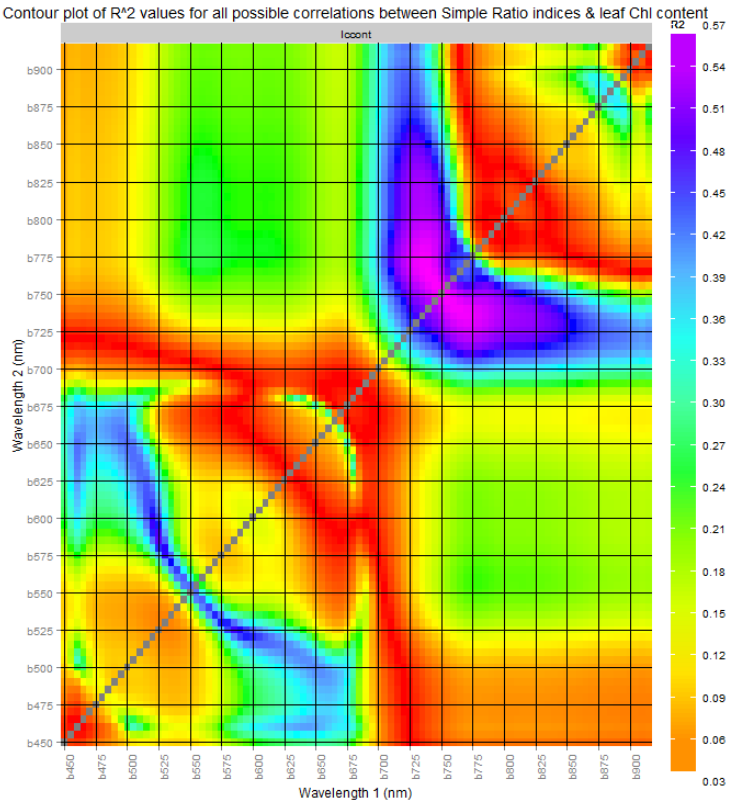

Normalized Difference Vegetation Indices: (λ2-λ1/λ2+λ1)

Height

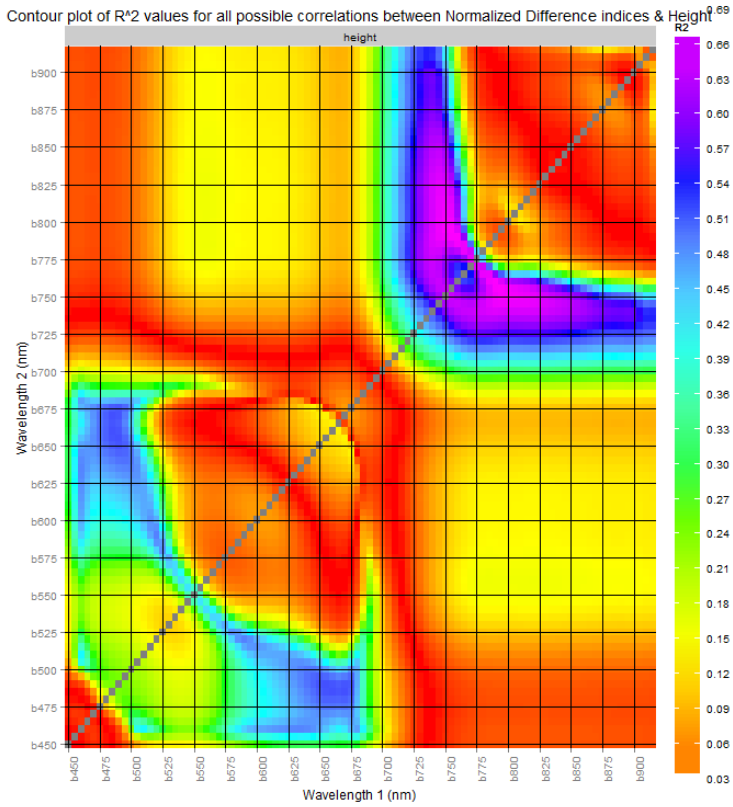

Fresh biomass (FBM)

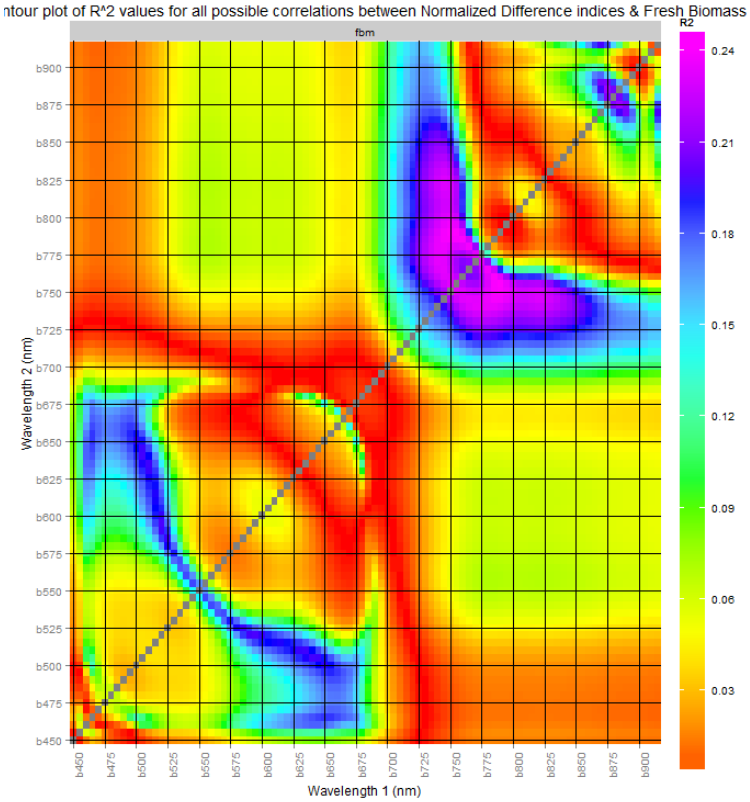

Nitrogen content (N)

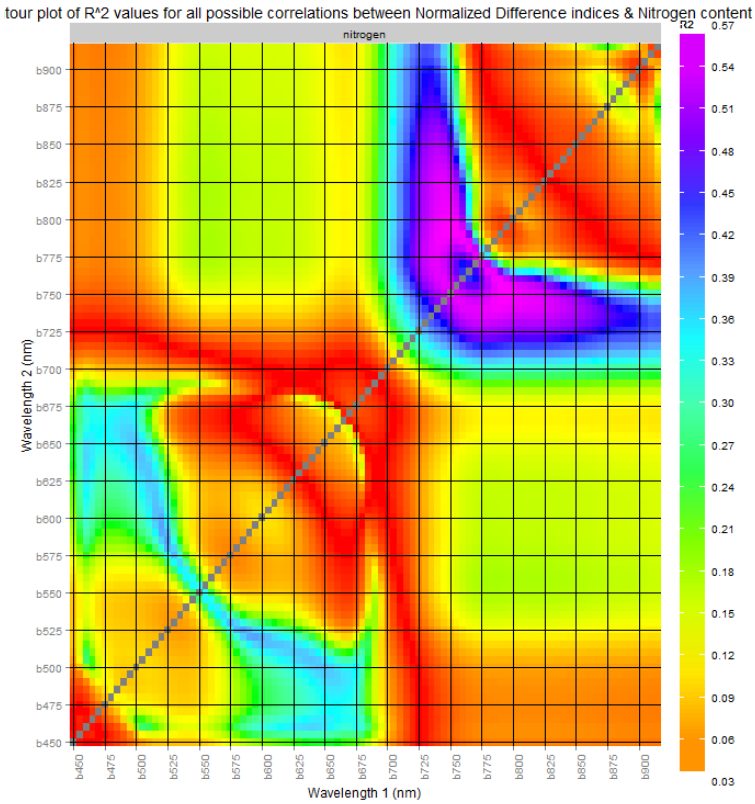

Carbon content (C)

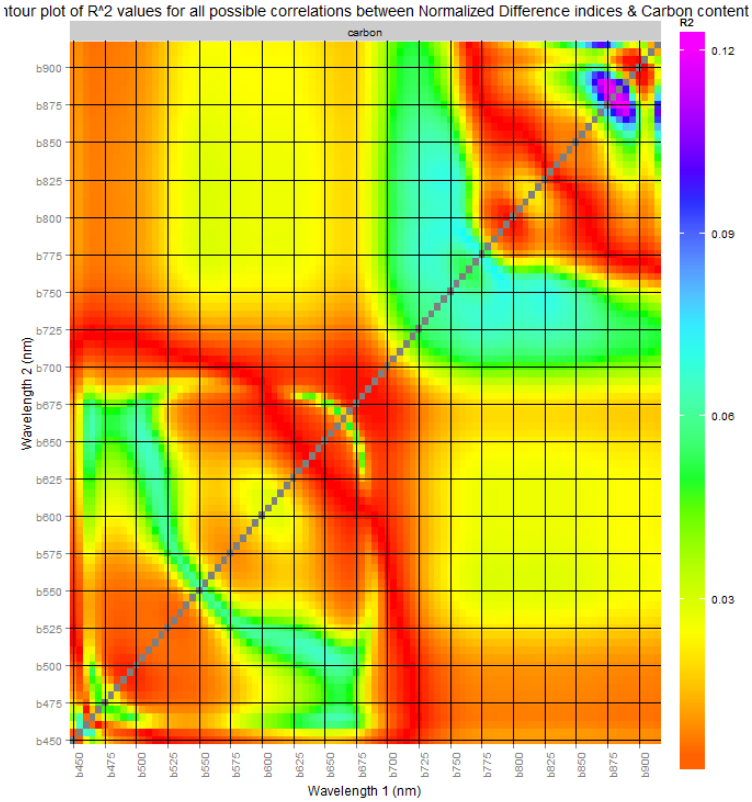

Leaf Chl content

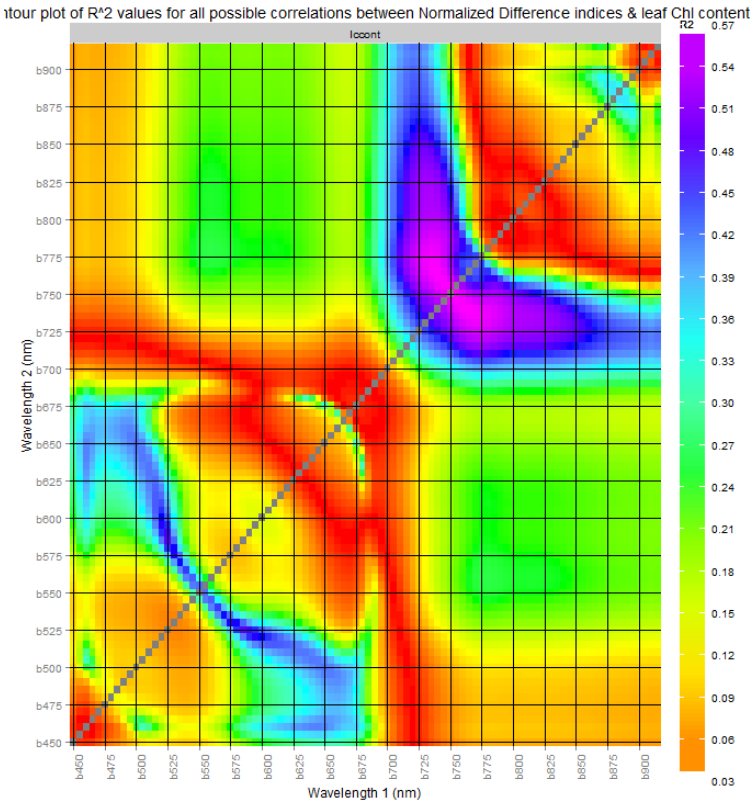

Simple Difference Indices: (λ1-λ2)

Height

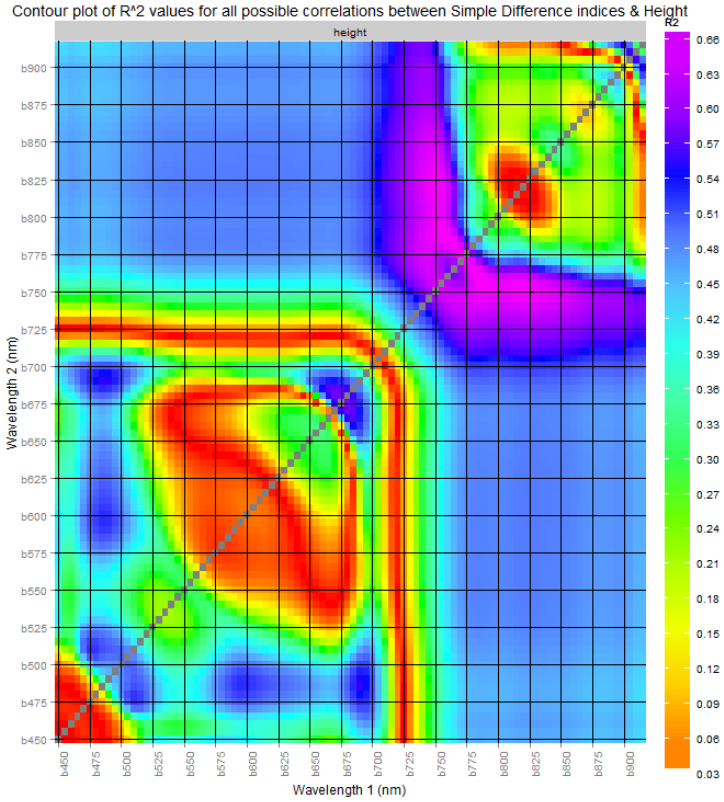

Fresh biomass (FBM)

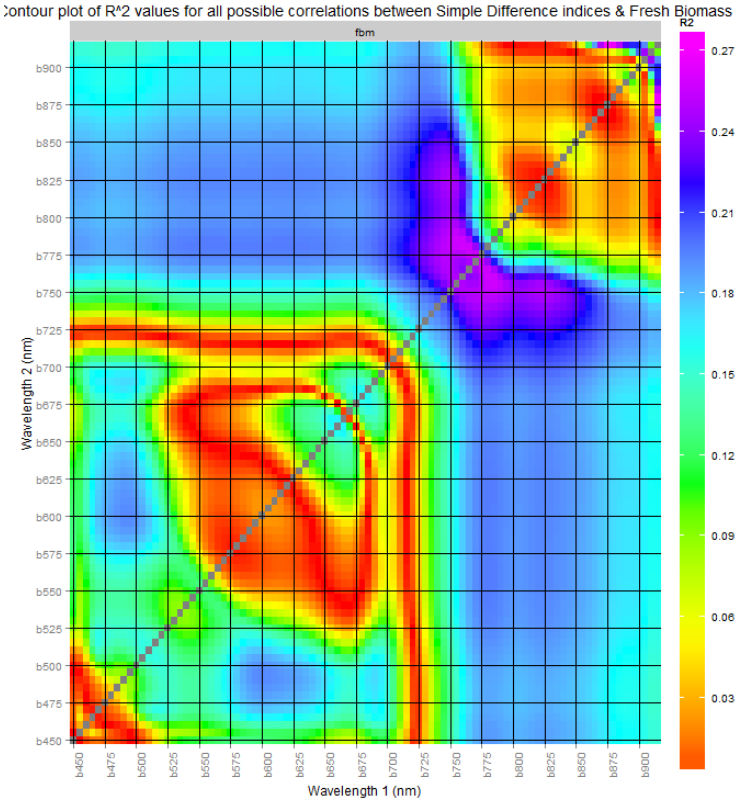

Nitrogen content (N)

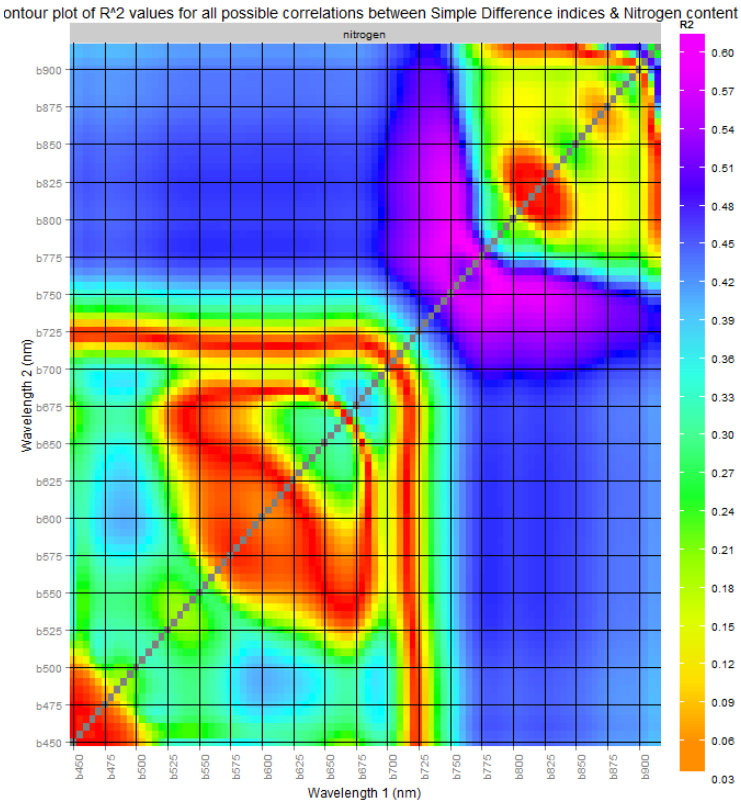

Carbon content (C)

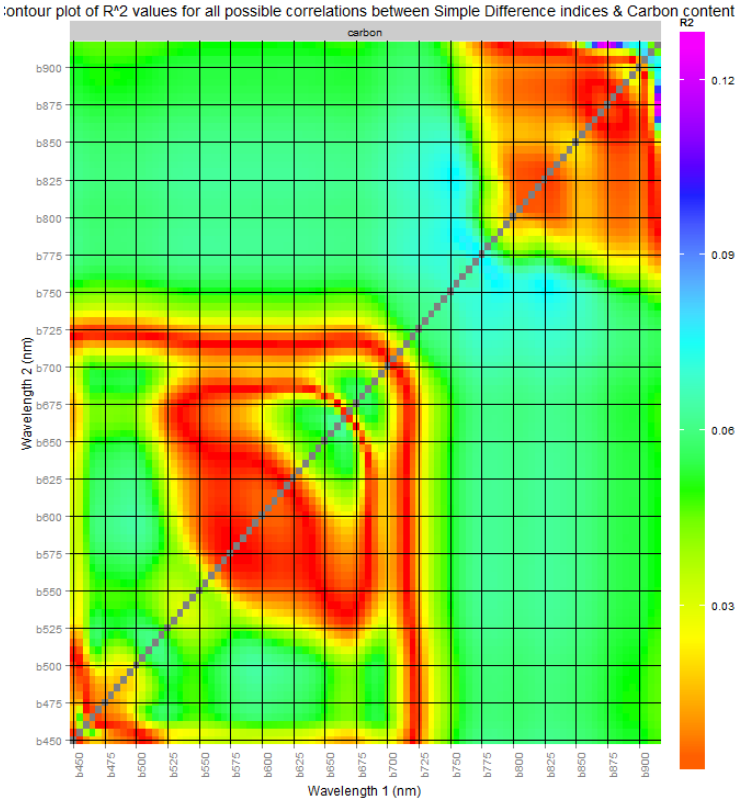

Leaf Chl content

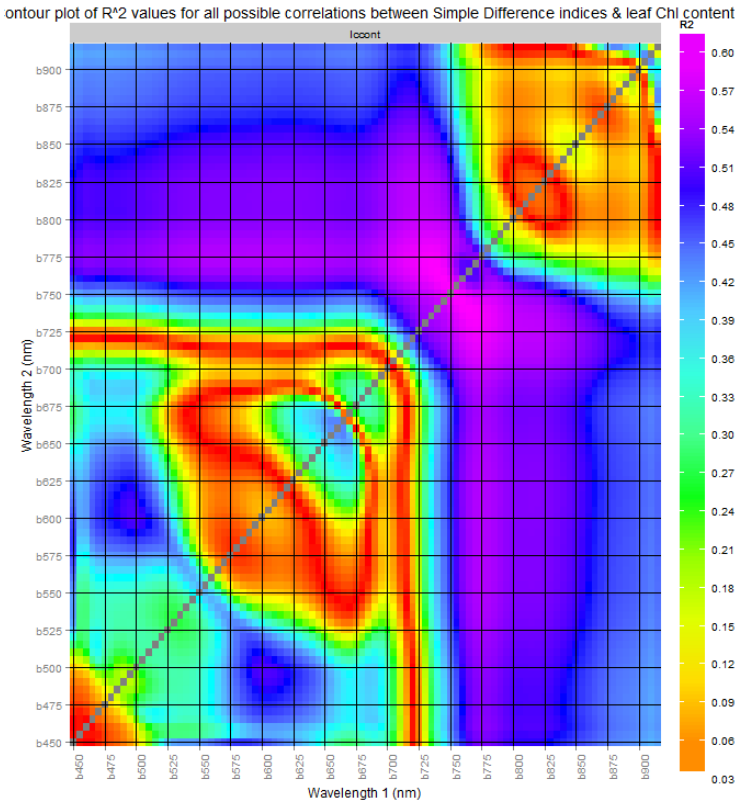

Appendix I: PLS figures (Calibration)

PLS calibration using spectral data only

Below, the plots used in the PLS calibration process are presented. For each trait, the first plot visualizes the relation between the number of components (latent variables) included in the model and the RMSEP associated with the resultant model. Subsequently, the plot depicting the loading weights for individual explanatory (x) variables is given for 1…*n* components, the values in parentheses in the legend depict the relative amount of x variance explained by each component. The third graph indicates the regression coefficients assigned to each explanatory (x) variable for 1…*n* components included in the PLS model.

Height

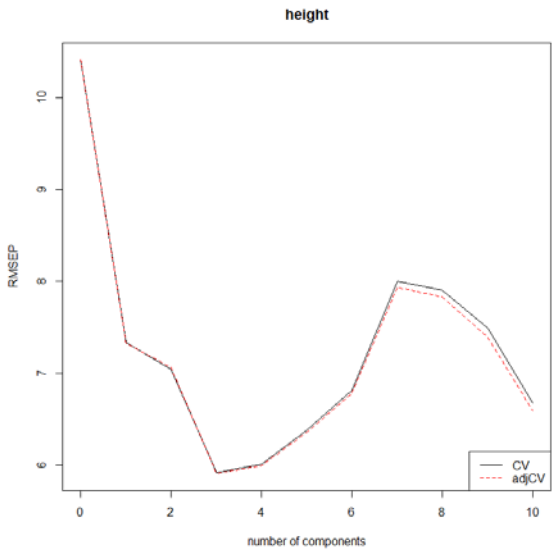

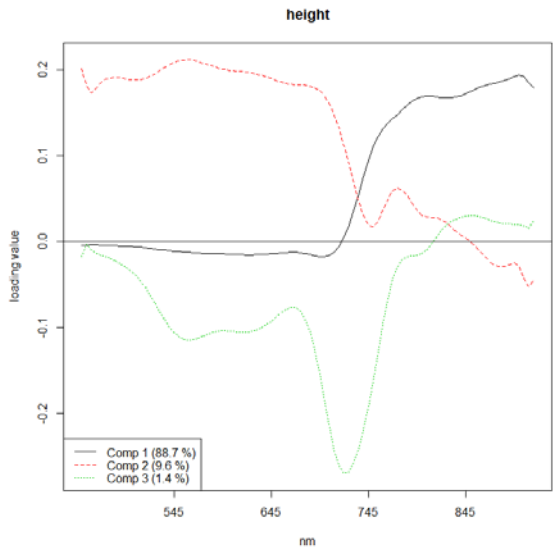

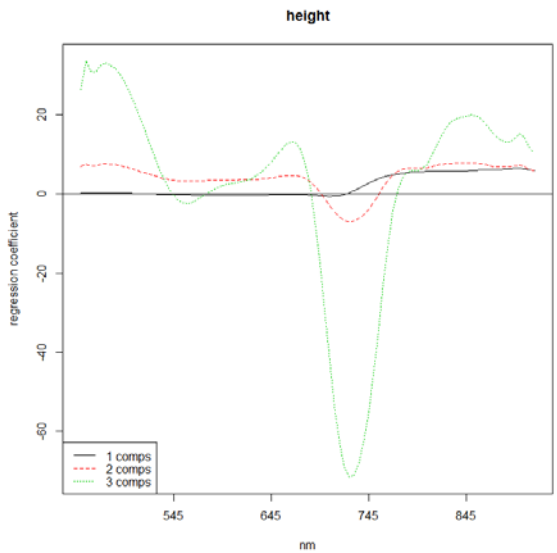

Fresh biomass (FBM)

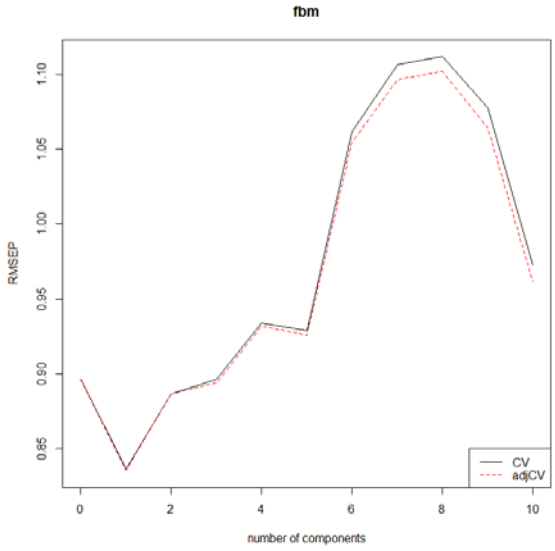

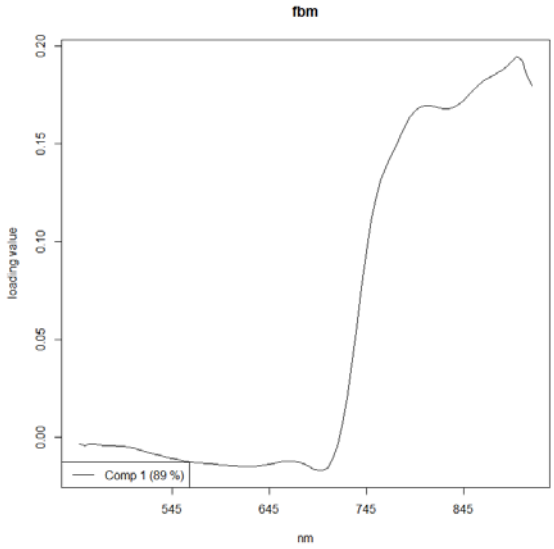

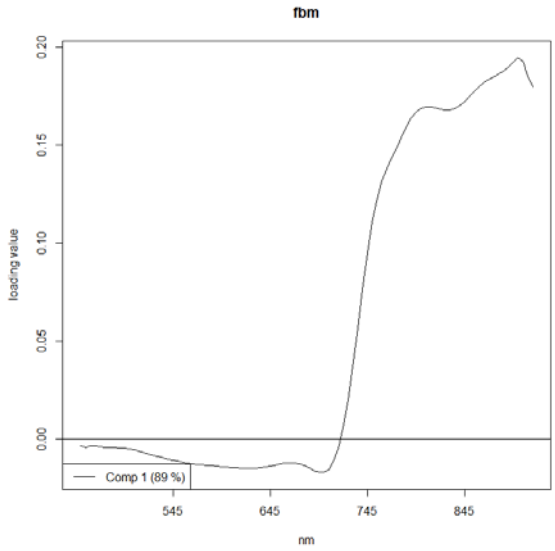

Nitrogen content (N)

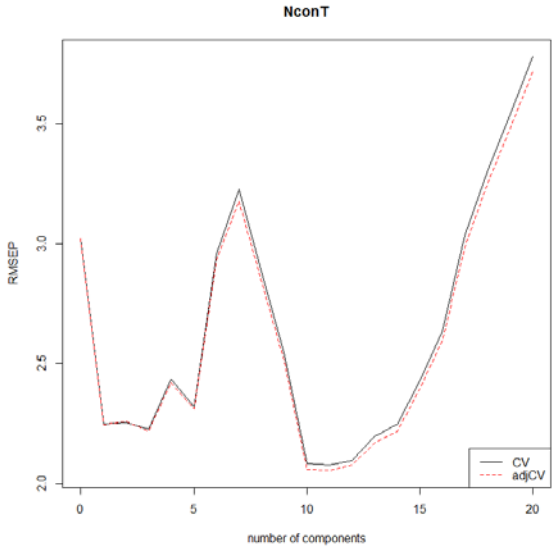

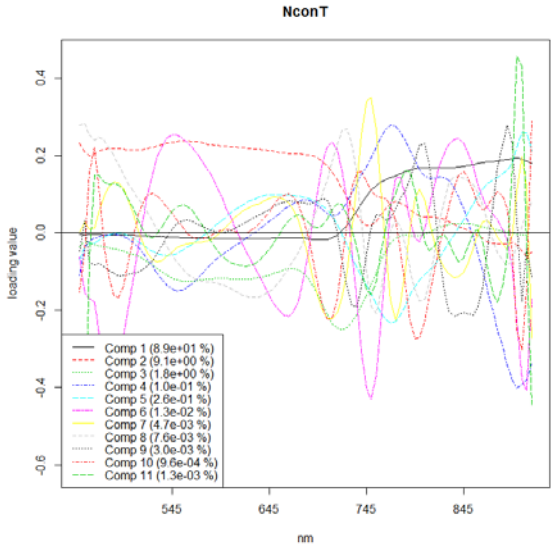

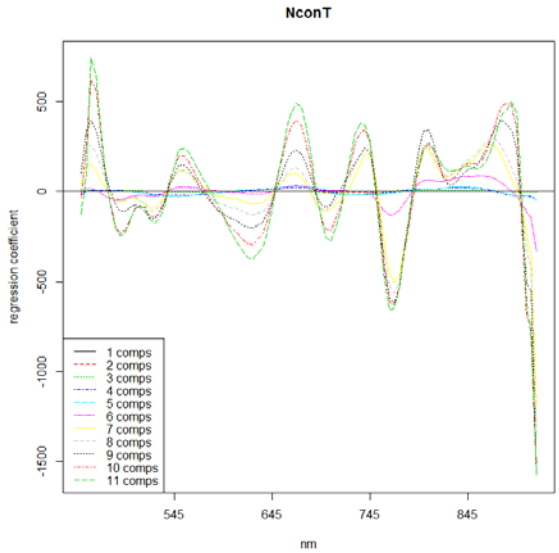

Carbon content (C)

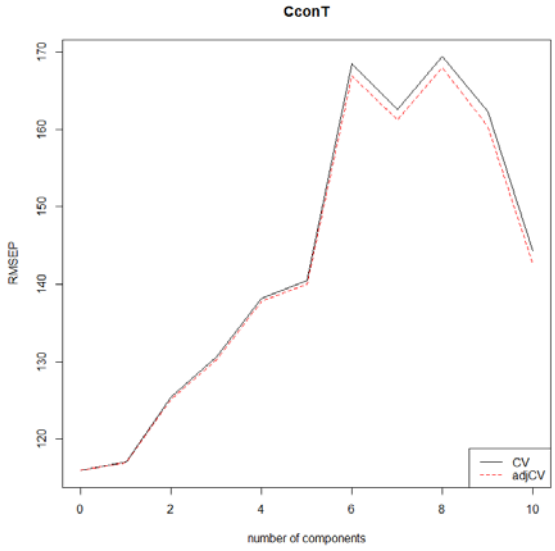

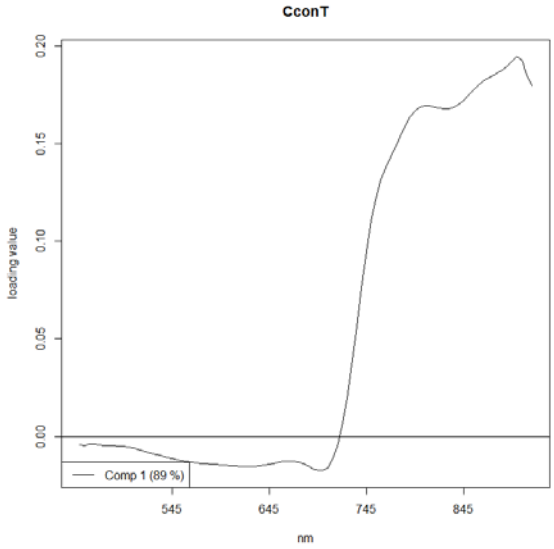

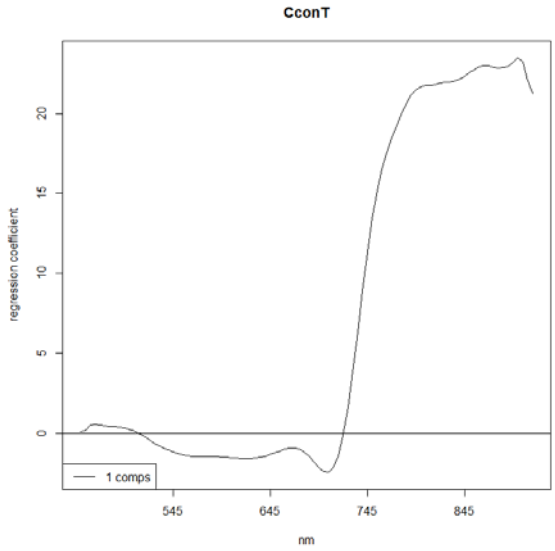

Leaf Chl content (CHL)

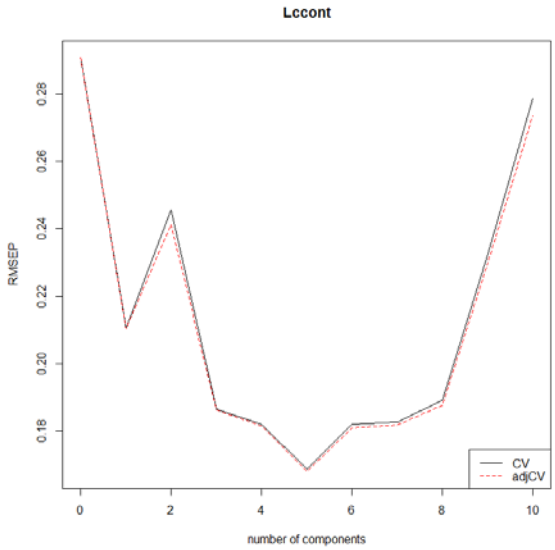

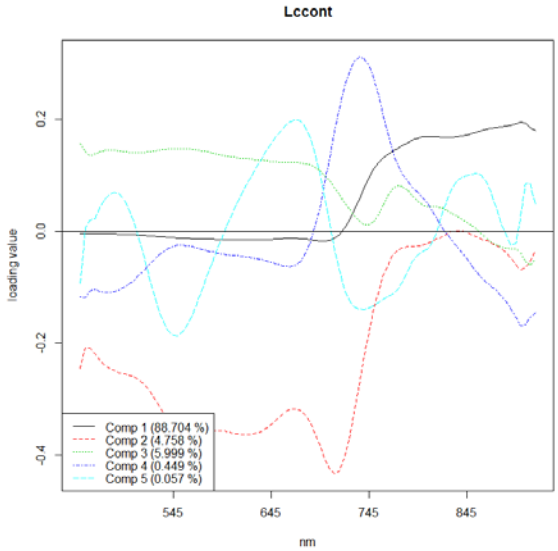

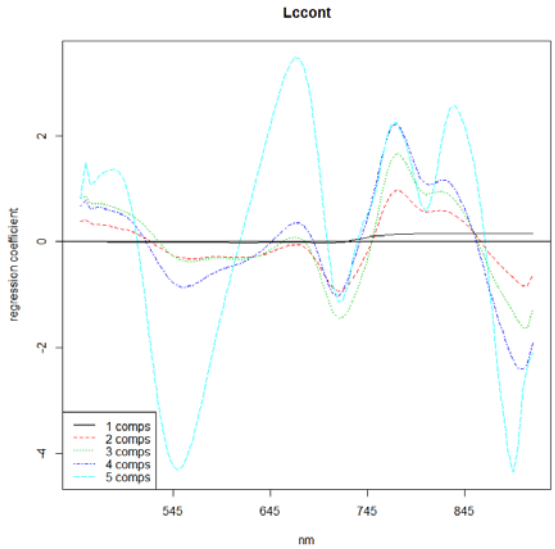

Tabular summaries

Height

Number of PLS factors	Percent variation accounted for				Cross-validation			
	Factors		Responses					
	Current	Total	Current	Total	R2	RMSEP	REP(%)	PRESS
1	88.68	88.68	54.78	54.78	0.466	7.327	8.03%	1507.3
2	9.56	98.24	4.32	59.1	0.5082	7.068	7.74%	1388.315
3	1.35	99.59	15.83	74.93	0.6519	5.909	6.47%	982.544
4	0.32	99.91	0.88	75.81	0.6417	5.997	6.57%	1011.361
5	0.05	99.96	2.5	78.31	0.5959	6.358	6.97%	1140.695
6	0.02	99.98	2	80.31	0.5397	6.78	7.43%	1299.262
7	0.01	99.99	4.86	85.17	0.365	7.935	8.69%	1792.418
8	0	99.99	3.52	88.69	0.3802	7.829	8.58%	1749.47
9	0.01	100	4.32	93.01	0.444	7.388	8.10%	1569.585
10	0	100	0.88	93.89	0.5581	6.597	7.23%	1247.364

Fresh biomass (FBM)

Number of PLS factors	Percent variation accounted for				Cross-validation			
	Factors		Responses					
	Current	Total	Current	Total	R2	RMSEP	REP(%)	PRESS
1	88.68	88.68	20.42	20.42	0.06358	0.8352	23.57%	19.5855
2	9.84	98.52	1.14	21.56	-0.05225	0.8865	25.02%	22.00801
3	1.06	99.58	5.01	26.57	-0.07607	0.8941	25.23%	22.50631
4	0.27	99.85	3.6	30.17	-0.1676	0.9316	26.29%	24.41996
5	0.12	99.97	5.83	36	-0.1548	0.9256	26.12%	24.15329

Nitrogen content (N)

Number of PLS factors	Percent variation accounted for				Cross-validation			
	Factors		Responses					
	Current	Total	Current	Total	R2	RMSEP	REP(%)	PRESS
1	88.7	88.7	50.07	50.07	0.4045	2.245	25.01%	141.5479
2	9.12	97.82	2.54	52.61	0.4018	2.26	25.18%	142.1901
3	1.78	99.6	8.1	60.71	0.4169	2.218	24.71%	138.6058
4	0.1	99.7	4.51	65.22	0.3022	2.418	26.94%	165.8602
5	0.27	99.97	1.03	66.25	0.3654	2.311	25.74%	150.8298
6	0.01	99.98	5.21	71.46	-0.03091	2.934	32.68%	245.0351
7	0	99.98	12.41	83.87	-0.2267	3.177	35.39%	291.5799
8	0.01	99.99	2.5	86.37	0.02131	2.847	31.71%	232.6222
9	0.01	100	3.28	89.65	0.2358	2.515	28.02%	181.6376
10	0	100	2.11	91.76	0.4886	2.058	22.92%	121.5517
11	0	100	0.77	92.53	0.492	2.054	22.88%	120.754
12	0	100	1.43	93.96	0.482	2.076	23.13%	123.1315

Carbon content (C)

Number of PLS factors	Percent variation accounted for				Cross-validation			
	Factors		Responses					
	Current	Total	Current	Total	R2	RMSEP	REP(%)	PRESS
1	88.698	88.698	6.357	6.357	-0.0964	116.9	21.82%	383674
2	9.153	97.851	0.449	6.806	-0.25861	125.1	23.35%	440455
3	1.699	99.55	1.814	8.62	-0.3653	130.3	24.32%	477791.4
4	0.3	99.85	2.54	11.16	-0.5266	137.8	25.72%	534255.6
5	0.12	99.97	4.85	16.01	-0.5793	140	26.13%	552669.2

Leaf Chl content (CHL)

Number of PLS factors	Percent variation accounted for				Cross-validation			
	Factors		Responses					
	Current	Total	Current	Total	R2	RMSEP	REP(%)	PRESS
1	88.7	88.7	52.17	52.17	0.4349	0.2104	28.08%	1.243245
2	4.76	93.46	10.19	62.36	0.2322	0.2413	32.20%	1.689276
3	6	99.46	7.02	69.38	0.557	0.1862	24.85%	0.974552
4	0.45	99.91	3.28	72.66	0.578	0.1816	24.24%	0.928465
5	0.06	99.97	6.77	79.43	0.6376	0.1681	22.43%	0.79723
6	0.01	99.98	2.35	81.78	0.5776	0.181	24.16%	0.92934
7	0.01	99.99	1.88	83.66	0.5746	0.1818	24.26%	0.935868
8	0	99.99	0.91	84.57	0.545	0.1877	25.05%	1.001035
9	0.01	100	1.87	86.44	0.3112	0.2298	30.67%	1.515389
10	0	100	2.92	89.36	0.01263	0.2735	36.50%	2.172275

Scatterplots for PLS fitted values –vs– known response variable values

Height

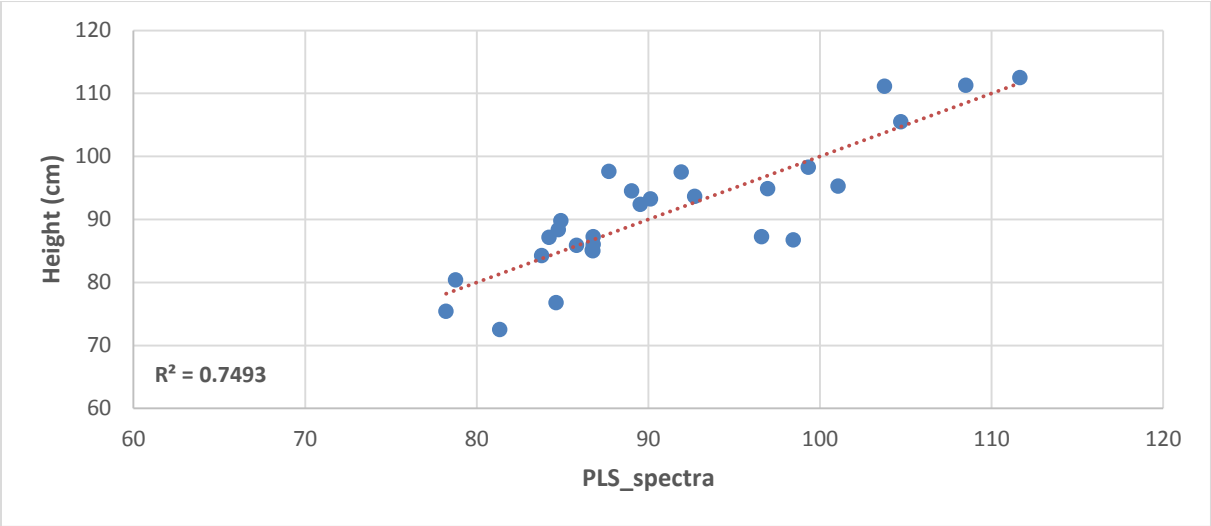

Fresh biomass (FBM)

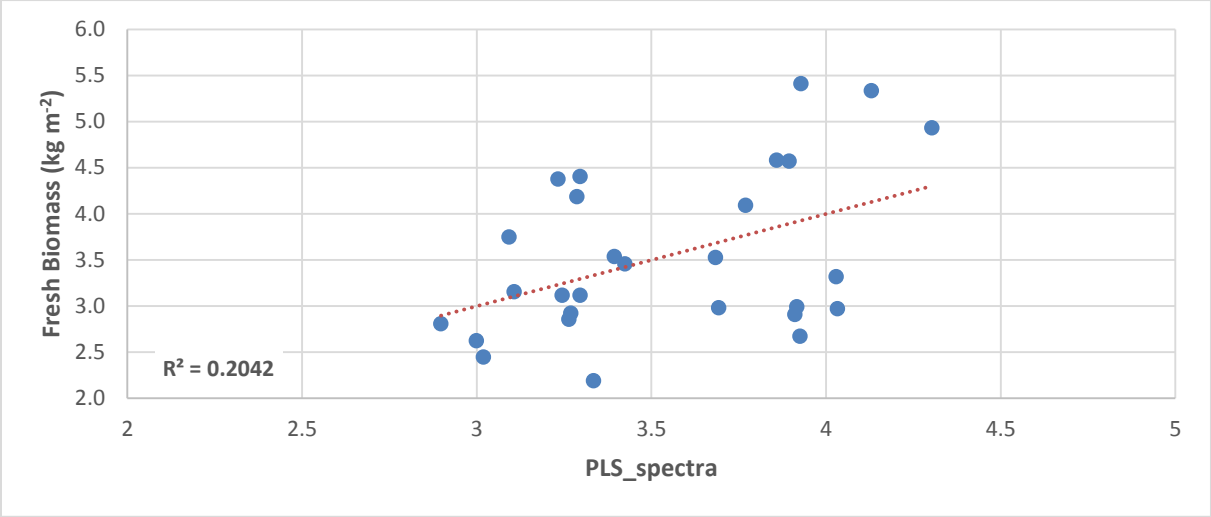

Nitrogen content (N)

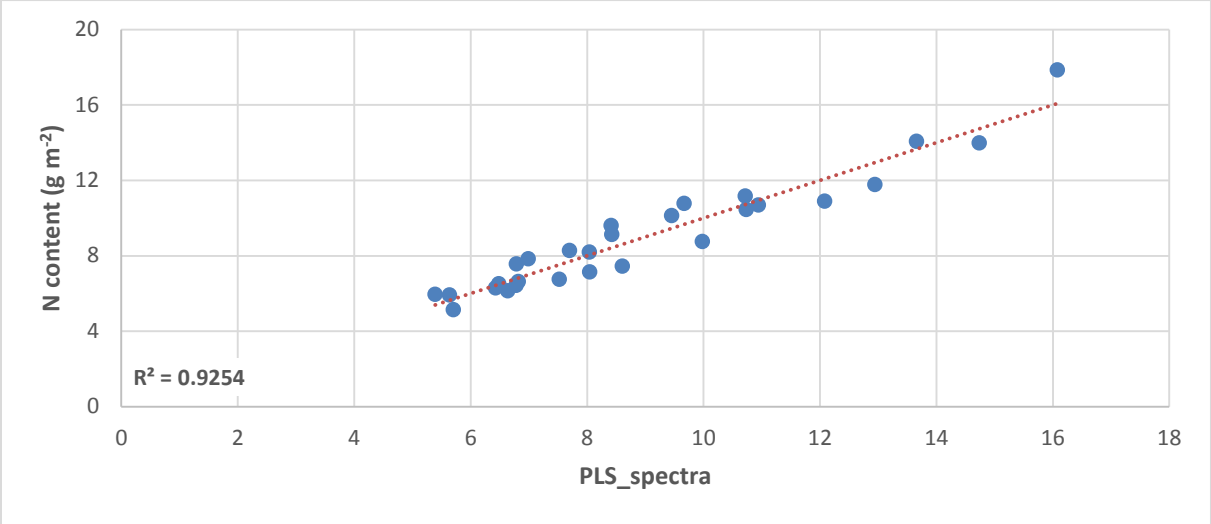

Carbon content (C)

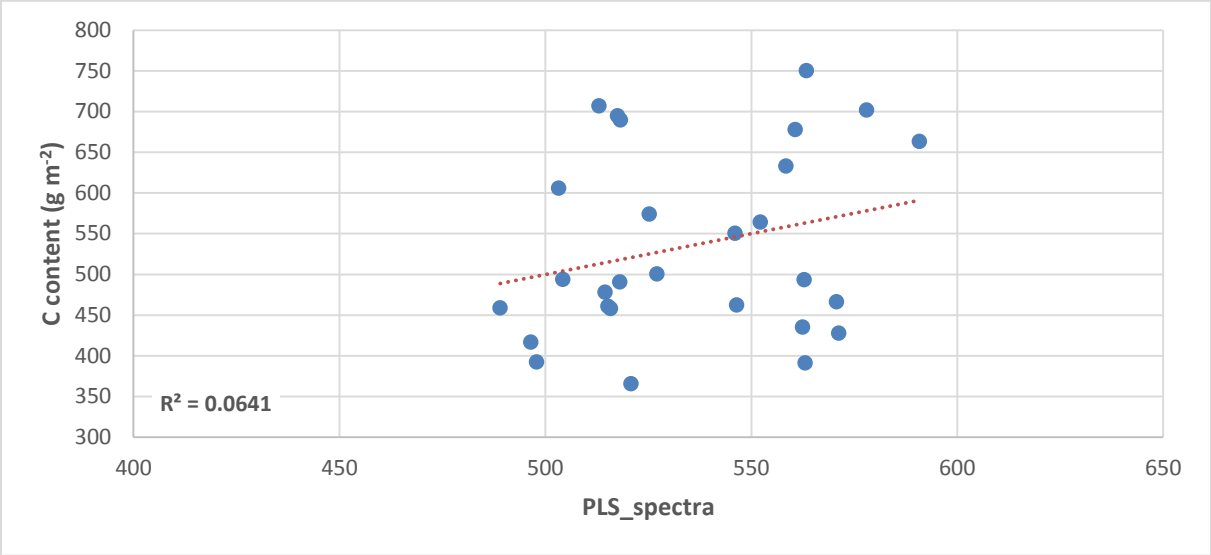

Leaf Chl content (CHL)

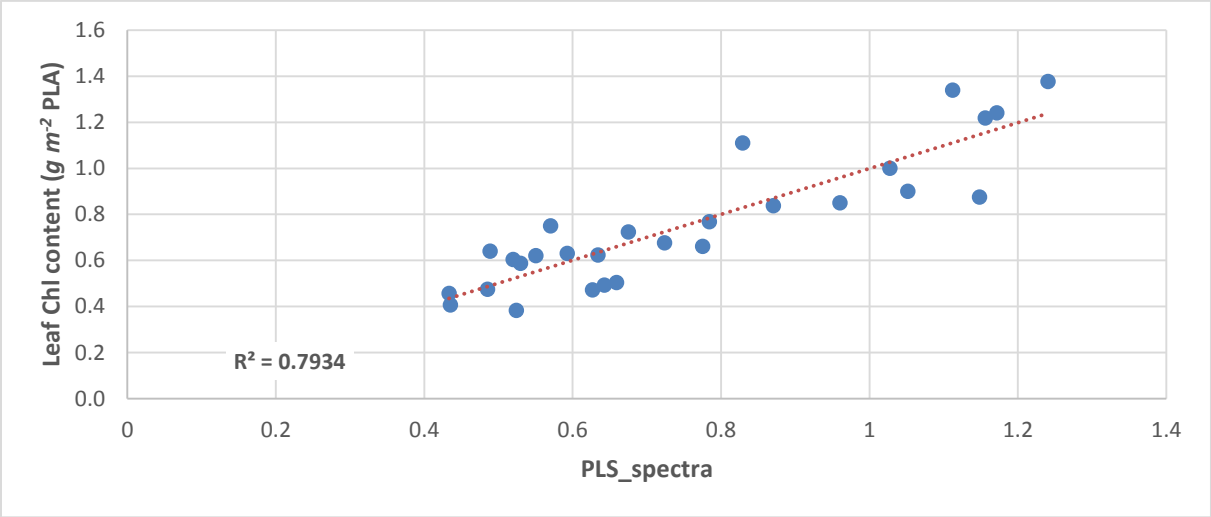

PLS calibration using spectral and CSM height data

Below, the same types of graphs are given as above, i.e. RMSEP, loading weights and regression coefficient plots. In contrast to the earlier figures, however, the ones below relate to the process of PLS model calibration in which the height stored in the CSM is included as an additional explanatory (x) variable. Unfortunately, labeling of the loading weights and regression coefficient plots did not allow reference to both wavelengths (in nm) and CSM height (in cm) on the horizontal axis. Hence, only references to the wavelengths as variables are included. The height explanatory variable, however, is included on the far left side of the horizontal axis, as is clearly discernible in the loading weights graphs allocating notable weight to this variable.

Height

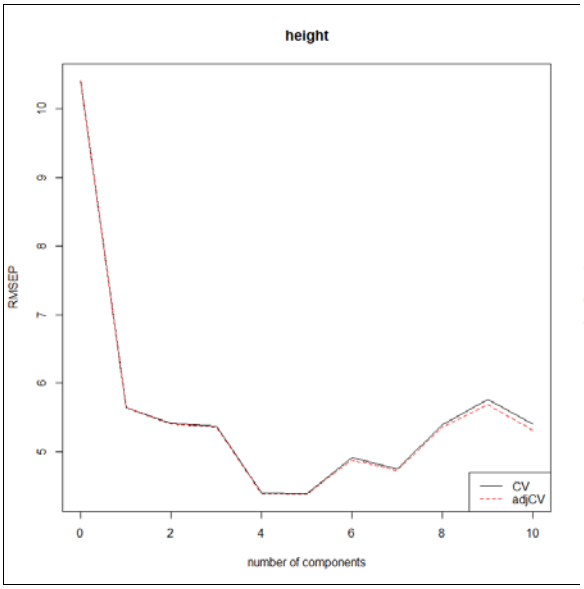

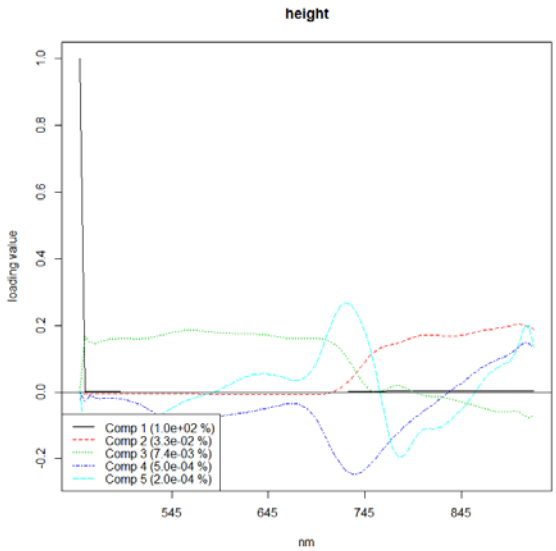

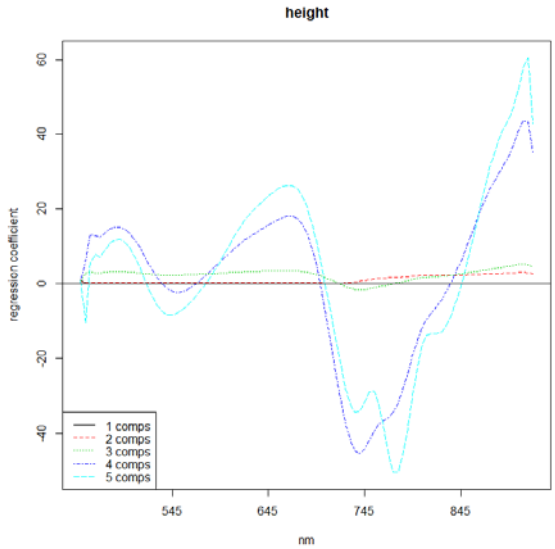

Fresh biomass (FBM)

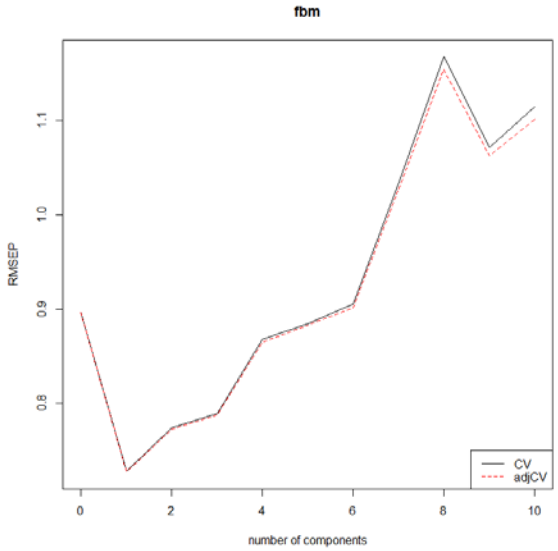

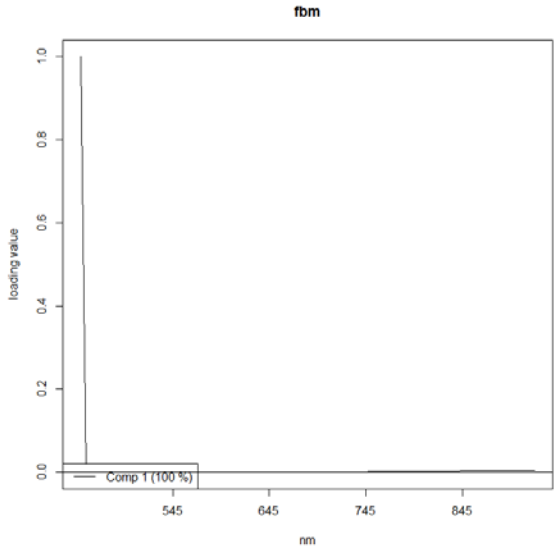

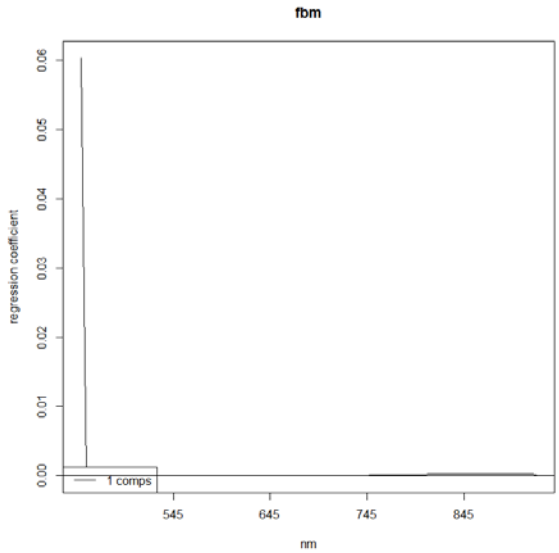

Nitrogen content (N)

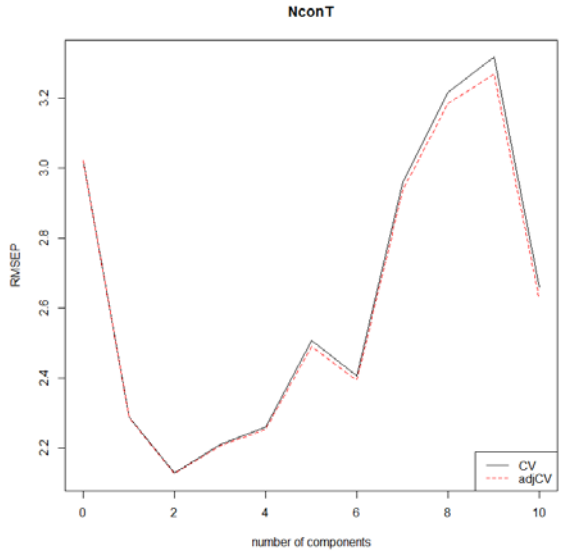

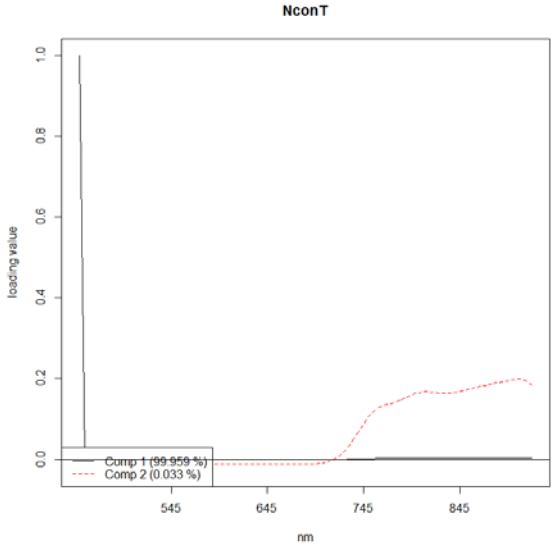

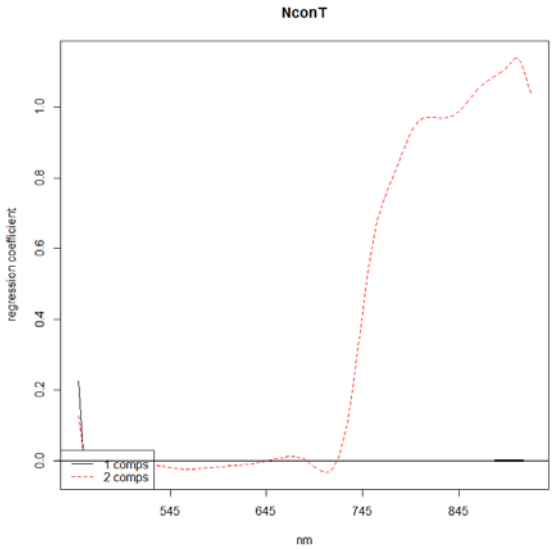

Carbon content (C)

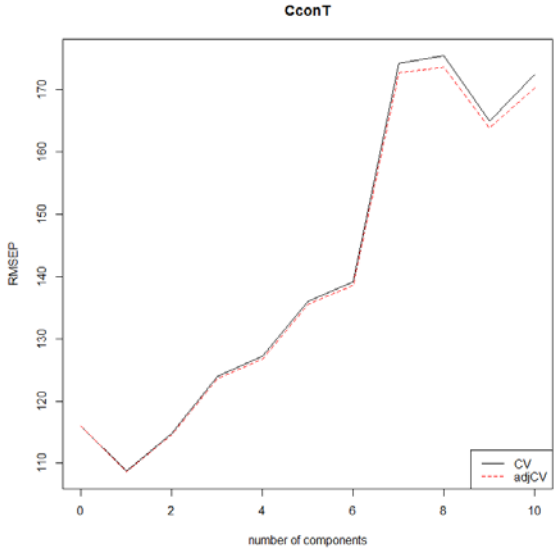

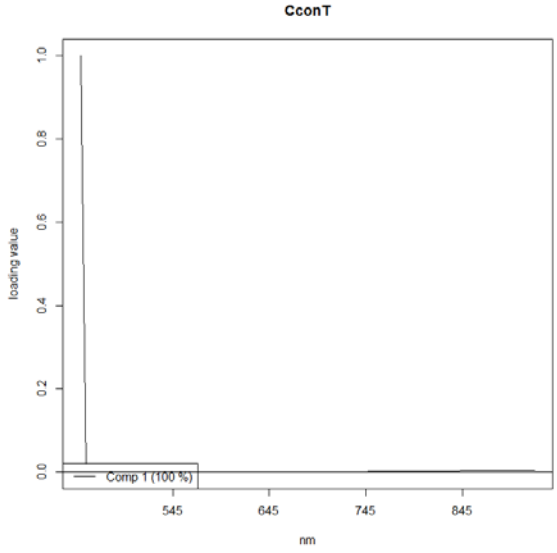

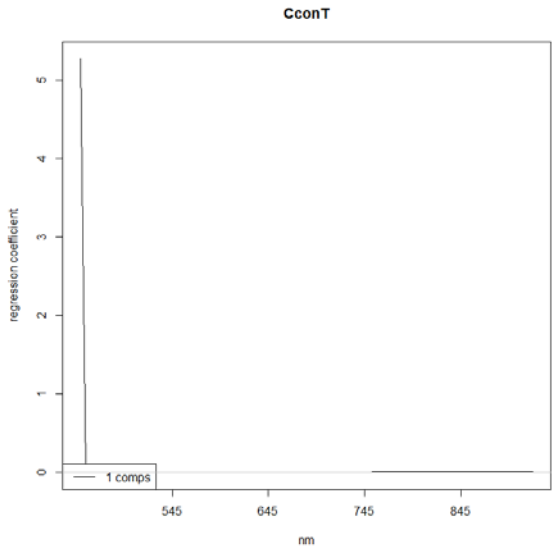

Leaf Chl content (CHL)

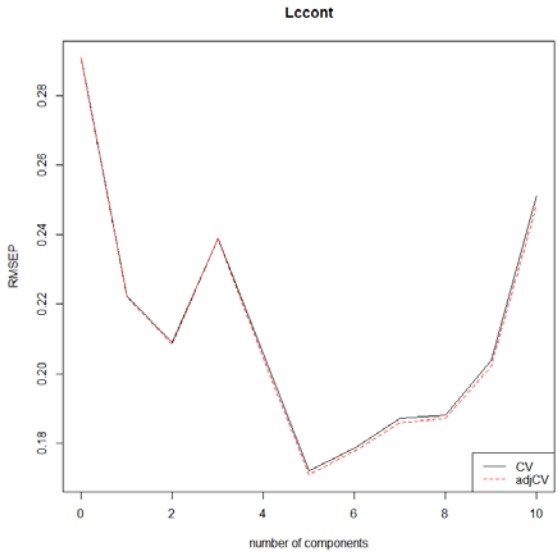

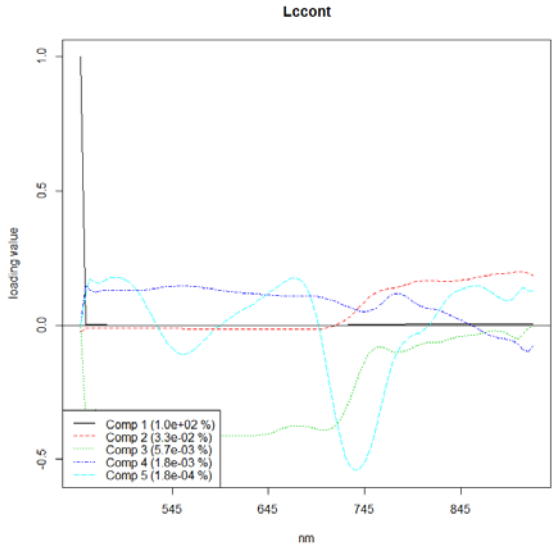

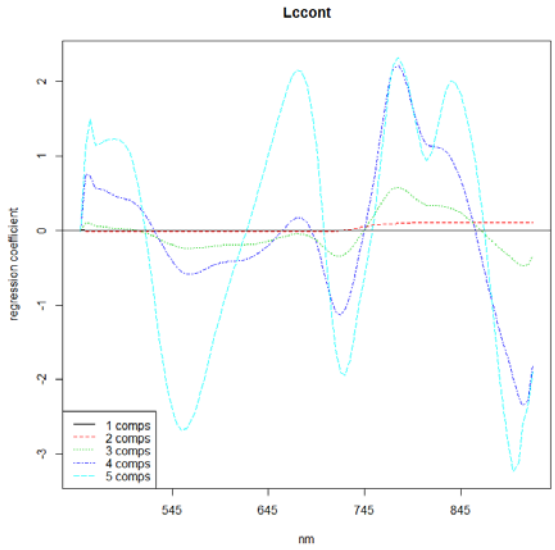

Tabular summaries

Height

Number of PLS factors	Percent variation accounted for				Cross-validation			
	Factors		Responses					
	Current	Total	Current	Total	R2	RMSEP	REP(%)	PRESS
1	99.96	99.96	72.76	72.76	0.6834	5.642	6.18%	893.6233
2	0.03	99.99	4.69	77.45	0.7095	5.402	5.92%	820.1065
3	0.01	100	1.54	78.99	0.7138	5.365	5.88%	807.827
4	0	100	8.65	87.64	0.8078	4.388	4.81%	542.624
5	0	100	0.78	88.42	0.8086	4.377	4.80%	540.333
6	0	100	1.55	89.97	0.7604	4.88	5.35%	676.4209
7	0	100	0.59	90.56	0.7761	4.725	5.18%	631.9449
8	0	100	1.25	91.81	0.7112	5.36	5.87%	815.2183
9	0	100	2.36	94.17	0.6709	5.694	6.24%	929.0757
10	0	100	2.22	96.39	0.7102	5.321	5.83%	818.1681

Fresh biomass (FBM)

Number of PLS factors	Percent variation accounted for				Cross-validation			
	Factors		Responses					
	Current	Total	Current	Total	R2	RMSEP	REP(%)	PRESS
1	99.96	99.96	38.67	38.67	0.291	0.7268	20.51%	14.8296
2	0.03	99.99	0.27	38.94	0.1975	0.7726	21.80%	16.78518
3	0.01	100	0.23	39.17	0.1663	0.7872	22.21%	17.43674
4	0	100	1.98	41.15	-0.00791	0.8646	24.40%	21.0807
5	0	100	2.41	43.56	-0.04713	0.883	24.92%	21.90112

Nitrogen content (N)

Number of PLS factors	Percent variation accounted for				Cross-validation			
	Factors		Responses					
	Current	Total	Current	Total	R2	RMSEP	REP(%)	PRESS
1	99.96	99.96	47.78	47.78	0.3824	2.286	25.46%	146.7963
2	0.03	99.99	10.12	57.9	0.4651	2.127	23.69%	127.13
3	0.01	100	0.64	58.54	0.4237	2.208	24.60%	136.9899
4	0	100	3.75	62.29	0.3976	2.254	25.11%	143.1722
5	0	100	3.79	66.08	0.2593	2.491	27.75%	176.0537
6	0	100	1.1	67.18	0.3178	2.395	26.68%	162.144
7	0	100	4	71.18	-0.03309	2.937	32.72%	245.5523
8	0	100	8.76	79.94	-0.2196	3.185	35.48%	289.8842
9	0	100	7.19	87.13	-0.2962	3.269	36.41%	308.0965
10	0	100	3.68	90.81	0.1663	2.627	29.26%	198.1681

Carbon content (C)

Number of PLS factors	Percent variation accounted for				Cross-validation			
	Factors		Responses					
	Current	Total	Current	Total	R2	RMSEP	REP(%)	PRESS
1	99.96	99.96	17.63	17.63	0.05505	108.5	20.25%	330691
2	0.03	99.99	0.32	17.95	-0.0535	114.5	21.37%	368677.4
3	0.01	100	0.45	18.4	-0.229	123.5	23.05%	430085.9
4	0	100	1.86	20.26	-0.2947	126.8	23.67%	453091.9
5	0	100	1.19	21.45	-0.4809	135.6	25.31%	518253

Leaf Chl content (CHL)

Number of PLS factors	Percent variation accounted for				Cross-validation			
	Factors		Responses					
	Current	Total	Current	Total	R2	RMSEP	REP(%)	PRESS
1	99.96	99.96	44.95	44.95	0.3713	0.222	29.63%	1.383216
2	0.03	99.99	12.82	57.77	0.4443	0.2085	27.83%	1.222653
3	0.01	100	3.64	61.41	0.2732	0.2388	31.87%	1.598954
4	0	100	10.34	71.75	0.4603	0.2046	27.31%	1.187331
5	0	100	4.71	76.46	0.6231	0.1709	22.81%	0.82913
6	0	100	3.37	79.83	0.5939	0.1778	23.73%	0.893517
7	0	100	2.72	82.55	0.5534	0.186	24.82%	0.982539
8	0	100	0.92	83.47	0.5493	0.1872	24.98%	0.991646
9	0	100	1.34	84.81	0.4715	0.2022	26.99%	1.162656
10	0	100	1.15	85.96	0.1987	0.2483	33.14%	1.762842

Scatterplots for PLS fitted values –vs– known response variable values

Height

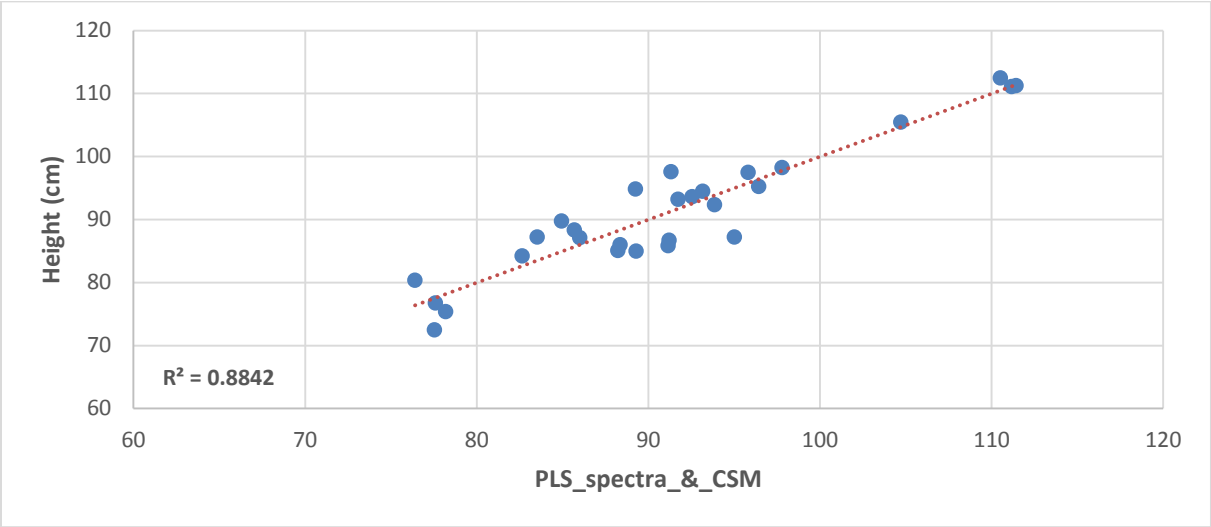

Fresh biomass (FBM)

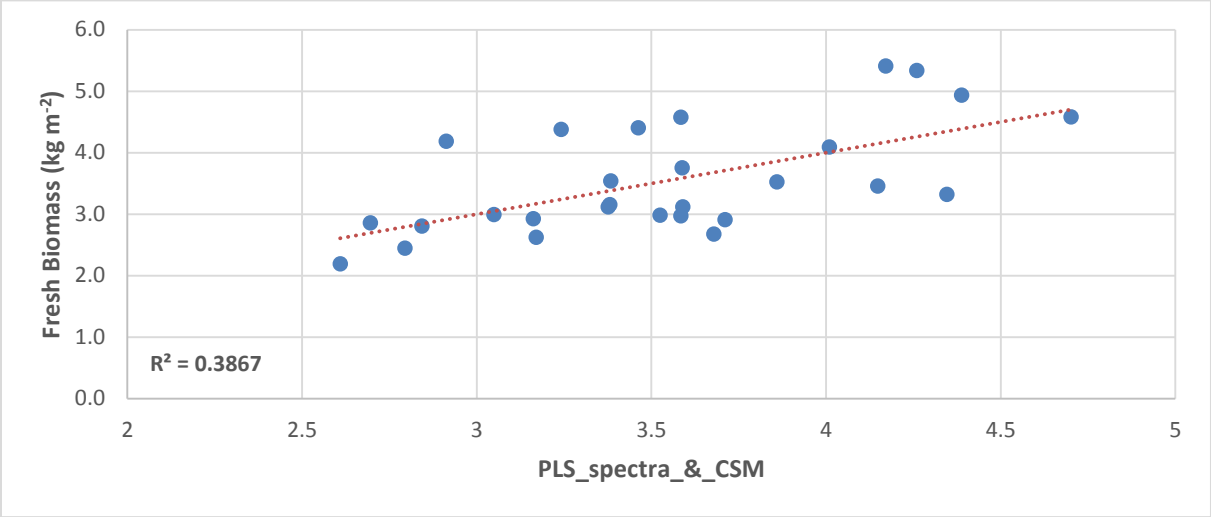

Nitrogen content (N)

Carbon content (C)

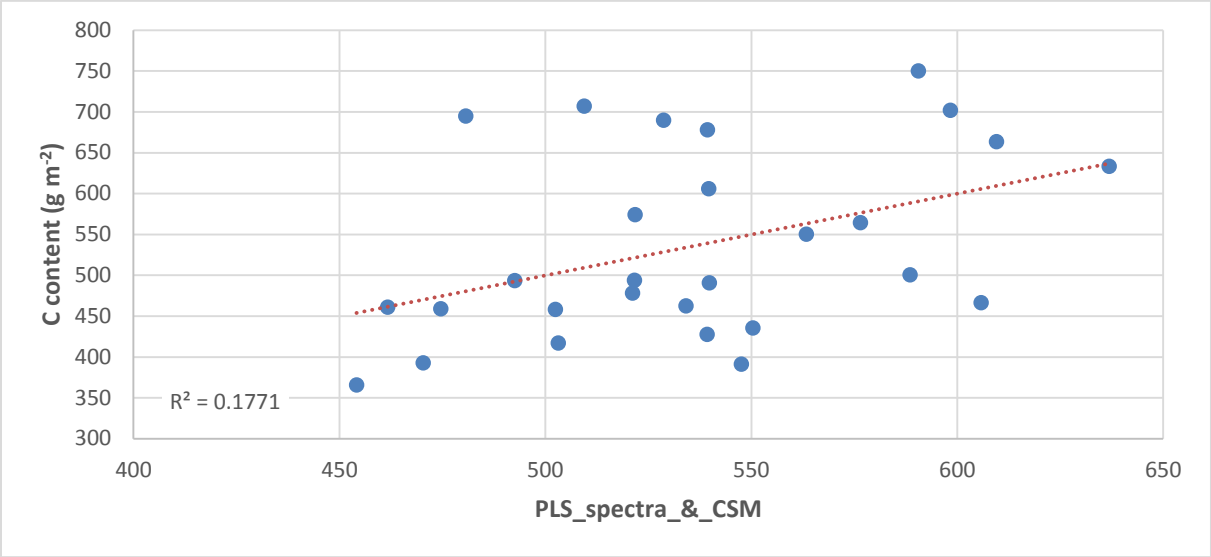

Leaf Chl content (CHL)

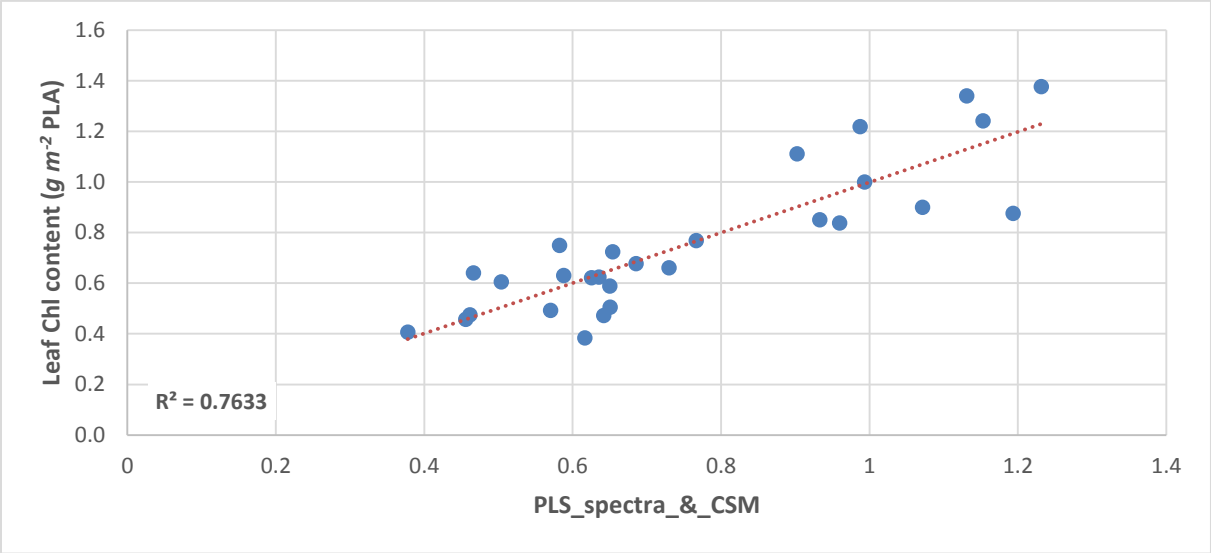

Appendix J: Predicted –vs– Observed values (Validation)

The below figures depict the scatter plots resulting from regression of trait values as predicted by vegetation indices and PLS models during validation, and in situ measured trait values, on the horizontal and vertical axis, respectively. The wording in parentheses on the horizontal axis relates the index or PLS model used to generate the predicted values in the corresponding scatter plot. The goodness-of-fit and the absolute and relative prediction accuracy are indicated by the R^2, RMSE and CV(RMSE), respectively, for each figure. For each trait, the first three scatter plots relate to the best selected existing indices that were identified during calibration (table 8.1). Subsequently, these are followed by the three (four for fresh biomass) best performing new optimized indices as given in table 8.3. For each trait, the last two scatter plots connect to the predictions of the optimal PLS models, i.e. based on only spectral data or both spectral and CSM height data, respectively (paragraph 8.3 and appendix I).

Height

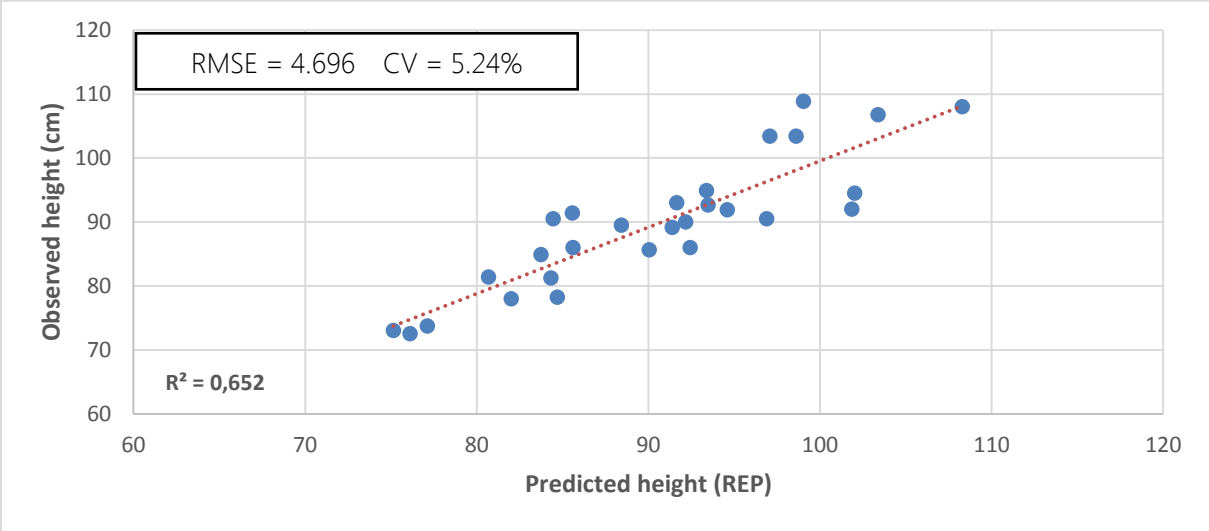

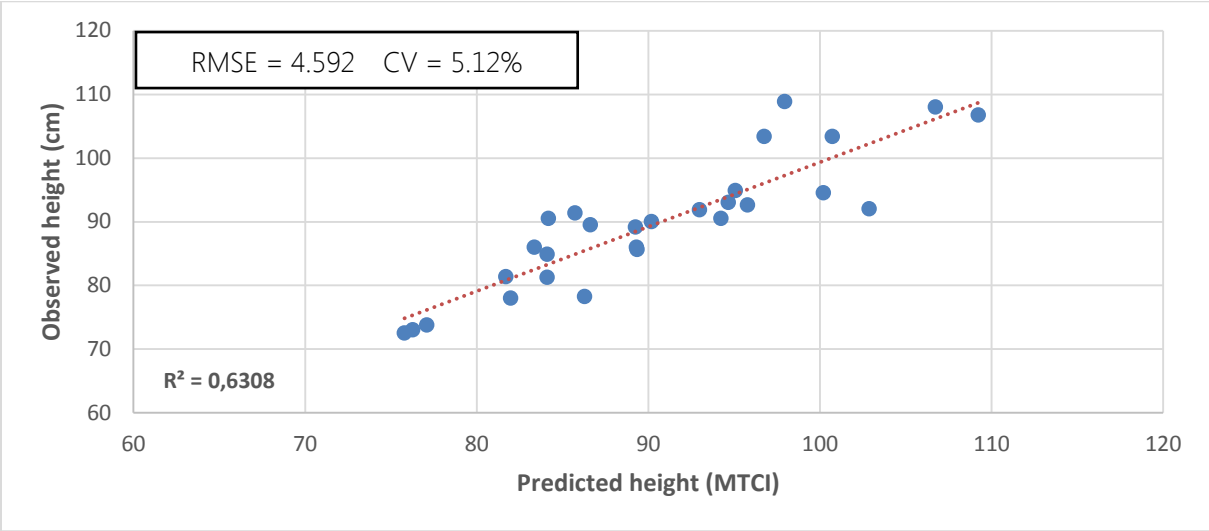

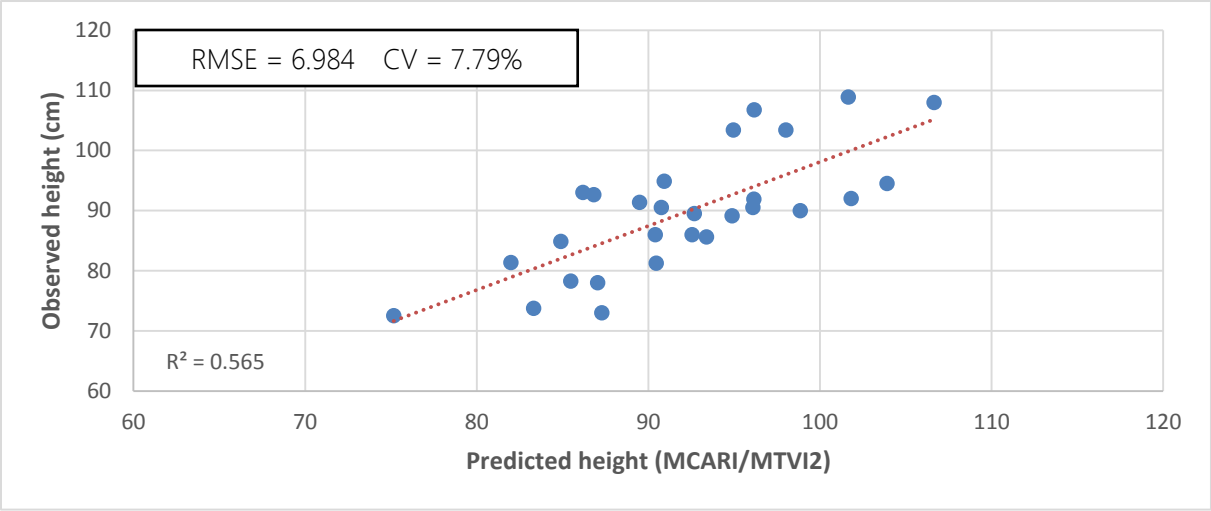
RMSE = 6.984 CV = 7.79%
R² = 0.565
Observed height (cm)
Predicted height (MCARI/MTVI2)
120
110
100
90
80
70
60
60
70
80
90
100
110
120

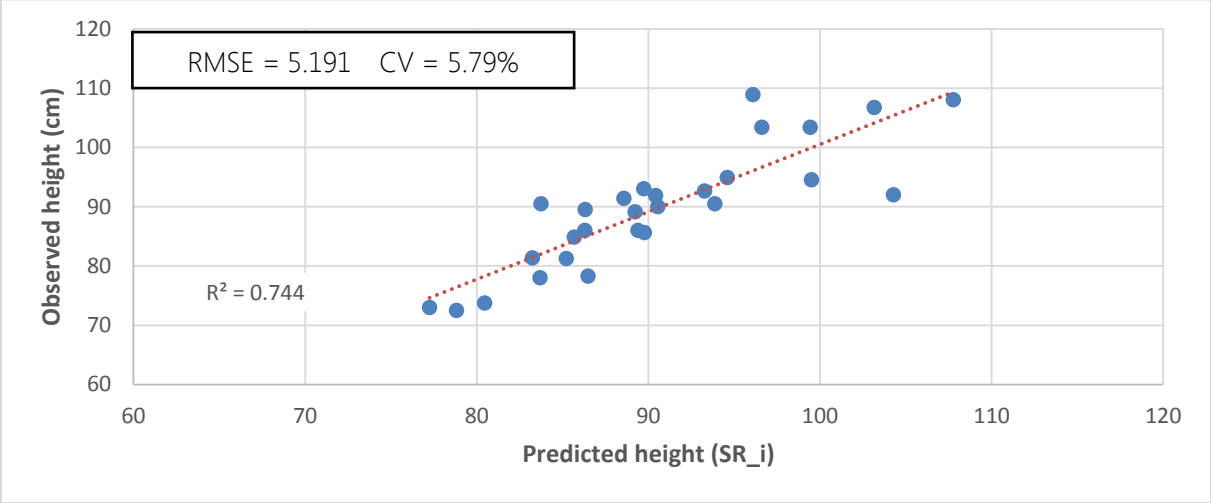
RMSE = 5.191 CV = 5.79%
R² = 0.744
Observed height (cm)
Predicted height (SR_i)
120
110
100
90
80
70
60
60
70
80
90
100
110
120

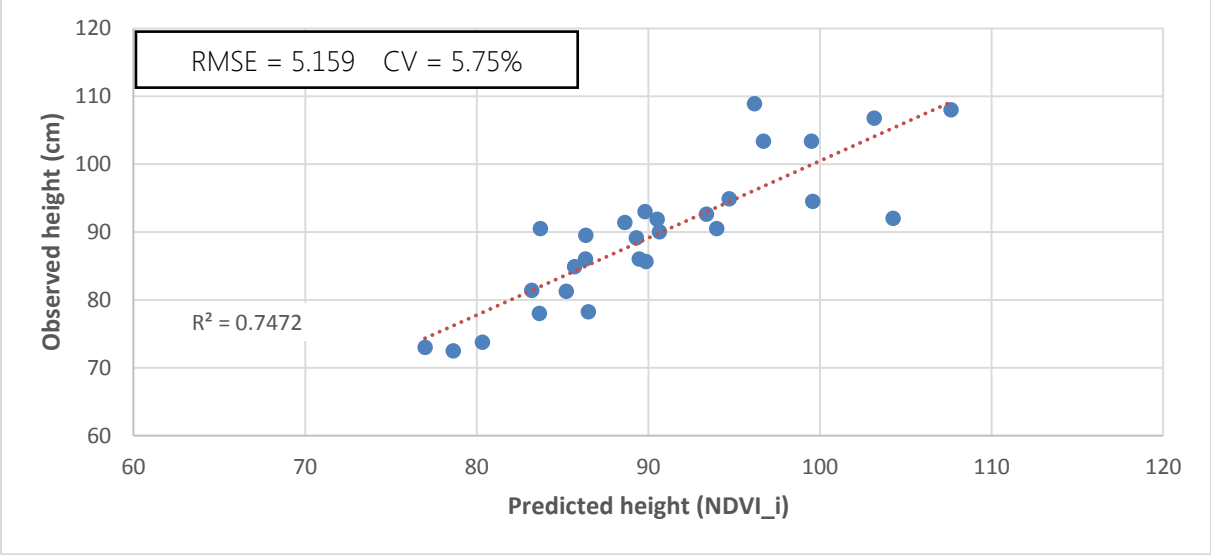
RMSE = 5.159 CV = 5.75%
R² = 0.7472
Observed height (cm)
Predicted height (NDVI_i)
120
110
100
90
80
70
60
60
70
80
90
100
110
120

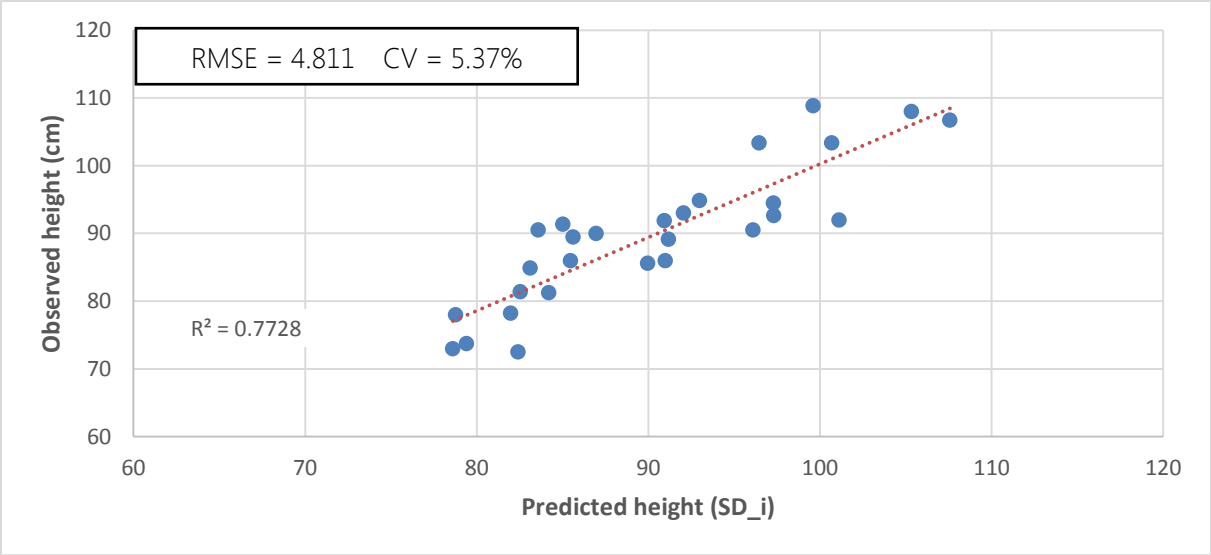
RMSE = 4.811 CV = 5.37%
R² = 0.7728
Observed height (cm)
Predicted height (SD_i)
120
110
100
90
80
70
60
60
70
80
90
100
110
120

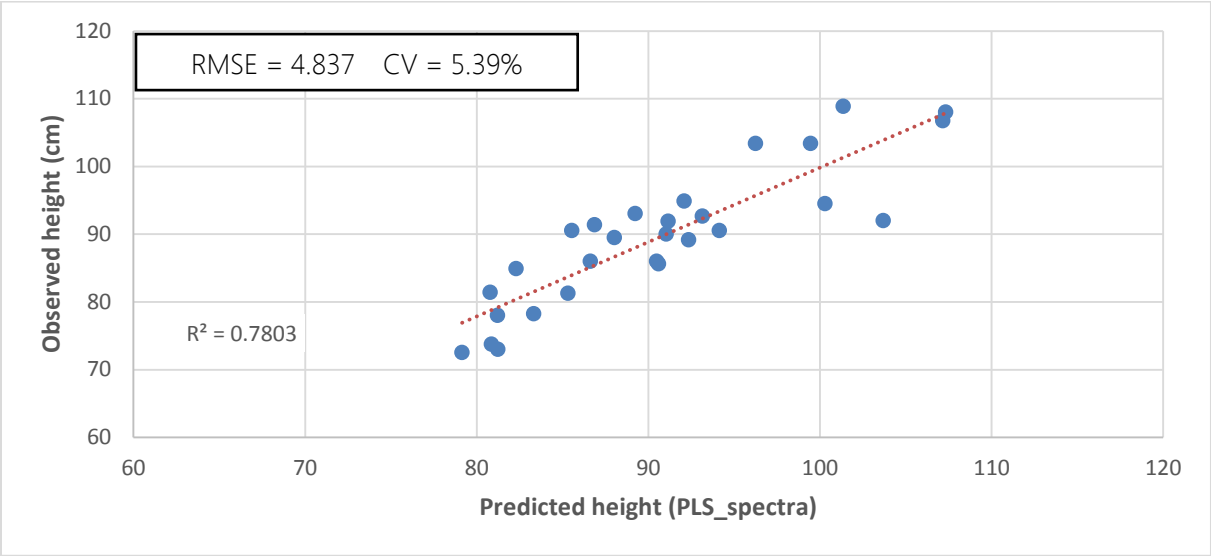
RMSE = 4.837 CV = 5.39%
R² = 0.7803
Observed height (cm)
Predicted height (PLS_spectra)
120
110
100
90
80
70
60
60
70
80
90
100
110
120

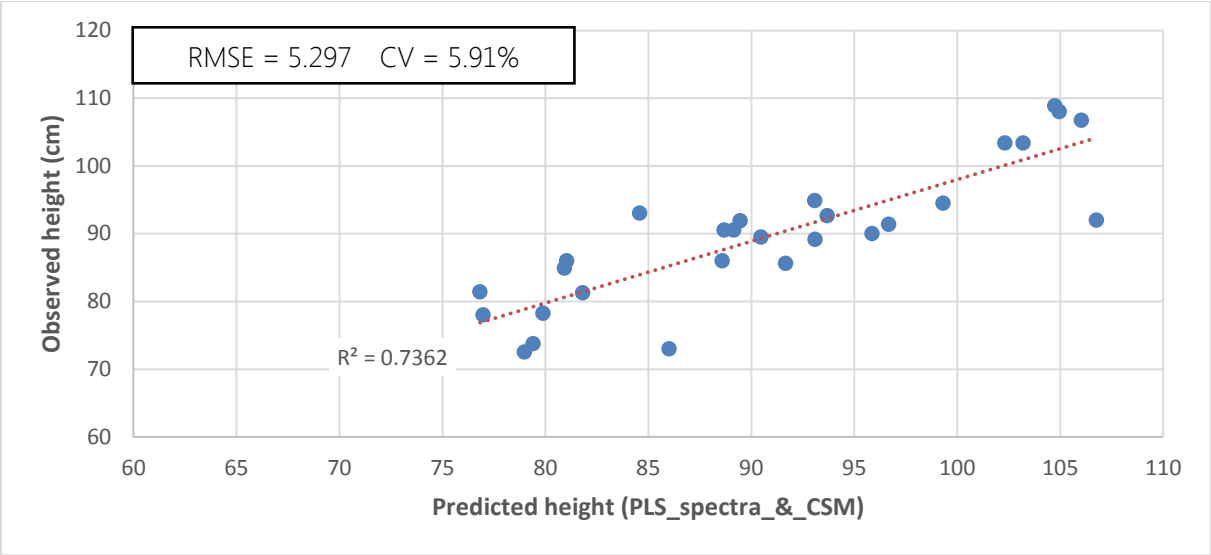
RMSE = 5.297 CV = 5.91%
R² = 0.7362
Observed height (cm)
Predicted height (PLS_spectra_&_CSM)
120
110
100
90
80
70
60
60
65
70
75
80
85
90
95
100
105
110

Fresh biomass (FBM)

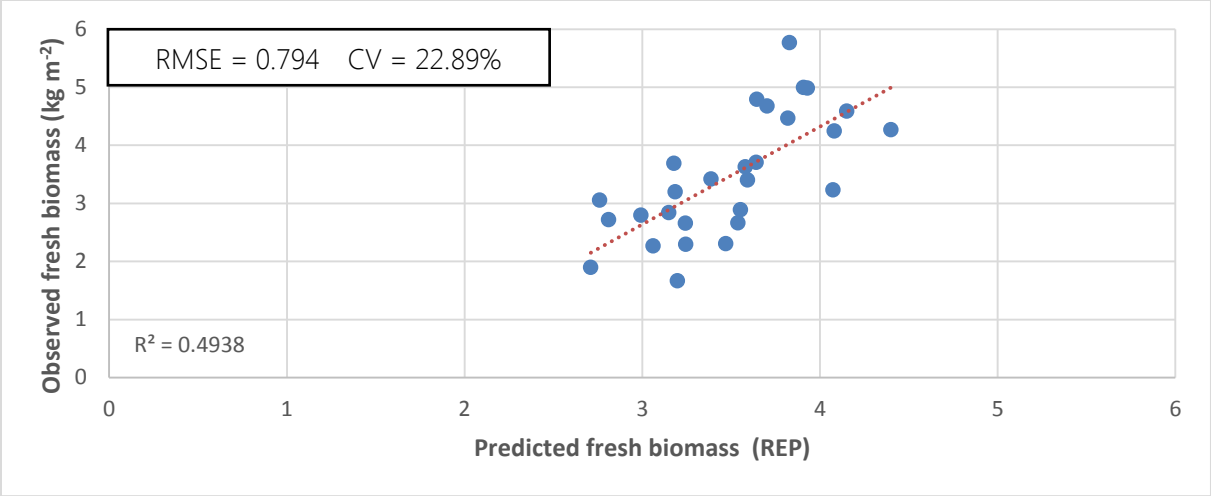

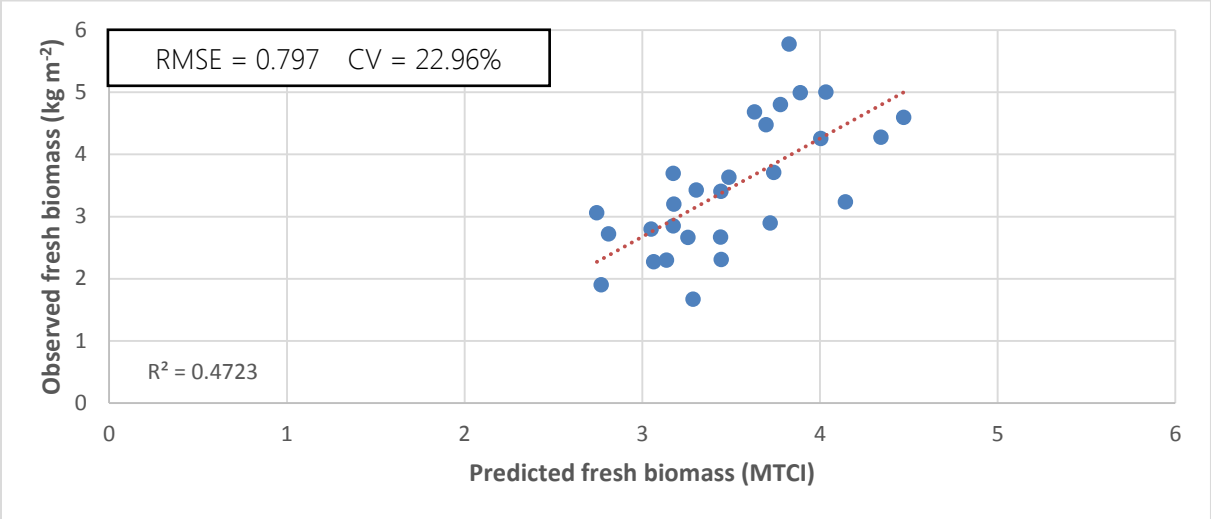

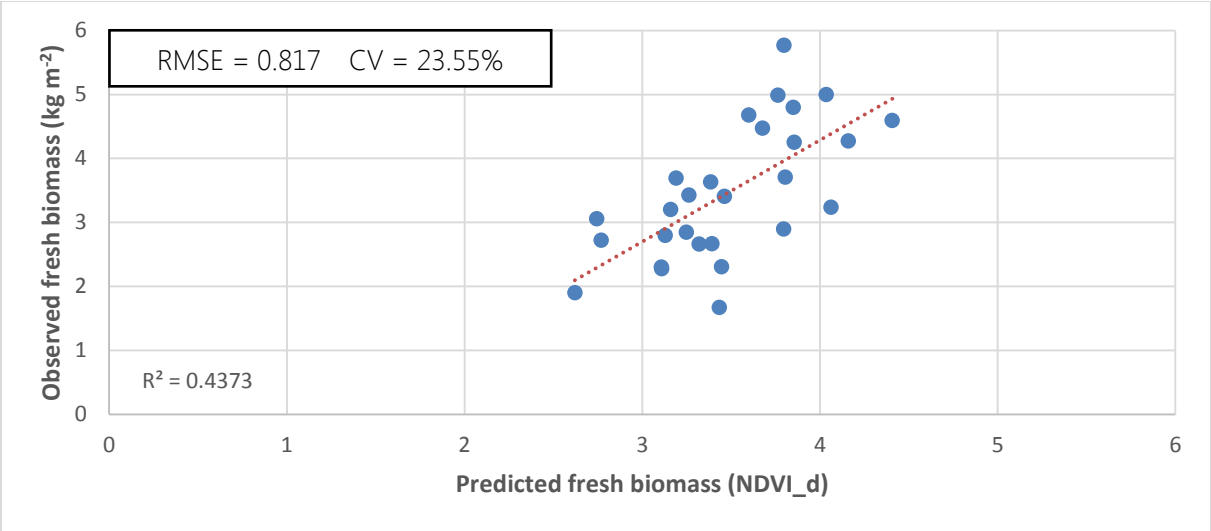

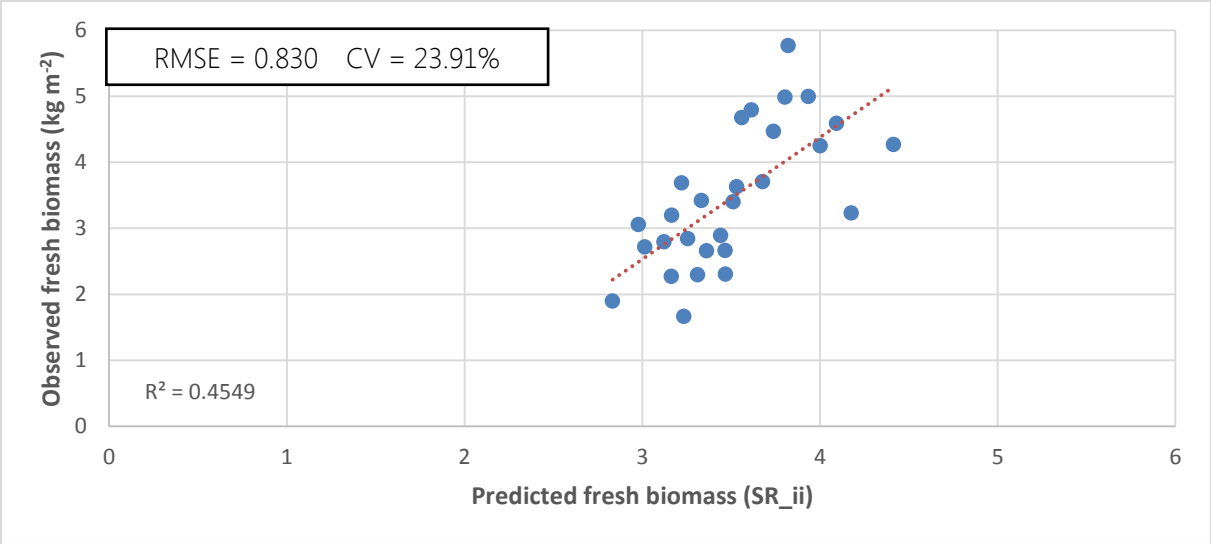
RMSE = 0.830 CV = 23.91%
R² = 0.4549
Observed fresh biomass (kg m-2)
Predicted fresh biomass (SR_ii)
0
1
2
3
4
5
6

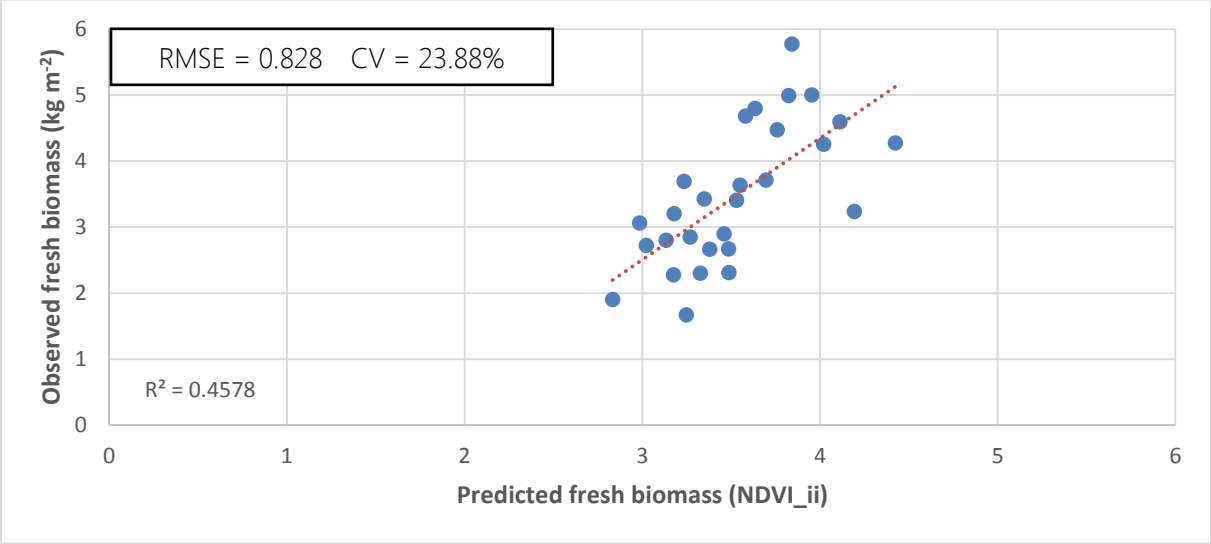
RMSE = 0.828 CV = 23.88%
R² = 0.4578
Observed fresh biomass (kg m-2)
Predicted fresh biomass (NDVI_ii)
0
1
2
3
4
5
6

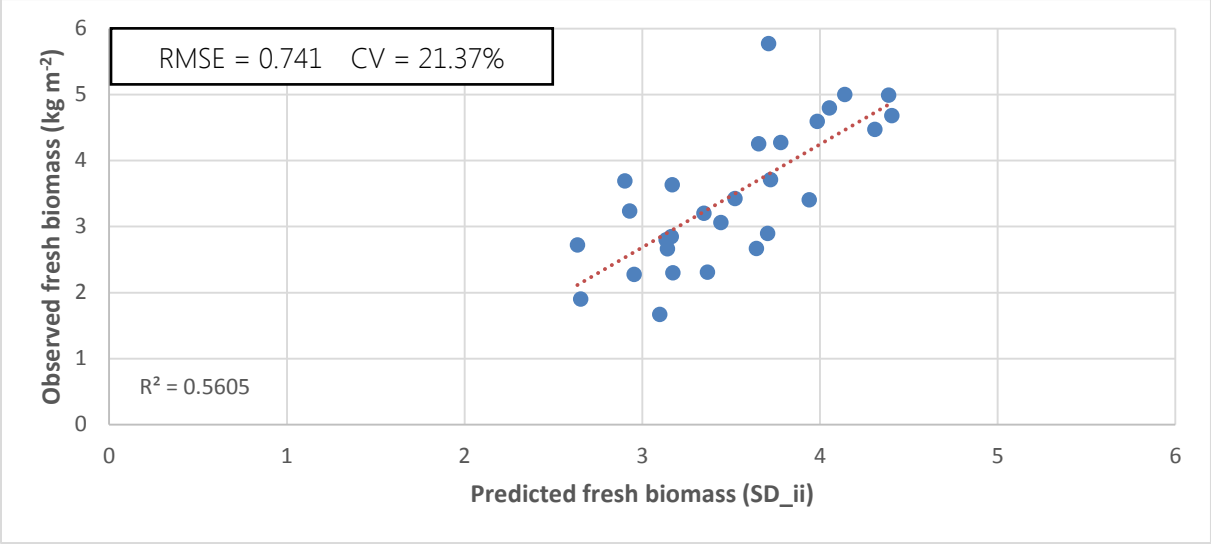
RMSE = 0.741 CV = 21.37%
R² = 0.5605
Observed fresh biomass (kg m-2)
Predicted fresh biomass (SD_ii)
0
1
2
3
4
5
6

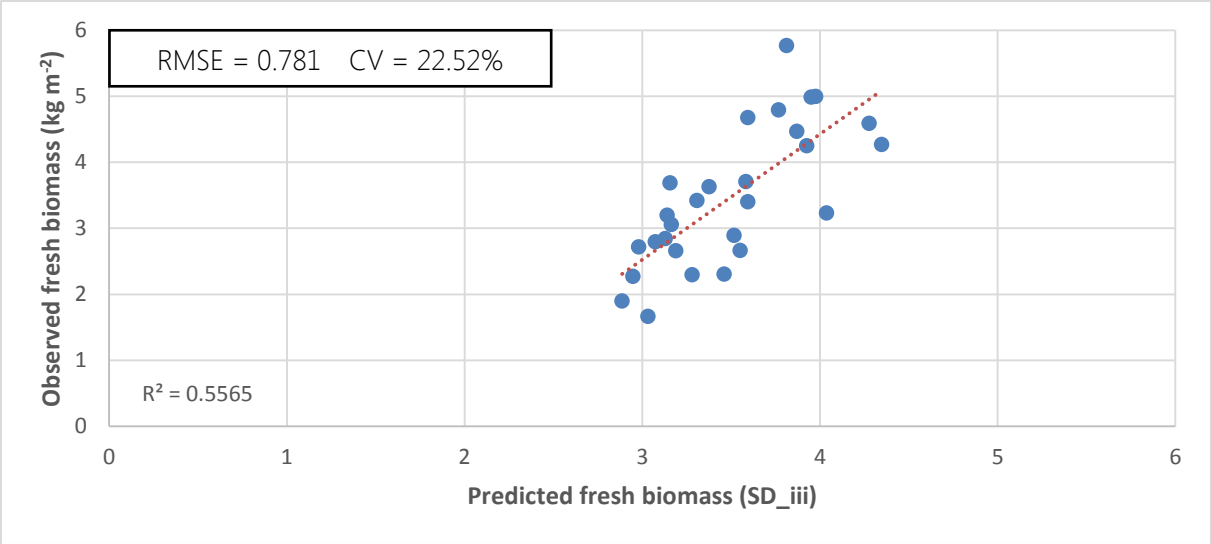
RMSE = 0.781 CV = 22.52%
R² = 0.5565
Observed fresh biomass (kg m-2)
Predicted fresh biomass (SD_iii)
0
1
2
3
4
5
6

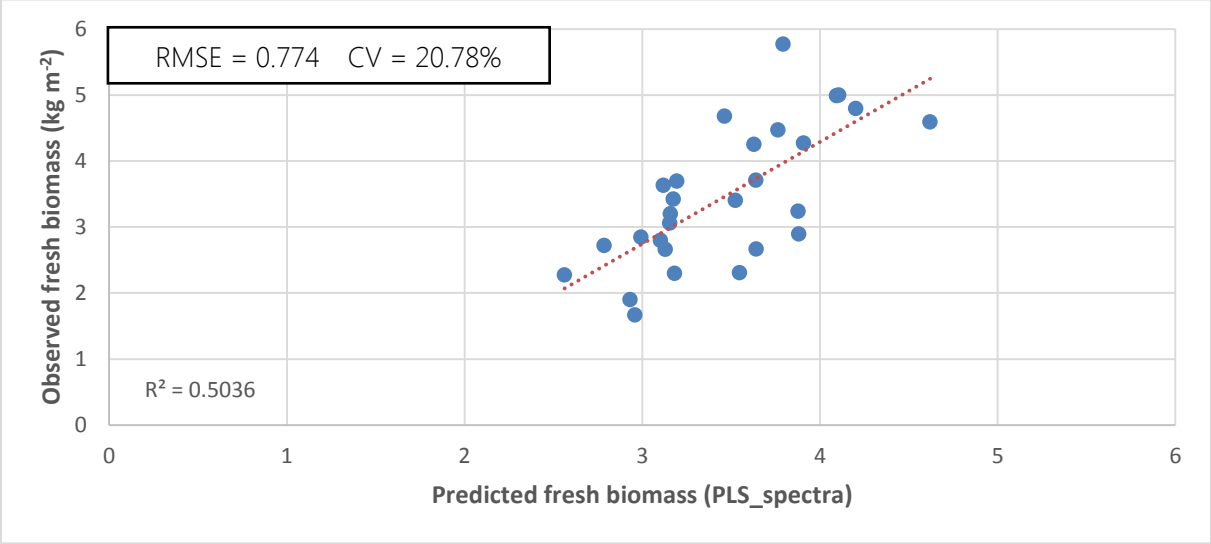
RMSE = 0.774 CV = 20.78%
R² = 0.5036
Observed fresh biomass (kg m-2)
Predicted fresh biomass (PLS_spectra)
0
1
2
3
4
5
6

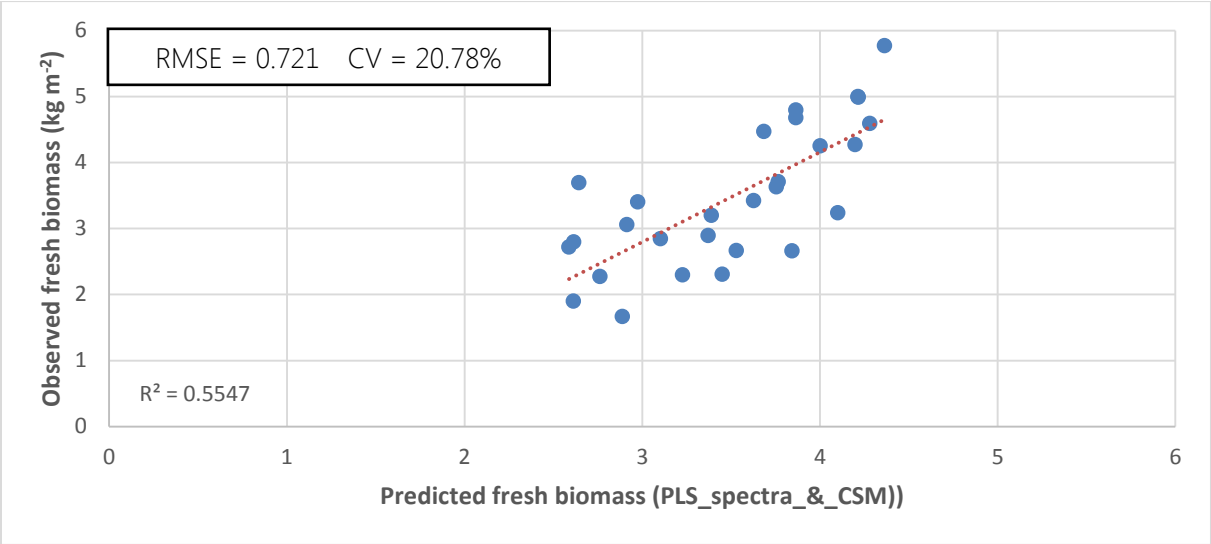
RMSE = 0.721 CV = 20.78%
R² = 0.5547
Observed fresh biomass (kg m-2)
Predicted fresh biomass (PLS_spectra_&_CSM))
0
1
2
3
4
5
6

Nitrogen content (N)

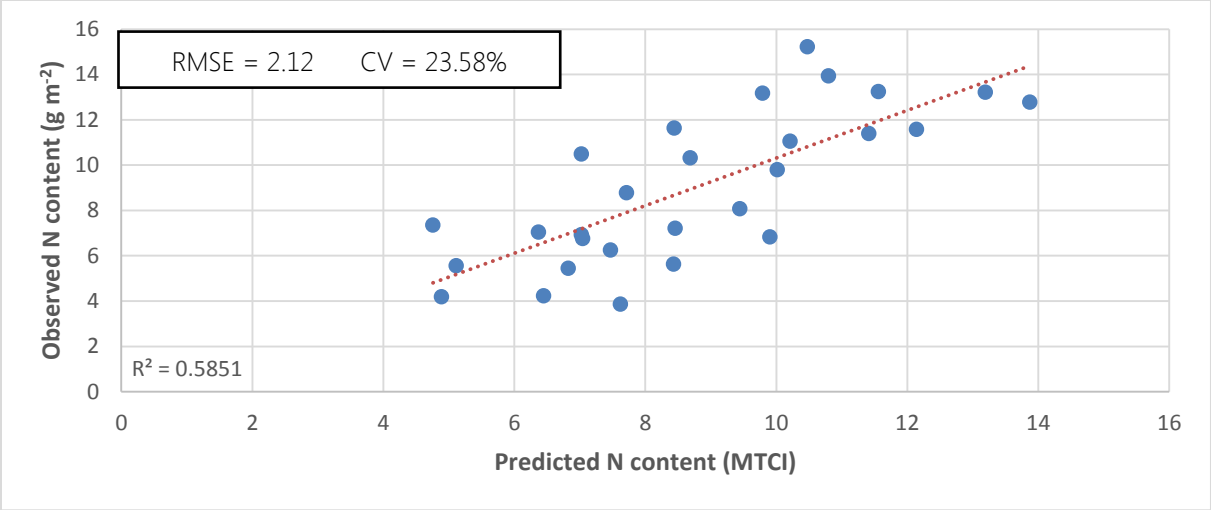

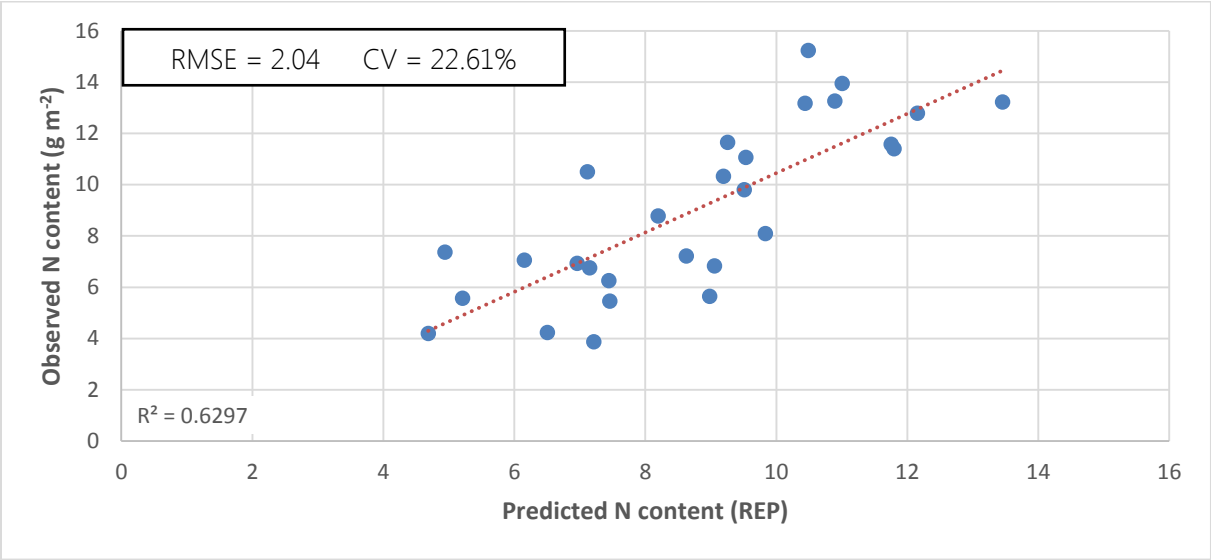

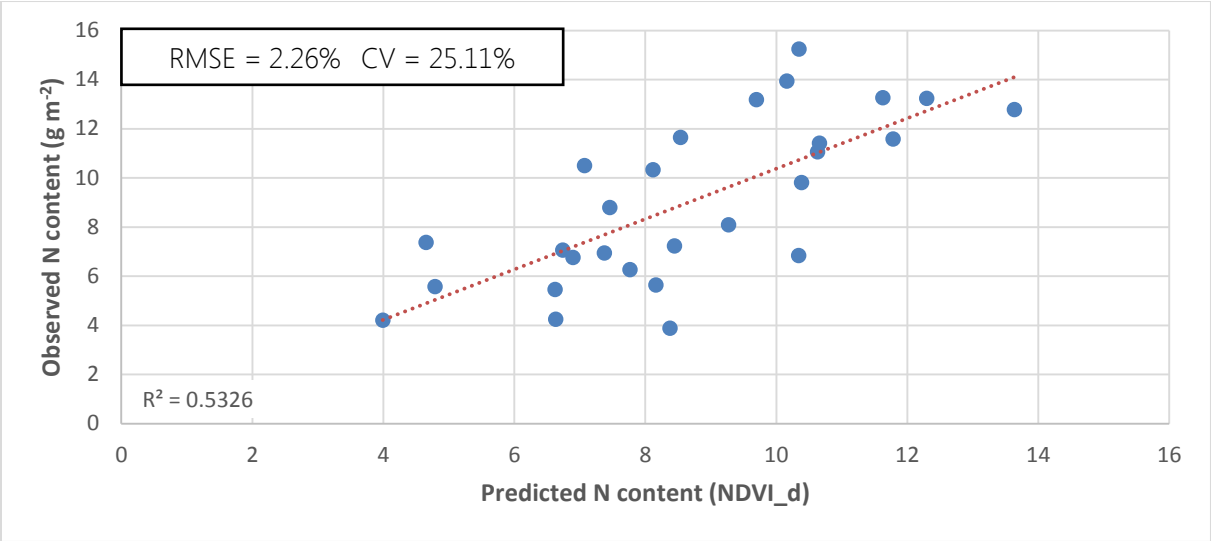

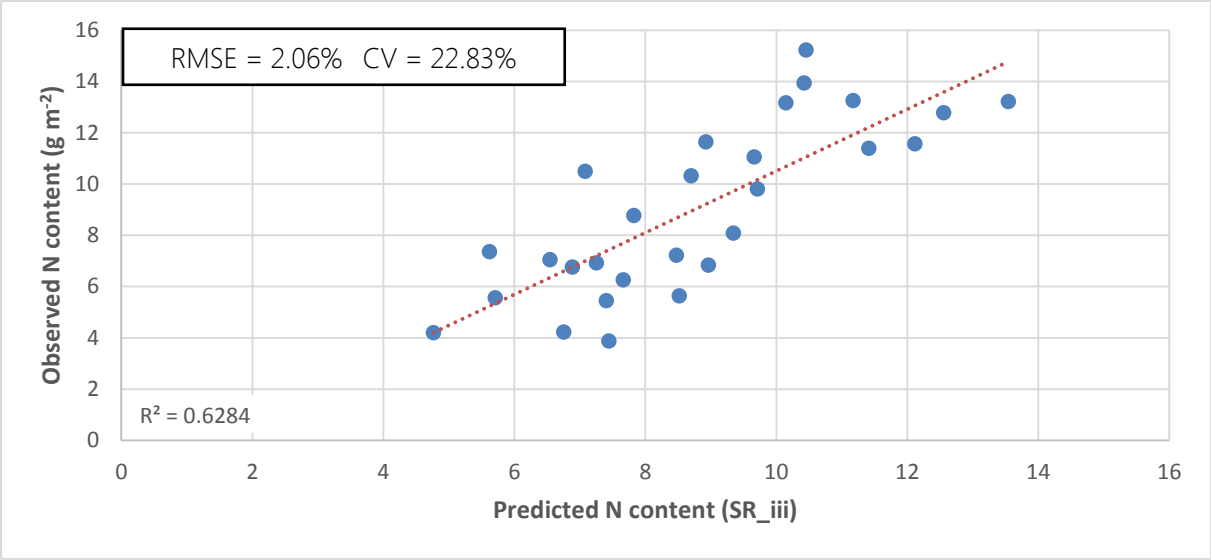
RMSE = 2.06% CV = 22.83%
R² = 0.6284
Observed N content (g m-2)
Predicted N content (SR_iii)
0
2
4
6
8
10
12
14
16

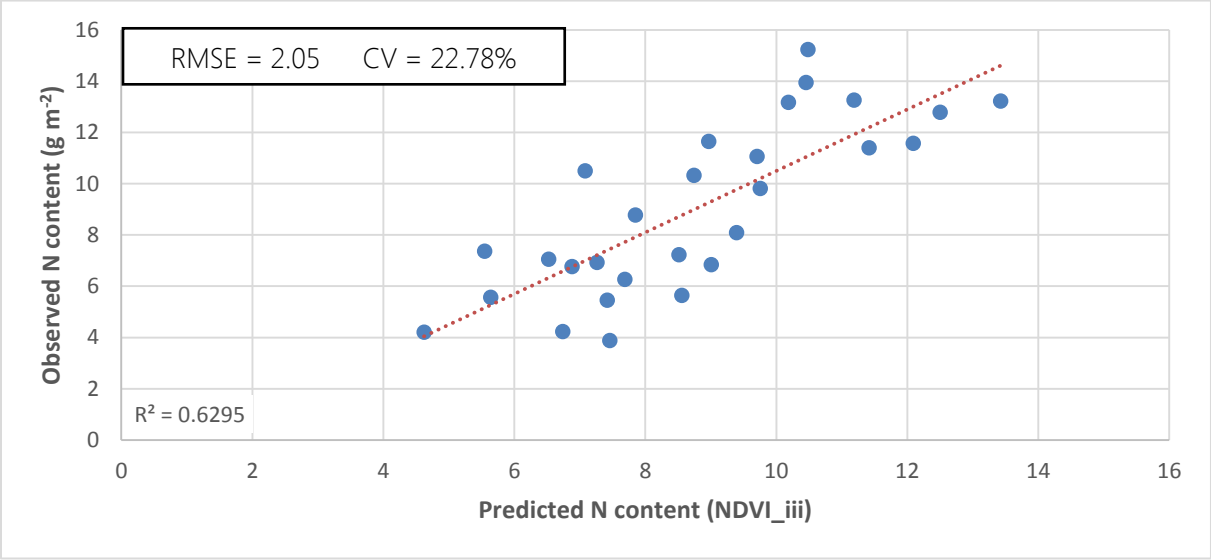
RMSE = 2.05 CV = 22.78%
R² = 0.6295
Observed N content (g m-2)
Predicted N content (NDVI_iii)
0
2
4
6
8
10
12
14
16

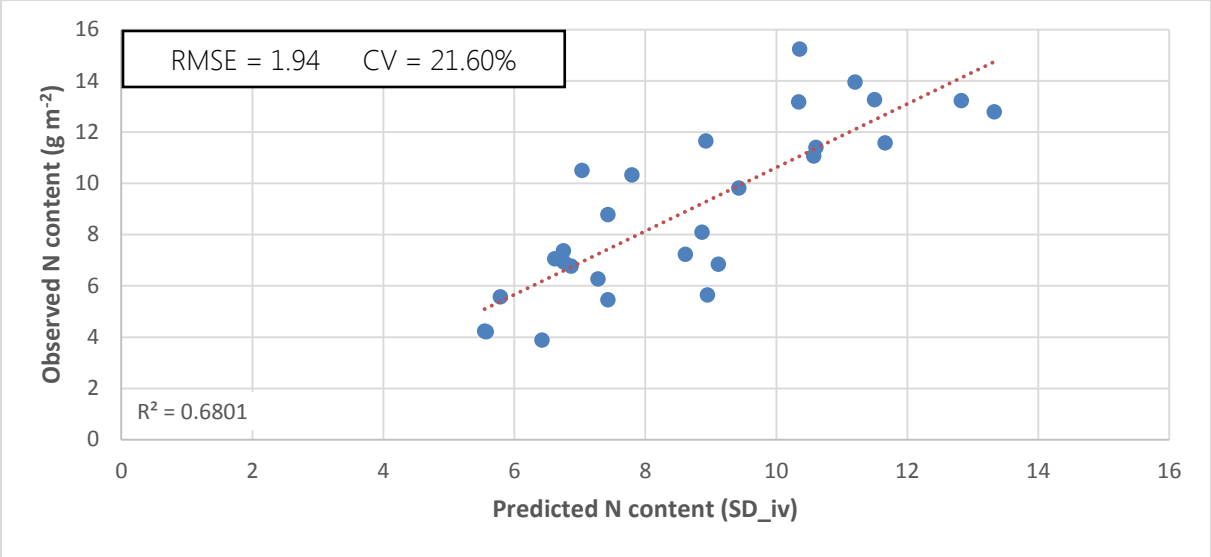
RMSE = 1.94 CV = 21.60%
R² = 0.6801
Observed N content (g m-2)
Predicted N content (SD_iv)
0
2
4
6
8
10
12
14
16

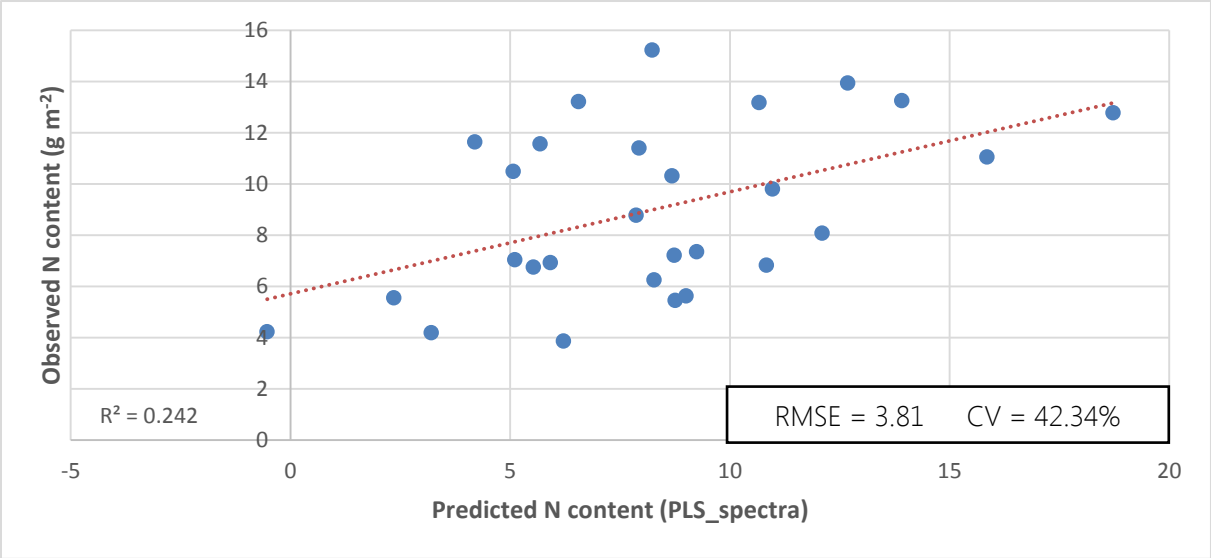
Observed N content (g m-2)
Predicted N content (PLS_spectra)
R² = 0.242
RMSE = 3.81 CV = 42.34%

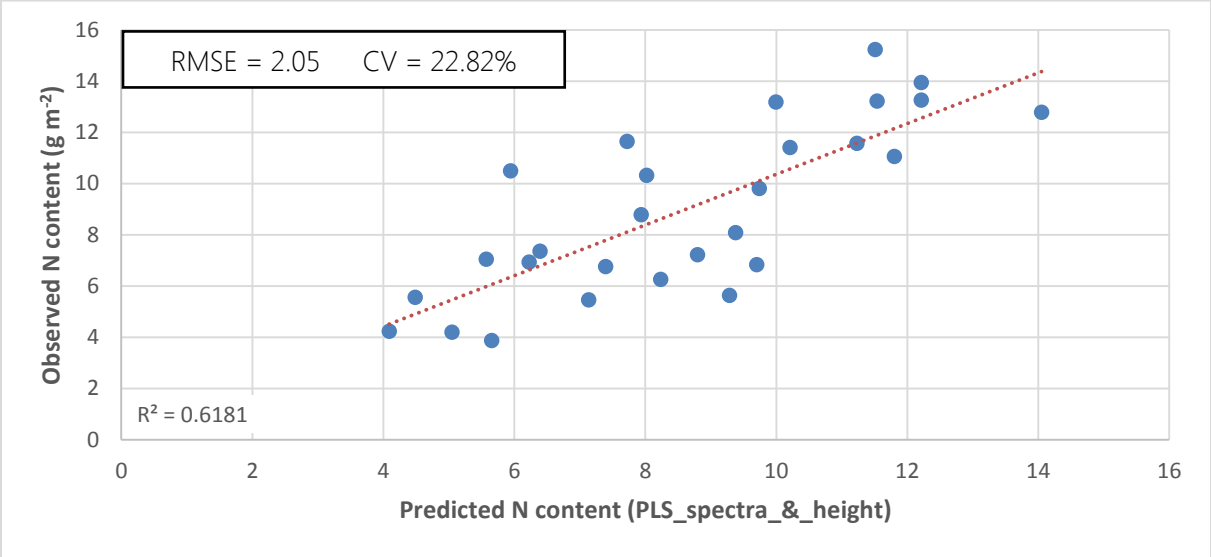
Observed N content (g m-2)
Predicted N content (PLS_spectra_&_height)
RMSE = 2.05 CV = 22.82%
R² = 0.6181

Carbon content (C)

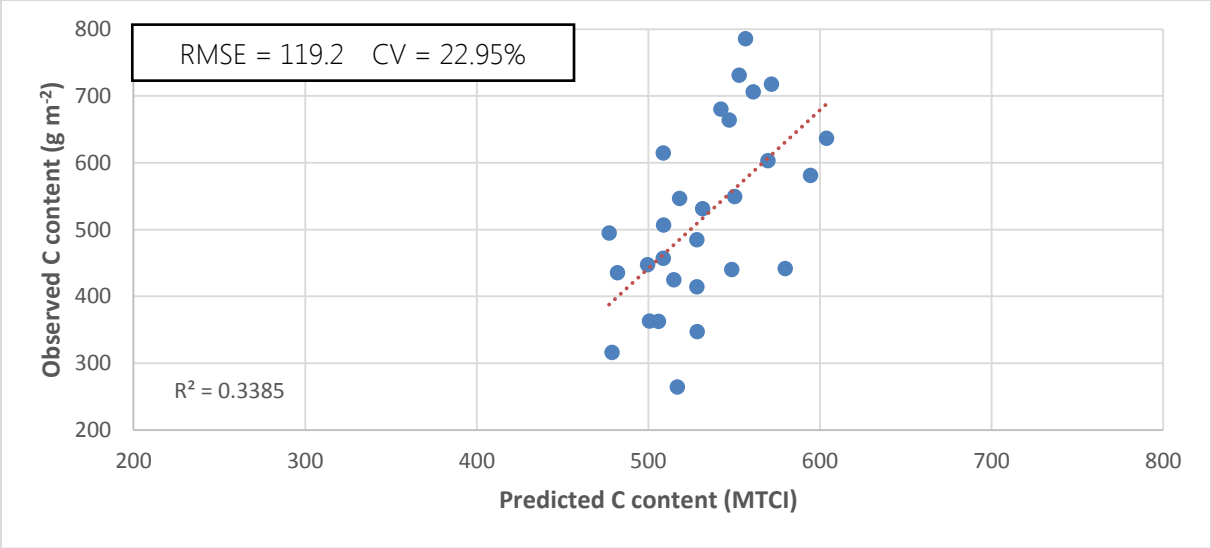

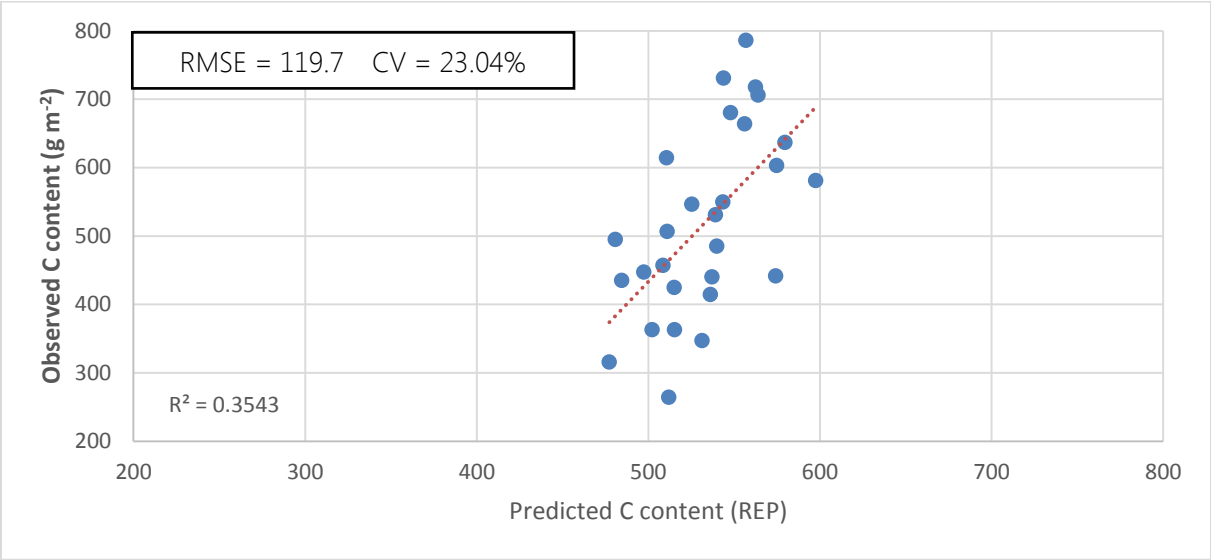

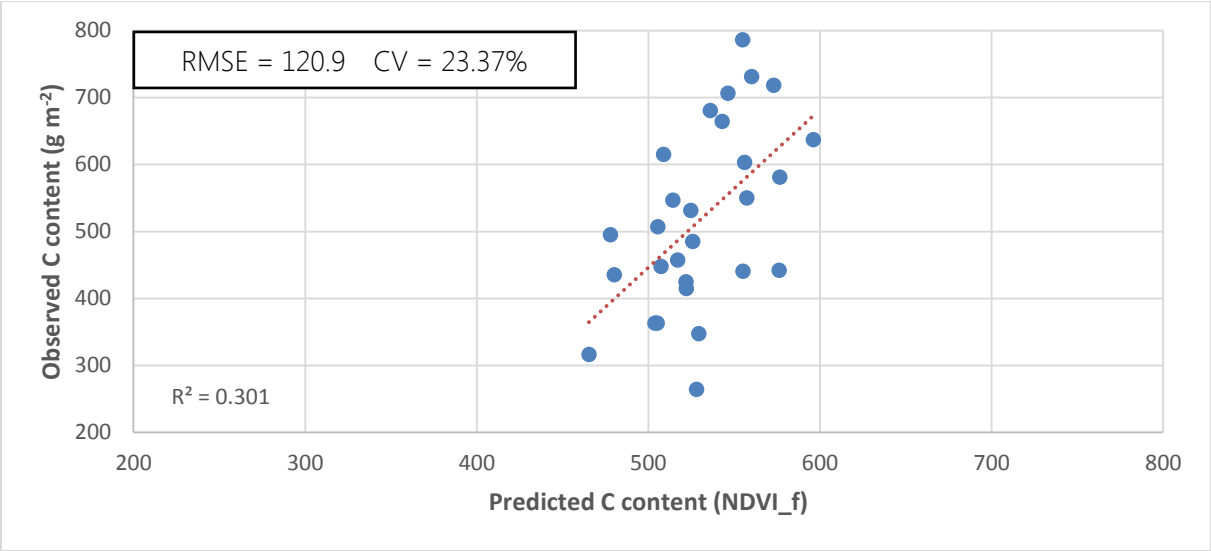

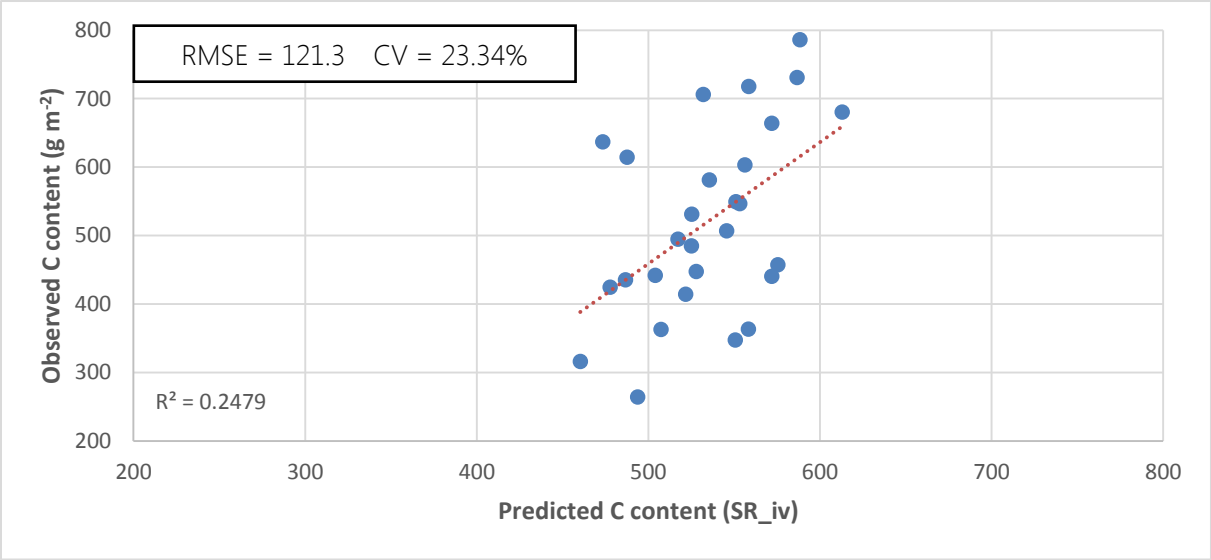
RMSE = 121.3 CV = 23.34%
R² = 0.2479
Observed C content (g m-2)
Predicted C content (SR_iv)
800
700
600
500
400
300
200
200
300
400
500
600
700
800

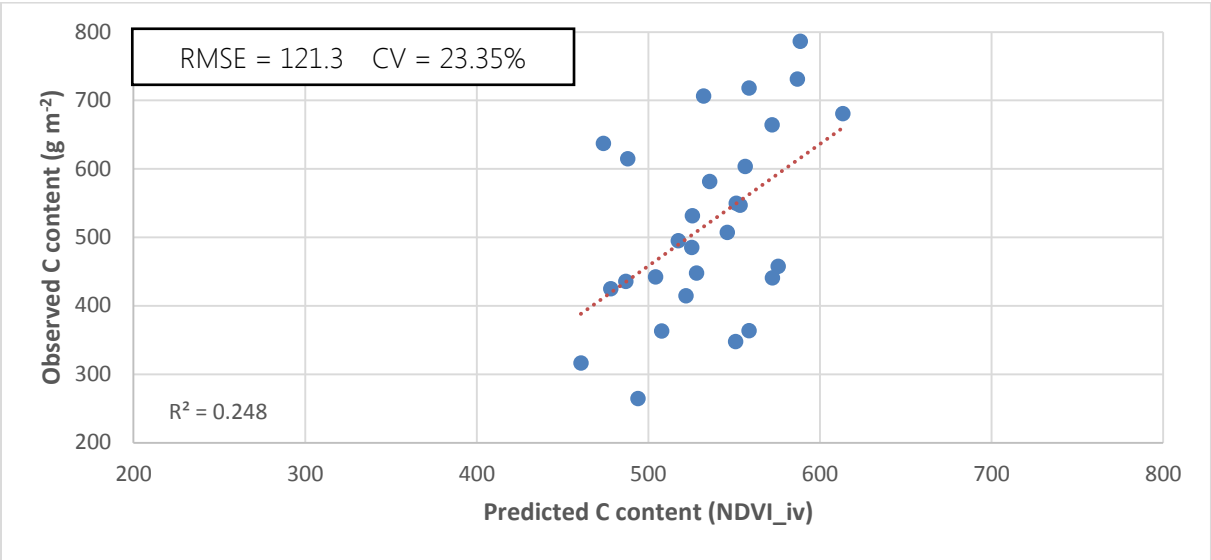
RMSE = 121.3 CV = 23.35%
R² = 0.248
Observed C content (g m-2)
Predicted C content (NDVI_iv)
800
700
600
500
400
300
200
200
300
400
500
600
700
800

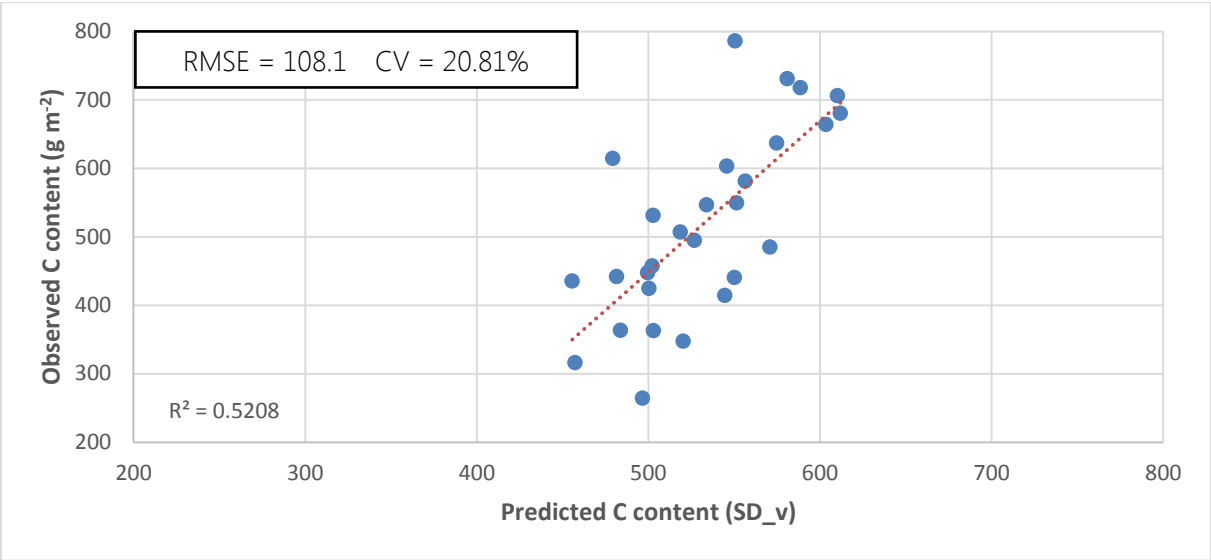
RMSE = 108.1 CV = 20.81%
R² = 0.5208
Observed C content (g m-2)
Predicted C content (SD_v)
800
700
600
500
400
300
200
200
300
400
500
600
700
800

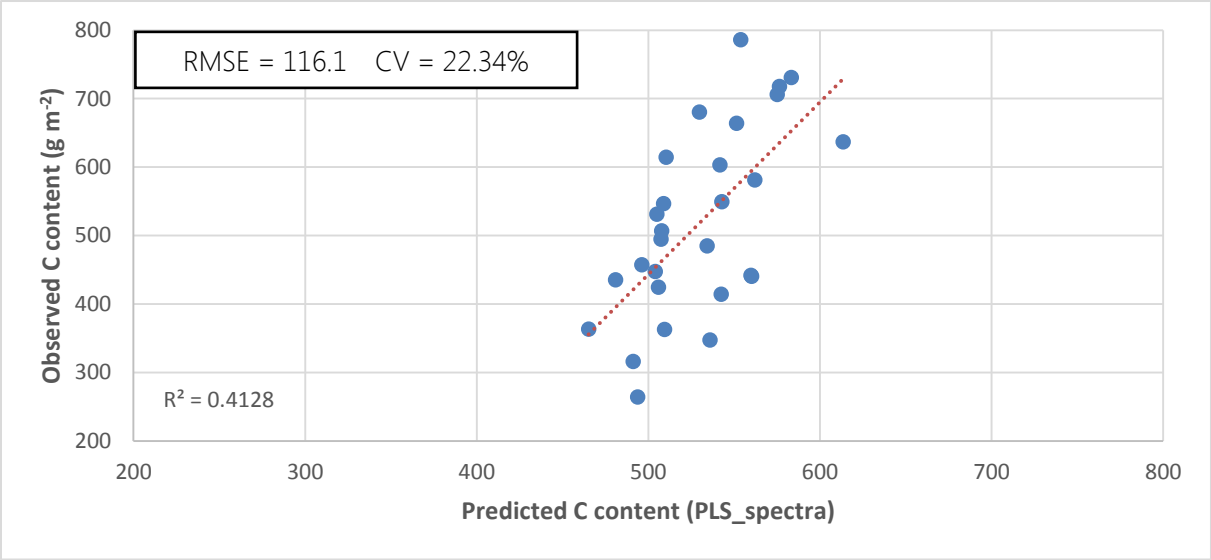
RMSE = 116.1 CV = 22.34%
R² = 0.4128
Observed C content (g m-2)
Predicted C content (PLS_spectra)
800
700
600
500
400
300
200
200
300
400
500
600
700
800

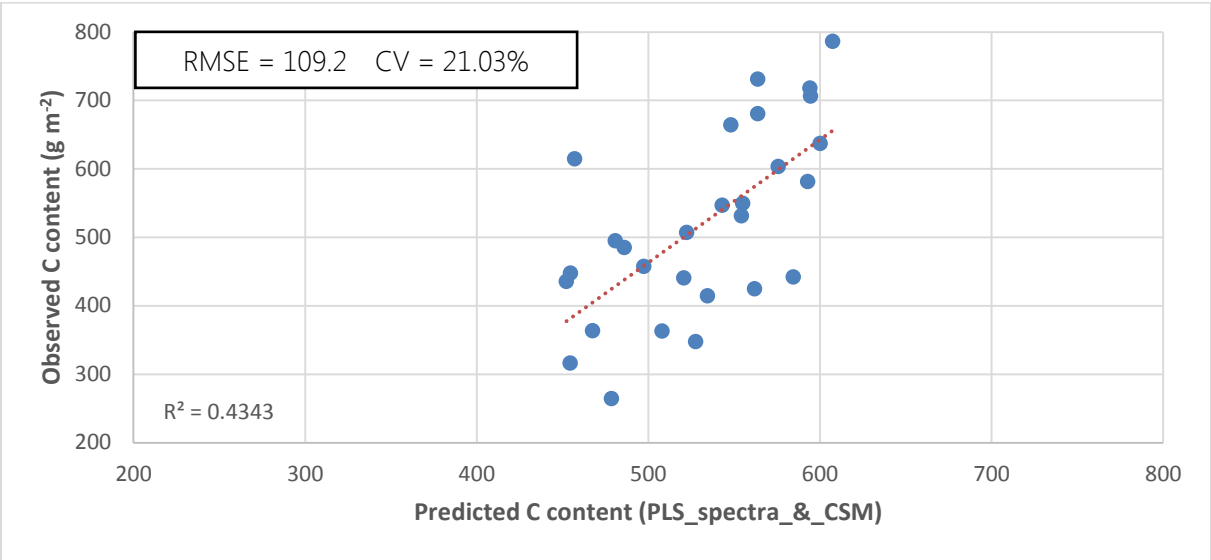
RMSE = 109.2 CV = 21.03%
R² = 0.4343
Observed C content (g m-2)
Predicted C content (PLS_spectra_&_CSM)
800
700
600
500
400
300
200
200
300
400
500
600
700
800

Leaf Chl content (CHL)

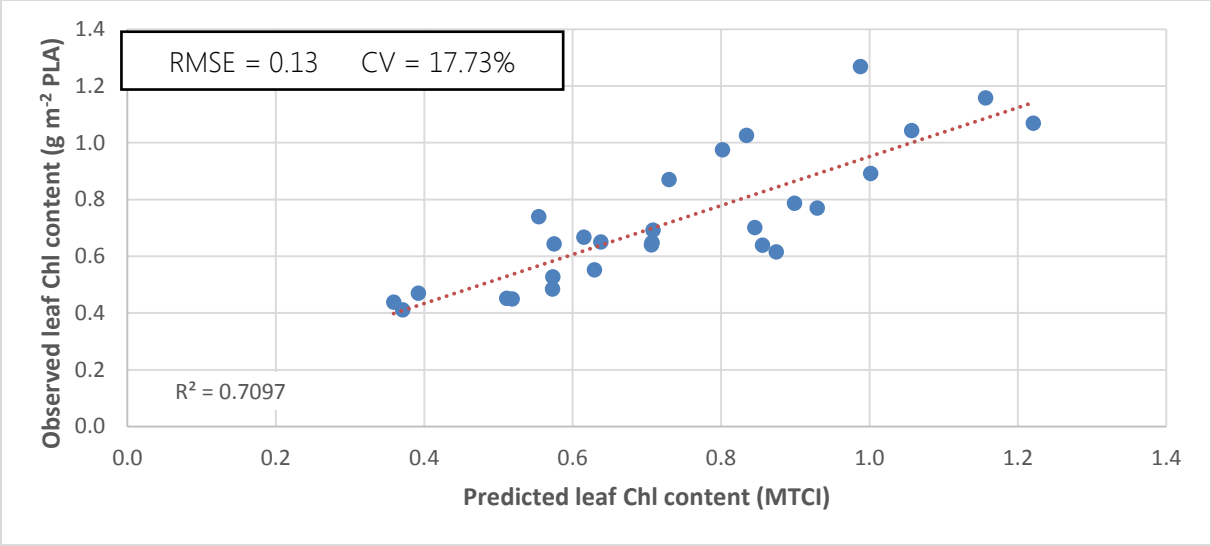

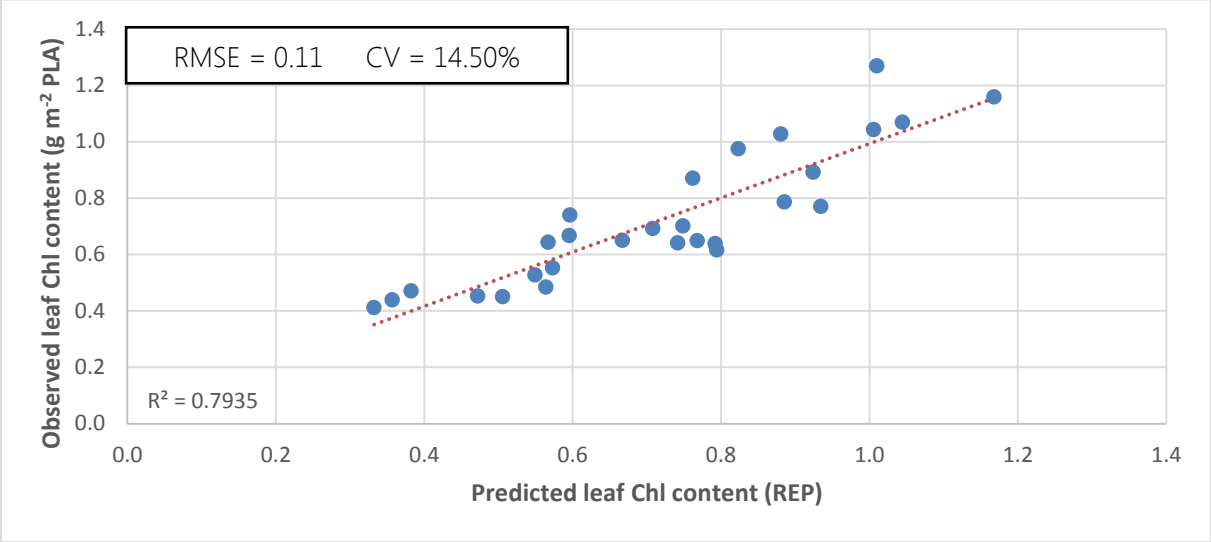

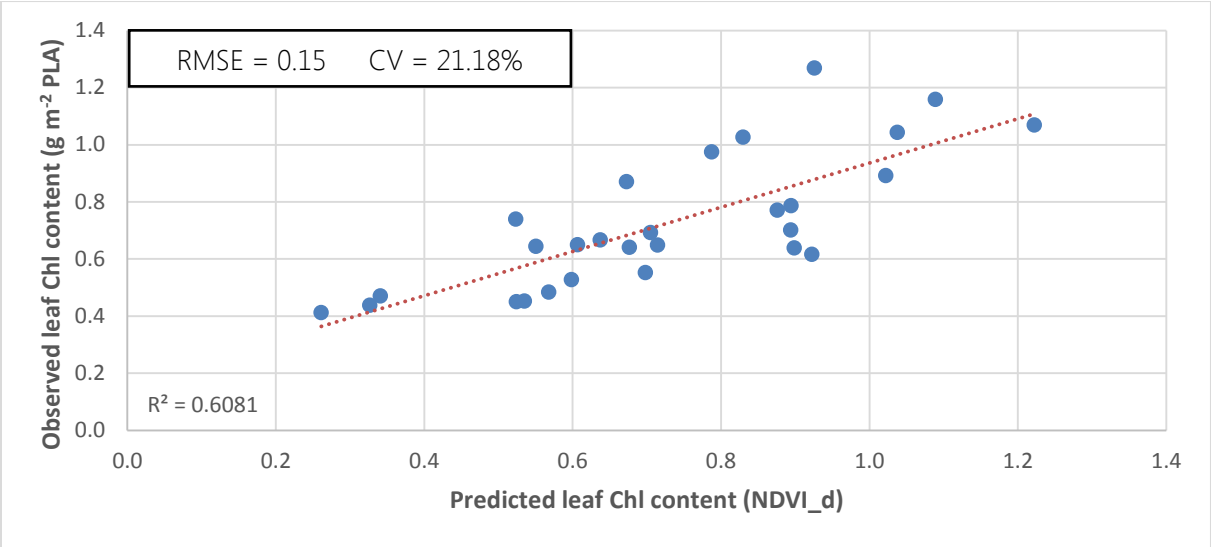

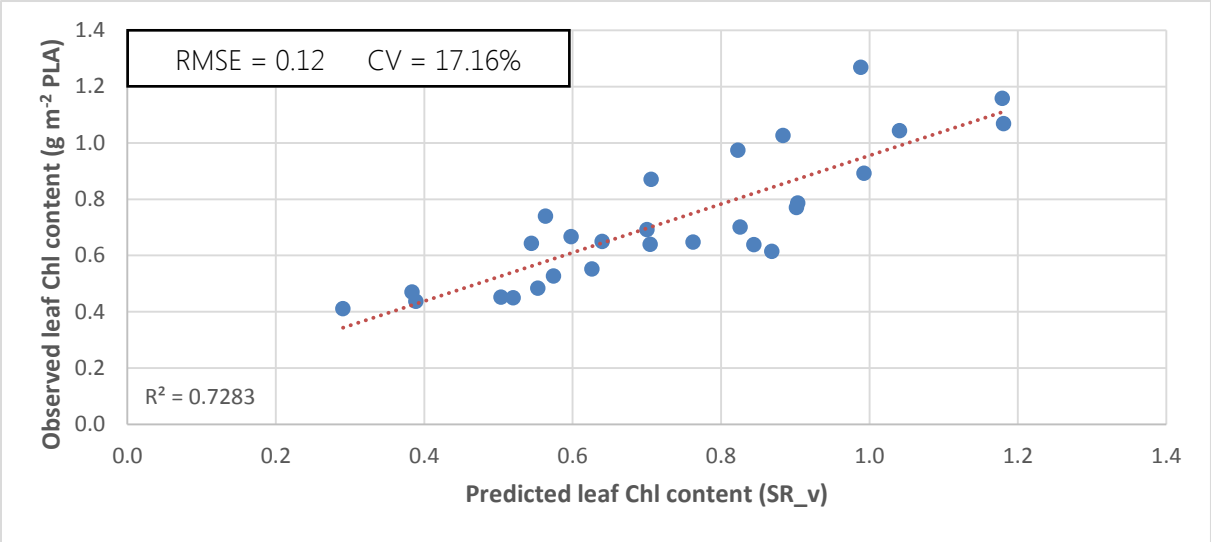
RMSE = 0.12 CV = 17.16%
R² = 0.7283
Observed leaf Chl content (g m-2 PLA)
Predicted leaf Chl content (SR_v)
0.0
0.2
0.4
0.6
0.8
1.0
1.2
1.4

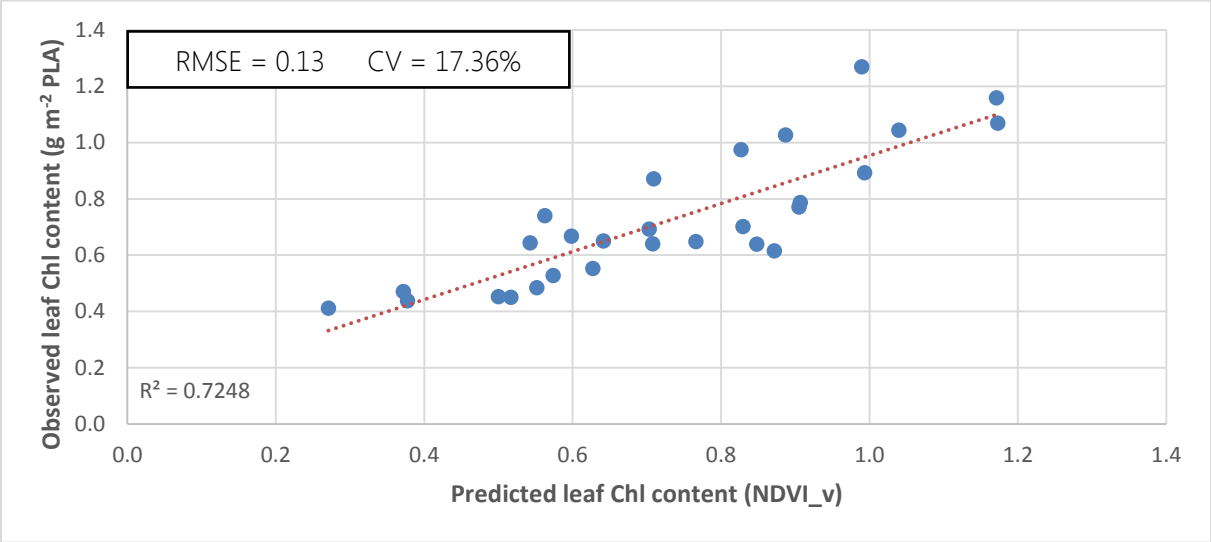
RMSE = 0.13 CV = 17.36%
R² = 0.7248
Observed leaf Chl content (g m-2 PLA)
Predicted leaf Chl content (NDVI_v)
0.0
0.2
0.4
0.6
0.8
1.0
1.2
1.4

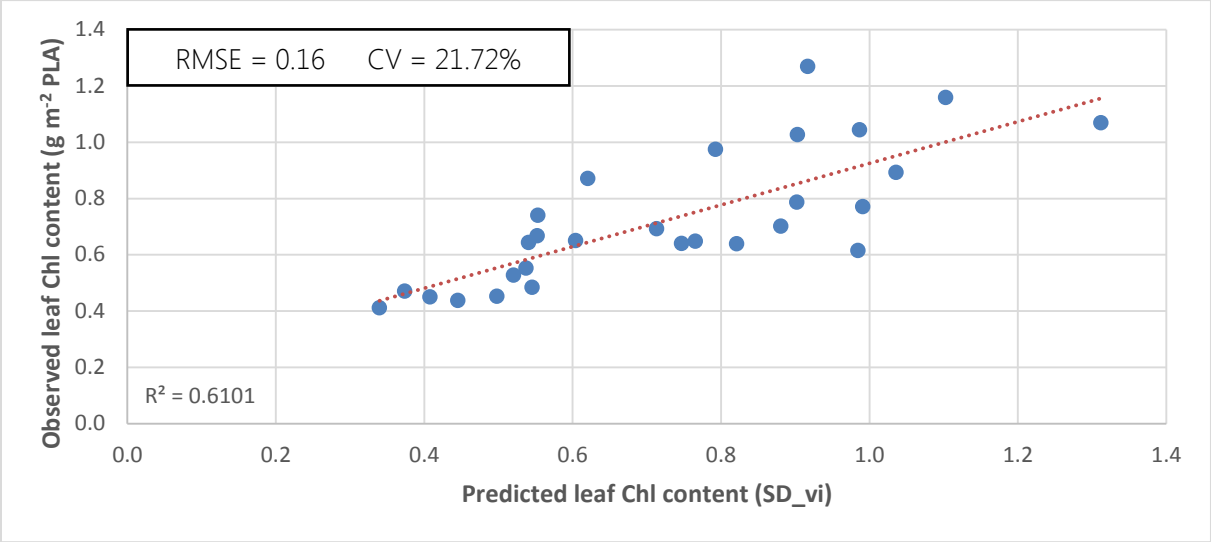
RMSE = 0.16 CV = 21.72%
R² = 0.6101
Observed leaf Chl content (g m-2 PLA)
Predicted leaf Chl content (SD_vi)
0.0
0.2
0.4
0.6
0.8
1.0
1.2
1.4

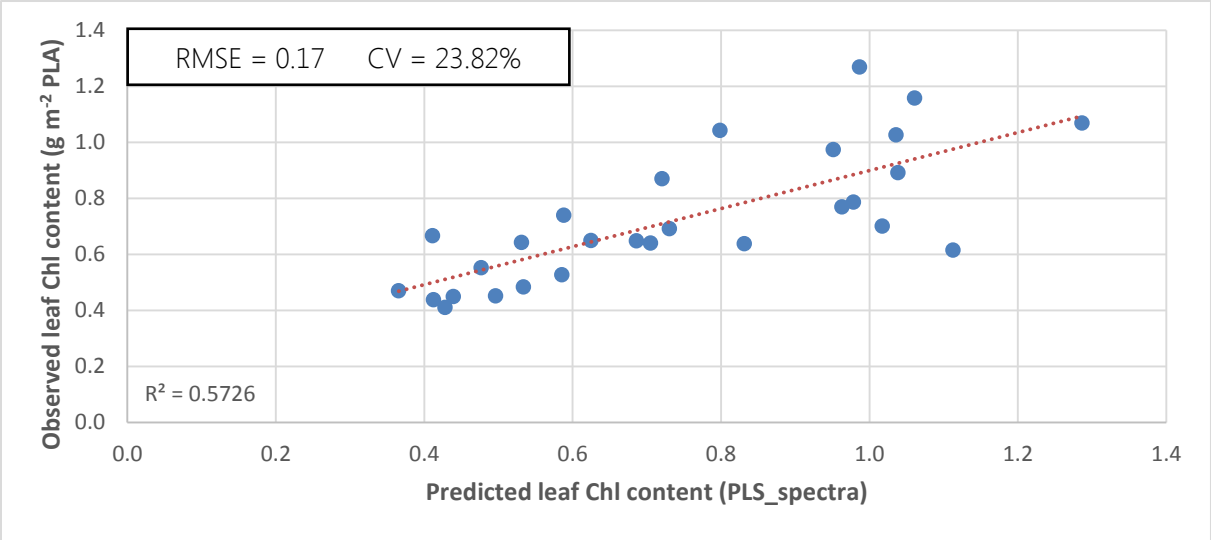
RMSE = 0.17 CV = 23.82%
R² = 0.5726
Observed leaf Chl content (g m-2 PLA)
Predicted leaf Chl content (PLS_spectra)
0.0
0.2
0.4
0.6
0.8
1.0
1.2
1.4

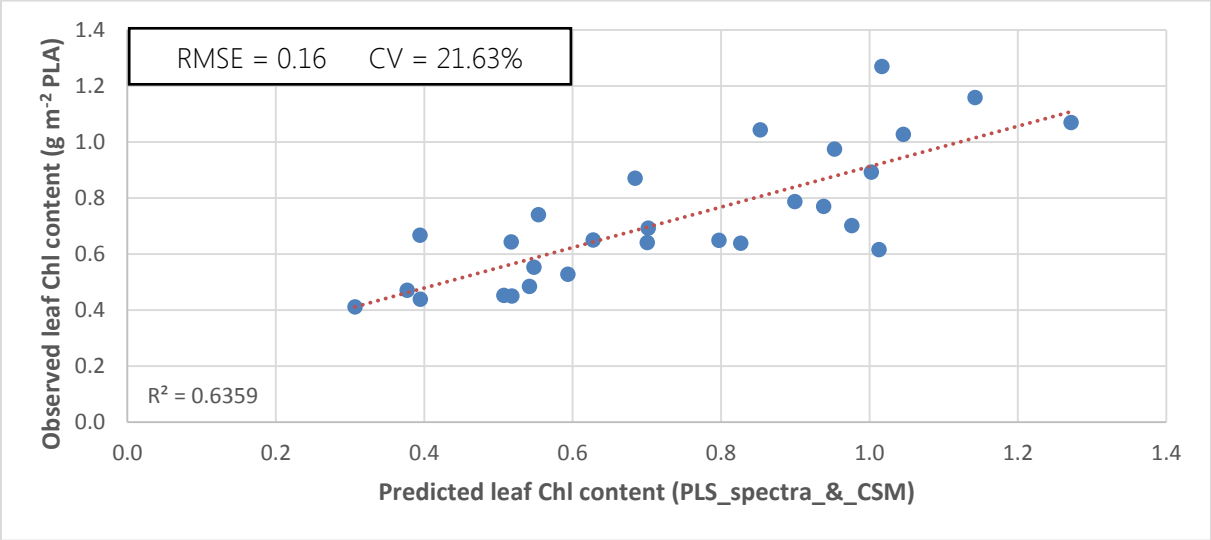
RMSE = 0.16 CV = 21.63%
R² = 0.6359
Observed leaf Chl content (g m-2 PLA)
Predicted leaf Chl content (PLS_spectra_&_CSM)
0.0
0.2
0.4
0.6
0.8
1.0
1.2
1.4

Appendix K: Residuals of predictions –vs– Observed values

The scatter plots below depict the relation between residuals of predictions (following from the best performing model) during validation on the one hand (y-axis) and the observed (i.e. in situ measured) trait values (x-axis) on the other (n=28). Based on these graphs, it is reasoned in paragraph 9.2.2 that models may be troubled regarding the prediction of extreme (low/high) values. It is argued that this notion is particularly valid for C content, fresh biomass and N content, indicated by the comparatively steeper (negative) regression lines and higher R^2 values with respect to the goodness-of-fit thereof. Following the scatterplots, tabular overviews are provided that display the absolute quantitative prediction residuals of all validated models for individual plots with respect to observed values.

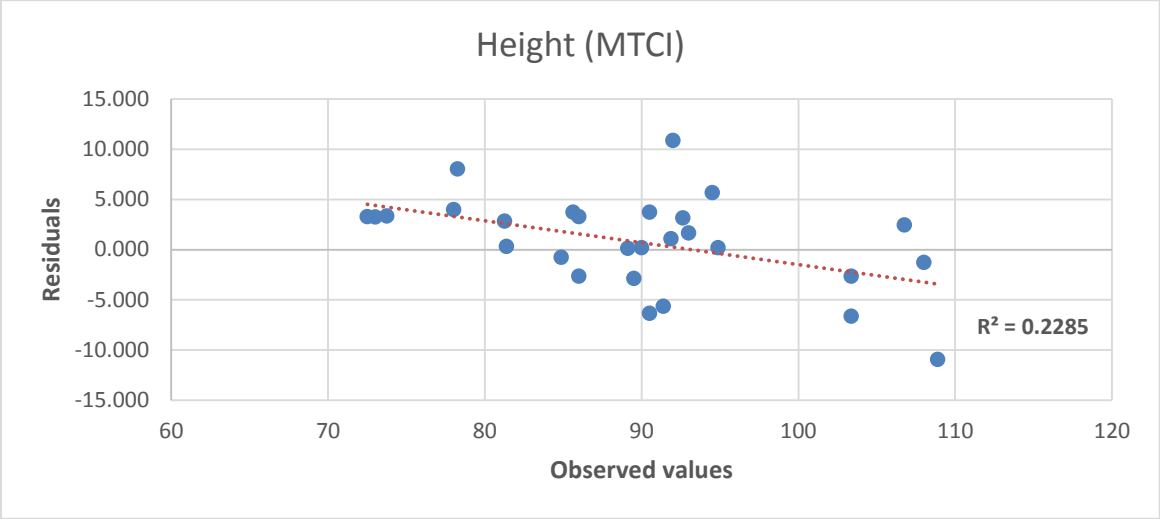

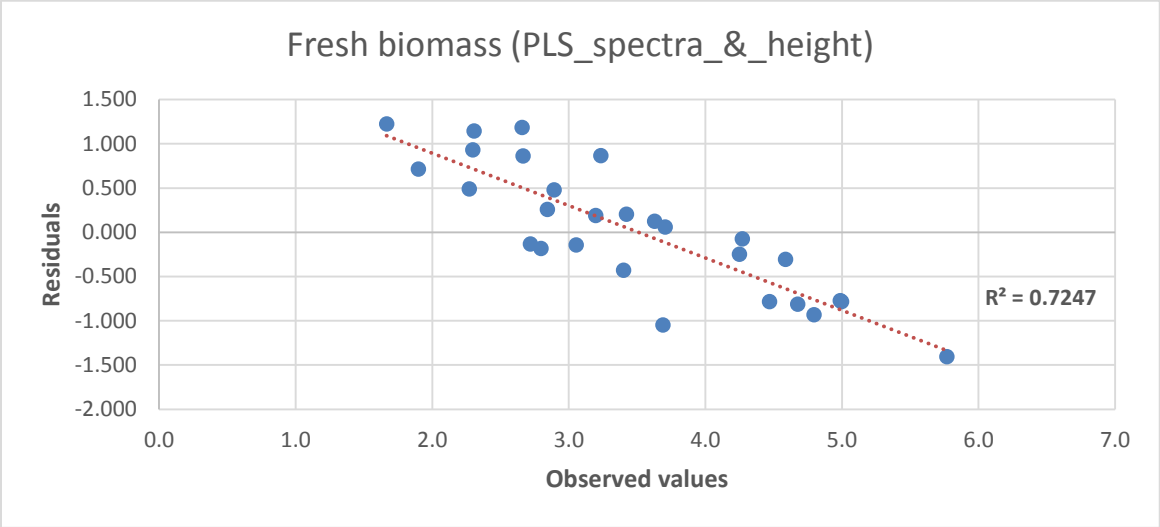

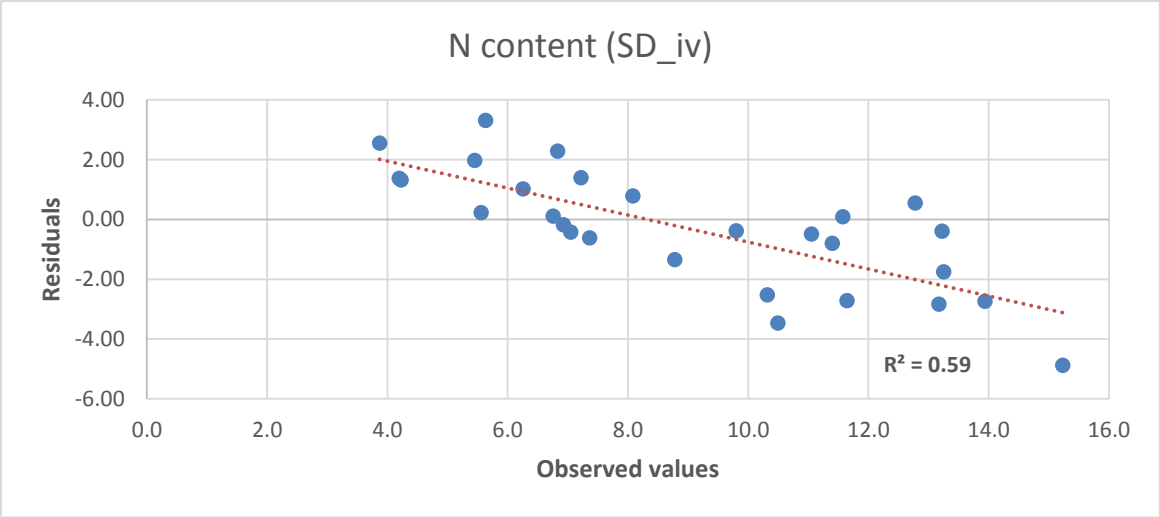
N content (SD_iv)
Residuals
Observed values
R² = 0.59
4.00
2.00
0.00
-2.00
-4.00
-6.00
0.0
2.0
4.0
6.0
8.0
10.0
12.0
14.0
16.0

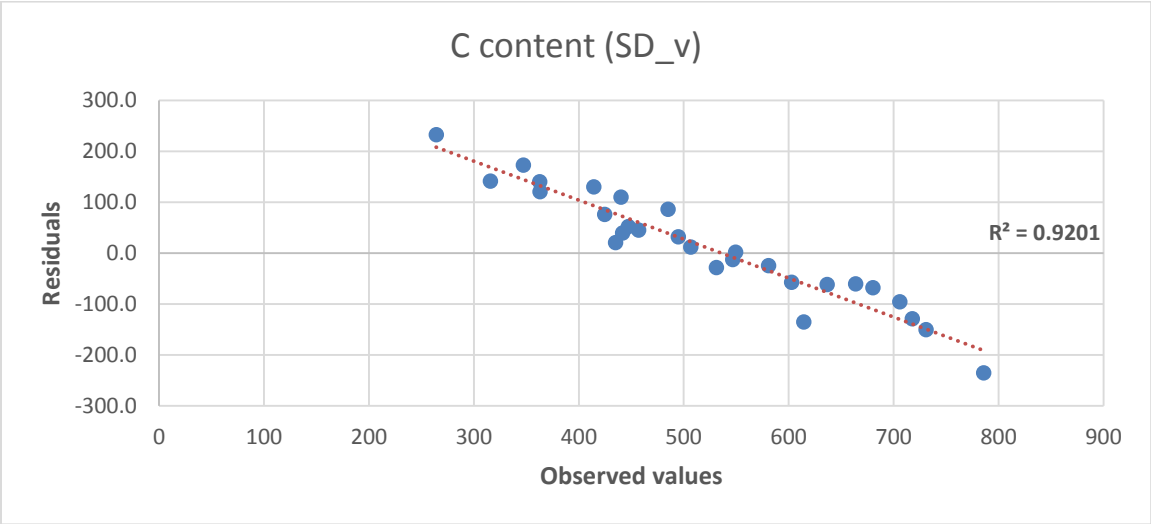
C content (SD_v)
Residuals
Observed values
R² = 0.9201
300.0
200.0
100.0
0.0
-100.0
-200.0
-300.0
0
100
200
300
400
500
600
700
800
900

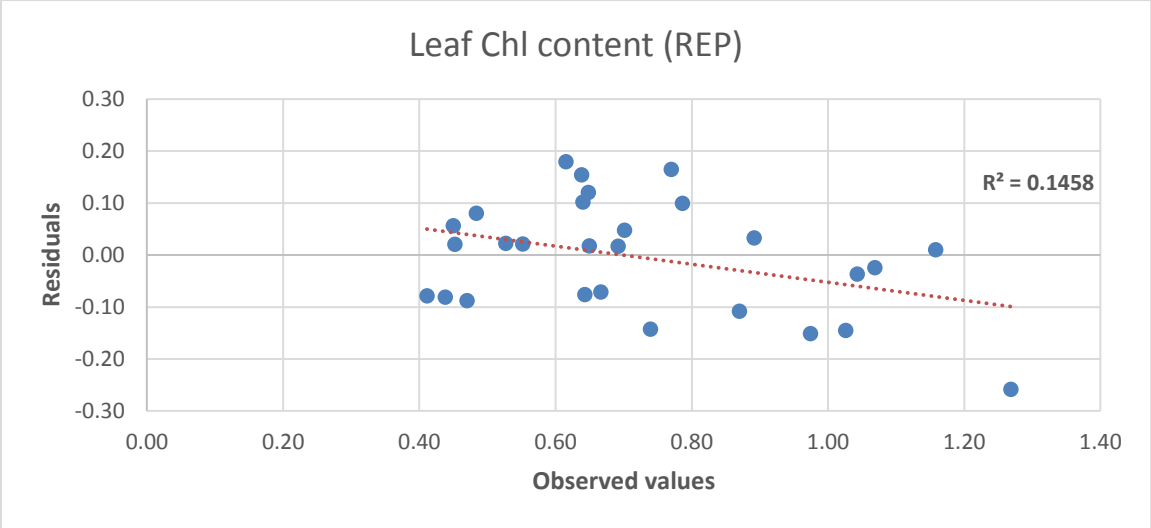
Leaf Chl content (REP)
Residuals
Observed values
R² = 0.1458
0.30
0.20
0.10
0.00
-0.10
-0.20
-0.30
0.00
0.20
0.40
0.60
0.80
1.00
1.20
1.40

Height prediction residuals

Table: Residuals of predictions of height during validation for all tested indices (units are in absolute numbers)

PlotID	REP	MTCI	MCARI/MTVI2	SR_i	NDVI_i	SD_i	PLS1	PLS2
8	6.391	3.733	5.584	3.379	3.482	5.588	3.643	-1.359
12	2.733	1.096	4.266	-1.454	-1.368	-0.941	-0.719	-2.428
15	7.524	5.691	9.398	5.013	5.077	2.783	5.783	4.816
19	-1.082	-2.877	3.179	-3.173	-3.145	-3.895	-1.492	0.972
20a	0.288	-1.276	-1.351	-0.233	-0.368	-2.667	-0.676	-3.052
20b	-0.382	-2.638	4.404	0.301	0.329	-0.538	0.610	2.583
22	3.368	3.334	9.566	6.717	6.586	5.646	7.108	5.647
30	2.179	0.184	8.855	0.552	0.640	-3.045	1.044	5.861
40a	4.018	3.976	9.050	5.682	5.650	0.763	3.203	-1.033
40b	9.859	10.862	9.817	12.283	12.252	9.111	11.679	14.751
41	-6.287	-6.633	-5.361	-6.766	-6.673	-6.921	-7.131	-0.181
46	-1.132	-0.772	0.028	0.811	0.826	-1.772	-2.591	-3.957
47	-0.690	0.316	0.624	1.875	1.830	1.165	-0.597	-4.556
48	-1.488	0.189	-3.951	-0.270	-0.169	-1.892	-2.790	-1.801
55	0.852	3.157	-5.807	0.657	0.758	4.672	0.515	1.051
62	-3.362	2.467	-10.589	-3.586	-3.590	0.821	0.407	-0.727
66	-1.340	1.659	-6.805	-3.269	-3.190	-0.957	-3.781	-8.433
69a	6.428	3.294	6.553	3.400	3.476	4.973	4.472	-4.964
72	3.608	3.283	2.661	6.325	6.133	9.910	6.638	6.483
78	-9.838	-10.942	-7.226	-12.789	-12.693	-9.276	-7.523	-4.136
79	2.262	0.129	5.747	0.108	0.182	2.049	3.225	3.961
89	-6.049	-6.332	0.250	-6.757	-6.787	-6.918	-4.964	-1.820
91b	3.073	2.844	9.209	3.964	3.969	2.943	4.059	0.564
93	2.145	3.257	14.294	4.249	3.992	5.601	8.225	13.003
104	4.424	3.718	7.766	4.149	4.230	4.333	4.968	6.035
107	-5.800	-5.647	-1.890	-2.806	-2.741	-6.370	-4.519	5.297
116a	6.447	8.037	7.234	8.232	8.263	3.728	5.068	1.635
117	-4.762	-2.652	-8.416	-3.940	-3.876	-2.704	-3.919	-1.074

Fresh biomass prediction residuals

Table: Residuals of predictions of fresh biomass during validation for all tested indices (units are in absolute numbers)

PlotID	REP	MTCI	NDVI_d	SR_iii	SR_iv	NDVI_iii	NDVI_iv	PLS1	PLS2
8	-0.651	-0.773	-0.793	-0.731	-0.709	-0.160	-0.601	-0.707	-0.785
12	-0.974	-1.045	-1.078	-1.117	-1.096	-0.271	-1.083	-1.214	-0.812
15	-0.168	-0.244	-0.393	-0.248	-0.228	-0.594	-0.324	-0.621	-0.248
19	-0.035	-0.118	-0.159	-0.090	-0.072	0.100	-0.115	-0.248	0.204
20a	0.128	0.071	-0.113	0.142	0.153	-0.493	0.075	-0.364	-0.075
20b	0.948	0.839	0.812	1.014	1.032	0.875	0.984	0.885	0.929
22	0.092	0.092	0.051	0.295	0.304	-0.083	0.261	0.066	-0.131
30	-0.051	-0.142	-0.244	-0.099	-0.079	-0.461	-0.254	-0.512	0.125
40a	0.789	0.793	0.839	0.891	0.905	0.683	0.675	0.291	0.490
40b	0.838	0.909	0.829	0.942	0.959	-0.305	0.802	0.642	0.866
41	-1.939	-1.941	-1.971	-1.947	-1.926	-2.057	-1.957	-1.975	-1.405
46	0.305	0.330	0.403	0.411	0.426	0.319	0.285	0.149	0.259
47	0.197	0.253	0.334	0.326	0.338	0.338	0.277	0.306	-0.182
48	-0.065	0.035	0.099	-0.030	-0.008	0.016	-0.123	-0.066	0.059
55	-1.151	-1.018	-0.946	-1.181	-1.160	-0.742	-1.029	-0.595	-0.932
62	-0.438	-0.117	-0.182	-0.495	-0.476	-0.604	-0.312	0.031	-0.308
66	0.659	0.827	0.904	0.548	0.567	0.812	0.624	0.987	0.477
69a	0.189	0.040	0.060	0.108	0.128	0.538	0.192	0.122	-0.429
72	-0.296	-0.312	-0.312	-0.078	-0.071	0.386	0.108	0.099	-0.143
78	-1.059	-1.099	-1.225	-1.185	-1.163	-0.601	-1.037	-0.895	-0.772
79	0.873	0.775	0.727	0.801	0.821	0.977	0.884	0.976	0.864
89	-0.014	-0.021	-0.040	-0.033	-0.020	0.149	-0.058	-0.040	0.191
91b	-0.512	-0.517	-0.499	-0.470	-0.455	-0.788	-0.534	-0.496	-1.048
93	0.812	0.870	0.723	0.934	0.935	0.755	0.988	1.034	0.714
104	1.164	1.139	1.140	1.161	1.181	1.062	1.155	1.241	1.144
107	0.583	0.599	0.661	0.702	0.721	0.484	0.529	0.469	1.184
116a	1.531	1.620	1.767	1.567	1.582	1.433	1.365	1.291	1.222
117	-1.091	-0.965	-0.963	-1.063	-1.043	-0.857	-1.021	-0.893	-0.785

N content prediction residuals

Table: Residuals of predictions of N content during validation for all tested indices (units are in absolute numbers)

PlotID	MTCI	REP	NDVI_d	SR_iii	NDVI_iii	SD_iv	PLS1	PLS2
8	-3.39	-2.74	-3.48	-3.03	-2.99	-2.83	-2.51	-3.18
12	1.36	1.75	1.19	1.27	1.31	0.79	4.02	1.30
15	0.01	0.40	-0.74	0.01	0.02	-0.79	-3.47	-1.19
19	-1.07	-0.58	-1.32	-0.95	-0.93	-1.35	-0.91	-0.84
20a	-0.03	0.23	-0.92	0.32	0.20	-0.40	-6.67	-1.69
20b	1.37	2.00	1.17	1.95	1.96	1.98	3.30	1.68
22	-0.45	-0.35	-0.77	0.15	0.08	0.23	-3.21	-1.07
30	-1.63	-1.12	-2.20	-1.62	-1.58	-2.52	-1.64	-2.30
40a	2.22	2.27	2.40	2.52	2.51	1.32	-4.76	-0.14
40b	0.57	0.18	0.21	0.54	0.52	0.09	-5.89	-0.34
41	-4.76	-4.74	-4.89	-4.78	-4.75	-4.88	-7.01	-3.72
46	0.10	0.03	0.45	0.33	0.34	-0.17	-1.02	-0.70
47	-0.68	-0.90	-0.31	-0.50	-0.52	-0.43	-1.95	-1.48
48	0.21	-0.29	0.58	-0.09	-0.05	-0.38	1.17	-0.06
55	-0.84	-1.52	-0.42	-1.39	-1.35	-0.48	4.80	0.75
62	1.10	-0.62	0.86	-0.22	-0.27	0.55	5.94	1.27
66	3.07	2.22	3.51	2.13	2.18	2.28	4.00	2.87
69a	-3.20	-2.39	-3.10	-2.72	-2.67	-2.72	-7.45	-3.92
72	-2.60	-2.42	-2.71	-1.74	-1.82	-0.61	1.88	-0.97
78	-3.14	-2.93	-3.78	-3.51	-3.48	-2.73	-1.26	-1.72
79	2.79	3.35	2.53	2.88	2.92	3.32	3.37	3.65
89	0.29	0.39	0.14	0.13	0.12	0.11	-1.23	0.64
91b	-3.47	-3.38	-3.42	-3.41	-3.41	-3.46	-5.42	-4.55
93	0.69	0.49	-0.20	0.57	0.43	1.37	-0.99	0.85
104	1.24	1.41	1.23	1.25	1.29	1.39	1.51	1.58
107	1.21	1.19	1.51	1.41	1.43	1.02	2.02	1.98
116a	3.75	3.34	4.51	3.57	3.59	2.55	2.34	1.79
117	-1.70	-2.36	-1.63	-2.08	-2.07	-1.75	0.66	-1.04

C content prediction residuals

Table: Residuals of predictions of C content during validation for all tested indices (units are in absolute numbers)

PlotID	MTCI	REP	NDVI_f	SR_iv	NDVI_iv	SD_v	PLS1	PLS2
8	-116.7	-107.7	-120.8	-91.9	-91.7	-60.4	-112.3	-115.7
12	-138.0	-132.4	-144.1	-67.3	-67.0	-68.4	-150.4	-116.5
15	-33.3	-28.3	-46.9	-46.8	-46.6	-57.3	-61.2	-27.3
19	-28.4	-21.2	-32.3	6.6	6.8	-12.8	-37.6	-3.7
20a	13.4	16.4	-4.4	-45.4	-45.2	-24.5	-19.1	11.8
20b	143.1	152.5	141.2	144.7	144.9	140.2	146.7	145.2
22	46.9	49.2	44.9	51.4	51.7	20.4	45.7	17.0
30	0.7	7.9	-6.3	-5.7	-5.5	-28.4	-26.1	23.2
40a	137.5	139.0	141.9	195.3	195.5	120.6	102.0	104.3
40b	138.0	132.3	134.5	62.2	62.5	39.7	118.1	142.6
41	-229.2	-229.0	-230.8	-197.4	-197.2	-235.3	-232.1	-178.5
46	51.6	51.3	60.0	118.4	118.6	45.1	39.1	40.2
47	52.2	50.0	60.1	80.5	80.7	52.3	56.6	7.2
48	0.7	-6.1	7.9	1.5	1.7	2.0	-6.6	5.5
55	-178.0	-187.3	-170.7	-144.3	-144.1	-150.2	-147.7	-167.3
62	-32.8	-57.0	-40.5	-163.2	-162.9	-61.9	-23.1	-36.5
66	108.3	96.8	114.9	131.6	131.9	109.7	119.9	80.2
69a	43.4	55.0	40.9	40.2	40.4	85.8	49.2	1.0
72	-17.7	-14.1	-17.0	22.4	22.7	32.0	12.5	-14.2
78	-145.0	-142.2	-159.6	-174.1	-173.9	-95.9	-131.0	-111.6
79	113.8	121.8	107.7	107.4	107.6	130.2	128.1	120.1
89	2.2	4.3	-1.2	39.0	39.2	11.8	1.1	15.5
91b	-105.9	-104.0	-105.7	-126.8	-126.5	-135.3	-104.0	-157.5
93	163.0	161.3	149.4	144.5	144.8	141.3	175.3	138.5
104	181.3	184.1	182.2	203.4	203.6	173.0	188.7	180.4
107	90.2	90.4	97.3	53.1	53.5	75.8	81.3	137.3
116a	252.8	247.7	264.0	229.6	229.9	232.4	229.6	214.4
117	-146.0	-155.4	-144.7	-159.2	-159.0	-129.3	-141.3	-123.5

Leaf Chl content prediction residuals

Table: Residuals of predictions of leaf Chl content during validation for all tested indices (units are in absolute numbers)

PlotID	MTCI	REP	NDVI_d	SR_v	NDVI_v	SD_vi	PLS1	PLS2
8	-0.19	-0.15	-0.20	-0.14	-0.14	-0.12	0.01	0.02
12	-0.17	-0.15	-0.19	-0.15	-0.15	-0.18	-0.02	-0.02
15	-0.28	-0.26	-0.34	-0.28	-0.28	-0.35	-0.28	-0.25
19	-0.01	0.02	-0.04	-0.01	-0.01	-0.05	-0.03	-0.02
20a	0.00	0.01	-0.07	0.02	0.01	-0.06	-0.10	-0.02
20b	-0.19	-0.14	-0.22	-0.18	-0.18	-0.19	-0.15	-0.19
22	-0.08	-0.09	-0.13	-0.09	-0.10	-0.10	-0.10	-0.09
30	-0.14	-0.11	-0.20	-0.16	-0.16	-0.25	-0.15	-0.19
40a	0.07	0.06	0.07	0.07	0.07	-0.04	-0.01	0.07
40b	0.01	-0.04	-0.01	0.00	0.00	-0.06	-0.24	-0.19
41	0.11	0.10	0.11	0.12	0.12	0.12	0.19	0.11
46	0.05	0.02	0.07	0.05	0.05	-0.01	0.06	0.07
47	0.06	0.02	0.08	0.05	0.05	0.05	0.04	0.06
48	0.22	0.15	0.26	0.21	0.21	0.18	0.19	0.19
55	0.26	0.18	0.31	0.25	0.26	0.37	0.50	0.40
62	0.15	-0.02	0.15	0.11	0.10	0.24	0.22	0.20
66	0.14	0.05	0.19	0.12	0.13	0.18	0.32	0.28
69a	0.06	0.12	0.07	0.11	0.12	0.12	0.04	0.15
72	-0.08	-0.08	-0.11	-0.05	-0.06	0.01	-0.03	-0.04
78	0.16	0.16	0.11	0.13	0.13	0.22	0.19	0.17
79	0.07	0.10	0.04	0.06	0.07	0.11	0.06	0.06
89	-0.07	-0.08	-0.09	-0.10	-0.10	-0.10	-0.11	-0.13
91b	0.09	0.08	0.08	0.07	0.07	0.06	0.05	0.06
93	-0.04	-0.08	-0.15	-0.12	-0.14	-0.07	0.02	-0.10
104	0.02	0.02	0.01	0.01	0.01	0.02	0.04	0.01
107	-0.05	-0.07	-0.03	-0.07	-0.07	-0.11	-0.26	-0.27
116a	0.08	0.02	0.15	0.07	0.08	-0.02	-0.08	0.00
117	0.11	0.03	0.13	0.10	0.10	0.14	0.15	0.11

Appendix L: Prediction maps

Below, using the best performing index during validation, prediction maps were generated for each trait separately to assess the within-plot variability of predictions. In order to enhance discrimination of heterogeneity by means of a visual inspection, the parts of the study not used in either calibration or validation procedures are not shown. Likewise, the gradient scale in the legend only relates to observed minimum and maximum predicted values within ROIs of the plots used.

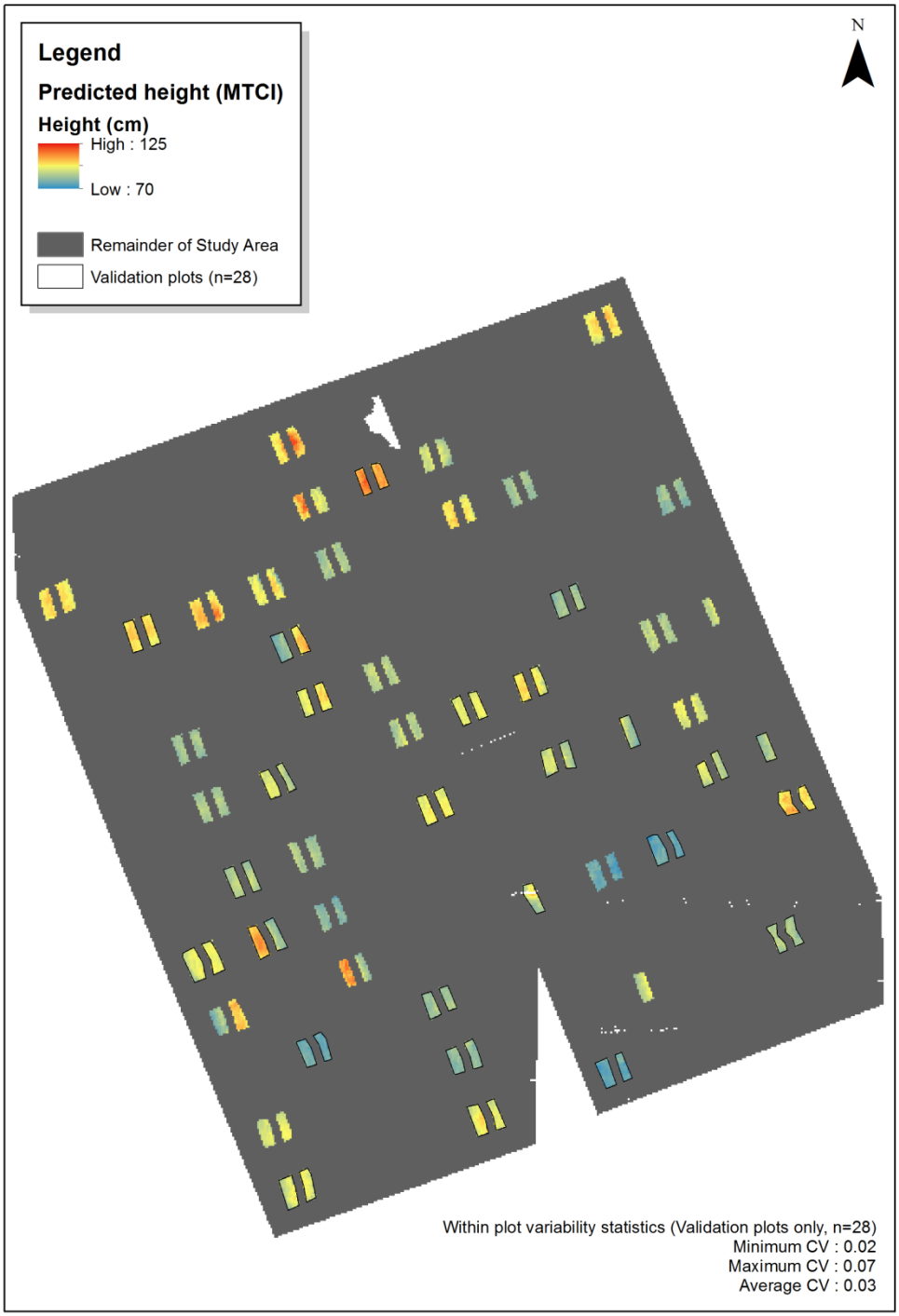

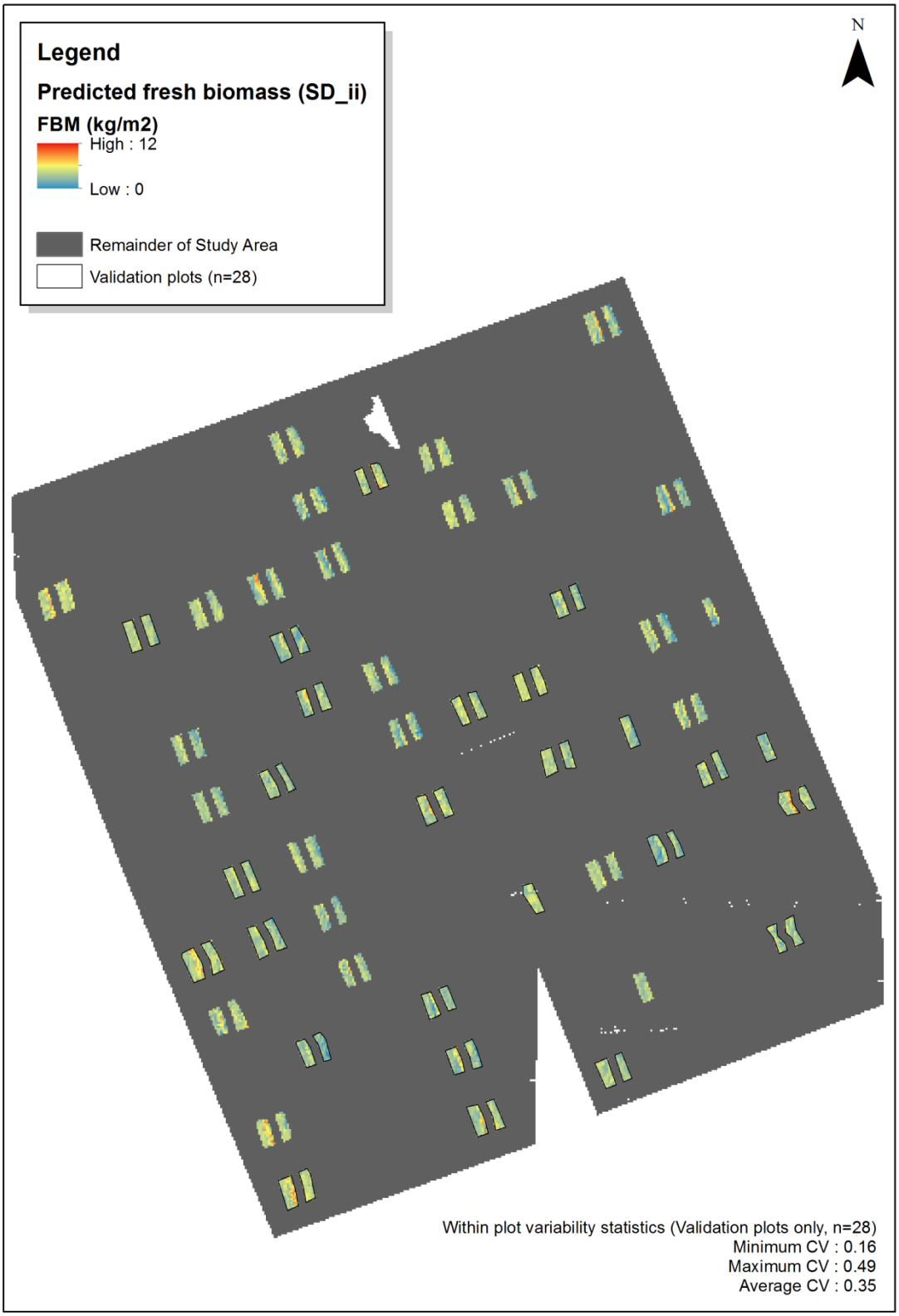
Legend
Predicted fresh biomass (SD_ii)
FBM (kg/m2)
High : 12
Low : 0
Remainder of Study Area
Validation plots (n=28)
N
Within plot variability statistics (Validation plots only, n=28)
Minimum CV : 0.16
Maximum CV : 0.49
Average CV : 0.35

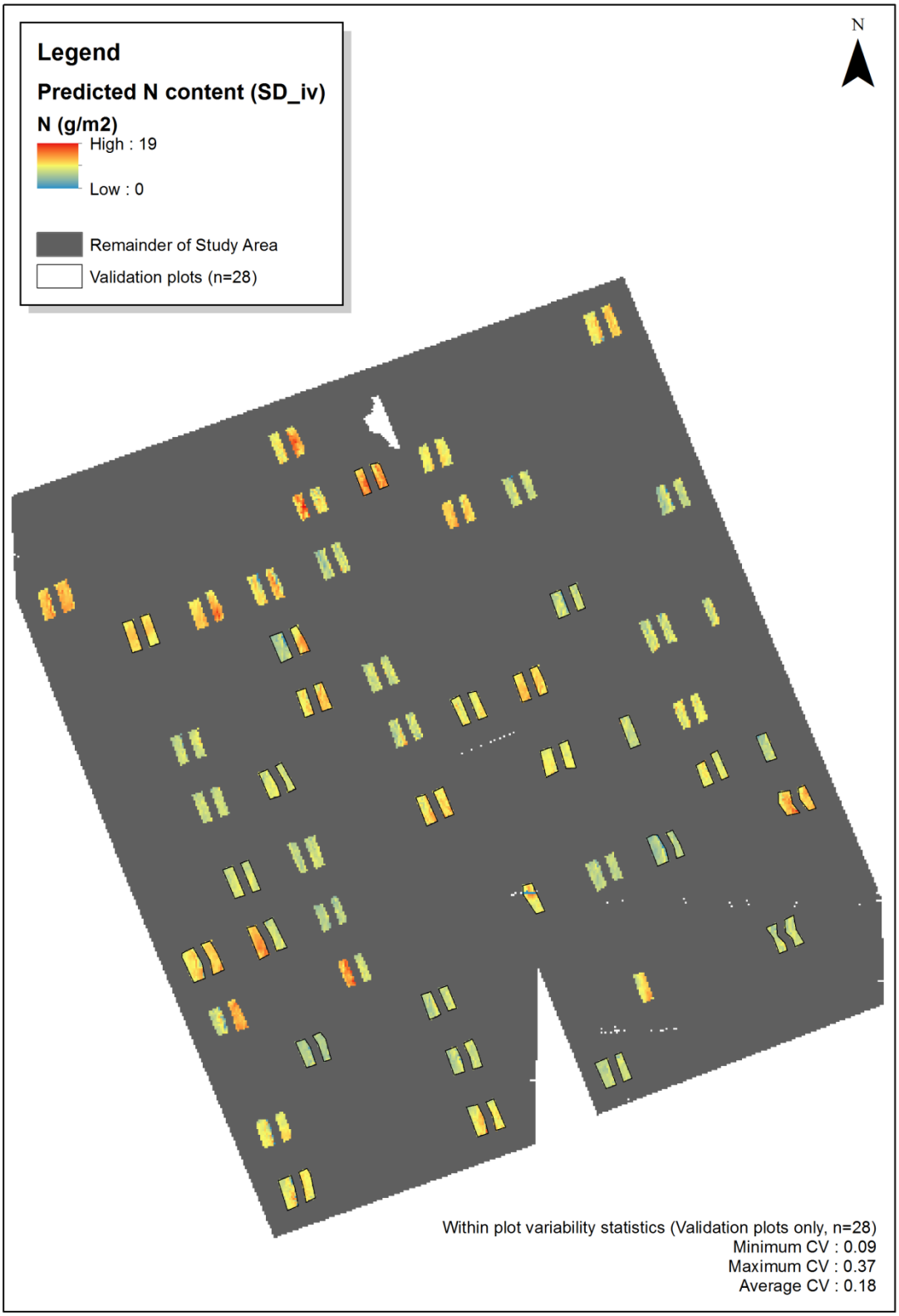
Legend
Predicted N content (SD_iv)
N (g/m2)
High : 19
Low : 0
Remainder of Study Area
Validation plots (n=28)
N
Within plot variability statistics (Validation plots only, n=28)
Minimum CV : 0.09
Maximum CV : 0.37
Average CV : 0.18

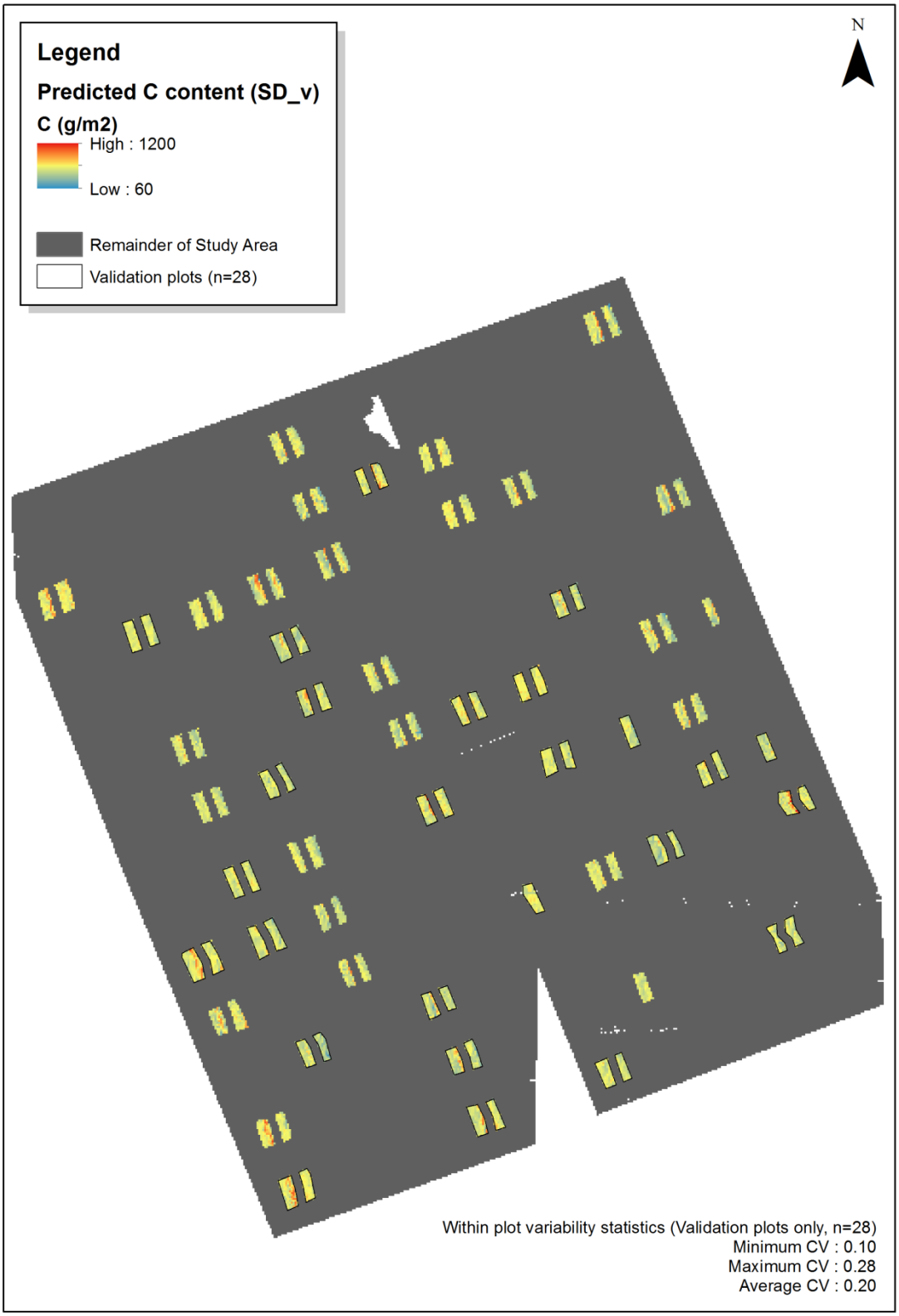
Legend
Predicted C content (SD_v)
C (g/m2)
High : 1200
Low : 60
Remainder of Study Area
Validation plots (n=28)
N
Within plot variability statistics (Validation plots only, n=28)
Minimum CV : 0.10
Maximum CV : 0.28
Average CV : 0.20

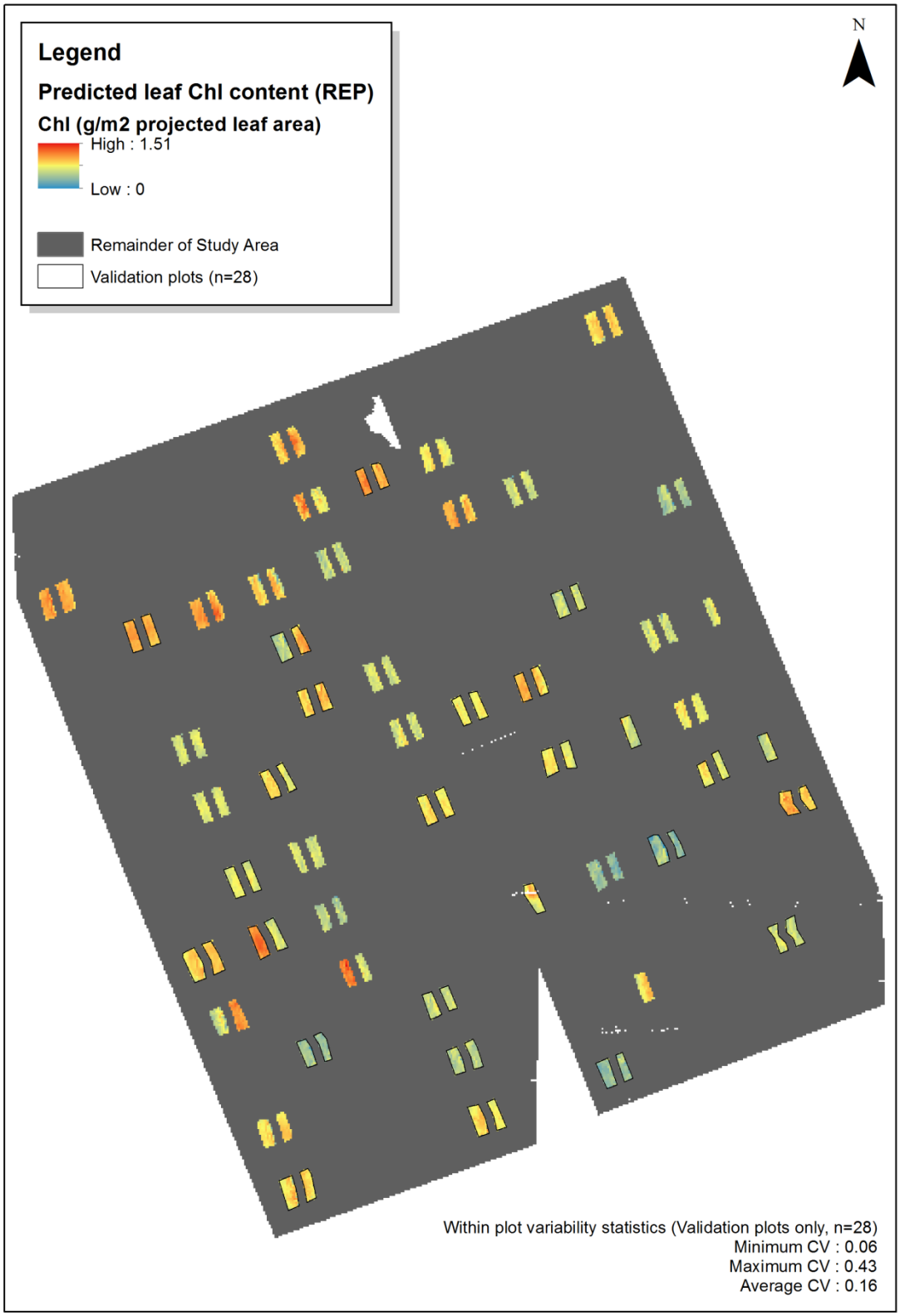
Legend
Predicted leaf Chl content (REP)
Chl (g/m2 projected leaf area)
High : 1.51
Low : 0
Remainder of Study Area
Validation plots (n=28)
N
Within plot variability statistics (Validation plots only, n=28)
Minimum CV : 0.06
Maximum CV : 0.43
Average CV : 0.16

Appendix M: List of formula's used

PRESS

$$\left\|Y - \tilde{Y}^{[L]}\right\|^2$$

Where Y is a vector storing the known values of the dependent variable. $\tilde{Y}$ represents a matrix in which the predicted values of the observations for the dependent variable are stored (Abdi, 2010).

REP

$$\frac{100}{\bar{y}}\left[\frac{1}{n}\sum_{i=1}^{n}\left(y_{i-\hat{y}_i}\right)^2\right]^{0.5}$$

Where y_i and $\hat{y}_i$ are observed and predicted values of crop trait, respectively. n represents the number of plots in datasets (28 for both calibration and validation). At last, $\bar{y}$ is the mean of the observed values of a crop trait (Nguyen & Lee, 2006 p. 352).

RMSE

$$\sqrt{\frac{\sum_{i=1}^{n}\left(y_{i-\hat{y}_i}\right)^2}{n}}$$

Where y_i and $\hat{y}_i$ are observed and predicted values of crop trait. n represents the number of plots in datasets (28 for both calibration and validation).

Coefficient of Variation CV (for relative (%) RMSE of validated indices/models)

$$\frac{RMSE}{\bar{y}}$$

Where RMSE represents the Root Mean Square Error, as formulated above. $\bar{y}$ is the mean of the observed values of a crop trait.

Coefficient of Variation CV (for prediction maps)

$$\frac{\sigma}{|\mu|}$$

Where σ represents the standard error of the population (all observed values within a plots ROI) and μ the mean value thereof.

Appendix N: Screen dumps of scripts utilized during this research

Extraction of plot averaged spectra (ESRI ArcMap)

The below script extracts the spectral data from individual plots based on the region of interest (ROI) defined for each. Subsequently, the average reflectance values of all pixels within the ROI are averaged over each separate waveband. The specific script below performs these tasks only for the first flight line, a separate script with slightly different inputs repeats is used for the second flight line for the same purpose.

```
import os, arcinfo
arcpy.CheckOutExtension('spatial')

# Import system modules
import arcpy
from arcpy import env
from arcpy.sa import *

#Collection of all bands in rasterfile
bands = []

# Set environment settings
env.workspace = "U:\\GIMA\\Thesis\\NEWDATA\\FWHM30_rectified_newdata\\HDC_fl1_FWHM30_2ndOrder.tif"

#Get all bands in raster
for band in arcpy.ListRasters():
    #append to list
    bands.append(band)
print bands

for idx, band in enumerate(bands):
#####ZONAL STATISTICS
    # Set local variables
    inZoneData = "U:\\GIMA\\Thesis\\NEWDATA\\HDCOats_plots_30cm_FL1.shp"
    zoneField = "PlotID"

    inValueRaster = "U:\\GIMA\\Thesis\\NEWDATA\\FWHM30_rectified_newdata\\HDC_fl1_FWHM30_2ndOrder.tif\\"+band
    outTable = "U:\GIMA\Thesis\NEWDATA\HDCSpectra_FL1.gdb\\"+band+"table"


    # Check out the ArcGIS Spatial Analyst extension license
    arcpy.CheckOutExtension("Spatial")

    # Execute ZonalStatisticsAsTable
    outZSaT = ZonalStatisticsAsTable(inZoneData, zoneField, inValueRaster,
                                     outTable, "NODATA", "MEAN")
##### CHANGE MEAN FIELD NAME
    arcpy.AlterField_management(r"U:\\GIMA\\Thesis\\NEWDATA\\HDCSpectra_FL1.gdb\\"+band+"table", 'MEAN', band+'MEAN')


    outFeatureClass = r"U:\\GIMA\\Thesis\NEWDATA\\HDCSpectra_FL1.gdb\\"+band+"table"


    if idx == 0:
        base_table = outFeatureClass

    else:
        inFeatures = base_table
        joinField = "PlotID"
        joinTable = outFeatureClass
        fieldList= (band+"MEAN")

        # Process: Join Field
        arcpy.JoinField_management(inFeatures, joinField, joinTable, joinField, fieldList)
```

Generation of correlation matrices/contour plots (R)

```
### GLOBALS ###

# Set number of bands
n_band=101

# Load (calibration) data
dat <- read.table("C:\\Users\\Bob\\Dropbox\\GIMAThesis\\Tables_NEW\\ContourPlots\\Cal_Refl_AND_Traits.txt", header=TRUE)

# Generate data frame containing all possible band combinations (based on band IDs)
res <- expand.grid(paste0("b", seq(from = 450, to = 950, by = 5)),paste0("b",seq(from = 450, to = 950, by = 5)),outcome=c("lccont"))

### SIMPLE RATIO'S ###

#Ignore warnings; correlation between similar variables is missing
res$R2 <- apply(res, MARGIN=1,FUN=function(x){
  return(cor(dat[,x[1]]/dat[,x[2]],dat[,x[3]])^2)
})

# Generate Contour Plot
library(scales)
library(ggplot2)
library(grid)
p1 <- ggplot(res, aes(x=Var1, y=Var2, fill=R2)) +
  geom_tile() +
  facet_grid(~outcome)
p1 +
  theme(axis.text.x=element_text(angle=+90)) +
  theme(legend.key.height = unit(7, "line")) +
  geom_vline(xintercept=c(seq(from = 1, to = 101, by = 5)),color="black") +
  geom_hline(yintercept=c(seq(from = 1, to = 101, by = 5)),color="black") +
  labs(list(title = "Contour plot of R^2 values for all possible correlations between Simple Ratio indices & leaf Chl content", x = "Wavelength 1 (nm)", y = "Wavelength 2 (nm)")) +
  scale_x_discrete(breaks = c("b450","b475","b500","b525","b550","b575","b600","b625","b650","b675","b700","b725","b750","b775","b800","b825","b850","b875","b900","b925","b950")) +
  scale_y_discrete(breaks = c("b450","b475","b500","b525","b550","b575","b600","b625","b650","b675","b700","b725","b750","b775","b800","b825","b850","b875","b900","b925","b950")) +
  scale_fill_gradientn(colours = rainbow(6), breaks = seq(from = 0, to = 1, by = 0.03))

### NDVIS ###


#Ignore warnings; correlation between similar variables is missing
res$R2 <- apply(res, MARGIN=1,FUN=function(x){
  return(cor((dat[,x[2]]-dat[,x[1]])/(dat[,x[2]]+dat[,x[1]]),dat[,x[3]])^2)
})

# Generate Contour Plot
library(scales)
library(ggplot2)
p1 <- ggplot(res, aes(x=Var1, y=Var2, fill=R2)) +
  geom_tile() +
  facet_grid(~outcome)
p1 +
  theme(axis.text.x=element_text(angle=+90)) +
  theme(legend.key.height = unit(7, "line")) +
  geom_vline(xintercept=c(seq(from = 1, to = 101, by = 5)),color="black") +
  geom_hline(yintercept=c(seq(from = 1, to = 101, by = 5)),color="black") +
  labs(list(title = "Contour plot of R^2 values for all possible correlations between Normalized Difference indices & leaf Chl content", x = "Wavelength 1 (nm)", y = "Wavelength 2
  scale_x_discrete(breaks = c("b450","b475","b500","b525","b550","b575","b600","b625","b650","b675","b700","b725","b750","b775","b800","b825","b850","b875","b900","b925","b950")) +
  scale_y_discrete(breaks = c("b450","b475","b500","b525","b550","b575","b600","b625","b650","b675","b700","b725","b750","b775","b800","b825","b850","b875","b900","b925","b950")) +
  scale_fill_gradientn(colours = rainbow(6), breaks = seq(from = 0, to = 1, by = 0.03))

### SIMPLE DIFFERENCES ###

#Ignore warnings; correlation between similar variables is missing
res$R2 <- apply(res, MARGIN=1,FUN=function(x){
  return(cor(dat[,x[1]]-dat[,x[2]],dat[,x[3]])^2)
})

# Generate Contour Plot
library(scales)
library(ggplot2)
p1 <- ggplot(res, aes(x=Var1, y=Var2, fill=R2)) +
  geom_tile() +
  facet_grid(~outcome)
p1 +
  theme(axis.text.x=element_text(angle=+90)) +
  theme(legend.key.height = unit(7, "line")) +
  geom_vline(xintercept=c(seq(from = 1, to = 101, by = 5)),color="black") +
  geom_hline(yintercept=c(seq(from = 1, to = 101, by = 5)),color="black") +
  labs(list(title = "Contour plot of R^2 values for all possible correlations between Simple Difference indices & leaf Chl content", x = "Wavelength 1 (nm)", y = "Wavelength 2 (nm)
  scale_x_discrete(breaks = c("b450","b475","b500","b525","b550","b575","b600","b625","b650","b675","b700","b725","b750","b775","b800","b825","b850","b875","b900","b925","b950")) +
  scale_y_discrete(breaks = c("b450","b475","b500","b525","b550","b575","b600","b625","b650","b675","b700","b725","b750","b775","b800","b825","b850","b875","b900","b925","b950")) +
  scale_fill_gradientn(colours = rainbow(6), breaks = seq(from = 0, to = 1, by = 0.03))
```

Building the PLS model (R)

```
# Define workspace
setwd("C:/Users/Bob/Dropbox/GIMAThesis/Tables_NEW/PLS")

# Load required data
data <- read.table("CALVAL_FWHM30_indices+spectra.txt", header=TRUE)
data <- as.data.frame(data)
head(data[1:10])
data

# Define train (cal) and test (val) data
caldata <- data[1:28,]
valdata <- data[29:56,]

# Define segment of training/testing dataframe comprising of spectral explanatory data (8=spectra only /  7=spectra + csm)
spectra <- caldata[,8:ncol(caldata)]
spectra <- valdata[,8:ncol(valdata)]

# Create variable to be used as label(s) on the horizontal axis of plots
wavelength <- as.data.frame(t(seq(from = 450, to = 950, by = 5)))

# Calibrate PLS model using Leave-One-Out cross-validation
library(pls)
refl.pls <- plsr(Lccont~ as.matrix(spectra), data = caldata, ncomp = 10, validation = "LOO", jackknife = TRUE)

# Retrieve summary statistics for the calibrated PLS model
summary(refl.pls)

# Generate PRESS values for cross-validation
refl.pls$validation$PRESS

# Generate the fitted values of calibration (ncomp is specified based on PLS model with lowest PRESS value)
predict(refl.pls, ncomp = 4)

## Generate values validation set (after spectra <- valdata[,8:ncol(valdata)] has been defined) (ncomp is specified based on PLS model with lowest PRESS value)
predict(refl.pls, ncomp = 4, newdata = valdata)

# Generate the RMSEP plot to indicate accuracy of the PLS model for different number of components
plot(RMSEP(refl.pls), legendpos = "bottomright")

# Generate the loading weights plot, indicating the loading weights ascribed to individual explanatory variables for
# individual components. The numbers in parentheses after the component labels are the relative amount of X variance
# explained by each component
plot(refl.pls, "loadings", comps = 1:4, legendpos = "bottomleft", labels = wavelength , xlab = "nm", main = "Lccont")
abline(h=0)

# Generate the coefficient plot, indicating the regression coefficients ascribed to individual explanatory variables for
# individual components.
plot(refl.pls, plottype = "coef", ncomp = 1:4, legendpos = "bottomleft", labels = wavelength , xlab = "nm")
abline(h=0)

# Generate R2 values for cross-validation/fitted values (estimate = "train" gives R2 for fitted values)
R2(refl.pls, estimate = "all", intercept = FALSE)
```

2